DEVELOPMENT AND CHARACTERIZATION OF III-NITRIDE

BIPOLAR DEVICES

A Dissertation
Presented to
The Academic Faculty

by

Tsung-Ting Kao

In Partial Fulfillment
of the Requirements for the Degree of Doctor of Philosophy
in the School of Electrical and Computer Engineering

Georgia Institute of Technology
December 2016

DEVELOPMENT AND CHARACTERIZATION OF III-NITRIDE BIPOLAR DEVICES

Approved by:

Dr. Shyh-Chiang Shen, Advisor
School of Electrical and Computer
Engineering
Georgia Institute of Technology

Dr. Russell D. Dupuis
School of Electrical and Computer
Engineering
Georgia Institute of Technology

Dr. P. Douglas Yoder
School of Electrical and Computer
Engineering
Georgia Institute of Technology

Dr. Muhannad S. Bakir
School of Electrical and Computer
Engineering
Georgia Institute of Technology

Dr. Samuel Graham
School of Mechanical Engineering
Georgia Institute of Technology

Date Approved: August 23rd, 2016

To my parents, Chei Kao and Huei-Yu Wu; my older brother, Tsung-Sheng Kao, my beloved wife and son, Yun-Ru Hong and Adam Kao

ACKNOLEDGEMENTS

TABLE OF CONTENTS

LIST OF TABLES

LIST OF FIGURES

LIST OF SYMBOLS AND ABBREVIATIONS

β	Common-emitter d.c. current gain
β_{PF}	Poole-Frenkel coefficient
ρ_c	Specific contact resistance
τ_a	Ambipolar lifetime
τ_c	Collector charging time
τ_e	Emitter charging time
τ_{ec}	Emitter-collector transit time
τ_{sc}	BC junction space-charge transit time
ε_0	Free-space permittivity
ε_s	Relative permittivity
k	Boltzmann constant
η	Ideality factor
η_d	Differential quantum efficiency
η_i	Internal quantum efficiency
α_T	Base transport factor
α	Common-base d.c. current gain
α_i	Internal loss
μ_a	Ambipolar mobility
γ	Emitter injection efficiency
ΔE_g	Bandgap-energy difference
ΔE_c	Conduction band energy difference
Φ_B	Barrier height
A_E	Emitter area
a_0	Lattice constant
AFM	Atomic force microscope
APT	Avalanche phototransistor
AlGaN	Aluminum gallium nitride
AlN	Aluminum nitride
APD	Avalanche photo-detector
BC	Base-collector
BEJ	Base-emitter junction
BCJ	Base-collector junction
BFOM	Baliga's figure of merit
BJT	Bipolar-junction transistor
BV_{CBO}	Open-emitter-open breakdown voltage
BV_{CEO}	Open-base breakdown voltage
$C\text{-}V$	Capacitance-voltage
CBA	Conduction-band-to-acceptor level

I_{Bp}	Back-injected base current
I_{Br}	Base recombination current
I_C	Collector current
I_{Cn}	Electron current of BC junction
$I_{C(OPT)}$	Optical component of the collector current
ICP	Inductive-coil-plasma
I_E	Emitter current
I_{En}	Electron current of BE junction
I_{ph}	Primary photocurrent
III-N	III-Nitride
InGaAs	Indium gallium arsenide
InGaN	Indium gallium nitride
InN	Indium nitride
InP	Indium phosphide
IR	Infrared
$I\text{-}V$	Current-voltage
J_{area}	Area-dependent current component
J_C	Emitter current density
$K_2S_2O_8$	Potassium persulfate
$K_{B,cont}$	Interface recombination current at the base contact
$K_{B,surf}$	Extrinsic base surface recombination current
KOH	Potassium hydroxide
$K_{perimeter}$	Perimeter-dependent recombination current
LD	Laser diode
L_E	Emitter perimeter
L_a	Ambipolar diffusion length
LED	Light-emitting diode
LET	Light-emitting transistor
MMIC	Monolithic microwave integrated circuit
MOCVD	Metalorganic chemical vapour deposition
MQWs	Multiple quantum wells
M	Avalanche multiplication coefficient
N_i	Free carrier concentration in the intrinsic region
N_{ph}	Photon density
OCVD	Open-circuit voltage decay
P	Degree of polarization
PD	Photodetector
PEC	Photon-enhanced chemical
PMT	Photomultiplier tubes
P_{th}	Threshold power density

p_B	Free-hole concentration of base layer
QW	Quantum well
RCLED	Resonant-cavity light emitting diode
R_{on}	On-resistance
R_{sh}	Sheet resistance
$R_{ON}A$	Specific on-resistance
R_λ	Responsivity
RTA	Rapid thermal annealing
RT	Room temperature
SEM	Scanning electron microscopy
RMS	Root-mean-square
Si	Silicon
SiO_2	Silicon dioxide
SiC	Silicon carbide
SBD	Schottky barrier diode
SOG	Spin-on-glass
SRH	Shockley-Read-Hall
S_d	Slope efficiency
TLM	Transmission-line model
TL	Transistor laser
TMA	Trimethylaluminium
UID	Unintentionally doped
UV	Ultraviolet
U	Recombination rate
V	Vanadium
VCSEL	Vertical cavity surface emitting laser
V_{on}	Turn on voltage
V_{bi}	Built-in potential
V_{BE}	Base-emitter junction voltage
V_{CE}	Collector-emitter voltage
V_N	Nitrogen vacancy states
W_B	Base layer thickness
W_E	Emitter layer thickness
XPS	X-ray photoelectron spectroscopy
YL	Yellow luminescence

SUMMARY

This dissertation describes the development and characterization of III-nitride (III-N) bipolar devices for optoelectronic and electronic applications. Research mainly involves device design, fabrication process development, and device characterization for Gallium nitride (GaN) Homojunction *p-i-n* rectifiers, GaN/InGaN *npn* heterojunction bipolar transistors (HBTs) and phototransistors (HPTs), and ultraviolet (UV) light-emitting diodes (LEDs) and lasers. All the epitaxial materials of these devices were grown in the Advanced Materials and Devices Group (AMDG) led by Prof. Russell D. Dupuis at the Georgia Institute of Technology using the metalorganic chemical vapor deposition (MOCVD) technique.

GaN *p-i-n* rectifiers possess several performance advantages over Schottky Barrier Diodes (SBDs) such as ultra-low leakage current and avalanche capabilities that are preferred for high-power applications. In the fabrication of GaN *p-i-n* rectifiers, the major technical challenge is the sidewall leakage current. To address this issue, Ti-based field-termination layer and ledged structure were both incorporated to form a surface depletion layer to partially passivate the sidewall. A vertical *p-i-n* rectifier with the breakdown voltage (V_B) > 800 V and extremely lower $R_{ON}A$ value of 0.28 mΩ-cm^2 were demonstrated. The corresponding Baliga's figure-of-merit (BFOM) of >2.5 GW/cm^2 is achieved. As plotting V_B versus $R_{ON}A$ for GaN power rectifiers reported to date, our device also demonstrated the same trend for GaN *p-i-n* rectifiers when it scales to the 800-V range and showed the lowest $R_{ON}A$ for 800-V devices reported to date.

III-N HBTs are promising devices for the next-generation RF and power electronics because of their advantages of high breakdown voltages, high power handling

capability, high-temperature and harsh-environment operation stability. The radiative recombination processes in direct bandgap semiconductors provide an approach to understand the carrier transport and photon-electron interactions in transistors. We conduct an electroluminescence (EL) study on *npn* GaN/InGaN HBTs by operating HBTs under different biasing conditions. Three radiative recombination paths are resolved in HBTs, corresponding to the band-to-band transition (3.3eV), conduction-band-to-acceptor-level transition (3.15 eV) and yellow luminescence (YL) with the emission peak at 2.2 eV. The band-to-band and the conduction-band-to-acceptor-level transitions mostly arise from the intrinsic base region, while a defect-related YL band could likely originate from the quasi-neutral base region of a GaN/InGaN HBT. The I_B-dependent EL intensities for these three recombination paths are discussed. The results also show the radiative emission under the forward-active transistor mode operation is more effective than that using a diode-based emitter due to the enhanced excess electron concentration in the base region as increasing the collector current increases. The study of the EL emission spectrum provides a method to help resolve the carrier recombination paths in III-N HBTs for further transistor performance improvement in conventional HBT power amplification.

By illuminating UV photons from the backside of a GaN/InGaN *npn* HBT under an open-base configuration, the responsivity (R_λ) of >1 A/W was measured for the device operating at collector-to-emitter voltage (V_{CE}) <15 V in the phototransistor mode. As V_{CE} increases, the carrier multiplication in the reversed biased collector leads to a photocurrent avalanche and a high-R_λ of > 300 A/W is achieved at V_{CE}= 140 V. This is the first demonstration of III-N avalanche phototransistor (APT) and an

open-base HBT under the UV illumination serves as proof-of-concept that the light absorbed in the InGaN base induces the photocurrent amplification.

On the other hand, the use of III-N materials allows for high-performance UV photodetectors (PDs) due to the inherently high UV-to-visible-band rejection ratio, ultra-low dark current, and high-temperature operation. By taking advantage of the inherent current gain and the active mode operation, we demonstrated a high-responsivity GaN/InGaN HPT that can operate in both open-base phototransistor mode and the avalanche phototransistor mode for NUV-to-DUV photodetection applications. The substrate-side illuminated HPT shows a peak R_λ of 1 A/W at $\lambda = 373$ nm, the bandgap wavelength of the $In_{0.03}Ga_{0.97}N$ base layer, and the relatively narrow spectral response due to the absorption of high-energy UV photon from the underlying GaN materials. Under the front-side illumination, the HPT shows a wide-band photoresponse spectrum with the short-wavelength cut-off wavelength well beyond $\lambda = 280$ nm. The HPT exhibits a high UV-to-visible-band rejection ratio ($R_\lambda|_{360nm}/ R_\lambda|_{450nm}$) greater than 8×10^3. At low voltage bias ($V_{CE} < 10$ V), R_λ is 8.2 A/W for $P_{opt} = 13.7$ $\mu W/cm^2$ at $\lambda = 373$ nm and R_λ is 3.4 A/W for $P_{opt} = 1.31$ $\mu W/cm^2$ at $\lambda = 280$ nm. At high V_{CE} (> 35 V), the responsivity performance was enhanced as the device was biased in the APT mode, resulting in $R_\lambda > 100$ A/W at $V_{CE} = 40$ V for $P_{opt} = 1.73$ $\mu W/cm^2$ at $\lambda = 373$ nm. The results demonstrate the feasibility of using III-nitride HPTs as a new form of ultra-low light detection in the entire UV spectral regions.

III-N-based optoelectronic devices have been actively studied and developed due to a wide range in bandgap energy, which covers the full spectrum of optical emission from the near-infrared to deep-ultraviolet (DUV). However, the development

of DUV light emitters has been challenging because of the difficulty in achieving high free-carrier concentrations in both p-type and n-type AlGaN layers with high aluminum mole fraction and high defect density arising from the lattice mismatch in epitaxial layers when these structures are grown on foreign substrates. At Georgia Tech, high reflectivity (R > 99 %) and wide stop-band (> 60 nm) distributed Bragg reflectors (DBRs) were achieved by using a small number of HfO_2/SiO_2 pairs to provide substantial optical feedback. Also, the lapping/polishing/cleaving processes of AlN and GaN substrates were developed and exercised multiple times to ensure high-quality mirror-like facets can be formed to create effective cavities. With the developed process recipes, we have demonstrated a sub-250 nm optically pumped deep-ultraviolet laser using an $Al_xGa_{1-x}N$-based multi-quantum-well structure grown on a bulk Al-polar c-plane AlN substrate. TE-polarization-dominant lasing action was observed at room temperature with a threshold pumping power density of 250 kW/cm^2. After employing high-reflectivity SiO_2/HfO_2 dielectric mirrors on both facets, the threshold pumping power density was further reduced to 180 kW/cm^2. The internal loss and threshold modal gain can be calculated to be 2 cm^{-1} and 10.9 cm^{-1}, respectively.

The achievements in the optical pumping experiments demonstrated the basic optical properties of these wide-bandgap ternary multiple-quantum-well (MQW) heterostructures. However, the demonstration of electrically-pumped UV laser diodes is still challenging and requires further processing recipe improvement. At Georgia Tech, we have established baseline processing flow and repeatable processing modules for AlGaN-based device frontside processing, including a photo-enhanced

surface treatment to remove post-dry-etching-induced surface damage, Vanadium (V)-based n-type ohmic contact for Al-rich n-AlGaN, indium tin-oxide (ITO) transparent contact, and a high reflectance (HR) facet coating using HfO_2/SiO_2 alternative pairs. We also studied and developed repeatable back-side processing modules including wafer lapping and polishing steps for devices grown on AlN and GaN substrates, m-plane facet cleaving, and device packaging. These processing modules in these development efforts will be directly transferred to the UV laser device development for processing integration. These pre-existing processing modules also helped formulate focused research subtasks for the device development. With these developed processing, we have fabricated a high-aluminum-containing ([Al]~ 0.6) AlGaN MQW light emitter employing an inverse-tapered-composition AlGaN:Mg p-type waveguide. The fabricated UV emitter can sustain a d.c. current of at least 10 kA/cm^2 and a pulsed current of at least 18 kA/cm^2 with the measured series resistance of 15 Ω and 11 Ω, respectively. We also established the processing modules for an UV vertical-cavity surface emitting lasers (VCSELs). Currently, resonant-cavity light-emitting diodes (RCLEDs) employing 40-pair GaN/AlGaN DBRs (R= 91%) and 10-pair HfO_2/SiO_2 high-reflectivity dielectric DBRs (R >99 %) were successfully fabricated. The device shows a dominant emission peak at 370 nm with a linewidth of 5.2 nm at a driving current density of 10 kA/cm^2. In addition, we further developed an efficient current confinement design using nitrogen ion implantation. Employing nitrogen ion implantation into p-Al$_{0.06}$Ga$_{0.94}$N layer effectively confines the injected current in a defined aperture without inducing excessive recombination centers. The nitrogen-implanted LEDs show the maximum current density of 20 kA/cm^2 and stable electrical

characteristics over ten-hour constant current stressing. These results suggest the current confinement using nitrogen ion implantation provide a suitable electrical injection design for VCSEL fabrication. The possibility of an UV VCSEL could be realized by future optimization of higher DBR reflectivities, lower resistive heating and better lateral mode confinement.

In conclusion, this dissertation covers the complete development and characterization on GaN *p-i-n* rectifiers, GaN/InGaN HBTs and AlGaN-based UV light emitters at Georgia Tech. The results not only indicated the great potential of III-N bipolar devices for electronics and optoelectronics applications but also revealed the issues and possible solutions to achieve better performance on III-N devices.

CHAPTER 1

INTRODUCTION OF III-NITRIDE MATERIALS AND DEVICES

1.1 Properties and applications of III-N materials

III-N materials, such as GaN, aluminum nitride (AlN), indium nitride (InN), and their ternary and quaternary alloys are formed by column-III elements with nitrogen atoms. Major properties of binary III-N compound semiconductors are listed in Table 1 [1-5]. As shown in Table 1, III-N materials possess both direct and wide bandgap properties ranging from 0.7 eV (InN) to 6.2 eV (AlN). The wide bandgap GaN and AlN materials enable blue and UV LEDs and LDs for optoelectronic applications. The wide-bandgap property also provides lower noise than other semiconductors for high-performance avalanche photo-detectors (APDs) demonstration. Using ternary or quaternary III-N alloys with InN, such as InGaN or InAlGaN, smaller bandgap can be achieved for bandgap engineering. This flexibility of bandgap engineering not only enables the design of optoelectronic devices for light wavelength from UV to infrared (IR), but also allows the design of different heterostructure, such as the quantum well and the electron blocking layer (EBL) to improve the performance of LEDs and LDs. Therefore, III-N devices have attracted tremendous research attention and become of great commercial importance within the past ten years. Nowadays, III-N-based high-brightness LEDs have dominated the solid-state lighting market. III-N-based LDs in the violet, blue, and green regions have been commercialized for high-density optical storage systems and laser projectors and displays.

Table 1 Semiconductor properties at 300 K [1-2345]

	Binary III-N			Si	GaAs	4H-SiC
	GaN	AlN	InN			
Lattice structure	Würtzite	Würtzite	Würtzite	Diamond	Zincblende	Würtzite
Lattice constant a (Å)	3.19	3.11	3.53	5.431	5.653	3.073
Refraction index at 3eV	2.29	2.15	3.05	5.56	4.5	2.69
Dielectric constant	9.5	8.5	15.3	11.9	13	9.7
Bandgap energy (eV)	3.4	6.2	0.7 ~ 1.0	1.12	1.43	3.26
Nature of bandgap	Direct bandgap	Direct bandgap	Direct bandgap	Indirect bandgap	Direct bandgap	Indirect bandgap
Breakdown field (MV/cm)	3.3	1.2 ~ 1.8	--	~0.25	~0.3	3.5
Electron saturation velocity (10^7 cm/s)	2.5	1.9	3.4	2.3	0.7	1.9
Electron mobility (cm^2/Vs)	1200	300	3200	1350	8500	650
Hole mobility (cm^2/Vs)	30	14	--	480	400	120
Thermal conductivity ($W/cm^{-1}K^{-1}$)	1.3	2.85	0.6 ~ 1.0	1.5	0.5	3.7

For electrical applications, III-N-based devices are suitable for high-power and high-voltage applications due to superior characteristics, such as having a wide bandgap and high breakdown electric field. To date, power electronics based on III-N-based platforms have been intensively studied and commercially available for high-power switching applications. The bandgap engineering of III-N materials also enables the design of heterojunction transistors, such as HBTs and heterojunction field-effect transistors (HFETs). As a result, III-N-based devices have been considered as the most promising candidate for the next generation of power electronics.

However, III-N-based material epitaxy growth and device fabrication processes are still challenging. For III-N epitaxy growth, the hetero-epitaxial growth on foreign substrates and the strain management in heterostructures are the major challenges. Because the cost of III-N native substrates is high, III-N materials are usually hetero-

epitaxially grown on foreign substrates, such as sapphire, SiC or Si substrates. As shown in Figure 1, the lattice constant (a_0) of III-N materials varies from 3.53 Å (InN) to 3.11 Å (AlN.) Compared to the lattice constant of sapphire (4.78 Å), SiC (3.08 Å) and Si (5.43 Å), a lattice mismatch is inevitable. A high density of threading dislocations (~10^8 to10^9 cm^{-2}) in epitaxial structures is commonly observed originating from the strained hetero-epitaxial growth on foreign substrates due to the lattice mismatch [6]. In addition, a lightly strained III-N heterostructure, such as AlN/GaN, may be preferred for improving device performance. The strain, however, may result in material cracks and defect formation if the growth condition is not well controlled. As a result, the strain management in III-N heterostructures is important to achieve the desired layer structure with minimal strain-induced defects.
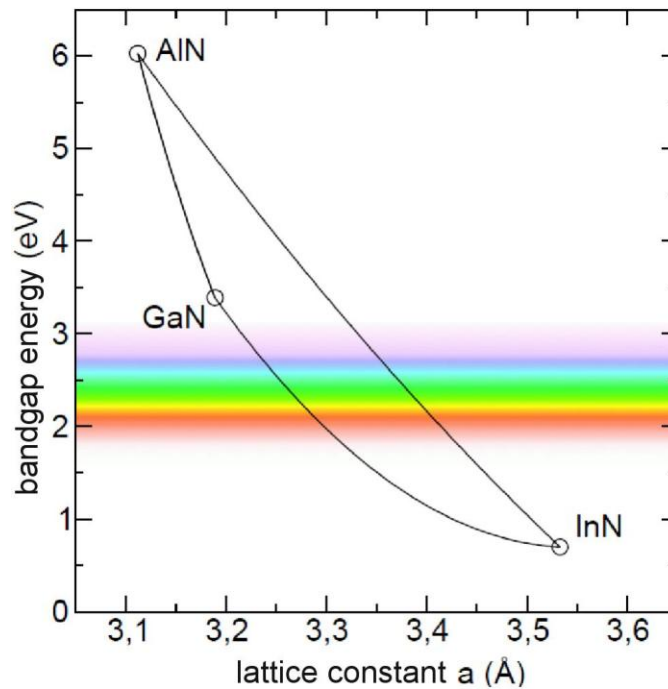
Figure 1. Bandgap energy (eV) versus lattice constant (Å) for Würtzite III-N semiconductors at 300 K.

The device fabrication processes of III-N devices are also challenging. Because III-N materials have good chemical stability, high-power chlorine-based plasma-enhanced dry etching techniques in reactive-ion-etching (RIE) or inductive-coil-plasma (ICP) etching tools are typically used to etch III-N materials [7-10]. Previous studies have shown that high-power plasma may damage III-N materials and create nitrogen vacancies [11,12] or deep-level traps [13,14], which reduce III-N device performance. Alternatively, photon-enhanced wet etching techniques with electrodes [15] and without electrodes [16,17] can prevent plasma damage but these wet etching techniques suffer from non-uniform etching if the process is not well controlled.

Because of the wide bandgap properties, on the other hand, high contact resistance or Schottky rectifying behavior are commonly observed on the metal contact of III-N devices. Although different metal stacks and annealing processes have been proposed and studied for *n*-type [18,19] and *p*-type contacts [20, 21], low-resistance contact for III-N bipolar devices still require further study and optimization. In addition to the issues of etching process and ohmic contact, there are still many challenges for processes development of III-N bipolar devices for different applications.

In this dissertation, the research work focus on the development and characterization for different III-N bipolar devices including GaN homojunction *p-i-n* rectifiers, III-N HBTs, HPTs and AlGaN-based UV light emitters. Several unique fabrication processes were developed to resolve the issues observed in these device and the research results at Georgia Tech will be discussed in the following sections.

1.2   GaN homojunction *p-i-n* rectifiers

High-efficiency power semiconductor devices are the key to improving the efficiency of power electronic systems. For the last three decades, Si power devices (such as MOSFETS, IGBTs, and diodes) have dominated the power device market. During this time, there have been tremendous improvements in silicon power device performance. However, these devices are now approaching the physical limits of silicon. Alternative materials, such as SiC and GaN are enabling a new generation of power devices that can far exceed the performance of silicon-based devices, which will allow continued improvement of the efficiency of power electronics. SiC diodes have already been commercialized and they are increasing market share in applications that demand the higher efficiency. However, there is also great interest in developing GaN-based power devices because the fundamental material-based figure of merit of GaN is at least five times better than SiC and nearly 1000 times that of Si. This is because the power device figure of merit for a majority-carrier device is proportional to the product of carrier mobility with the critical electric field to the power of three ($\mu_n E_c^3$), where E_c is the critical field at which avalanche breakdown occurs. The critical electric field is mostly determined by the bandgap of the semiconductor and hence the recent emergence of wide-bandgap semiconductors for use in power electronics. The implications of a larger figure of merit are profound; increased temperature of operation, reduced device area and capacitance, reduced losses during switching, conduction, and off-state.

GaN-based power rectifiers including *p-i-n* diodes [22-29] and SBDs [30-34] have attracted much research interest in recent years because of their ultra-low conduction loss, high-voltage and high-temperature operations for next-generation power

5

electronic circuits. GaN *p-i-n* rectifiers in particular possess several performance advantages over SBDs such as ultra-low leakage current and avalanche capabilities that are preferred for high-power applications. Previously, these devices were fabricated on foreign substrates such as silicon, sapphire [25], and silicon carbide (SiC) [26], which force the devices to be fabricated as lateral devices. However, a high density of threading dislocations (in the order of $10^8 \sim 10^9$ cm^{-2}) originating from the strained heteroepitaxial growth on foreign substrates may become problematic for high-voltage *p-i-n* rectifiers as the drift layer becomes thicker.

The technical challenges for GaN *p-i-n* power rectifiers are primarily on the semiconductor device development, including low-defect-density, large-area heterojunction epitaxy, appropriate passivation and field-termination techniques, and ohmic contact for exploiting the inherent advantages of vertical GaN power switches. Most recently, the availability of sufficiently large GaN substrates enabled the homoepitaxial growth of GaN-based devices. Among these high-quality native substrates prepared by different techniques, free-standing GaN (FS-GaN) substrates [35] currently offer a threading dislocation density $<10^6$ cm^{-2} with a large size of >2 in. diameter. Using conducting FS-GaN substrates, one may realize a vertical power switch in III-N power electronic devices that allow for high-power operations in the on-state and lowest possible conduction loss at a given blocking voltage rating. For example, Hatakeyama *et. al.* reported GaN *p-i-n* diodes on FS-GaN substrates with low specific on-resistances ($R_{ON}A$) of 0.4 mΩ-cm^2 and breakdown voltages (V_B) of 1.1 kV. The corresponding Baliga's figure of merit ($V_B^2/R_{ON}A$) of 3 GW/cm^2 was obtained. Kizilyalli *et. al.* reported

6

vertical GaN *p-i-n* rectifiers with $R_{ON}A$= 2 mΩ-cm^2 and high V_B of 2.6 kV. A summary of state-of-the-art performance for GaN *p-i-n* vertical rectifiers is given in Table 2.

Table 2. Summary of state-of-the-art performance for GaN *p-i-n* vertical rectifiers

Affiliation	Doping concentration in *p*-GaN (cm^{-3})	Doping concentration in *n*-GaN (cm^{-3})	*i*-GaN thickness (μm)	Leakage current density at -200 V (A/cm^2)	$R_{ON}A$ (mΩ-cm^2)	V_B (kV)	*Ref.* (year)
Avogy	5×10^{17}	--	>15	~2×10^{-8}	2	2.6	[22] (2013)
Hitachi cable	5×10^{17}	2×10^{18}	10	~5×10^{-6}	0.4	1.1	[23] (2011)
General Electric	10^{19}	2×10^{18}	4	--	24-56	0.17-0.265	[27] (2005)
Hitachi cable	10^{18}	2×10^{18}	10	~10^{-4}	1.2	0.8	[24] (2013)
Sumitomo	3×10^{18}	--	7	~2×10^{-7}	6.3	0.925	[25] (2007)
Georgia Tech	10^{18}	5×10^{18}	2.5	>10^{-4}	3	0.54	[36] 2006
Hitachi cable	10^{18}	2×10^{18}	20	~10^{-4}	0.9	3	[24] 2013
Cornell	10^{18}	2×10^{18}	10	~2×10^{-8}	0.55	1.7	[28] 2016
Sandia Lab	2×10^{19}	2×10^{18}	15	<10^{-4}	1	2.6	[29] 2016

At Georgia Tech, we fabricated homojunction GaN *p-i-n* rectifiers grown on either FS-GaN or sapphire substrate. The *p-i-n* rectifier grown on sapphire shows V_B of 600 V and a specific on-resistance ($R_{ON}A$) of 0.66 mΩ-cm^2. On the other hand, a *p-i-n* rectifier grown on a FS-GaN substrate shows substantial improvement with V_B> 800 V and $R_{ON}A$ = 0.28 mΩ-cm^2. The corresponding BFOM of >2.5 GW/cm^2 is achieved. As plotting V_B versus $R_{ON}A$ for GaN power rectifiers reported to date, our device also

demonstrated the same trend for GaN *p-i-n* rectifiers when it scales to the 800-V range and showed the lowest $R_{ON}A$ for 800-V devices reported to date.

We then performed temperature-dependent capacitance-voltage (*C-V*), current-voltage (*I-V*), and open-circuit voltage decay (OCVD) measurements to understand the carrier transport mechanism in vertical GaN *p-i-n* rectifiers. The *C-V* data shows the free-carrier concentration of the drift layer is 1.3×10^{16} cm^{-3} at 298 K and increases to 2.0×10^{16} cm^{-3} at 448 K. The *T-I-V* results show a low $R_{ON}A$ of 0.28 mΩ-cm^2 at 298 K and increases slightly (by <10 %) at 448 K. By performing OCVD measurement under high-level injection, τ_a can be extracted to be 9.6 ns at 298 K and monotonically increases to 22 ns at 448 K. The reverse *T-I-V* measurement reveals the leakage current up to -200 V is mainly attributed to the field-assisted ionization process from deep-level traps. These results can be explained by the Poole-Frenkel effect and the corresponding Poole-Frenkel coefficient is 3.1×10^{-4} eV·V$^{-1/2}$·cm$^{-1/2}$.

1.3   GaN/InGaN heterojunction bipolar transistors

Compared to FETs with horizontal channels, the vertical structure of HBTs provides higher current density and higher power handling capability. Nowadays, Gallium arsenide (GaAs)-based HBTs have become important commercial technologies for wireless communication applications. However, the small breakdown voltage, attributed to small bandgap of GaAs and Indium phosphide (InP), limits the maximum deliverable power of GaAs-based HBTs.

Because of the wide bandgap of AlN and GaN, III-N HBTs are expected to have high power handling capability, high breakdown voltage and high-temperature-operation capability than GaAs-based HBTs. A number of *npn* AlGaN/GaN HBTs have been

8

demonstrated with good current gain and high breakdown voltage [37-41] and the capability to operate at 250 °C and 600 °C [42, 43, 44]. However, only few of the reported devices are capable of achieving high collector current density (J_C) greater than 1 kA/cm^2. This is attributed to the highly resistive p-type base layer which cannot be effectively doped. To reduce the base resistance, GaN/InGaN HBTs were implemented to increase the free-hole concentration in the Mg-doped InGaN base layer [45, 46]. A re-growth technique is also used to grow a highly doped *p*-type contact region after the emitter mesa etching step [47, 48]. The re-grown *p*-layer helps reduce the contact resistance to retain good current gain and collector current drive in GaN/InGaN HBTs [49]. Nevertheless, low-resistance metal contact to the *p*-InGaN base layer is still challenging because of the inevitable plasma etching damage and associated type conversion during fabrication processes [50].

Tremendous efforts have been made and lead to successful demonstration of high-performance *npn* GaN/InGaN HBTs in the past few years at Georgia Tech. High current gain (>110), high current drive (>141 kA/cm^2) and high breakdown voltage (>160 V) have been achieved on direct-grown *npn* GaN/InGaN HBTs [51]. The measured unity current gain frequency (f_T) and maximum oscillation frequency (f_{max}) on the GaN/InGaN HBTs are 5 GHz and 1.2 GHz, respectively [52]. Further improvement has been made to achieve f_T= 8 GHz and f_{max}= 1.8 GHz [53]. Compared to the direct-grown *npn* AlGaN/GaN HBTs reported with f_T of 1 GHz [54], the GaN/InGaN HBTs developed at Georgia Tech demonstrated a great potential for the high-power amplification applications. On the other hand, the radiative recombination processes in direct bandgap semiconductors provide an approach to understand the carrier transport and photon-

9

electron interactions in transistors. It has also been proposed to enable next-generation optoelectronic integrated circuitssuch as light-emitting transistors (LETs) and transistor lasers (TLs) [55-57]. Although the LET action of GaN/InGaN HBTs was previously reported [58,59], the origin of radiative recombination processes was not clearly resolved.

At Georgia Tech, we conduct an electroluminescence (EL) study of *npn* GaN/InGaN HBTs to understand their possible radiative recombination paths and impacts on the device performance [60]. Through the EL analysis for devices operating at the diode modes and the forward-active modes, we are able to resolve the origins of three distinct radiative recombination paths and their possible origin of radiative recombination in physical devices. The base current (I_B)-dependent EL intensities for these three recombination paths are discussed. The results also show the radiative emission under the forward-active transistor mode operation is more effective than that using a diode-based emitter due to the enhanced excess electron concentration in the base region as increasing the collector current increases. The study of the EL emission spectrum provides a method to help resolve the carrier recombination paths in III-N HBTs for further transistor performance improvement in conventional HBT power amplification.

By illuminating UV photons from the backside of an open-bas HBT device, we further observed the photocurrent amplification and multiplication from an open-base GaN/InGaN HBT and demonstrated the first III-N APT operation [61]. A responsivity of ~1 A/W was achieved for V_{CE}< 15 V and it was further increased to R_λ > 300 A/W as the device was operated near the avalanche breakdown voltage. The results suggest that the light absorbed in the base of HBT device can induce the photocurrent amplification and

further multiplication. As a result, the results demonstrate the feasibility of using III-nitride HPTs as a new form of ultra-low light detection in the entire UV spectral regions

1.4   GaN/InGaN heterojunction phototransistors

UV photon detectors have a wide range of applications in astronomy, environmental monitoring, advanced optical communications, bio-chemical sensing, and other emerging technologies. Photomultiplier tubes (PMTs) are widely used because they provide optical gains on the order of 10^6 with low dark current. But PMTs have the disadvantages of low photocathode quantum efficiency for UV light, high operation voltages (>1000 V), and cooling system requirement [62]. The expensive filters for visible-blind or solar-blind detection and the large and fragile body also seriously restrict their applications. On the other hand, the use of wide-bandgap semiconductors allows for high-performance UV photodetectors to possess inherently high visible-to-UV rejection ratio, ultra-low dark current, and high-temperature operation. Furthermore, the flexibility of employing bandgap engineering for the III-N material system enables selective photon detection of specific wavelengths in different UV bands, which offers further reduction of size, weight and cost in advanced UV detection systems.

To date, high-sensitivity UV photodetectors using III-N material platforms have been actively studied. For example, III-N *p-i-n* diodes can achieve ultra-low-noise equivalent power and high detectivity at room temperature [63 - 65]; III-N metal-semiconductor-metal (MSM) detectors were also widely reported [66,67]; and high-performance single-photon Geiger-mode avalanche photodiodes (GM-APDs) have been reported [68, 69].

In the context of high-sensitivity, low-photon-flux detection, a large photocurrent gain is highly desired for photodetectors. Although semiconductor APDs can provide a comparable large optical gain with the PMTs, combined with the benefits of small size, high reliability, high speed, low operation voltage, low power consumption, low cost, all-solid-state integration, and the Geiger-mode operation, the photocurrent gain commonly achieved in APDs usually comes at a cost of noisy operation due to concurrent amplification of the leakage current and the photocurrent under high electric fields.

On the other hand, HPTs offer large optical gain at low bias voltage and are comparable with the HBTs in terms of their epitaxial structures and fabrication processes. In the past, HPTs were demonstrated on smaller-bandgap materials for infrared detection and fiber-optic communications [70‐73]. In 1981, Campbell *et. al.* achieved high-performance InP/InGaAs HPTs with high gain ($h_{FE}\sim$100 at 20 nW incident power) and a gain-bandwidth product in excess of 1.7 GHz. In 1983, avalanche HPTs were successfully demonstrated InP/InGaAs HPTs with extremely high gain ($h_{FE}> 10^4$) as the bias voltage near the device's breakdown voltage. III-N-based HPTs were also demonstrated in recent years [74,75,76]. Yang *et. al.* reported a GaN/AlGaN HPT with gain in excess of 10^5 [74]. From 360 to 400 nm, an eight orders of magnitude drop in responsivity was achieved. Mouillet *et. al.* demonstrated a visible-blind AlGaN/GaN HPT with the dark current as low as 34.6 pA/mm^2 at 3 V and the responsivity of 160 A/W under 0.78 nW/cm^2 illumination [75]. Lee *et. al.* reported an UV Al$_{0.17}$Ga$_{0.83}$N/GaN-based HPTs with a bandpass spectral responsivity ranging from 280 to 390 nm [76]. With a bias voltage of 6 V, the responsivity at an incident of 340 nm was as high as 1500 A/W. However, these III-N HPT devices can only be operated at low

voltage bias (< 5 V). The performance of these devices was severely limited by defect densities from various sources and the extended operation of III-N phototransistors under high electric field is rarely addressed.

At Georgia Tech, we demonstrated a high-responsivity GaN/InGaN HPT that can operate in both open-base phototransistor mode and the avalanche phototransistor mode for NUV-to-DUV photon detection [77, 78]. The substrate-side illuminated HPT shows a peak R_λ of 1 A/W at $\lambda = 373$ nm, the bandgap wavelength of the $In_{0.03}Ga_{0.97}N$ base layer, and the relatively narrow spectral response due to the absorption of high-energy UV photon from the underlying GaN materials. Under the front-side illumination, the HPT shows a wide-band photoresponse spectrum with the short-wavelength cut-off wavelength well beyond $\lambda = 280$ nm. The HPT exhibits a high UV-to-visible-band rejection ratio ($R_\lambda|_{360nm}/R_\lambda|_{450nm}$) greater than 8×10^3. At low voltage bias ($V_{CE} < 10$ V), R_λ is 8.2 A/W for $P_{opt} = 13.7$ µW/cm^2 at $\lambda = 373$ nm and R_λ is 3.4 A/W for $P_{opt} = 1.31$ µW/cm^2 at $\lambda = 280$ nm. At high V_{CE} (> 35 V), the responsivity performance was enhanced as the device was biased in the APT mode, resulting in $R_\lambda > 100$ A/W at $V_{CE} = 40$ V for $P_{opt} = 1.73$ µW/cm^2 at $\lambda = 373$ nm. The results demonstrate the feasibility of using III-nitride HPTs as a new form of ultra-low light detection in the entire UV spectral regions.

1.5 AlGaN-based UV light emitters

III-N-based optoelectronic devices have been actively studied and developed for over two decades. The wide range of the bandgap energy in III-N materials (from 0.7 eV to 6.2 eV) covers the full spectrum of photon emission from the near-infrared to DUV wavelengths. Today, III-N-based solid state lighting is the viable technology for future energy-efficient light sources. High-quality DUV LEDs have also been commercialized

for water sanitation and bio-chemical agent detection applications. These UV emitters typically use AlGaN alloy system to achieve wavelengths below 280 nm [79-83]. On the other hand, the development of DUV LDs for $\lambda < 280$ nm has been challenging because of the difficulty in achieving high free-carrier concentrations in both p-type and n-type AlGaN layers with high aluminum mole fraction and high defect density arising from the lattice mismatch in epitaxial layers when these structures are grown on foreign substrates. As the emission wavelength decreases, threshold pumping power density (P_{th}) for laser action will also increase due to the fact that spontaneous emission rate increases and is approximately proportional to $1/\lambda^3$.

The primary technical challenges for the realization of UV laser diodes primarily include low-defect-density epitaxy, appropriate passivation and thermal dissipation techniques, and ohmic contact for Al-rich AlGaN materials. In particular, efficient p-type doping of wide-bandgap semiconductor material poses the greatest obstacle to design. Specifically, the high activation energy of Mg acceptors in wide-bandgap III-nitride alloys places constraints on the electrical conductivity of p-type material, leading to challenges in the formation of p-type ohmic contact, parasitic series resistance, Joule heating, hole injection into the active region, and electron leakage. The use of narrower-bandgap AlInGaN materials to ensure higher p-type conductivity is not an appealing alternative due to both a reduction in optical confinement as well as the introduction of severe absorption loss. Inefficient p-type doping furthermore renders perfectly symmetric optical waveguides non-optimal, as asymmetry becomes necessary to maximize the overlap of the lasing mode(s) with the active region, yet minimize this overlap with the p-type ohmic metal, which can represent a severe source of optical loss.

To date, electrically-pumped LDs have not been reported for the lasing wavelength shorter than 336 nm [84].

Recently, various AlGaN-based MQWs lasers with lasing wavelength between 255-305 nm were reported under optical pumping conditions at room temperature (RT) [85-89]. However, lasing actions in sub-250 nm region and internal laser parameters are rarely reported [90, 91]. A summary of state-of-the-art performance characteristics for optically-pumped DUV lasers is given in Table 3. At Georgia Tech, Lochner, *et al.*, demonstrated an optically pumped AlGaN-based MQW laser grown on an AlN substrate with an emission wavelength at 243 nm and a P_{th} of 427 kW/cm^2 [91]. To improve the lasing characteristics, high-reflectivity HfO$_2$/SiO$_2$ mirrors were further developed and employed on the cleaved facets to reduce P_{th} from 250 to 180 kW/cm^2 [92]. The lasing wavelength of 249 nm and a preferential TE-type emission were observed with a degree of polarization ~100 %. The internal loss and threshold gain of this deep-UV laser are estimated to be 2 cm^{-1} and 10.9 cm^{-1}, respectively.

Table 3. Summary of state-of-the-art performance for optically-pumped DUV lasers

Affiliation	Substrate	Excitation wavelength (nm)	Cavity length (mm)	Lasing wavelength (nm)	P_{th} (kW/cm^2)	*Ref.* (year)
Kohgakuin University	4H-SiC	193	0.45	241.5	1200	[93] (2004)
Ioffe Physical-Technical Institute, Russia	Sapphire	266	1	303	800	[94] (2004)
PARC	AlN	248	1	267	126	[95] (2011)

Georgia Tech	AlN	193	1.23	243.5	427	[91] (2013)
Georgia Tech	AlN	193	1.4	249	250 (no HR coating) 180 (w/ HR coating)	[92] (2014)
Georgia Tech	Sapphire	193	1.2	249	95	[96] (2014)

The achievements in the optical pumping experiments demonstrated the basic optical properties of these wide-bandgap ternary MQW heterostructures; however, another requirement for a diode emitter is to have electrically conducting layers and low-resistance ohmic contact. To address these issues, an inverse-tapered p-$Al_xGa_{1-x}N$ waveguide design was employed to improve the hole transport in wide-bandgap p-$Al_xGa_{1-x}N$ layers. For the device fabrication, we applied a unique electrode-less photon-enhanced chemical (PEC) surface treatment techniques using potassium persulfate ($K_2S_2O_8$) and potassium hydroxide (KOH) wet chemicals to reduce the leakage current from the etched sidewall in III-N bipolar devices. Furthermore, V-based ohmic contact was developed for n-AlGaN layers to reduce the contact resistance for AlGaN-based UV light emitters. Compared to Ti-based metal stacks, V-based ohmic contact can achieve one order of magnitude lower specific contact resistance from 3×10^{-4} Ω-cm^2 to 2×10^{-5} Ω-cm^2 on n-$Al_{0.55}Ga_{0.45}N$ layer with reduced post-deposition annealing temperature from 825 ^{o}C to 775 ^{o}C. The x-ray photoelectron spectroscopy (XPS) results suggest that the formation of N-V bonds lead to the increase in binding energy at V/AlGaN interface. With these processing schemes, the fabricated Al-rich AlGaN-based diodes show a smaller turn-on voltage while maintaining a high level of current conduction [97]. The

fabricated devices can sustain a d.c. current of at least 10 kA/cm^2 and a pulsed current of at least 18 kA/cm^2 with the measured series resistance of 15 Ω and 11Ω, respectively.

On the other hand, VCSEL is a vertical-emitting-type laser. It is formed by sandwiching a few-lambda cavity in a pair of reflectors, usually in the form of DBRs, with a very high reflectivity (> 99.9 %). In contrast to edge-emitting LDs, photons in the cavity of VCSEL are vertically in resonance and emit outside perpendicularly to the surface of the structure. This laser diode can have many advantageous properties than conventional edge emitting laser, such as circular beam shape, lower divergence angle, two-dimensional laser array possible, efficient testing, low threshold, and so on. Owing to these superior performances, VCSELs had become commercial products at long wavelength range. In fact, short-wavelength VCSELs are also very promising for the applications of storage, display, and projection. In particular, the use of two-dimensional arrays of blue VCSELs could further reduce the read-out time in high density optical storage and increase the scan speed in high-resolution laser printing technology.

However, the demonstration of electrically-pumped UV VCSELs is still challenging. First, the requirement for high reflectivity and high quality DBRs using AlGaN and GaN materials is quite formidable since these two materials have large lattice mismatch and difference in thermal expansion coefficients that tends to form cracks in the epitaxially grown DBR structure. These cracks in DBR could result in the reduction of reflectivity and increase in scattering loss. Second, a lack of conductivity in the mirrors used in UV VCSELs makes it harder to deliver uniform current injection into the active region, and ultimately to realize high modal gain. Carriers are introduced into the active region with sophisticated current injection schemes, such as single or double intra-cavity

contact. With these approaches, a highly conductive layer spreads the current laterally, prior to injection into the active region. Third, III-N materials are unsuitable for current-spreading, due to their very low conductivity, especially for AlGaN materials. The ITO transparent contact has significant optical loss in the UV spectral range, making the placement of this layer critical to device performance. A further challenge for the UV VCSELs is the current confinement. The selective oxidation process, which is repeatable and reliable for manufacturing GaAs VCSELs, is still under investigation for III-N WBG materials. Currently researchers have turned to current confinement schemes that include patterning apertures in SiO_2 or Si_3N_4 and ion implantation of p-AlGaN. With these challenges, the electrically-pumped UV VCSELs have not been demonstrated for the lasing wavelength shorter than 400 nm. A summary of prior work in III-N VCSELs is shown below in Table 4.

Table 4. Summary of III-N electrically pumped VCSEL reported to date (as of Dec. 2015)

Affiliation	Top DBR structure	Bottom DBR	λ (nm)	Pumping mode	J_{th} (kA/cm²)	Aperture (µm in Dia)	P_{out} (mW)	Ref. (year)
NCTU	8x Ta_2O_5/SiO_2	29x AlN/GaN	462.8	CW (77K)	1.8	10	-	[98] (2008)
Nichia	11.5x Nb_2O_5/SiO_2	7x Nb_2O_5/SiO_2	414	CW	13.9	8	0.14	[99] (2008)
Nichia	11.5x Nb_2O_5/SiO_2	7x Nb_2O_5/SiO_2	420	CW	15.9	8	0.62	[100] (2009)
NCTU	10x Ta_2O_5/SiO_2	29x AlN/GaN	412	CW	12.4	10	-	[101] (2010)
Nichia	Nb_2O_5/SiO_2	Nb_2O_5/SiO_2	451	CW	3	8	0.7	[102] (2011)
Nichia	Nb_2O_5/SiO_2	Nb_2O_5/SiO_2	503	Pulse	28	10	0.8	[102] (2011)
Panasonic	13x ZrO_2/SiO_2	13x ZrO_2/SiO_2		CW	0.6	20	0.003	[103] (2012)
EPFL	7x TiO_2/SiO_2	41.5x $l_{0.8}In_{0.2}N$/GaN	~420	Pulse	140	8	-	[104] (2012)

UCSB	13x Ta$_2$O$_5$/SiO$_2$	10x Ta$_2$O$_5$/SiO$_2$	411.9	Pulse	102	10	0.0195	[105] (2012)
South China University of Technology	17.5x ZrO$_2$/SiO$_2$	14x ZrO$_2$/SiO$_2$	408~ 436	CW	1.2	15	-	[106] (2014)
Sony	12x Ta$_2$O$_5$/SiO$_2$	14.5x SiO$_2$/SiN$_x$	446	CW	16	8	0.9	[107] (2015)
UCSB	16x SiO$_2$/Ta$_2$O$_5$	12x SiO$_2$/Ta$_2$O$_5$	405	CW	3.5	12	0.55	[108] (2015)

As summarized above in Table 4, the development of VCSEL laser diode structures has been focused on the spectral range around 405-420 nm. This is the spectral range where the threshold of normal Fabry-Perot III-N LDs has a minimum value. This fact may be related to fundamental properties of the InGaN QWs in this composition range and the doping properties of the relatively low aluminum composition of the AlGaN waveguides required for this wavelength range. At Georgia Tech, we have established the fabrication process for an electrically-pumped III-N VCSEL operating at 370 nm, including HfO$_2$/SiO$_2$ dielectric DBR, vanadium-based ohmic contact, ITO transparent contact, and the lapping/polishing of GaN substrate. Currently, we have demonstrated an UV RCLED employing 40-pair high-reflectivity (91%) GaN/AlGaN DBR, a 10-pair HfO$_2$/SiO$_2$ dielectric DBR (>99 %), and a 2-λ optical thickness GaN/InGaN active region. The device shows a dominant emission peak at 370 nm with a linewidth of 5.2 nm at a driving current density of 10 kA/cm^2. The possibility of an UV VCSEL could be realized by future optimization of higher DBR reflectivities and ITO transparency, lower resistive heating and better lateral mode confinement.

1.6   The scope of the dissertation

The purpose of this dissertation is to develop the fabrication processes, to characterize the device performance and to investigate the issues for III-N bipolar devices. The III-N materials properties, the current development status, and technical challenges for III-N bipolar devices, including GaN homojunction *p-i-n* rectifiers, III-N HBTs, HPTs and AlGaN-based UV light emitters have been introduced in this chapter.

Chapter 2 describes the fabrication process development and device characterization of GaN homojunction *p-i-n* rectifiers grown on *c*-plane FS-GaN and sapphire substrates at Georgia Tech. The *C-V*, *I-V*, and breakdown characteristics of GaN *p-i-n* rectifiers will be presented. The ambipolar transport of GaN *p-i-n* rectifiers will be discussed using the open-circuit voltage decay measurement. The temperature-dependent characteristics and the reverse mechanism of GaN vertical *p-i-n* rectifiers will be presented. Finally, the device performance will be compared to other reported results in this chapter

Chapter 3 will first discuss the light-emitting characteristics of GaN/InGaN HBTs that Georgia Tech developed in the past few years. Three radiative recombination paths can be identified and the origin of each transition path will be discussed through the EL study. A theoretical model based on the four-level rate equation is developed to understand their impacts on the device performance. The photoresponse characteristics of a backside-illuminated GaN/InGaN HBTs under open-base configuration will be then presented. The observation of carrier multiplication and the demonstration of first III-N APT under the UV illumination will be discussed. These results present the photocurrent amplification can be realized using an open-base GaN/InGaN HBT under the backside

illumination. Finally, the fabrication and characterization of a GaN/InGaN HPT will be presented. The device performance under frontside and backside illumination will be discussed. Finally, the responsivity performance of GaN/InGaN HPTs operating under HPT and APT modes will be presented and compared to other reported results in this chapter.

Chapter 4 will cover the fabrication process development and device characterization for AlGaN-based UV light emitters, including the optically pumped DUV lasers, electrically-pumped AlGaN-based MQW light emitters and UV RCLEDs with hybrid DBR structures. These devices share similar processing recipes, including Vanadium-based ohmic contact for Al-rich AlGaN layer, high-reflectivity HfO_2/SiO_2 DBRs, and lapping/polishing of AlN and GaN substrates. For the optically-pumped DUV lasers, the improvement in threshold and polarization characteristics after high-reflectivity HfO_2/SiO_2 DBR deposition will be shown. The internal parameters, including the threshold gain and material loss, of AlGaN-based materials will also be presented. For the electrically-pumped AlGaN-based MQW light emitters, the optimization of V-based ohmic contact on AlGaN films will be shown. Furthermore, a XPS analysis is presented to study the interaction at V-AlGaN interface. The improved contact resistance and the incorporation of inverse-tapered structure help facilitate the current transport and lead to high-current injection. Finally, additional processing development, including ITO transparent contact and ion implantation for current confinement, will be shown for the realization toward electrically-pumped UV VCSEL. *I-V* and EL characteristics of UV RCLED with hybrid mirrors will be presented.

CHAPTER 2

DEVELOPMENT OF GAN HOMOJUNCTION *P-I-N* RECTIFIERS

2.1   Introduction

High-efficiency power semiconductor devices are the key to improve the efficiency of power electronic systems. For the last three decades, Si power devices (such as MOSFETS, IGBTs, and diodes) have dominated the power device market. During this time, there have been tremendous improvements in silicon power device performance. However, these devices are now approaching the physical limits of silicon. Alternative materials, such as SiC and GaN are enabling a new generation of power devices that can far exceed the performance of silicon-based devices, which will allow continued improvement of the efficiency of power electronics. SiC diodes have already been commercialized and they are increasing market share in applications that demand the higher efficiency. For example, Bakowski *et. al.* demosonstrated 10 kV/2A SiC power *p-i-n* rectifiers that feature excellent stability of forward characteristics and robust junction termination with avalanche capability of 1 J [109].

On the other hand, there is also great interest in developing GaN-based power devices because the fundamental material-based figure of merit of GaN is at least five times better than SiC and nearly 1000 times that of Si. This is because the power device figure of merit for a majority-carrier device is proportional to the product of carrier mobility with the critical electric field to the power of three ($\mu_n E_c^3$), where E_c is the critical field at which avalanche breakdown occurs. The critical electric field is mostly determined by the bandgap of the semiconductor and hence the recent emergence of

wide-bandgap semiconductors for use in power electronics. The implications of a larger figure of merit are profound; increased temperature of operation, reduced device area and capacitance, reduced losses during switching, conduction, and off-state.

Most recently, the availability of sufficiently large GaN substrates enabled the homoepitaxial growth of GaN-based devices. Among these high-quality native substrates prepared by different techniques, FS-GaN substrates [35] currently offer a threading dislocation density $<10^6$ cm^{-2} with a large size of >2 in. diameter. Using conducting FS-GaN substrates, one may realize a vertical power switch in III-N power electronic devices that allow for high-power operations in the on-state and lowest possible conduction loss at a given blocking voltage rating.

In this chapter, we will desbribe our works on the development and characteristics of GaN homojunction *p-i-n* rectifiers. The field termination plate, *p*-GaN ledge design, and SOG passivation were employed in the device fabrication schemes. Furthermore, electrode-less PEC surface treatment techniques were incorporated to reduce the leakage current from the etched sidewall. Furthermore, the temperature-dependent *I-V*, *C-V*, and OCVD measurements were performed to understand the carrier transport mechanism in GaN *p-i-n* vertical rectifiers.

2.2   Device fundamentals

2.2.1   *p-i-n* diode basic structure

After the *p-n* junction was understood and further developed in the 1940s, other research into variants of the basic *p-n* junction was undertaken. The first reference to this was a low frequency high power rectifier that was developed in 1952 by Hall [110], and

23

some later developments undertaken by Prince in 1956 [111]. As shown in Figure 2, the *p-i-n* diode can be shown diagrammatically as being a *p-n* junction, but with an intrinsic layer between the *p-n* and layers. The intrinsic layer of the *p-i-n* diode is a layer without intentional doping, and as a result this increases the size of the depletion region, the region between the *p* and *n* layers where there are no majority carriers. This change in the structure gives the *p-i-n* diode its unique properties.
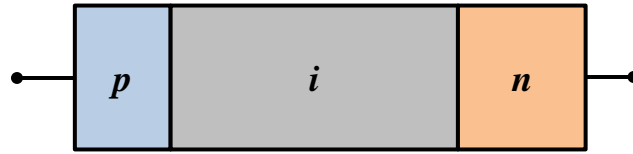
Figure 2. Basic structure of *p-i-n* diode

2.2.2 Forward characteristics of *p-i-n* diodes

The theory of *p-i-n* diode has been discussed in textbooks, for example, J. Lutz *et. al.* [112]. As the *p-i-n* diode is operated under forward bias, the carriers are injected from the highly-doped outer regions into the intrinsic region. The free carrier concentration is signifincantly increased by a few orders of magnitude above the intrinsic carrier concentration and thus the conductivity of the intrinsic region is strongly enhanced. Under the forward bias operation, the hole and electron concentrations in the intrinsic region (*i*-region) are approximately equal, ie. $n(\mathrm{x}) \approx p(\mathrm{x})$. The carrier distribution in the *i*-region can be written as [112]:

$$n(x) = p(x) = \frac{J\tau_a}{2qL_a}\left(\frac{\cosh\frac{x}{L_a}}{\sinh\frac{d}{2L_a}} - \frac{\mu_n - \mu_p}{\mu_n + \mu_p}\frac{\sinh\frac{x}{L_a}}{\cosh\frac{d}{2L_a}}\right) \tag{2.1}$$

, where L_a, and τ_a denote the ambipolar diffusion length and lifetime of the *i*-region, respectively. d is the thickness of the *i*-region and J is the current density. μ_n and μ_p are

24

the electron and hole mobility, respectively. If we assume that the intrinsic carrier concentration throughout the i-region is approximately constant, the diffusion current can be neglected. As the injected carrier density is much higher than the intrinsic concentration, the p-i-n is generally operated under the high-level injection, that is, $n \approx p \gg n_i$, where p is the average injected hole density in the i-region. Figure 3 shows the simulated electron carrier distribution of a GaN p-i-n diode under different voltage bias using the T-CAD simulation software. The simulated GaN p-i-n diode has a 1.1-µm thick n^+-GaN ($n\sim 1.5\times10^{18}$/cm^3), a 6-µm GaN i-region ($n\sim 1.3\times10^{16}$/cm^3), a 260-nm thick p-GaN ($p\sim 1\times10^{18}$/cm^3), and a 20-nm thick heavily doped p^+-GaN cap layer ($p> 2\times10^{20}$/cm^3). As the applied bias is greater than 4 V, the excess carrier concentration in the GaN i-region is above the intrinsic carrier concentration, which ensures the p-i-n diode is operated under high-level injection.
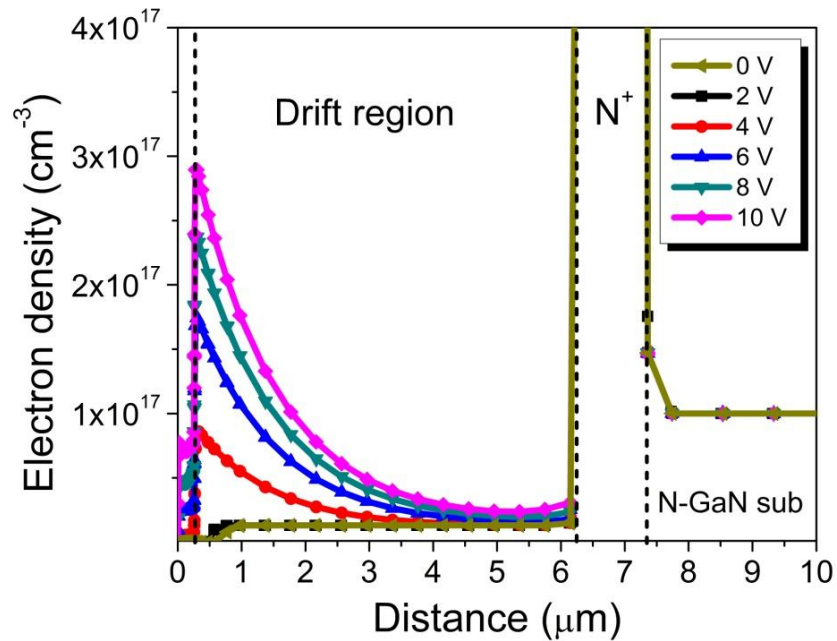
Figure 3. Electron carrier distribution of GaN *p-i-n* diode under different voltage bias conditions.

Under the high-level injection, the resistance (R_i) in the i-region is given by [113]:

$$R_i = R_{ON} - R_C = \frac{V_i}{I_f} = \frac{kT}{2qI_f}(\frac{d}{L_a})^2 = \frac{d^2}{2\mu_a\tau_aI_f} \tag{2.2}$$

, where R_{ON} is the total resistance of the p-i-n diode. R_c is the contact resistance from p-type and n-type contact metals, I_f is the forward-biased current, and μ_a, denote the ambipolar mobility of the i-region. As a result, R_C can be extrapolated as $1/I_f$.

The ambipolar lifetime of the i-region is one of the important characteristics for high-performance p-i-n diodes since it controls the level of conductivity modulation and, consequently, the voltage drop across the devices at high current densities. Open circuit voltage decay (OCVD) method is a convenient approach to the study of the transient response for determining τ_a of a diode switch [114,115].

At high-level injection, τ_a can be extracted from the OCVD process and can be estimated as [116,117]:

$$\tau_a = -\frac{2kT}{q}(\frac{dV}{dt})^{-1} \tag{2.3}$$

, where (dV/dt) is the slope of the voltage decay curve, q is the electron charge, and k is the Boltzmann constant.

2.2.3 Breakdown voltage of p-i-n diodes

The electric-field distribution in p-i-n diodes under the reverse bias is shown in Figure 4. The electric field in the drift region at breakdown is given by [112]:

$$E(x) = -E_C + \frac{qN_i}{\varepsilon}x \tag{2.4}$$

, where E_C denotes the critical electric field. The absolute value of the electric field (E_1) at the n^-n^+-junction can be given by the Eq. (2.4) with $x = d$:

$$E_1 = E_C - \frac{qN_i}{\varepsilon}d \qquad (2.5)$$

Therefore, the breakdown voltage of a *p-i-n* diode can be given by:

$$V_B = \frac{E_1 + E_C}{2}d = (E_C - \frac{qN_i}{2\varepsilon}d) \times d \qquad (2.6)$$
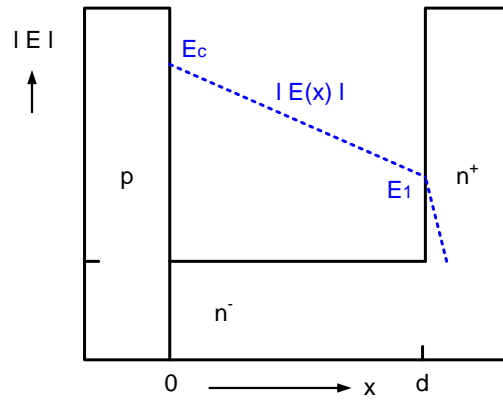
Figure 4. Electric-field distribution of a *p-i-n* rectifier

2.3 Simulation of GaN *p-i-n* rectifiers

Before actual device fabrication, Synopsys Sentaurus Device simulator was used to study different *p*-GaN ledge thickness and field plate designs for GaN *p-i-n* rectifiers with the intrinsic region of 6 µm. The device simulation helps study more process variation for optimizing device designs and provides more insight to the electric properties of GaN *p-i-n* rectifiers before actual device fabrication.

2.3.1 *p*-GaN ledge design

An effective sidewall leakage reduction technique is using a built-in *p-n* junction surface depletion layer to reduce the sidewall electrical field and hence to suppress the sidewall leakage. This is similar to the ledged structure in HBTs [118]. As shown in

Figure 5 (a), a thin layer of the *p*-type III-N layer is left outside of the mesa to form a surface depletion layer. The electric field distributions of *p-i-n* diodes with and without the ledged structure are simulated using the Sentaurus™ device simulator and the results are shown in Figure 6. This *p*-GaN ledged structure forms a surface depletion layer that can electrically isolate the sidewall defects from the metal contact and suppress the sidewall leakage current. In addition, the electrical field at the edge of the anode field-plate is signifincantly reduced. As a result, the device surface breakdown voltage can be extended.

(a)   **(b)**
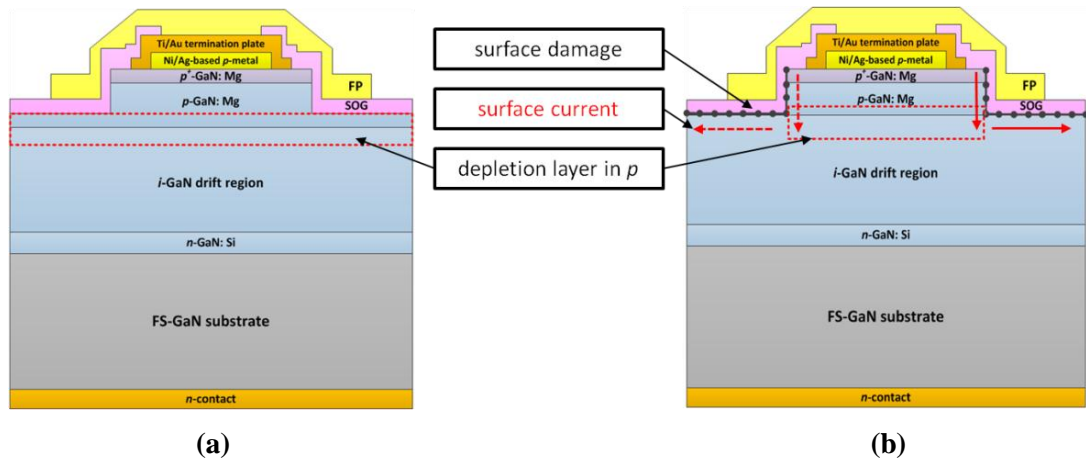
Figure 5. Schematic drawings of GaN *p-i-n* diodes (a) with and (b) without the *p*-GaN ledged structure.

(a)   **(b)**
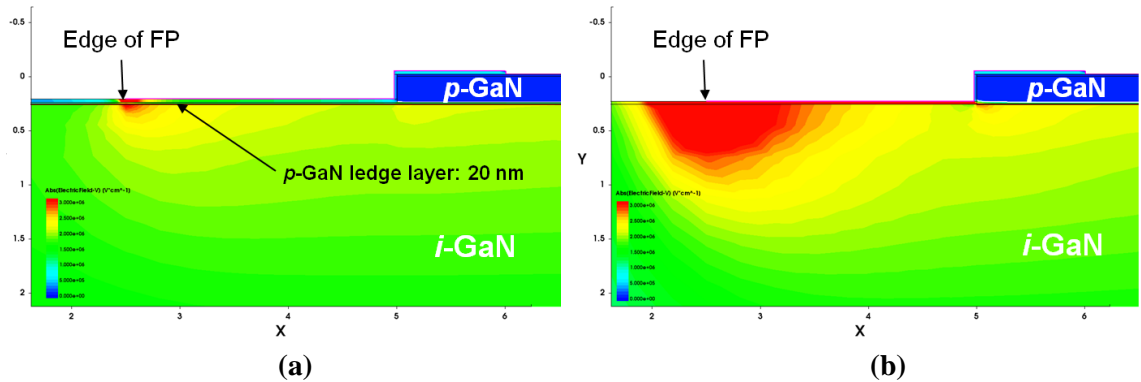
Figure 6. Simulated electric field distribution using the Sentaurus™ device simulator for GaN *p-i-n* diodes (a) with and (b) without the *p*-GaN ledged structure.

2.3.1.1 Study of *p*-GaN ledge thickness

In previous simulation results, a thin *p*-GaN ledged structure helps reduce the electrical field insided the exposed *i*-GaN region. In this study, the electric field of GaN *p-i-n* diodes with different *p*-GaN ledged thickness was simulated. The schematics of GaN *p-i-n* diode is shown in Figure 7 (a). The simulated GaN *p-i-n* diode has a 1.1-µm n^+-GaN ($n\sim$ 1.5×10^{18}/cm^3), a 6-µm unintentionally-doped GaN drift layer, a 260-nm thick *p*-GaN ($p\sim$ 1×10^{18}/cm^3), and a 20-nm thick heavily doped p^+-GaN cap layer ($p>$ 2×10^{20}/cm^3). The *p*-GaN ledged thickness varies from 20 nm to 200 nm. The mesa size is fixed at 10 µm in diameter. A 300 nm-thick SiO$_2$ layer is used as the passivation and the field plate structure is incorporated in the simulation.

At the reverse bias at -800 V, the simulated electric field distribution inside a GaN *p-i-n* diode is shown in Figure 7 (a). It can be seen that the maximum electric field is observed at the edge of the field plate. By plotting the electric field distribution along the vertical direction of the field plate edge, as shown in Figure 7 (b), it can be seen that the the electric field insided the *p*-GaN and SiO$_2$ passivation decreases as the *p*-GaN ledged thickness increases. However, the thinner *p*-GaN ledged thickness is prefered to provide effective device isolation. critical electric field for the GaN material and SiO$_2$ is about 3.5 MV/cm and ~8 MV/cm, respectively, Therefore, the result indicates that a 20-nm-thick *p*-GaN ledged structure is sufficient to maintain the peak electric field < 8 MV/cm inside the SiO$_2$ dielectric layer up to -800 V. The simulation results provide a viable approach to improve the breakdown voltage of GaN *p-i-n* diodes.
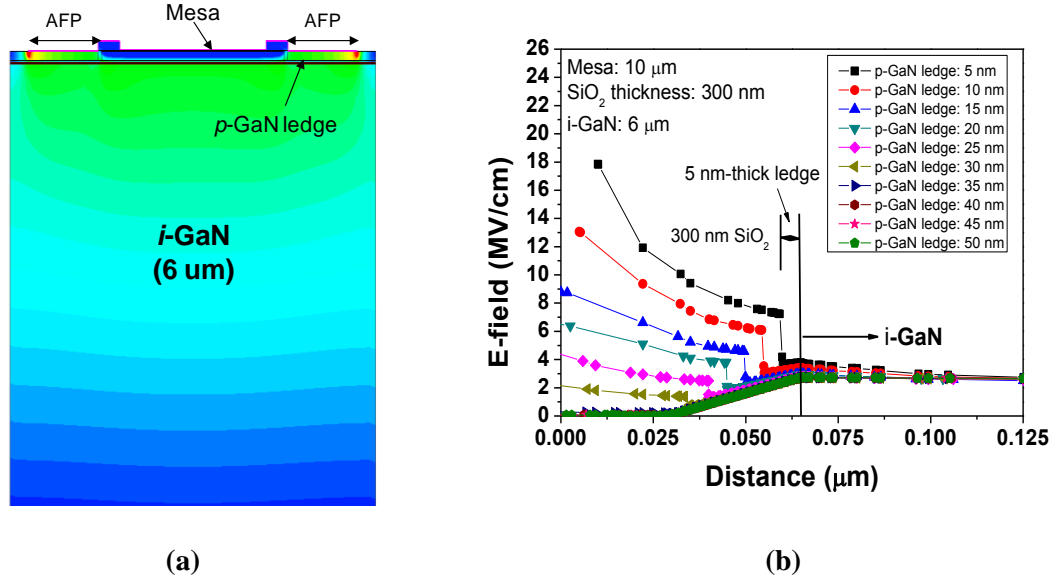
Figure 7. Simulated electric field distribution using the Sentaurus™ device simulator for GaN *p-i-n* diodes with 6 μm-thick drift region. The reverse bias is at -800 V. (b) The electric field distribution along the vertical direction of the field plate edge for GaN *p-i-n* diodes with various ledge thickness.

2.4   Fabrication of GaN *p-i-n* rectifiers

In this section, the fabrication of GaN *p-i-n* rectifiers grown on either FS-GaN or sapphire substrates will be described in detail. The field termination plate, *p*-GaN ledge design, and spin-on-glass passivation were employed in the device fabrication schemes.

2.4.1   Epitaxy layer structure

In this study, GaN *p-i-n* rectifiers were grown on either *c*-plane sapphire (wafer#: 2-3218-3) substrates or *c*-plane FS-GaN substrate (wafer#: 2-3218-3) using a Thomas–Swam MOCVD system. As shown in Table 5, GaN *p-i-n* rectifier structure consists of a 1.1-μm n^+-GaN ($n\sim 1.5\times10^{18}$/cm^3), a 6-μm unintentionally-doped GaN drift layer, a 260-nm thick *p*-GaN ($p\sim 1\times10^{18}$/cm^3), and a 20-nm thick heavily doped p^+-GaN cap layer ($p> 2\times10^{20}$/cm^3). For the sample grown on sapphire, a 4 μm-thick GaN buffer layer was grown on top of the non-conductive substrate. On the other hand, for the devices grown

on FS-GaN substrate ($n > 1 \times 10^{18}/\text{cm}^3$), the thickness of GaN buffer layer is ~ 1 μm. The carrier concentrations for *p*-type and *n*-type regions were estimated by the Hall-effect measurement on thicker epitaxial layers grown in separate calibration runs under similar conditions.

Table 5. Layer structure of GaN *p-i-n* rectifiers on sapphire (wafer#: 2-3218-3) and FS-GaN (wafer#: 2-3272-3) substrates

Layers	Thickness (nm)		Free carrier concentration (cm⁻³)
p^+-GaN	20		$p > 2 \times 10^{20}$
p-GaN	260		$p = 1 \times 10^{18}$
GaN drift layer	6000		$n \sim 1.3 \times 10^{16}$
n^+-GaN	1100		$n = 1.5 \times 10^{18}$
GaN Buffer	4000	1000	$n \approx 10^{16}$
Substrate	Sapphire	FS-GaN	-

2.4.2 Fabrication of GaN *p-i-n* rectifiers

In Figure 8 (a), the fabrication *p-i-n* rectifier on FS-GaN started with the mesa etching using a STS™ ICP etching tool. Ni/Ag-based metal stacks were deposited to form the *p*-type contact. Ti/Al-based metal stacks were deposited on the exposed *n*-type GaN region for devices grown on sapphire substrates to form *n*-type contact on the top side of the wafer. For devices grown on the *n*-type conducting FS-GaN substrate, the *n*-type ohmic contact was formed on the backside of the wafer. An additional Ti/Au metal layer was deposited to serve as a field termination plate. The SOG was coated for the device passivation with the spin speed of 4000 rpm for 40 sec. After the spin coating, the devices were baked at 150 °C for 2 mins. After the SOG passivation, the accessing via-holes were opened using an Oxford Endpoint RIE system. Finally, a 1-um-thick Ti/Au metal layer was deposited to form the anode electrode. The fabricated *p-i-n* rectifier grown on FS-GaN was mounted on a copper plate for the device testing.

For the *p-i-n* rectifier grown sapphire substrate, a deep mesa etching was first performed to expose the n^+-GaN. Ti/Al/Ti/Au metal stacks were then deposited on the exposed n^+-GaN to form *n*-type contact. Nevertheless, the devices grown on sapphire were processed under similar processing recipes to minimize the processing variation in the performance evaluation. The schematic cross-section of completed *p-i-n* rectifier on FS-GaN is shown in Figure 8 (b). The SEM pictures of *p-i-n* rectifier grown on FS-GaN or sapphire substrates are shown in Figure 9 (a) and (b), respectively.

(a)

(b)
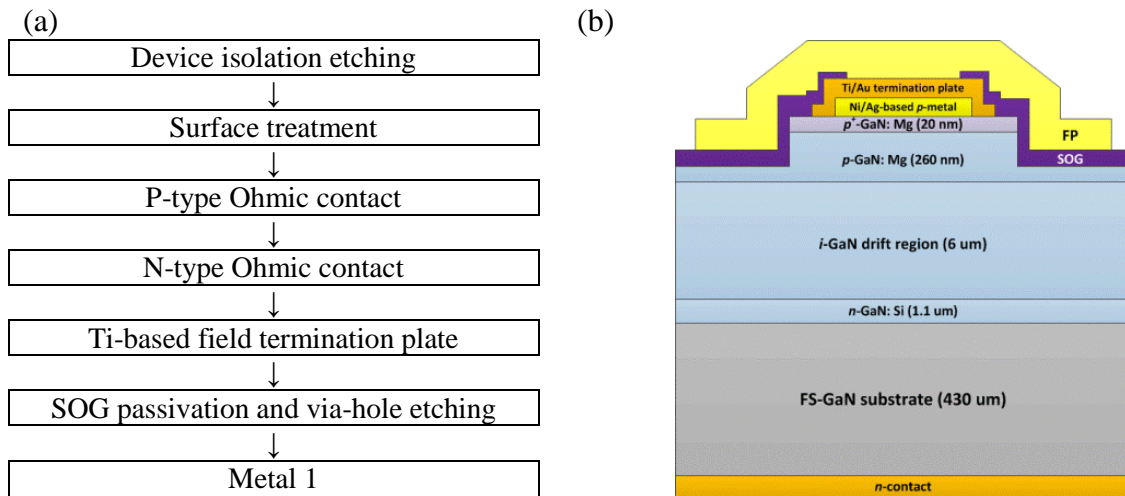
Figure 8. (a) The fabrication process flow and (b) the schematics of the GaN *p-i-n* rectifier on FS-GaN.

(a)   (b)
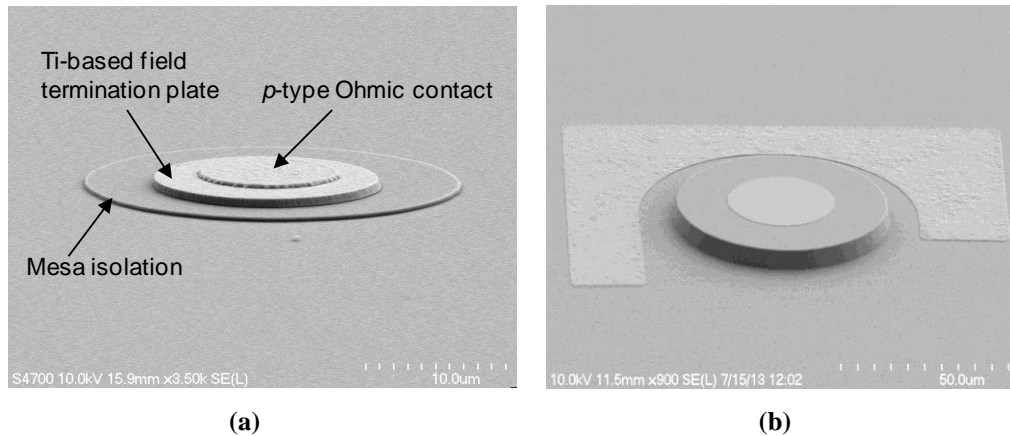
Figure 9. SEM pictures of (a) GaN *p-i-n* rectifier on FS-GaN (wafer#: 2-3272-3) (b) GaN *p-i-n* rectifier on sapphire prior to the device passivation (wafer#: 2-3218-3).

2.4.2.1 Ohmic contact on *p*-GaN and *n*-GaN

Low-resistance ohmic contacts are critical to high-performance semiconductor devices. However, achieving low-resistance ohmic contacts is a challenge for WBG materials, especially for *p*-type III-N materials due to the difficulty in *p*-type doping and the high dopant activation energy. To obtain ohmic contact to *p*-GaN, metals with large work functions (> 5 V), such as Ni, Pd, or Pt are used as the direct contact layer to the III-N materials. Recently, Ni/Ag-based metal stacks annealed in air or O_2 ambient for *p*-GaN ohmic contact have been widely reported. The Ag layer helps absorbing Ga from the *p*-GaN surface. As a result, Ga vacancies are generated near the *p*-GaN surface, thereby increasing the free-hole concentration at the metal-semiconductor interface and forming the tunneling contacts. At Georgia Tech, an e-gun evaporated Ni/Ag/Ni/Au metal stack is applied as the ohmic contact to p^+-GaN. The Au layer acts as a protection layer for smoother metal surface and better thermal stability. The Ni layer between Au and Ag is a diffusion blocking layer. The transmission line method (TLM) is used to estimate sheet resistance (R_{sh}) and ρ_c. As shown in Figure 10 (a), *I-V* curves are measured across 40 µm×80 µm pads with 64, 32, 16, 8-µm spaces. By linear fitting, R_{sh} of the *p*-GaN is 100 kΩ/□ and ρ_c is about 1×10^{-3} Ω·cm^2.

Compared to *p*-type GaN, forming a low-resistance ohmic contact is much easier on *n*-type GaN because of the high free-electron concentration. At Georgia Tech, an e-gun evaporated Ti/Al/Ti/Au metal stack is applied as the ohmic contact layer to *n*-GaN. After annealed at 700 °C for 1 min under the N_2 ambient, as shown in Figure 10 (b), R_{sh} of the *n*-GaN is 47 Ω/□ and ρ_c is about 1×10^{-5} Ω·cm^2.
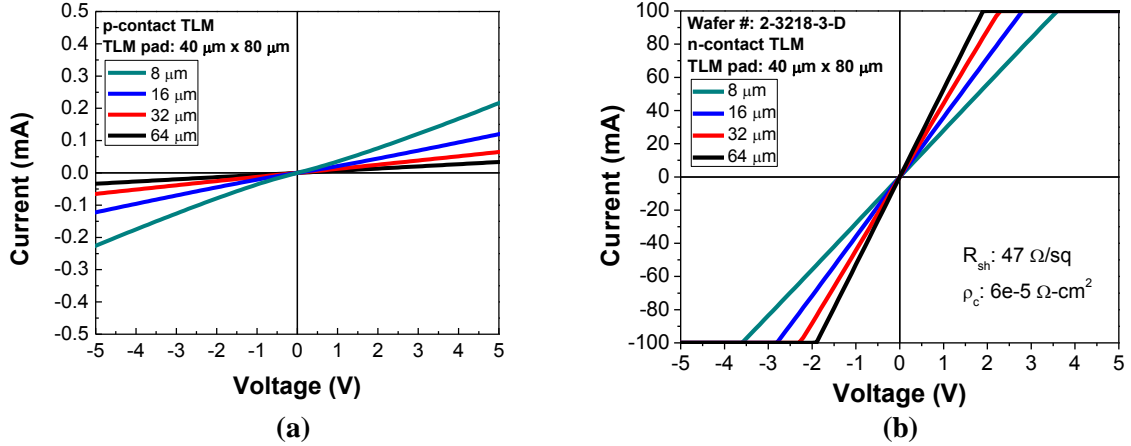
Figure 10. TLM results for (a) *p*-type and (b) *n*-type ohmic contact

2.4.2.2 Comparison of benzocyclobutene and spin-on-glass passivation

Spin-on-glass (SOG), an interlayer dielectric material applied in liquid form to fill narrow gaps in the sub-dielectric surface and thus conducive to planarization, is an alternative to silicon dioxide (SiO_2) deposited using CVD processes. The similar electrical properties between SOG and silicon dioxide guarantee that the SOG technique will provide comparable benefits to SiO_2 as an inter-metal dielectric layer. In fact, SOG exhibits several advantages over benzocyclobutene (BCB) such as a simple manufacturing process and a lower curing temperature.

At GT, both BCB and SOG passivation were compared on GaN p-i-n rectifiers grown on sapphire substrates. For the BCB process, the primer (AP3000) was first coated on the sample surface with a spin rate of 2500 rpm for 20 sec. BCB (3022-35) was then applied with the spin rate of 5000 rpm for 30 sec. After the spin coating, the sample was baked at 270 ^{o}C for 1 hour in a vacuum oven (Heraeus Vacuum Oven). The vacuum is < 100 mT and the temperatue ramping rate is less than 4 ^{o}C/min. The resulting BCB thickness is ~ 1 µm. For the SOG process, on the other hand, the SOG was coated on the sample surface with a spin rate of 3000 rpm for 40 sec. Hard bake at 150 ^{o}C for 2 mins is

required after SOG sping coating. The resulting SOG thickness is about 2800 Å. Shown in Figure 11 are the *I-V* curves of GaN *p-i-n* rectifiers before and after BCB passivation. It is seen that the turn-on voltage shifts by ~ 1 V after BCB passivation while the leakage current and the on-resistance remains similar. The increase in the turn-on voltage may suggest an additional voltage drop at the BCB/*p*-type contact interface after BCB passivation. On the other hand, Figure 12 shows the *I-V* curves of GaN *p-i-n* rectifiers before and after SOG passivation. It is clearly observed the SOG passivation can provide effective electrical insulation without degrading the device performance.

(a)   **(b)**
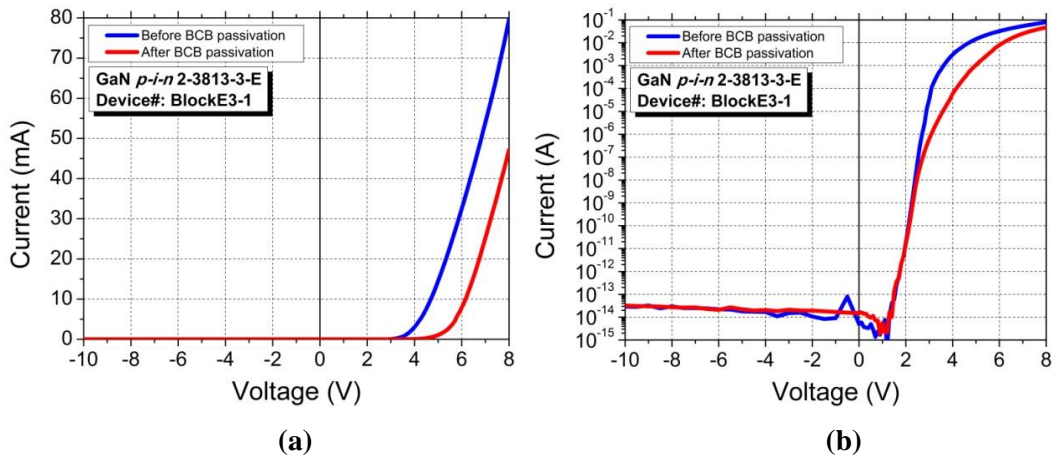
Figure 11. *I-V* characteristics of GaN *p-i-n* rectifiers (wafer#: 2-3218-3F-BE3-1) befoe and after BCB passivation. (a) linear scale. (b) log scale.

(a)   **(b)**
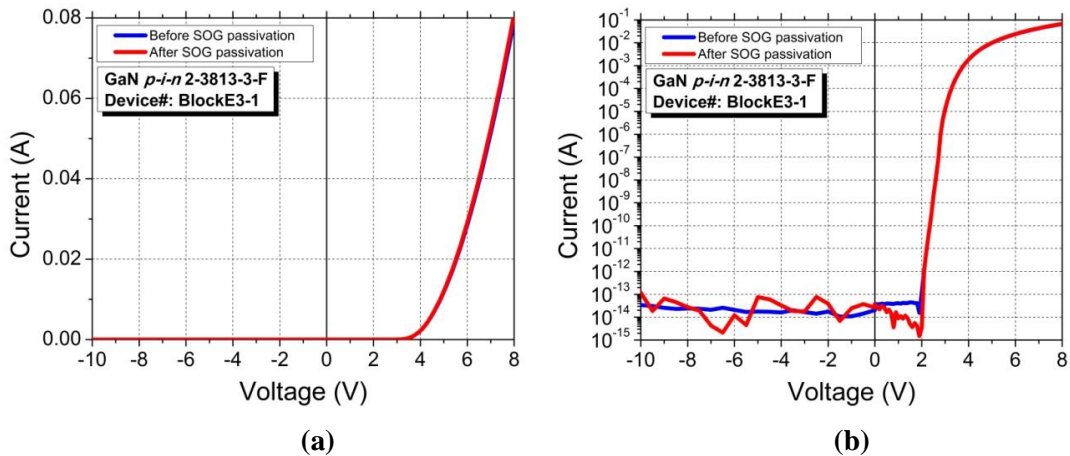
Figure 12. *I-V* characteristics of GaN *p-i-n* rectifiers (wafer#: 2-3218-3E-BE3-1) befoe and after SOG passivation. (a) linear scale. (b) log scale.

2.5   Characteristics of GaN *p-i-n* rectifiers on FS-GaN and sapphire substrates

The fabricated GaN *p-i-n* rectifiers were characterized using a Keithley 4200 semiconductor characterization system (SCS-4200) for d.c characteristics at room temperature. The *C-V* measurement was carried out in an Agilent 4284A LCR meter at a frequency of 1 MHz.

2.5.1   Capacitance-voltage (*C-V*) characteristics

Figure 13 (a) shows the measured *C-V* characteristics for two *p-i-n* rectifiers grown on sapphire and FS-GaN substrates, respectively. Since the free-hole concentration in *p*-type GaN is presumably much higher than the free-electron concentration in the unintentionally-doped "*i*" layer, the depletion width under the reverse bias falls mostly in the drift layer. The free-carrier concentration of the unintentionally-doped layer (N_i) is

$$N_i(W_{dep}) = \frac{2}{q\varepsilon_s\varepsilon_0} \cdot \frac{A_M{}^2}{d(1/C^2)/dV} \tag{2.7}$$

, where ε_0 is the free-space permittivity, A_M is the total area of mesa, V_{bi} is the built-in potential, and ε_s is the relative permittivity of the un-doped GaN layer. The depletion width (W_{dep}) is given by: $W_{dep} = \varepsilon_s\varepsilon_0 A_M / C$. Therefore, N_i can be determined by the slope of $1/C^2$ plots under the reverse bias. As shown in Figure 13, the calculated N_i is 1.3×10^{16} cm^{-3} for the device grown on sapphire or FS-GaN substrate. These results suggest the heteroepitaxial growth yields similar unintentionally doped drift layer as in the case of homoepitaxy on FS-GaN substrates.
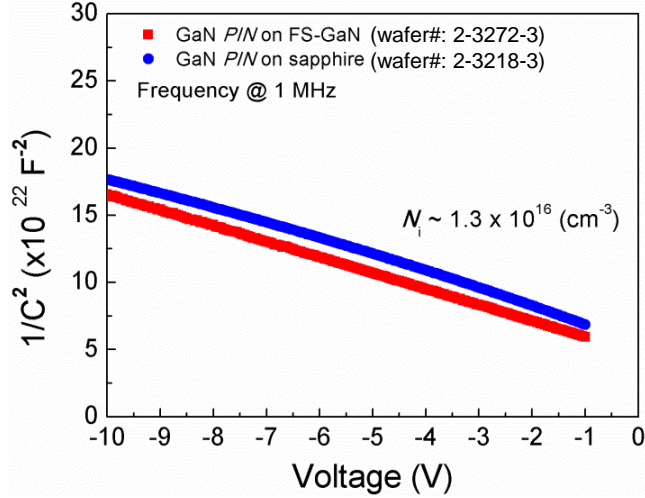
Figure 13. Measured $1/C^2$ plots versus reverse voltage for the *p-i-n* rectifiers grown on FS-GaN (wafer#: 2-3272-3) or sapphire substrate (wafer#: 2-3218-3).

Figure 14 (a) shows a comparison of the forward *I-V* characteristics of GaN *p-i-n* rectifiers grown on sapphire and FS-GaN substrate, respectively. The *p-i-n* rectifier under test has anode contact diameter of 30 microns. For the device grown on sapphire, the ideality factors (η) are 3.1~3.6 and the lowest $R_{ON}A$ at J= 2.5 kA/cm^2 is ~0.66 mΩ-cm^2. This unrealistic η value may simply result from the resistive *p-i-n* structure grown on sapphire substrate. On the other hand, for the devices grown on FS-GaN, η is ~2 and the lowest $R_{ON}A$ value is significantly reduced to 0.28 mΩ-cm^2 at the same *J*. These results indicate a high-quality *p-i-n* structure was realized on the native substrate with improved $R_{ON}A$ due to less scattering centers arising from the extensive defects in the epitaxial layers.

Figure 14 (b) shows the reverse *I-V* characteristics of these *p-i-n* rectifiers up to -200 V. For the devices grown on sapphire, the leakage current increases with the reverse bias voltage and reaches >30 nA (or J> 1 mA/cm^2) at -200 V. The off-state V_B was also evaluated using a Tektronix 576 curve tracer, where V_B is the voltage as *J* reaches 1 A/cm^2 under reverse bias. The devices under test were measured in a fluorinert

environment to prevent outer electric discharge at a high voltage. V_B of ~600 V was achieved for the device grown on sapphire (data not shown here). On the other hand, the device fabricated on FS-GaN substrate shows low leakage current below 1 pA (or $J < 0.1$ μA/cm^2) for voltage up to –200 V. It represents at least four orders of magnitude of reduction in the leakage current at –200 V. Figure 14 (c) shows the reverse characteristics of the same *p-i-n* device grown on FS-GaN substrate. The left and right axes represent the measured reverse voltage and current, respectively. As shown in the graph, the reverse current is ~1 μA (J~ 0.14 A/cm^2) at –800 V and the off-state V_B is $>$ –800 V. Since the depletion width (W_{dep}) can be given by: $W_{dep} = \sqrt{2\varepsilon_s\varepsilon_0(V_{bi} + V_B)/qN_i}$. At $V_B = -800$ V, W_{dep} is $>$ 8 μm, which ensures our *p-i-n* diode is PT diode. Furthermore, the corresponding BFOM ($V_B^2/ R_{ON}A$) of >2.5 GW/cm^2 was achieved. It is also noted the BFOM obtained in the homojunction GaN *p-i-n* rectifier shows better performance when compared to the reported vertical GaN SBDs (BFOM = 1.7 GW/cm^2) [30]. Since *p-i-n* rectifiers grown on either substrate have similar doping concentrations, the nature of low reverse current and high breakdown voltage can be ascribed to the adoption of low-dislocation-density epitaxial layers using native substrates. With the extracted N_i and measured breakdown voltage, a lower limit of the critical electric field for GaN can be estimated by: $V_B = \dfrac{\varepsilon_s\varepsilon_0 E_C^2}{2qN_i}$. In this analysis, it is assumed that the breakdown occurs when the maximum electric field in the depletion region of an abrupt junction reaches E_C of GaN. The calculated E_C value for our *p-i-n* rectifiers is ~ 2 MV/cm.
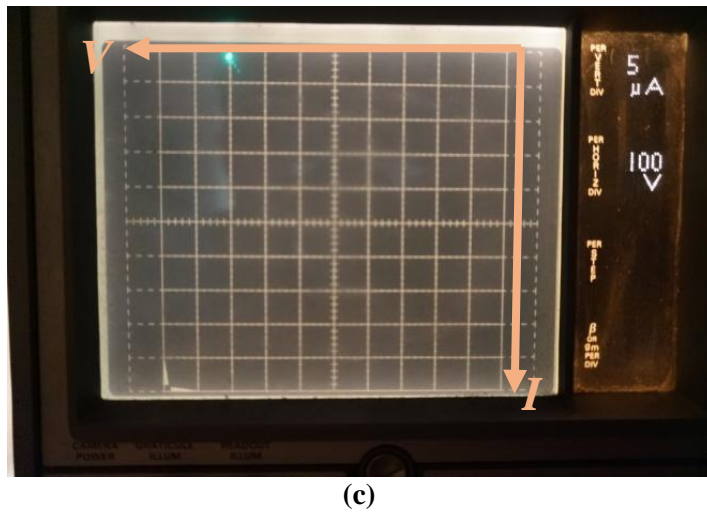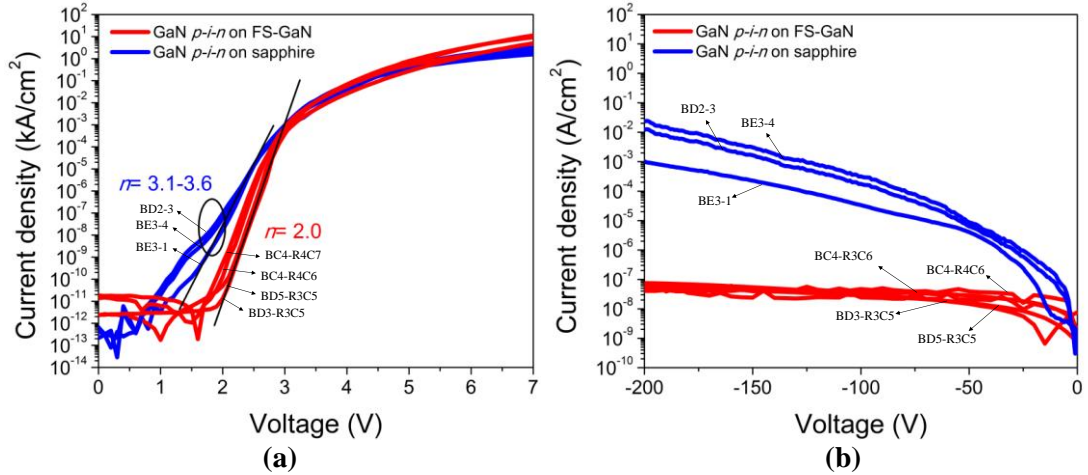
Figure 14. (a) The forward and (b) reverse *I-V* characteristics of the GaN *p-i-n* rectifiers grown on FS-GaN (solid line in red: wafer#: 2-3272-3A) and sapphire substrate (solid line in blue: wafer#: 2-3218-3E), respectively. (c) The off-state characteristics (as indicated by the bright dot) for a GaN *p-i-n* rectifier grown on FS-GaN. The device has an anode contact diameter of 30 microns. The reverse current is ~1 μA at −800 V. (Horizontal: 100 V/Division. Vertical: 5 μA/Divisions).

2.6 Temperature-dependent characteristics of GaN *p-i-n* rectifiers on FS-GaN

In this section, temperature-dependent characteristics of GaN *p-i-n* rectifiers were studied. This study helps understand the device performance under higher temperature operation as well as extract several internal parameters. Since the lateral device grown on sapphire substrate may cause various edge effects such as current crowding, this study will be focused on the vertical *p-i-n* rectifiers.

2.6.1 Temperature-dependent *C-V* characteristics

The temperature-dependent *C-V* measurements were performed on the *p-i-n* rectifier. The temperature was increased from 298 K to 448 K with an increment of 25 K. Shown in Figure 15 (a) are the $1/C^2$ plots for a *p-i-n* rectifier operating at different temperatures. Since the free-hole concentration in *p*-type GaN is presumably much higher than the free-electron concentration in the *i*-GaN drift layer, the depletion width under the reverse bias falls mostly in the drift layer. Figure 15 (b) shows the temperature-dependent N_i from three *p-i-n* rectifiers with identical dimensions. The averaged N_i is approximately 1.4×10^{16} (cm^{-3}) at 298 K and increases to 2.1×10^{16} (cm^{-3}) as T increases to 448 K.
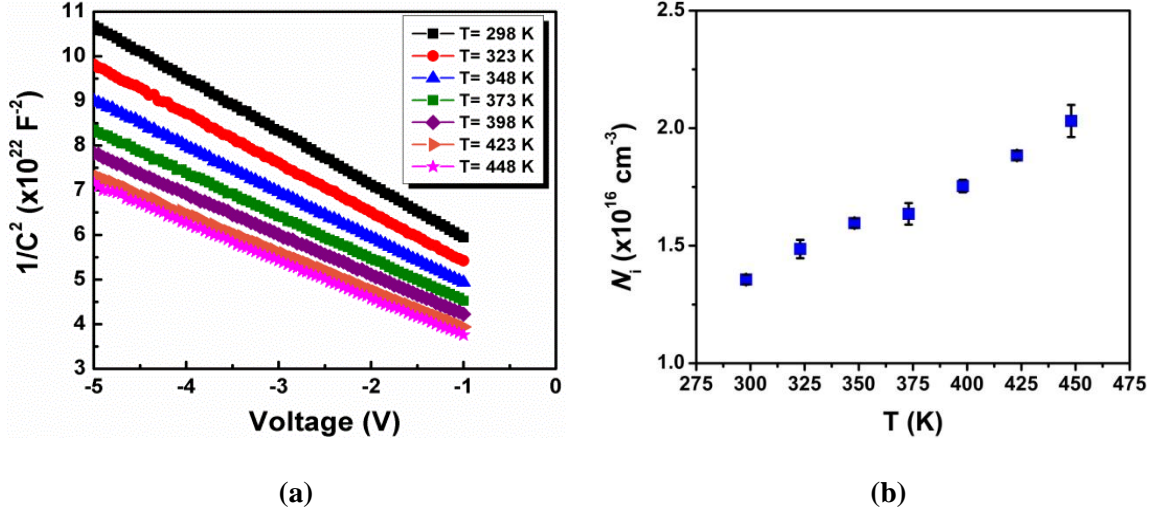
Figure 15. (a) Measured $1/C^2$ plots versus reverse voltage of a fabricated *p-i-n* rectifier (wafer#: 2-3272-3-BlockC2-SectionA-R3C7) in the temperature range of 298–448 K. (b) Temperature-dependent N_i from three *p-i-n* rectifiers with identical dimension.

2.6.2   Temperature-dependent forward *I-V* characteristics

Forward *T-I-V* measurements were then performed using a Keithley 4200-SCS semiconductor parameter analyzer. Shown in Figure 16 (a) are the forward characteristics of a fabricated GaN *p-i-n* rectifier with an anode contact diameter of 30 microns. At 298 K, the electrical characteristics show the turn-on voltage of 3.3 V at $J= 10$ A/cm^2 and the maximum $J> 10$ kA/cm^2 is achieved. An ideality factor (η) of 2, determined from the slope of a semi-logarithmic plot in the voltage range of 1.5–2.5 V, is also obtained at RT. The reverse saturation current can be also extracted to be 2×10^{-29} (A) (or $J= 2.83\times10^{-24}$ A/cm^2) and 1×10^{-16} (A) (or $J= 1.4\times10^{-11}$ A/cm^2) at T= 298 K and 448 K, respectively. The reverse saturation current density at 298 K is lower than the value reported for 6H-SiC *p-n* junctions [119] because of the larger band gap of GaN. However, this value is slightly higher than the value for the recently reported GaN *p-i-n* diodes [120]. Figure 16 (b) shows $R_{ON}A$ as a function of J at different T. In the on-state, strong conductivity

modulation of the drift region is observed due to high-level injection. The resistance of a *p-i-n* rectifier can be expressed as: [121]

$$R_i = R_{ON} - R_C = \frac{d^2}{2\mu_a \tau_a I_f}$$ (2.8)

As shown in Figure 16 (b), the $R_{ON}A$ value is inversely proportional to *J* at a fixed *T*. At 298 K, the obtained $R_{ON}A$ is 0.43 mΩ-cm^2 at *J*= 1.5 kA/cm^2, 0.34 mΩ-cm^2 at *J*= 2.0 kA/cm^2, and 0.28 mΩ-cm^2 at *J*= 2.5 kA/cm^2. As *J* increases, the total resistance of the *p-i-n* diode is mostly attributed to R_c, which can be estimated to be ~ 0.1 mΩ-cm^2. As *T* increases to 448 K, $R_{ON}A$ *i*ncreases slightly (< 10 %) for a fixed *J*, indicating a good thermal conductivity is achieved through homoepitaxial growth. In addition, a curve fitting by Eq. (2.8) yields $\mu_a\tau_a$ value is ~9×10^{-8} cm^2/V in the temperature range of 298–448 K.

In Figure 17, the ideality factors extracted from the forward *I-V* curves are plotted. The minimal ideality factors at 298 K and 348 K are ~2, suggesting the Shockley-Read-Hall (SRH) recombination is dominant below *T*= 348 K. As the temperature increases, the minimal ideality factors increase to 2.3 and 2.4 at *T*= 398 K and 453 K, respectively. The increase of η at higher temperature can be attributed to the increase in resistance due to the enhanced scattering centers arising from defects in the epitaxial layers. This thermal excitation of electrons from deep-level traps will be discussed further in detail.
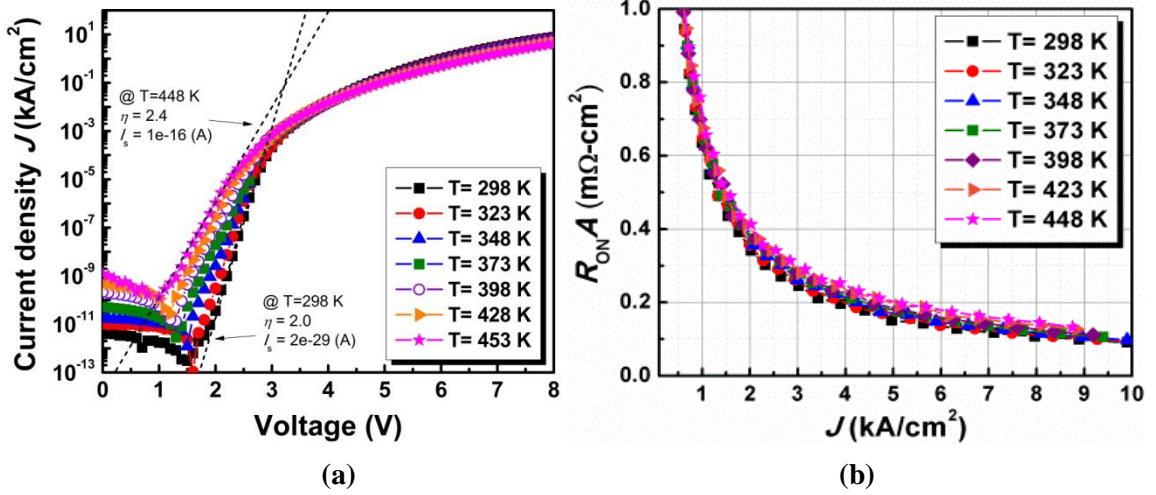
Figure 16. (a) Forward *T-I-V* characteristics of a fabricated GaN *p-i-n* rectifier with an anode contact diameter of 30 μm. (b) $R_{ON}A$ as a function of forward *J* in the temperature range of 298 K–448 K (wafer#: 2-3272-3-BlockC2-SectionA-R3C7).
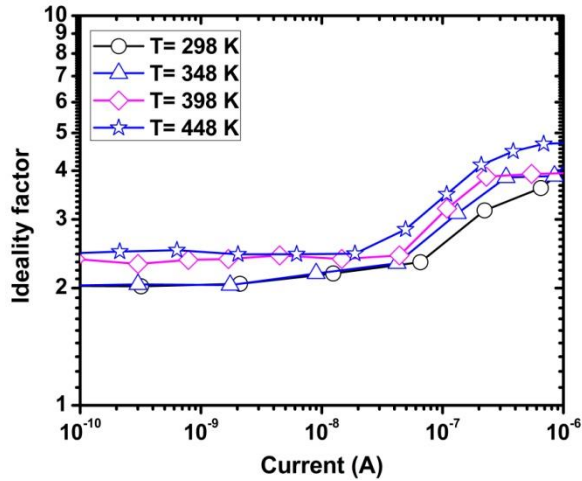
Figure 17. Ideality factors of GaN *p-i-n* rectifiers at various temperature.

2.6.3 Open-circuit voltage decay (OCVD) measurement

Figure 18 (a) shows the temperature-dependent voltage-time diagram of OCVD process. At *t*= 0 s, a pulsed forward current density of *J*= 10 kA/cm^2 is applied to the device with a pulse width of 1 μs. The *p-i-n* rectifier is connected in series with a 50 Ω load and the voltage across the device is monitored by a high-resolution oscilloscope (Model: Rohde & Schwarz RTO 1024). This *J* value ensures a high-level injection in the drift region ($\Delta n \approx \Delta p > 10^{17}$ cm^{-3}). As shown in the inset of Figure 18 (a), as the current is

terminated at $t = 1$ μs, we can observed a voltage drop followed by a rapid initial decay, a plateau, and finally slow voltage decay. The voltage decay rate of a *p-i-n* diode can be expressed as: [116, 117]

$$\frac{dV(t)}{dt} = \frac{-kT}{q}\left(\frac{1}{\tau_a} - \frac{1}{\xi(t)}\frac{d\xi}{dt}\right) \tag{2.9}$$

, where q is the electron charge and k is the Boltzmann constant. $\xi(t)$ accounts for the initial rapid decay due to the carrier recombination at *p*-GaN/*i*-GaN interface [117] and can be given by the following expression: $\xi(t) = [1 + \beta(1 - \exp[-t/\tau_a])]^{-1}$, where β is designated as the coupling parameter of the *p*-GaN/*i*-GaN junction. As t increases, $\xi(t)$ becomes practically constant and, hence, the voltage decay rate can be simplified as:

$$\frac{dV(t)}{dt} = \frac{-2kT}{q}\left(\frac{1}{\tau_a}\right) \tag{2.10}$$

Therefore, τ_a can be determined from the slow voltage decay portion using Eq. (2.10) and μ_a can be therefore estimated from the product of $\mu_a\tau_a$. Shown in Figure 18 (b) are the calculated τ_a and μ_a as a function of temperature. As the temperature increases from 298 K to 448 K, τ_a increases from 9.6 ns to 22 ns and μ_a decreases from 31 cm^2/V-s to 12.4 cm^2/V-s, respectively. Therfore, the ambipolar diffusion length can be further extracted and estimated as 0.87 μm at 298 K and the value is increased to 1.02 μm at 448 K.
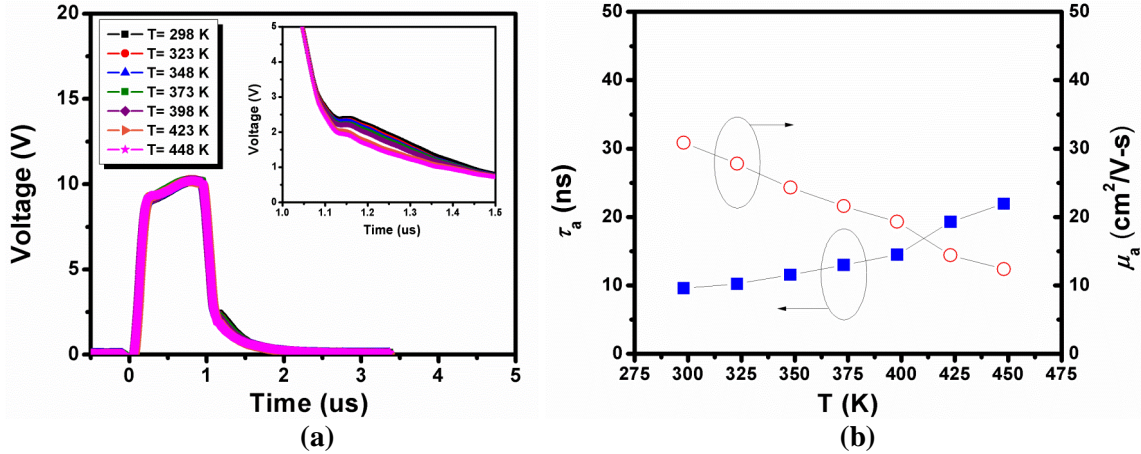
Figure 18. (a) Temperature-dependent time diagram of forward voltage drop across a *p-i-n* diode. The forward current density is 10 kA/cm^2 under pulsed operation (pulse width: 1 μs). The inset shows the voltage versus time as the current is terminated. (b) Calculated τ_a and μ_a in the temperature range of 298 K–448 K.

2.6.4   Temperature-dependent reverse *I-V* characteristics

Figure 19 (a) shows the temperature-dependent leakage current of the same *p-i-n* rectifier. The data show that the leakage current is <1 pA (or *J*< 0.1 μA/cm^2) up to –200 V at 298 K, suggesting that high-quality epitaxial material is realized on the FS-GaN substrate. The measured leakage current doesn't follow the most common generation-recombination model of $I_R \propto \sqrt{V}$ relation. Instead, the curves fit well with the Poole-Frenkel model [122] for the reverse biased *p-i-n* rectifiers up to –200 V. It suggested that the field-assisted ionization process from deep-level traps could be one of the possible leakage mechanisms for our fabricated *p-i-n* rectifiers up to –200 V. According to the Poole-Frenkel theory, the leakage current can be expressed as:

$$I_R \propto E_{avg} \exp(-\frac{E_a}{kT}) \tag{2.11}$$

$$E_a = q\Phi_B - \beta_{PF}\sqrt{E_{avg}} \tag{2.12}$$

$$E_{avg} = (V_{bi} - V_R)/W = \sqrt{\frac{qN_i(V_{bi} - V_R)}{2\varepsilon_s\varepsilon_0}} \tag{2.13}$$

, where E_a is the thermal activation energy, E_{avg} is the average electric field exerted on the deep centers. Φ_B is the effective barrier height of carrier trapped in deep centers without an external electric field. β_{PF} is the Poole-Frenkel coefficient. V_{bi} is the built-in voltage of p^+-n junction, which can be estimated to be 3.4 V based on the basic p-n junction theory. V_R is the reverse voltage, and W is the depletion width. In theory, $\beta_{PF} = (q/\pi\varepsilon_0\varepsilon_s)^{1/2}$, where ε_0 is the free-space permittivity and ε_s is the relative permittivity of the GaN material.

As shown in Figure 19 (a), the reverse *T-I-V* curves can be well fitted by Eq. (2.11). An Arrhenius plot for the leakage current at −100 V reverse bias is shown in Figure 19 (b), and the activation energy (E_a), defined as *-d(lnI)/d(kT)⁻¹*, can be obtained in the temperature range of 300–450 K. E_a are then plotted as a function of the square-root of E_{avg}, as shown in Figure 19 (c). According to the Poole-Frenkel theory, the barrier lowering of a deep center can be expressed as: $\Delta E_a = \beta_{PF}E_{avg}^{1/2}$. A linear fitting of the data in Figure 19 (c) yields the Poole-Frenkel coefficient of 3.1×10^{-4} eV·V$^{-1/2}$·cm$^{-1/2}$, which is very close to the theoretical value of 2.5×10^{-4} eV·V$^{-1/2}$·cm$^{-1/2}$ for a GaN material. The average Φ_B can be estimated to be ~0.7 eV at E_{avg}= 0 V/cm. This barrier height is close to one of the reported deep levels (~650-800 meV below conduction band) found in un-doped GaN using a deep-level transient spectroscopy (DLTS) and believed to correspond to the nitrogen energy level [123, 124].
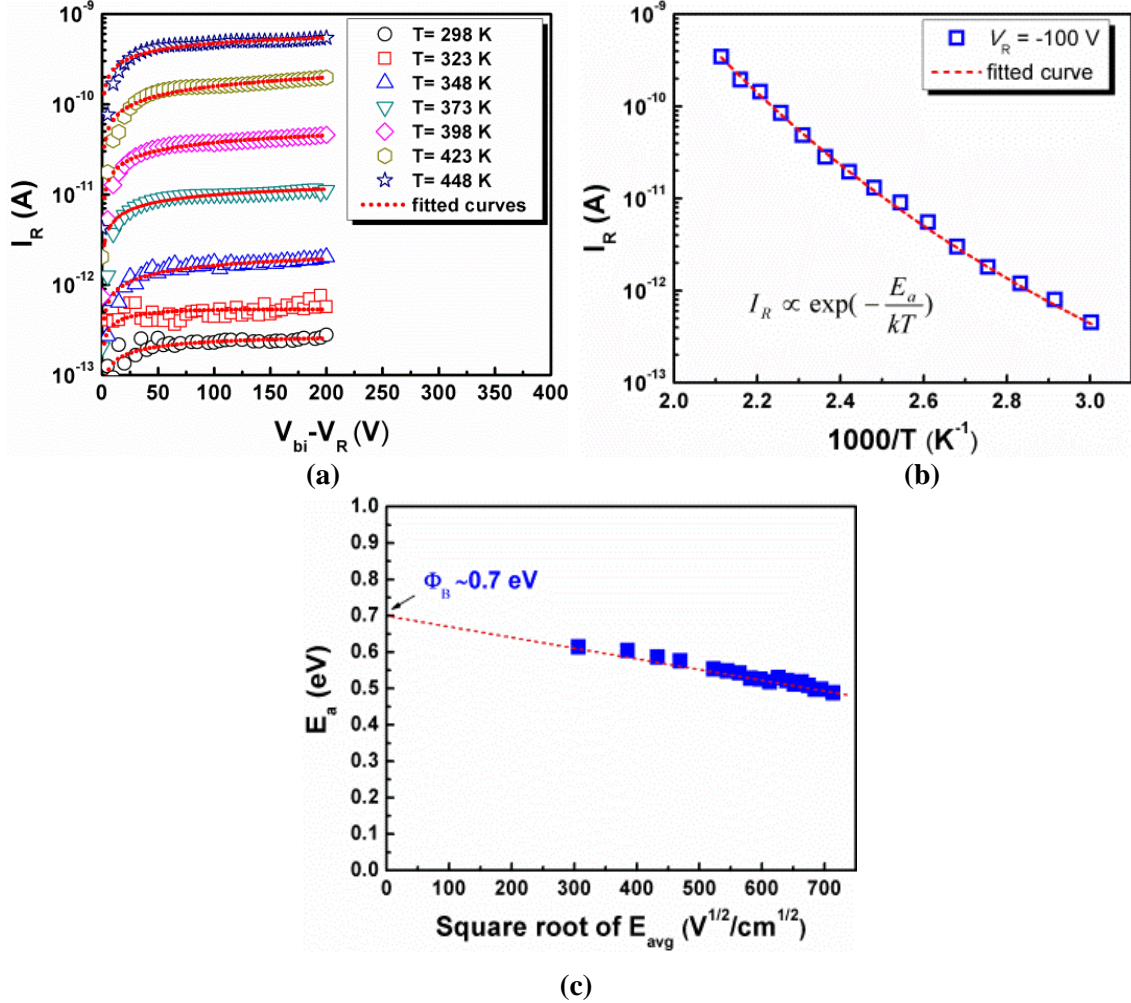
Figure 19. (a) *T-I-V* **characteristics of a fabricated GaN** *p-i-n* **rectifier (wafer#: 2-3272-3-BlockC2-SectionA-R3C7) from** *T*= 298 K to 448 K. The dot curves are the fitted data using Eq. (2.11). (b) Arrhenius plot of the reverse leakage current measured at –100 V. (c) The thermal activation energy as a function of the square root of the average electric field in the drift region of a GaN *p-i-n* rectifier.

2.7 Summary

In summary, high-performance GaN homojunction *p-i-n* rectifiers were developed and studied at Georgia Tech. *P*-GaN ledge design and SOG passivation were developed and incorporated in the device fabrication to improve device performance. We first present a comparative study of GaN homojunction *p-i-n* rectifiers grown on either FS-GaN or sapphire substrate. The *p-i-n* rectifier grown on sapphire shows a V_B of 600 V

47

and $R_{ON}A$ of 0.66 mΩ-cm^2. On the other hand, a *p-i-n* rectifier grown on a FS-GaN substrate shows substantial improvement with $V_B > 800$ V and $R_{ON}A = 0.28$ mΩ-cm^2. The corresponding Baliga's Figure of Merit (BFOM) of >2.5 GW/cm^2 is achieved. The device performance follows the same trend for GaN switches and demonstrated the lowest on-resistance for 800-V diode switches reported to date.

Furthermore, we study the temperature-dependent *I-V* and *C-V* characteristics of a GaN *p-i-n* rectifier grown on a FS-GaN substrate. The *C-V* data shows the free-carrier concentration of the drift layer is 1.3×10^{16} cm^{-3} at $T = 298$ K and increases to 2.0×10^{16} cm^{-3} at 448 K. *I-V* results show a low $R_{ON}A$ of 0.28 mΩ-cm^2 at 298 K and increases slightly (by <10 %) at 448 K. By performing OCVD measurement under high-level injection, τ_a can be extracted to be 9.6 ns at 298 K and increases to 22 ns at 448 K. The reverse *I-V* measurements reveal that the leakage current up to −200 V can be mainly attributed to a field-assisted ionization process from deep-level traps. These results can be well explained by the Poole-Frenkel effect and the corresponding Poole-Frenkel coefficient of 3.1×10^{-4} eV·V$^{-1/2}$·cm$^{-1/2}$ is obtained.

Figure 20 shows a competitive study of state-of-the-art GaN *p-i-n* rectifiers grown on different substrates (sapphire [25], SiC [26] and FS-GaN [22-24, 27-29]) and SBDs [30-34]. The dotted lines on the plot represent the theoretical limits for Si, SiC, GaN materials using the equation: $R_{ON}A = 4V_B^2 / (\varepsilon_0 \varepsilon_r \mu E_C^3)$ [125]. For a given breakdown voltage rating, GaN *p-i-n* rectifiers on FS-GaN substrates show at least 10 times lower $R_{ON} \times A$ values when compared to GaN *p-i-n* rectifiers on foreign substrates and III-N-based SBDs achieved so far. These *p-i-n* devices are consistently demonstrating the best BFOM for GaN-based switches and approaching to the theoretical limit for GaN. Our

device also demonstrated the same trend for GaN *p-i-n* rectifiers when it scales to the 800-V range and, as our best knowledge, showed the lowest on-state resistance for 800-V devices reported to date.
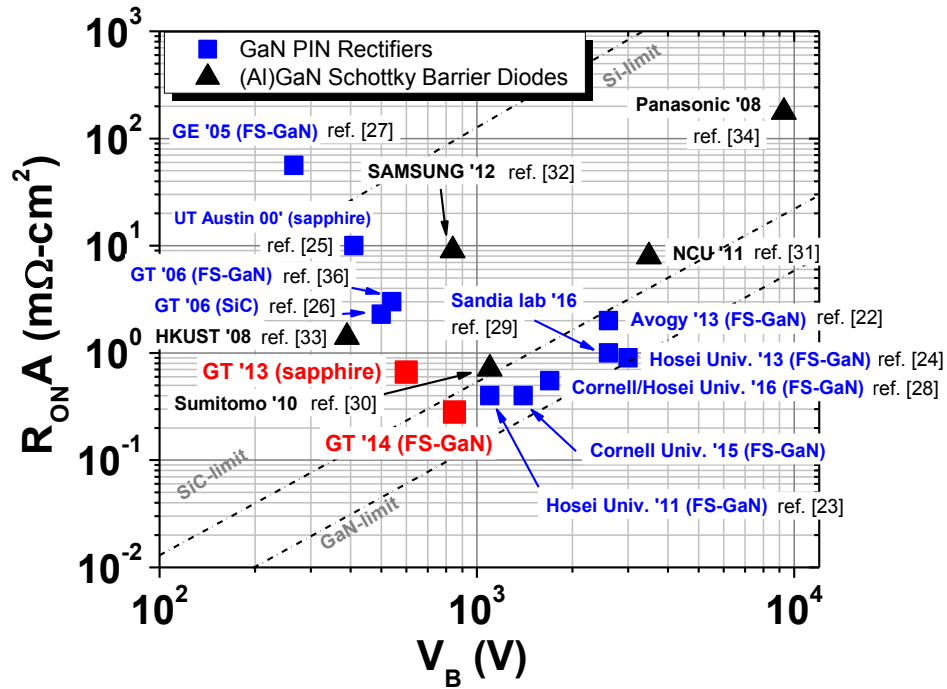
Figure 20. A comparison chart showing the breakdown voltage versus specific on-state resistanc for GaN power rectifiers grown on different substrates (sapphire, SiC and FS-GaN), and III-N SBDs.

CHAPTER 3

GAN/INGAN HETEROJUNCTION BIPOLAR TRANSISTORS AND PHOTOTRANSISTORS

2.8   Introduction

III-N HBTs have many inherent advantages over III-N FETs including normally-off characteristics, high-power handling capability and vertical current conduction. To date, III-N HBTs have demonstrated their potential for high-power-handling capability [126] and high-temperature operation [127,128,129]. More recently, the microwave amplification characteristics with f_T of greater than 8 GHz were also demonstrated in GaN/InGaN HBTs [128].

The radiative recombination processes in direct bandgap semiconductors provide an approach to understand the carrier transport and photon-electron interactions in transistors. It has also been proposed to enable next-generation devices such as LETs and TLs [130-132]. These devices demonstrated high-efficiency light sources with a compact "three-port" electro-optical operation with wider modulation bandwidths when compared to conventional two-terminal light-emitting devices. Although the LET action of GaN/InGaN HBTs was previously reported [133 , 134], the origin of radiative recombination processes was not clearly resolved. In this paper, we report the light-emitting characteristics of a GaN/InGaN HBT. By operating the device at the diode modes and the forward-active transistor modes, three radiative recombination paths were identified in the base region. The study of the EL emission spectrum provides a method to help resolve the carrier recombination paths in III-N HBTs for further transistor

performance improvement in conventional HBT power amplification and advanced LETs/TLs with high emission spectral purity.

UV photon detectors have a wide range of applications in astronomy, environmental monitoring, advanced optical communications, bio-chemical sensing, and other emerging technologies. PMTs are widely used because they provide optical gains on the order of 10^6 with low dark current. But PMTs have the disadvantages of low photocathode quantum efficiency for UV light, high operation voltages (> 1000 V), and cooling system requirement [135]. The expensive filters for visible-blind or solar-blind detection and the large and fragile body also seriously restrict their applications. With their large bandgap energy, superior thermal conductivity, high electron saturation velocity and excellent physical stability, on the other hand, III-N materials have been an attractive candidate material suitable for making UV PDs. Furthermore, these materials also have the benefit of large-size commercial native substrate and correspondingly much lower defect density within the device active area. As a result, UV PDs based on III-N platforms should have an advantage of lower leakage and better stability when working in high temperature harsh environment, which is often required in critical applications such as flame detection in turbine engine or battlefield environment, gammaray detection for down-hole natural gas and petroleum exploration, and UV-space missions with the lowest cooling budget.

Among various types of PDs having been reported, *p-i-n* type PDs should have lower noise and better detectivity for UV detection since this type of structure can achieve low dark current. For example, III-N *p-i-n* PDs can achieve peak responsivity > 0.15 A/W at λ= 360 nm and high UV-to-visible-band rejection ratio >8×10^3 [136,137];

High-performance *p-i-n* avalanche photodetectors (APDs) with the avalanche gain$> 10^4$ [138-141] were also widely reported. However, until recently, III-N *p-i-n* PDs did not show decent performance. The dark current is high on the devices grown on sapphire substrates because the lattice mismatch between sapphire and GaN is ~ 11 %, resulting in a high dislocation density of $10^8 \sim 10^{10}$ cm^{-2}. For APDs, dislocations cause the junction premature breakdown before the electric field becomes high enough for impact ionization to generate avalanche gains.

On the other hand, III-N MSM photodiodes and Schottky photodiodes have the advantages of high response speed and simple fabrication process compatible with the FET technology. However, the dark current densities of the state-of-the-art III-N MSM and Schottky-barrier photodiodes are usually three orders higher than those of the *p-i-n* photodiodes. To achieve low dark current densities, some studies have been reported to form a high Schottky barrier height at the metal-semiconductor interface by using un-activated magnesium (Mg)-doped GaN layers [142 , 143] or dielectric/GaN heterojunctions [144]. Though the dark current can be significantly suppressed, the cost is that responsivity is greatly reduced. To date, MSM APDs have been demonstrated with the avalanche gain > 1100.

In the context of high-sensitivity, low-photon-flux detection, a large photocurrent gain is highly desired for photodetectors. Semiconductor APDs can provide a comparable large optical gain with the PMTs, combined with the benefits of small size, high reliability, high speed, low operation voltage, low power consumption, low cost, all-solid-state integration, and the Geiger-mode operation. However, the photocurrent gain

commonly achieved in APDs usually comes at a cost of noisy operation due to concurrent amplification of the leakage current and the photocurrent under high electric fields.

HPTs, on the other hand, offer an alternative for high-gain photodetectors by taking advantage of the inherent transistor current gain and controlled carrier multiplication at the operation voltage below the device's dielectric breakdown. Since HPTs are compatible with HBTs in terms of their epitaxial structures and fabrication processes, HPTs would also be a promising form of high-gain photodetectors that can be monolithically integrated with HBT-based optical receiver circuits in optical communication systems. In the past, HPTs were demonstrated on smaller-bandgap materials for infrared detection and fiber-optic communications [145-150]. However, the reports on III-N HPTs were very few [151-154], partly because of the tremendous material growth and device processing challenges in the fabrication of functional III-N HBTs. Also, the performance of III-N HPTs was severely limited by defect densities from various sources and the extended operation of III-N phototransistors under high electric field has been rarely studied. Table summarizes the pros and cons of various type of PD structures.

Table 6. Pros and cons of various types of PD structures

Type	*PIN*	MSM	APD	Phototransistor
Pros	• Vertical device • Low reverse bias • Low noise • Low dark current • High detectivity	• Simple fabrication • High speed	• Vertical device • Internal gain • Better S/N ratio	• Vertical device • Layer- & process-compatible with HBTs • Internal gain • Controlled carrier multiplication
Cons	• Less sensitive • No internal gain	• Lateral device • No internal gain	• Higher noise • High reverse bias	• Higher noise • Complex growth scheme • Higher defect density

In this chaper, both HBT and HPT device fundamentals will be addressed in Section 3.2. In Section 3.3, the light-emitting characteristics of GaN/InGaN HBTs will be first discussed. By biasing the HBT device under different configurations, the origin of each radiative recombination path can be identified. In Section 3.4, we will discuss the photoresponse characteristics of a backside-illuminated GaN/InGaN HBT under an open-base configuration. The backside-illuminated HBT operates as photodetectors and the reversed biased BCJ leads to a photocurrent avalanche as V_{CE} approaches to the bareakdown voltage. This is the first demonstration of III-N avalanche phototransistor and an open-base HBT under the UV illumination serves as proof-of-concept that the light absorbed in the InGaN base induces the photocurrent amplification. In Section 3.5, we report a frontside-illuminated GaN/InGaN HPT that can operate in both open-base phototransistor mode and the avalanche phototransistor mode for NUV-to-DUV photodetection applications. The results demonstrate the feasibility of using III-nitride HPTs as a new form of low light detection in the entire UV spectral regions.

2.9   Device fundamentals

2.9.1   Heterojunction bipolar transistors

HBTs are minority-carrier devices controlled by the vertical minority-carrier distribution in the base layer. BJTs and HBTs are normally-off devices because the two back-to-back *pn* homojunctions or heterojunctions in BJTs or HBTs prevent the current flowing through the transistor.

The current flow through the BEJ (I_E) and BCJ (I_C) can then be described by the diffusion current equations of the *pn* junction. In the case of a *npn* bipolar transistor as shown in Figure 21, I_E and I_C can be expressed as [155]:

$$I_E = I_{En} + I_{Bp} \tag{3.1}$$

$$I_C \sim I_{Cn} \tag{3.2}$$

, where I_{En} and I_{Cn} are the electron current flowing through the BEJ and BCJ, respectively. I_{Bp} is the back-injected hole current from the base to emitter. At forward-active mode, BEJ is under forward bias while BCJ is reverse-biased. The holes injected from the base to collector can be neglected because BCJ is reverse biased. The base current (I_B) can be expressed as the difference between I_C and I_E [155]:

$$I_B = I_E - I_C = (I_{En} - I_{Cn}) + I_{Bp} = I_{Br} + I_{Bp} \tag{3.3}$$

, where I_{Br} represents the recombination current in the base region.
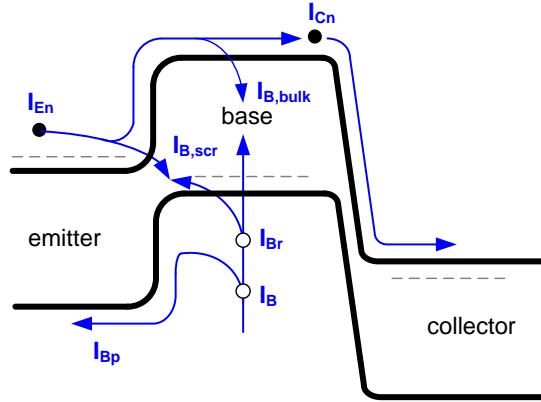
Figure 21. The band diagram of a *npn* bipolar transistor under forward-active mode.

The *emitter injection efficiency* (γ) is defined as the ratio of the useful emitter output (I_{En}) to the total emitter input (I_E) [155]:

$$\gamma \equiv \frac{I_{En}}{I_E} \tag{3.1}$$

The recombination current (I_{Br}) in the base region represents the difference in electron current when electrons traveling from the emitter to the collector side and can be given by [155]:

$$I_{Br} = I_{En} - I_{Cn} \tag{3.2}$$

Therefore, I_{Br} needs to be minimized and the ration between I_{En} and I_{Bp} has to be increased to achieve high current gain. Obviously, $0 \leq \gamma \leq 1$ and the current gain of bipolar transistor is maximized by making γ close to the unity

The fraction of the minority carriers injected into the base that successfully diffuse across the quasineutral width of the base and enter the collector is known as the base transport factor (α_T). For a *npn* bipolar transistor, the *common-base current gain (α)*, which is also known as the current gain transfer ratio, is defined as [155]:

$$\alpha_T = \frac{I_{Cn}}{I_{En}} \tag{3.3}$$

Note that $0 \leq \alpha_T \leq 1$. The smaller the loss of injected carriers via recombination in the quasineutral base, the smaller the degradation of bipolar transistor performance and the larger α_T. Therefore, maximum amplification occurs when α_T is as close as to unity.

Under the forward-active mode operation, the electrons in the reverse biased BCJ experience an electric field pointing to the base and are rapidly swept to the sub-collector. If the electric field is high enough, the impact ionization process becomes significant and these carriers will dramatically increase by the avalanche process. The *avalanche multiplication coefficient (M)* is used to present the amount of carrier multiplication [155]:

$$M \equiv \frac{I_C}{I_{Cn}} \tag{3.4}$$

, where I_C is the total collector current consisting of I_{Cn} and the holes current I_{Cp} [155]:

$$I_C = I_{Cn} + I_{Cp} \tag{3.5}$$

Therefore, α should be the product of γ, α_T, and M [155]:

$$\alpha = \gamma \alpha_T M = \frac{I_{En}}{I_E} \frac{I_{Cn}}{I_{En}} \frac{I_C}{I_{Cn}} = \frac{I_C}{I_E} \tag{3.6}$$

The *common-emitter current gain β*, which is the most important figure of merit in bipolar transistors, is defined as [155]:

$$\beta \equiv \frac{I_C}{I_B} = \frac{I_C}{I_E - I_C} \tag{3.7}$$

According to Eq. (3.6), β can be further expressed as [155]:

$$\beta = \frac{1}{\frac{I_E}{I_C} - 1} = \frac{1}{\frac{1}{\alpha} - 1} = \frac{\alpha}{1 - \alpha} = \frac{\gamma \alpha_T M}{1 - \gamma \alpha_T M} \tag{3.8}$$

As GaN/InGaN *npn* HBTs are usually operated at relatively low reverse bias at BCJ, the expression of β can be simplified by setting M to unity ($I_{Cp} \ll I_C$) [155]:

$$\beta = \frac{\gamma \alpha_T}{1 - \gamma \alpha_T} \tag{3.9}$$

According to Eq. (3.9), it is apparent that a high β value can be achieved as γ and α_T close to unity.

2.9.2 Heterojunction phototransistors

The main difference between heterojunction phototransistors (HPTs) and HBTs is that the base current of HPTs is generated optically rather than being injected through a base contact. The photo-generated holes which accumulate in the base alter the base-emitter potential causing electrons to be injected from the emitter. The current-gain mechanism is the same as that in a standard bipolar transistor. The photocurrent gain (h_{FE}) of a phototransistor is defined as [156]:

$$h_{FE} + 1 = I_{C(opt)} / I_{ph} \tag{3.10}$$

, where $I_{C(opt)}$ is the optical component of the collector current and I_{ph} is the photocurrent generated in the base region. The photocurrent is related to incident optical power level P_0 and can be written by [156]:

$$I_{ph} = (qh\nu)\eta_i P_0 \tag{3.11}$$

, where η_i is the internal quantum efficiency and $h\nu$ is the energy of the incident photons.

The analysis of Miller and Ebers for an avalanche bipolar transistor [157] can be extended to the case of a phototransistor under the floating base configuration. Considering the current continuity, $I_{C(opt)}$ for an avalanche phototransistor can be expressed as [156]:

$$I_{C(opt)} = \frac{(h_{FE}+1)M}{1-(M-1)h_{FE}} I_{ph} = h'_{FE} I_{ph} \tag{3.12}$$

, where M is the multiplication factor. Thus, the effective gain, h'_{FE}, is a function of the bias voltage through M and the incident optical power level through h_{FE}. An increase in the bias voltage, and thus the electric field in the base-collector depletion region, results in an increase in M and leads to an enhanced h'_{FE}. Since h'_{FE} is typically quite large, M needs to be slightly larger than unity to increase h'_{FE} significantly. Physically, the reason the transistor is so sensitive to such small multiplication factors is the regenerative nature of the effect. Initially, the photo-generated holes which are trapped in the base cause electrons to be injected from the emitter. As these electrons pass through the depletion regions of the base-collector junction, secondary electrons and holes are created by impact ionization. The secondary holes are swept back into the base and represent an effective increase in the signal current. This leads to increased injection from the emitter and increased multiplication in the collector; thus increases the number of secondary

58

holes swept into the base, calling for more electron injection from the emitter. In addition, the apparent breakdown of avalanche phototransistors moves to lower voltages as the incident optical power level increases [156, 158]. This is due to the fact that h_{FE} is an increasing function of the signal level. As h_{FE}, increases, the breakdown condition $(M-1)h_{FE}=1$ is satisfied for lower values of M, which implies lower bias voltage.

2.10   Light-emitting characteristics of GaN/InGaN HBTs

2.10.1   Epitaxy layer structure and fabrication of GaN/InGaN HBTs

The material growth and the fabrication processes of the GaN/InGaN HBTs have been reported earlier [159, 160]. As shown in Table 7, the layer structures were grown on either n-type FS-GaN or sapphire substrate using a Thomas–Swan close-coupled-showerhead MOCVD reactor. The device structure consists of a 2.5-μm-thick unintentionally doped (UID) GaN buffer layer, a 1000-nm Si-doped n-GaN sub-collector (free electron concentration (n)= 3×10^{18} cm^{-3}), a 500-nm n-GaN collector ($n = 1\times10^{17}$ cm^{-3}), a 30-nm In$_x$Ga$_{1-x}$N ($x = 0$-0.03) graded layer, a 100-nm Mg-doped In$_{0.03}$Ga$_{0.97}$N base ($p\sim 8.76\times10^{17}$ cm^{-3}), a 30-nm In$_x$Ga$_{1-x}$N ($x= 0.03$–0) n^+ graded layer and a 70-nm n-GaN emitter ($n \approx 1\times10^{19}$ cm^{-3}).

In Figure 22 (a), the device fabrication process starts with a three-step chlorine-based mesa etching in a STS™ ICP etching system using e-beam evaporated SiO$_2$ layers as etching masks. The first mesa etching step is to isolate the GaN/InGaN HBTs by removing the highly conductive sub-collector layer. The following etching process is used to expose the base layer, and the third mesa etching stops at the sub-collector to expose the contact area for collector contact. After the ICP etching steps, HBT samples

are treated in a diluted KOH/$K_2S_2O_8$ solution under the ultraviolet light illumination to remove the dry-etching-induced damage [173]. Ti/Al/Ti/Au and Ti/Al/Ti/Pt metal stacks are patterned and annealed in a nitrogen environment for the collector and emitter contact, respectively. Ni/Au is finally patterned and annealed at 500 ^{o}C for 1 minute in air to to form base contact. Figure 22 (b) shows the the schematics of GaN/InGaN *npn* HBTs before passivation.

Table 7. A summary of layer structure variations of *npn* GaN/InGaN HBTs on sapphire (wafer#: 1-1785-6F) and FS-GaN (wafer#: 1-1793-6M) substrates

Layer	Material	Thickness (nm)	Free carrier concentration (cm^{-3})
Emitter cap	GaN	70	$n = 1 \times 10^{19}$
Emitter grading	In$_x$Ga$_{1-x}$N (x = 0–0.03)	30	$n = 1 \times 10^{19}$
Base	In$_x$Ga$_{1-x}$N (x = 0.03)	100	$p = 2 \times 10^{18}$
Collector grading	In$_x$Ga$_{1-x}$N (x = 0.03–0)	30	$n = 1 \times 10^{18}$
Collector	GaN	500	$n = 1 \times 10^{17}$
Sub-collector	GaN	1000	$n = 3 \times 10^{18}$
Buffer layer	GaN	2500	UID
Substrate	Sapphire or FS-GaN Substrate		

(a)

Device isolation etching

↓

Emitter-base mesa etching

↓

Base-collector mesa etching

↓

PEC surface treatment

↓

Collector metal

↓

Emitter metal

↓

Base metal

(b)
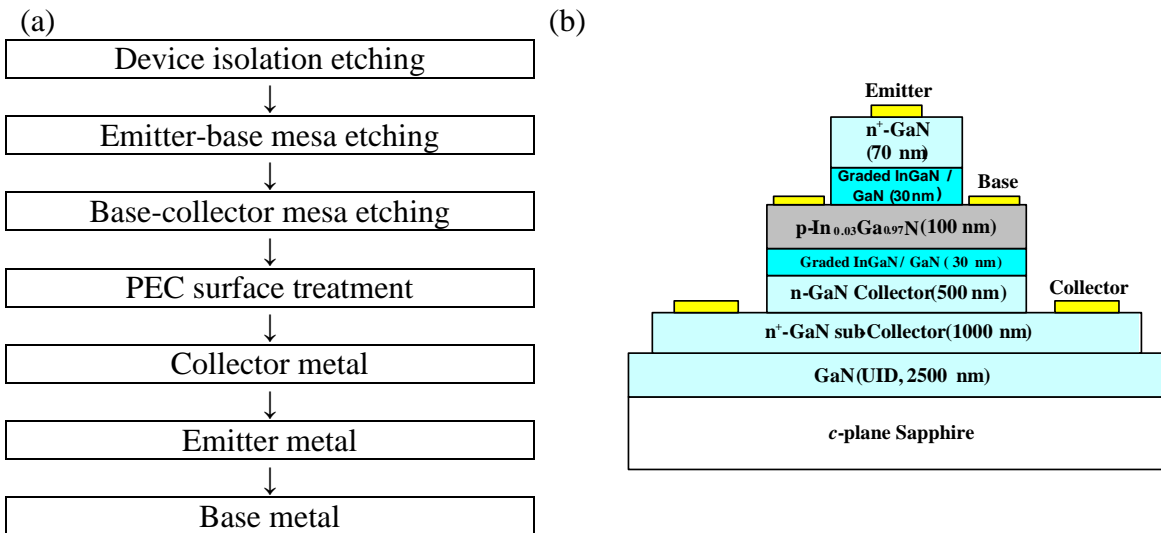
Figure 22. (a) The fabrication process flow and (b) the schematics of GaN/InGaN *npn* HBTs before passivation.

2.10.2 Electroluminescence (EL) measurement setup

The EL measurement setup is shown in Figure 23. photons emitted from the same HBT under test was collected through an UV-grade optical fiber with a diameter of 600 μm with a tilt angle of 45° with respect to the HBT's top surface. The emission spectrum was analyzed in an Ocean Optics spectrometer (Model: HR2000CG-UV-NIR) with an integration time of 1 second and a spectral resolution of 0.1 nm.
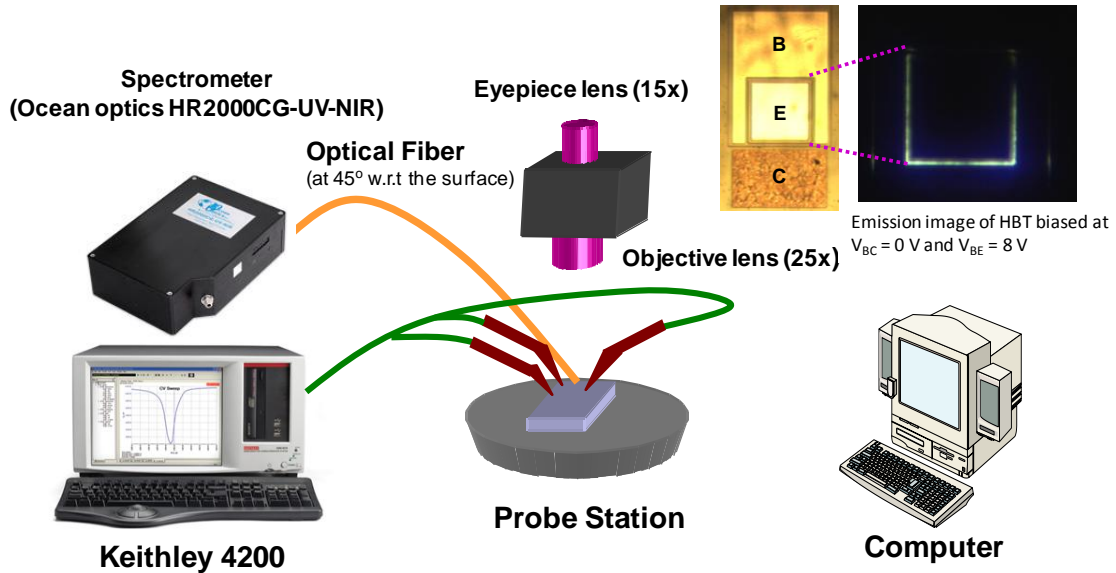
Figure 23. EL measurement setup

2.10.3 Light-emitting characteristics of GaN/InGaN HBTs

The d.c transistor characteristics were evaluated in a Keithley 4200-SCS semiconductor parameter analyzer at the room temperature. Figure 24 shows the Gummel plot of a fabricated InGaN HBT at V_{BC}= 0 V. The device under test has an emitter area (A_E) of 20×20 μm^2. The maximum *d.c.* current gain (β= I_C/I_B) is 30 at J_C= 5 kA/cm^2. The EL spectra were measured in the diode modes for the base- BCJ and the BEJ, respectively, as well as in the HBT's forward-active transistor mode (or the LET mode). Figure 25 (a) shows the measured emission spectrum for the device operating in the LET

mode with I_B= 100 μA, I_C= 800 μA and V_{BC}= 0 V. The EL from the BEJ and the BCJ of

the same HBT with a current injection of 100 μA are also shown in the same plot for

comparison. The inset of Figure 25 (a) shows the microscope photograph of a HBT under

the LET mode. Most of the radiative recombination processes seem to occur in the

intrinsic transistor region, i.e., the area directly underneath the emitter electrode. Since

the back-injected hole current is insignificant at the BEJ, the radiative recombination

processes most likely take place either in the space charge region of the BEJ or the quasi-

neutral base region. This observation is supported by the fact that insignificant band-to-

band (BB) radiative recombination from the GaN layers, the constituent material of the

emitter and the collector, was observed in the EL spectrum ($\lambda_{GaN} \approx 365$ nm).
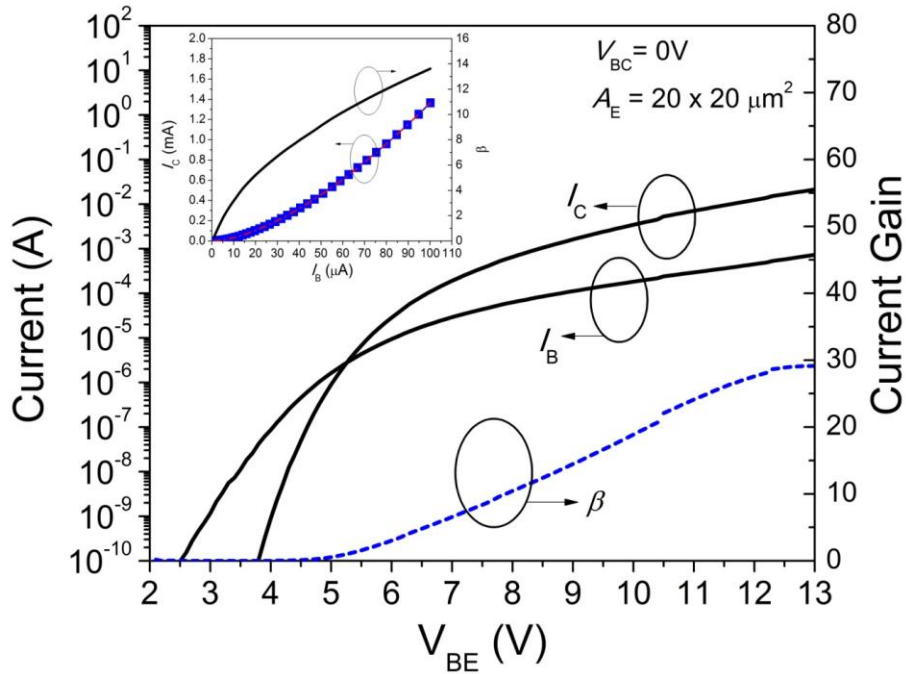
Figure 24. The Gummel plot (V_{BC}= 0 V) of HBTs with A_E=20×20 μm² grown on sapphire substrate (wafer#: 1-1785-6F-B12RA2; A_E= 20×20 μm²). The inset of Figure 24 shows I_C and β as increasing I_B from 10 μA to 110 μA.

Using a Lorentzian fitting, three peaks can be resolved in the emission spectrum

in Figure 25 (a). The shortest wavelength of the emission peaks is λ_1= 375 nm (3.3 eV)

with a full-width at half-maximum (FWHM) of 5 nm. It matches well with the bandgap wavelength of $In_{0.03}Ga_{0.97}N$ based on a prior report [161]. The second emission peak occurs at λ_2= 393 nm (3.15 eV) with a FWHM of 30 nm. Since the acceptor-level energies for Mg-doped InGaN alloys are170 meV for *p*-GaN and 130 meV for *p*-$In_{0.06}Ga_{0.94}N$ [162], respectively, the acceptor-level for Mg-doped $In_{0.03}Ga_{0.97}N$ is 150 meV above the valence band using a linear interpolation and the second peak emission wavelength could be associated with the conduction-band-to-acceptor (CBA) transition in the Mg-doped base region. A broad emission peak was also observed in the visible band with a center wavelength (λ_3) at ~560 nm (2.2 eV). This YL band is commonly known in a *p*-type III-N layer as the deep donor-acceptor pairs (DAP) such as Mg_{Ga} acceptors or deep-level the nitrogen vacancy states (V_N) are present [163-166]. Figure 25 (b) shows three possible radiative recombination paths that involve the conduction (E_C) and valence-band (E_V) states, deep-level states (E_T) and acceptor-level states (E_A) in the *p*-InGaN region of HBT.

In the forward-biased BEJ, the electron current path involves the extrinsic base region and the intrinsic BEJ region with significant current crowding at the edge of the emitter mesa (20×20 μm^2). Possible radiative recombination paths could be through the BEJ sidewall, etched *p*-type InGaN surface, the *n*-type emitter and the intrinsic BEJ. On the other hand, in a forward-biased BCJ, the major current path goes directly underneath the base electrode, commonly known as the extrinsic base region, and through the sub-collector. The curve fitting of Figure 25 (a) shows that both forward-biased BEJ and BCJ emission spectra have the same emission peak wavelengths as those in the LET mode measurement. No BB emission peak of GaN was observed at λ= 365 nm from the three

measurements. The result suggests that the major radiative recombination only occurs in the InGaN base region. However, the YL intensity obtained from these three configurations is almost identical. This result shows that the defect-related YL could mostly originate from the quasi-neutral base region, which is the common recombination path for these three measurements.
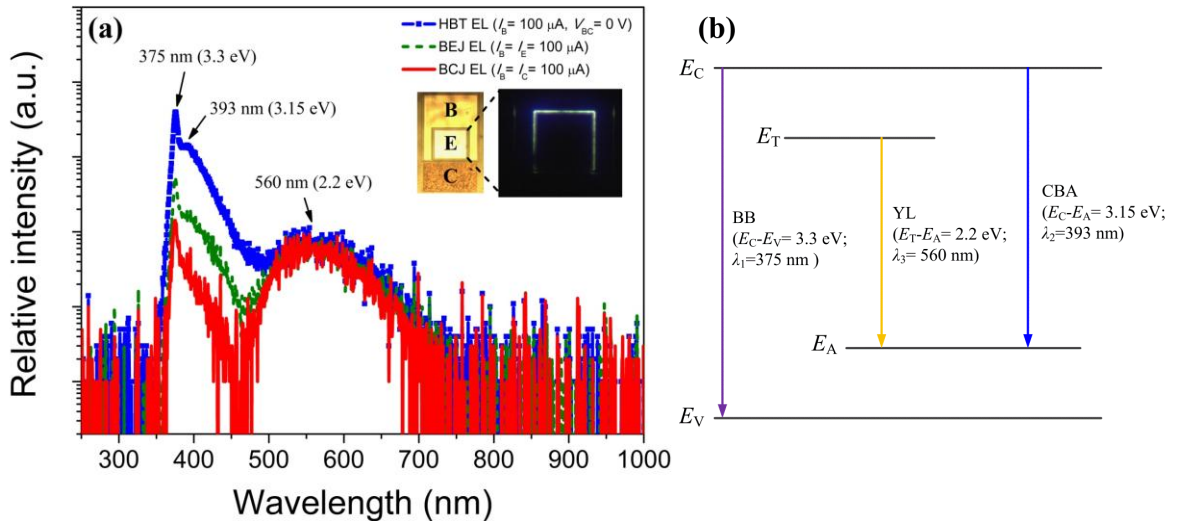
Figure 25. (a) The EL spectrum of GaN/InGaN HBTs (wafer#: 1-1785-6F-B12RA2; A_E= 20×20 μm²) operated at I_B= 100 μA and V_{BC}= 0 V. The inset shows the microscope image of the device when operating in the forward-active mode configuration. The EL spectra from a HBT and its BEJ and BCJ, respectively, are also compared at the same I_B values; (b) A schematic diagram shows three radiative recombination paths resolved in HBTs, corresponding to the band-to-band (BB) transition, conduction-band-to-acceptor-level (CBA) transition, and yellow luminescence (YL) occuring at 3.3 eV, 3.15 eV, and 2.2 eV, respectively.

Figure 26 (a) shows the integrated EL intensity (I_L) of the BB and CBA emissions as a function of I_B for different bias configurations. The emission intensity from the BB and the CBA transition is more pronounced for the HBT operated in the LET mode than those measured in the diode modes. For the LET mode biasing, I_L associated with the BB and CBA transition increases abruptly and follows a nonlinear dependence of I_B. On the other hand, I_L associated with the BB and CBA transitions increases linearly with the

injected base current (I_B) for the forward-biased BEJ and BCJ. For the YL, as shown in Figure 26 (b), the data show that I_L have nearly identical intensity and increase linearly with I_B in either the diode modes or LET mode measurements. The intensity, however, follows a slower growth rate for I_B >110 μA. The slower increase of the YL intensity at higher I_B comes from the fact that E_T and E_A tend to be filled with electrons at higher current injection, as the quasi-Fermi level for electrons moves above the acceptor states in the base region, resulting in reduced downward transition rate for the YL emission.

As shown in Figure 26 (c), the emission light intensity through the BB and CBA paths seems to be linearly proportional to I_C. The dependency of these two emission paths on I_C can be understood as follows. For a radiative recombination process, the luminescence intensity for each transition path is proportional to the electron density at the initial state and the empty state density at the final state. In the BB transition, the light intensity is proportional to the product of n and p, while the light intensity in the CBA transition is proportional to n only for a given current injection level. As shown in the inset of Figure 24 (a), $β$, and hence I_C, increases nonlinearly as I_B increases from 10 μA to 110 μA. The enhanced radiative recombination in the LET mode is mainly attributed to the enhanced excess electron injections from the emitter as the V_{BE} increases. As the transistor is operated in the forward-active transistor mode, the excess electron density (n) in the InGaN base can be approximated as:

$$n \approx \frac{Q_B}{qA_E W_B} = \frac{I_C W_B}{2qA_E D_n} \tag{3.13}$$

, where D_n is the diffusion coefficient; W_B is the thickness of the base region and Q_B is the total stored base charge in the forward-active mode [167]. For a given I_B, both the BB and the CBA recombination are proportional to the injected electron concentration from

65

the emitter, and hence is proportional to I_C. The results also support the observation that these two radiative emission paths occur at the intrinsic part of the base region.
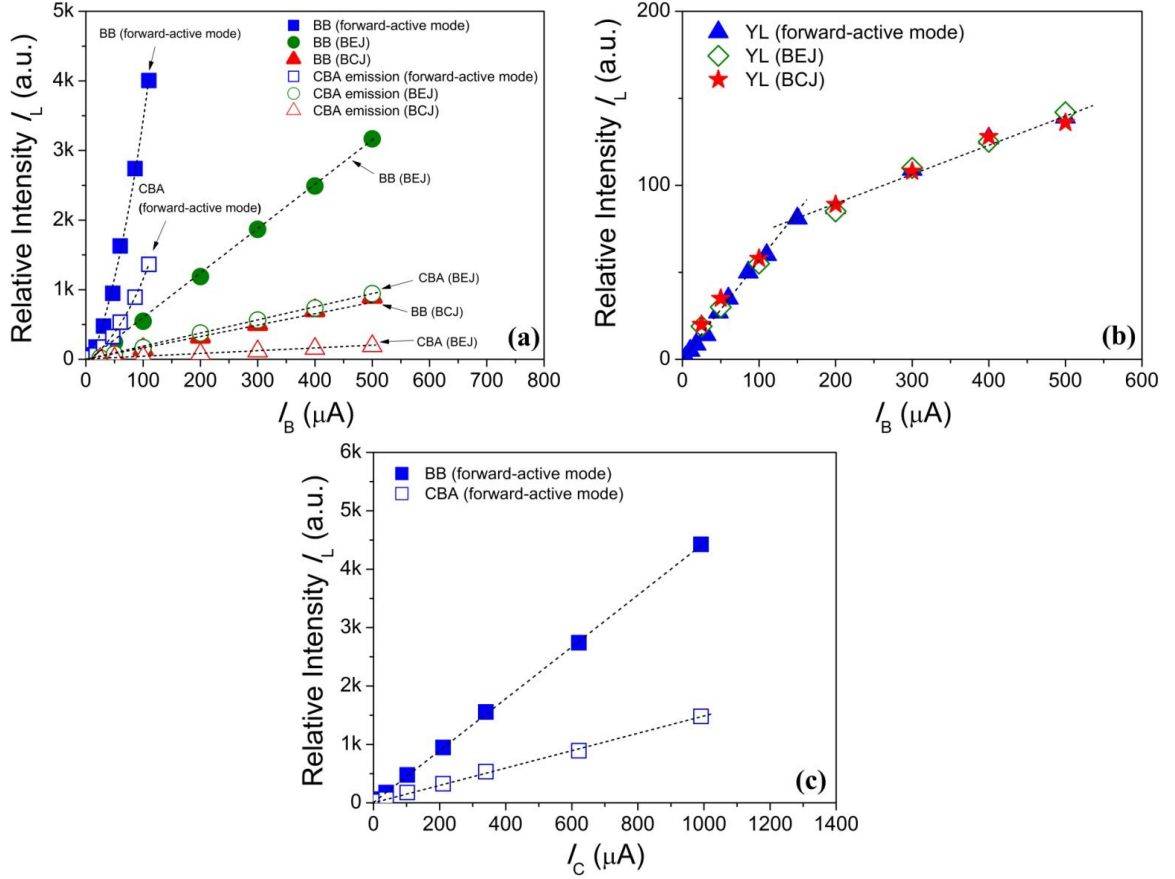
Figure 26. I_B-**dependent EL intensity for (a) the BB and CBA transitions and (b) YL under different biasing configurations. (c) the EL intensity for the BB and CBA transitions as a function of** I_C **in the forward-active transistor mode (**$V_{BC} = 0$ **V).**

2.10.4 Model fitting

A radiative recombination model for the HBT EL can be established using a set of rate-equations in the p-InGaN by considering possible radiative recombination paths of (i) conduction-and valence-band states, (ii) deep-level states and (iii) acceptor-level states, as shown in Figure 25 (b). n and p are denoted as the total electron and hole concentrations of the p-InGaN, respectively. D_o is the deep-level-state density and N_A ($=8.76\times10^{17}$ cm^{-3}) is the ionized dopant concentration of the p-InGaN base layer. N_2 and

N_3 are the number of states that were occupied by electrons in N_A and D_o, respectively.

Under the steady state, the rate equations can be expressed as:

$$\frac{\partial n}{\partial t} = \frac{I_{EN} - I_{CN}}{qA_E W_B} - B_{41}np - C_{42}n(N_A - N_2) - C_{43}n(D_0 - N_3) = 0 \tag{3.14}$$

$$\frac{\partial N_3}{\partial t} = C_{43}n(D_0 - N_3) - C_{32}N_3(N_A - N_2) = 0 \tag{3.15}$$

$$\frac{\partial N_2}{\partial t} = C_{32}N_3(N_A - N_2) + C_{42}n(N_A - N_2) - C_{21}N_2 p = 0 \tag{3.16}$$

, where B_{41} is the band-to-band radiative recombination coefficient for InGaN (3%); C_{ij} (*i, j= 1,2,3,4)* are proportionality constants and are characteristic of each downward transition path from state *i* to state *j*; q is the unit charge. Assuming the back-injected hole current is negligible; I_{EN}–I_{CN} is approximately equal to I_B in the case of HBT biased in the forward active mode. The impact of the surface-recombination current ($K_{B,surf}$) can be ignored, as is evident by the fact that $K_{B,surf}$ value is as low as $9.6 \times 10^{-5} - 5.8 \times 10^{-4}$ (A/cm) for $J_c = 0.5 - 50$ A/cm^2 according to our previous study [168]. The Auger recombination was not included in the equations because the transistor was driven in the low-level injection conditions. In the base region, n can be approximated as [167]:

$$n \approx \Delta n = \frac{Q_B}{qA_E W_B} = \frac{I_C \tau_B}{qA_E W_B} = \frac{\beta I_B \tau_B}{qA_E W_B} = \frac{\beta I_B W_B}{2qA_E D_n} \tag{3.17}$$

, where Δn is the excess electrons of the *p*-InGaN region. As the excess electrons generated in the *p*-InGaN region, the quasi-Fermi level (E_{Fn}) for electrons can be expressed as:

$$E_{Fn} = E_{Fi} + kT\ln(\frac{\Delta n}{n_i}) \tag{3.18}$$

, where E_{Fi} is the intrinsic Fermi energy and n_i is the intrinsic carrier concentration of p-InGaN layer. Therefore, N_3 can be expressed as:

$$N_3 = D_0 f(E_{D_0}) = D_0(1 + \exp(\frac{E_{D_0} - E_{Fn}}{kT}))^{-1} \tag{3.19}$$

, where E_{D0} is the deep-level energy, which is ~950 meV below the conduction band of p-InGaN layer. The number of states that are occupied by electrons can be also solved from Eqns. (3.14) to (3.16):

$$N_3 = \frac{C_{21}N_2 p - C_{42}n(N_A - N_2)}{C_{32}(N_A - N_2)} \tag{3.20}$$

$$N_2 = \frac{C_{43}n(D_0 - N_3) + C_{32}N_3 N_A}{C_{32}N_3} \tag{3.21}$$

The luminescence intensity for each transition path can be expressed as:

$$I_{41} = K_1 np \tag{3.22}$$

$$I_{32} = K_2 N_3(N_A - N_2) \tag{3.23}$$

$$I_{42} = K_3 n(N_A - N_2) \tag{3.24}$$

, where K_1, K_2, and K_3 are the proportionality factors. From this set of equations, one may solve for n, N_2 and N_3 for a given I_B and β from Eqns. (3.17)-(3.21) and the EL intensities corresponding to each transition path (i.e., I_{41} for band-edge emission, I_{32} for CBA and I_{42} for YL intensities) can be derived from Eqns. (3.22)-(3.24). Figure 27 shows the calculated and measured EL intensity dependence as a function of I_B for the same HBT (A_E= 20×20 µm^2) under forward-active mode. The theoretically predicted dependences of three radiative recombination paths are in agreement with the experimental results. As E_{Fn} is above E_{D0} under high excess electron concentrations in the p-InGaN region, $N_3 \approx D_0$ from Eq. (3.20) and $N_2 \approx N_A$ from Eq. (3.21) are both obtained.

According to Eq. (3.23), the recombination rate of YL transition decreases, which is consistent with experimental results shown in Figure 26 (b) at I_B >110 mA. Using this model, furthermore, one may expect stronger band-edge (I_{41}) and CBA emission (I_{42}) but suppressed YL intensity (I_{32}) as decreasing D_0, which were observed in HBTs grown on a FS-GaN substrate in our previous study [169]. Since the large lattice mismatch between the substrate and the epitaxial layers may severely affect the minority carrier transport in III-N bipolar transistors due to the "native" defect formation, the base current would increase without effectively contributing to the increase in the emitter injection. It is therefore evident that the drastic reduction of the threading dislocation density through homoepitaxial growth leads to better HBT device performance (β> 90 and maximum J_c> 100 kA/cm^2) compared to those devices grown and fabricated on the sapphire substrate platform.
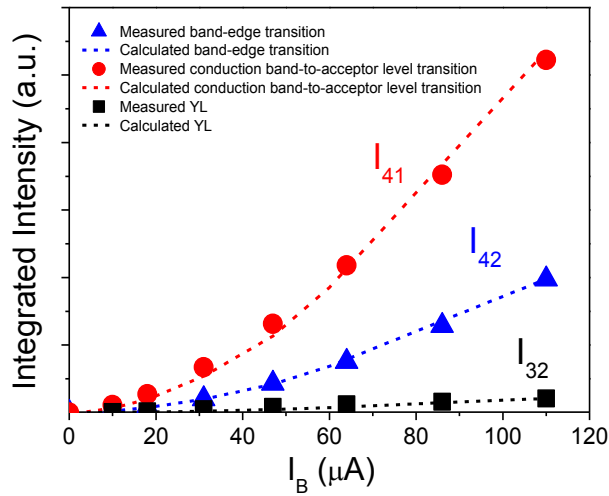
Figure 27. Measured (dotted line) and calculated (solid line) EL peak intensities (band-edge transition, conduction-band-to-acceptor-level transition, and YL) as a function of I_B.

2.10.5 Study of FS-GaN and sapphire substrates

To further understand the origin of the YL, we compared the EL spectrum of two devices of the same epitaxial layer structure. One was grown ona sapphire substrate and the other on a FS-GaN substrate. Two devices ofthe same dimensions (A_E= 60×60 µm^2, A_{Bext}= 6372 µm^2) were chosen for the performance comparison under the froward-active HBT mode. Figure 28 shows a comparison of the EL spectra for these two devices stressed at I_B = 1mA. The emission spectra are normalized with respect to the band-edge peak intensity. For the device grown on the FS-GaN substrate, the emission spectrum shows a red-shift in the band-edge emission peak and a narrower FWHM of 4 nm when compared to that grown on a sapphire substrate. The result is consistent with prior reports in that the p-InGaN layer has a narrower bandgap if it is grown on a FS-GaN substrate when compared to that grown on a sapphire substrate [170]. Regarding the YL intensity, the result shows that it is muchpronounced for the devicegrown on a sapphire substrate. Since both growth conditions and device fabrication recipes are identical, one may conclude that the deep-level states induced by the plasma etching damage have less significant influence on the creation of YL emission source. On the other hand, the presence of significant deep-level luminescence from devices grown on a sapphire substrate may suggest that a much higher dislocation density arising from the hetero-epitaxy of the sapphire substrate plays significant roles in the transistor's performance as the devices size up. As the carriers recombine via these crystalline defects in the HBT, the base current would increase without effectively contributing to the increase in the emitter injection. It is therefore evident that the drastic reduction of the threading dislocation density is critically beneficial for realizing high-quality III-N bipolar devices.
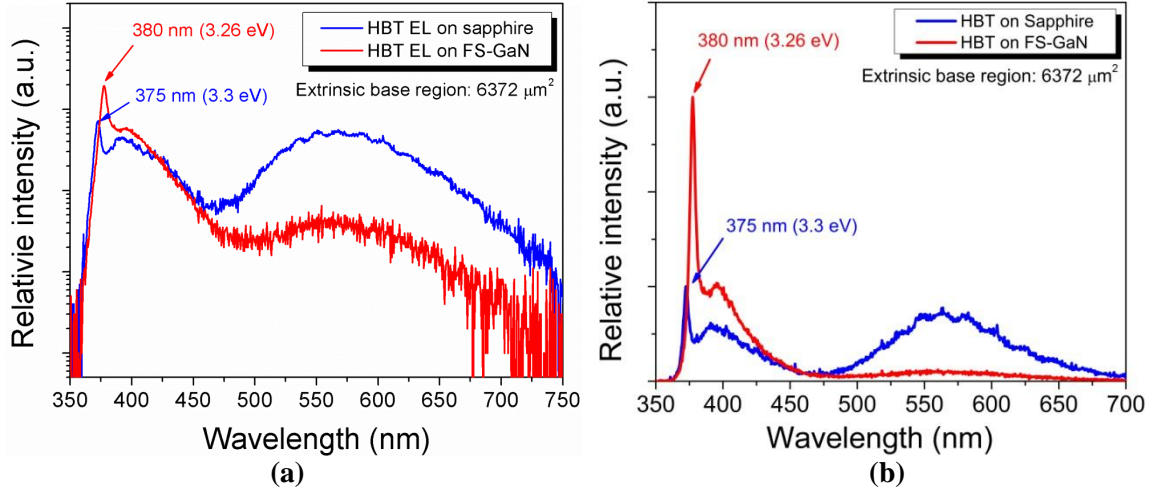
Figure 28. The EL spectra of HBTs grown on a sapphire (wafer#: 1-1785-6F-B12LC3; A_E= 60×60 µm^2) or FS-GaN substrate (wafer#: 1-1793-6M-B10-RC3; A_E= 60×60 µm^2) with the extrinsic base area of 6372 µm^2. (a) in log scale. (b) in linear scale.

2.10.6 Conclusions

We report an EL study on *npn* GaN/InGaN HBTs. Three radiative recombination paths are resolved in HBTs, corresponding to the band-to-band transition (3.3 eV), conduction-band-to-acceptor-level transition (3.15 eV) and YL with the emission peak at 2.2 eV. We further study possible light emission paths by operating the HBTs under different biasing conditions. The band-to-band and the conduction-band-to-acceptor-level transitions mostly arise from the intrinsic base region, while a defect-related YL band could likely originate from the quasi-neutral base region of a GaN/InGaN HBT. The I_B-dependent EL intensities for these three recombination paths are discussed. The results also show the radiative emission under the forward-active transistor mode operation is more effective than that using a diode-based emitter due to the enhanced excess electron concentration in the base region as increasing the collector current increases.

71

2.11 Photoresponse characteristics of GaN/InGaN HBTs

2.11.1 Photoresponse measurement setup

The photoresponse measurement setup is shown in Figure 29. The devices were tested using a Keithley 4200 semiconductor characterization system for *d.c. I-V* characteristics under the dark condition and UV illumination to determine the photocurrent response. The light source used in this study was a 150-W Oriel xenon (ozone-free) lamp that is integrated with a Newport 1/4-m Cornerstone 260 monochromator for single-wavelength selection. An optical chopper is inserted in the light path as necessary for the photocurrent spectroscopy measurement. The output from the monochromator was coupled into a 600-µm-diameter UV-grade optical fiber and the light output at the other end of the fiber is incident on the HPT from either the back (substrate) side or fronside of the wafer. The incident optical power (P_o) was controlled by adjusting the slit openings of the monochromator and the P_o of different slit openings was measured using a calibrated UV-enhanced Si detector (Hamamatsu, S2281–04).
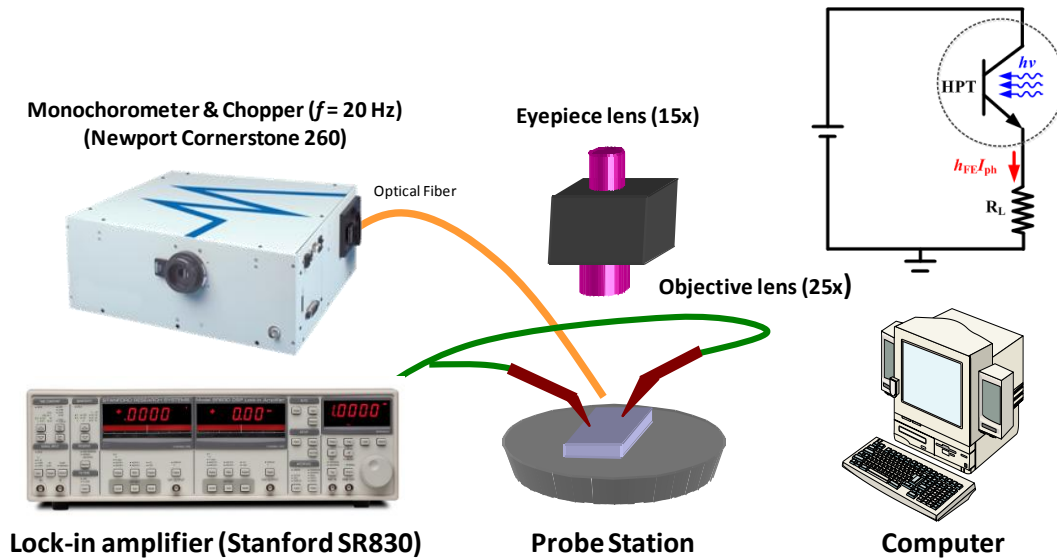
Figure 29. Photoresponse measurement setup

2.11.2 Photoresponse characteristics of backside-illuminated GaN/InGaN HBTs

The transistors under test had an emitter area (A_E) of 20×20 μm^2. Since the devices were biased in the forward-active mode, under the dark condition, the transistors show typical HBT characteristics with an offset voltage of 0.1 V, a knee voltage of 3 V at $I_B = 100$ μA, and a current gain ($h_{fe} = \Delta I_C / \Delta I_B$) of >100 for $I_C > 3mA$, as shown in Figure 30 (a). The BV_{CEO} of this device is 148 V (see the inset of Figure 30 (a)). As the base electrode is left open-circuited and, in this study, the UV light ($\lambda = 380$ nm) is illuminated on the transistor from the back side of the wafer, the transistor is operating in the HPT mode. As shown in Figure 30 (b), the collector current (I_c) remains constant for low V_{CE} (<15 V) for a fixed input optical power. We assume that the optical output from the fiber is uniformly distributed over the device active area and only the UV light absorbed in the intrinsic transistor area (A_E) contributes to the photocurrent generation. The R_λ of the device can be calculated as $R_\lambda = (I_C - I_{C(dark)}) / P_{opt}$, where P_{opt} is the total optical power incident on the active transistor area. We observe that R_λ increases from 1.03 A/W at V_{CE} =1 V to greater than 1.27 A/W at $V_{CE} = 15$ V for $P_{opt} = 51$ $\mu W/cm^2$. For a fixed V_{CE}, R_λ decreases slightly (by <10%) as P_{opt} increases from 51 $\mu W/cm^2$ to 793 $\mu W/cm^2$.

(a)

(b)
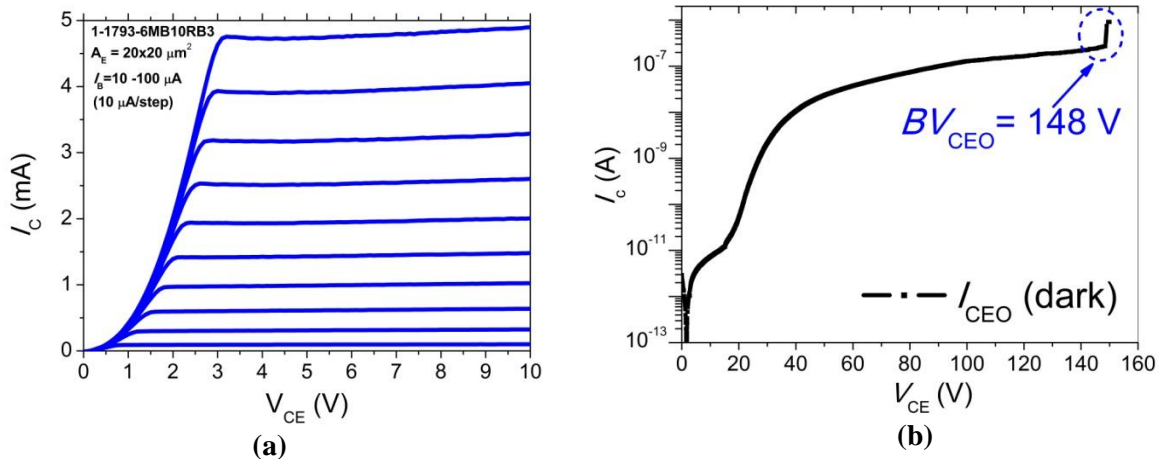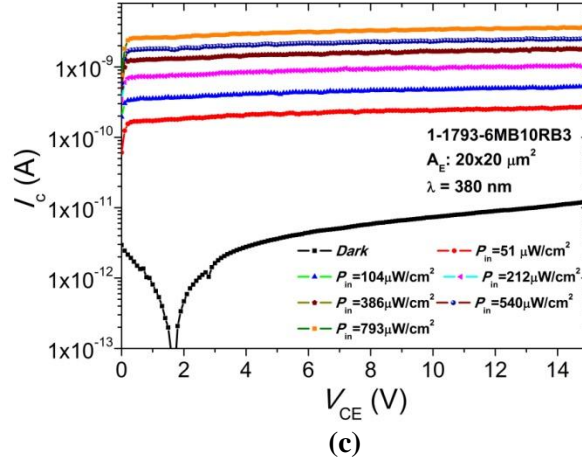
Figure 30. (a) The d.c. family *I-V* characteristics of the HPT transistor (wafer#: 1-1793-6M-B10-RB3; A_E= 20×20 μm²) under test. The inset shows the BV_{CEO} measurement of the device. (b) Low-voltage *I-V* characteristics the transistor in the (open-base) HPT mode under the dark and the UV illumination at λ= 380 nm.

Figure 31 (a) shows the V_{CE}-dependent spectral response of the phototransistor. The single-wavelength optical output from the monochromator was modulated by an optical chopper at 20 Hz. Photocurrent spectroscopy for this pulsed optical input was measured at fixed V_{CE} using a lock-in amplifier (Stanford Research, Model SR 830) and was calculated from the voltage drop across a resistor (R_L= 99.38-kΩ) attached to the emitter terminal of the transistor. The data show that the HPT responds to photons with $\lambda > 370$ nm and the peak responsivity was observed near $\lambda \sim 380$ nm. The peak photon absorption energy is similar to the bandgap energy of the $In_{0.03}Ga_{0.97}N$ base layer at room temperature ($\lambda_{Eg} = 377$ nm), which was confirmed by photoluminescence measurements. The data also show no significant photocurrent contribution from shorter wavelengths, as the back-side illuminated UV photons with $\lambda < 370$ nm could be absorbed in the substrate and the underlying *n*-GaN layers. One may conclude that the photon generation in these regions does not contribute to the photocurrent amplification in the transistor.

As shown in Figure 31 (b), R_λ increases gradually from 1.1 A/W at $V_{CE} = 5$ V to 1.5 A/W at $V_{CE} = 50$ V. For $V_{CE} > 50$ V, R_λ increases significantly and reaches a value of 68 A/W at $V_{CE} = 95$ V. The peak absorption wavelength however shifted slightly from 380 nm to 382 nm as V_{CE} increases. The R_λ enhancement is a direct consequence of the carrier multiplication in the reverse-biased BCJ at high V_{CE} as the open-base phototransistor is self-biased in the forward-active mode under illumination. As V_{CE} increases, the electric field in the reverse-biased collector increases. Considering the collector multiplication factor (M), the current gain (β) of a phototransistor can be expressed as $\beta = \alpha_F M /(1 - \alpha_F M)$ [171]. At low V_{CE}, M is approximately 1. Since α_F is a close-to-unity value, a slight increase of M will lead to a rapid increase of β, and hence R_λ. The phototransistor was in turn operating at the APT mode when $M > 1$. When $\alpha_F M$ equals 1, β approaches infinity and the transistor is driven into avalanche breakdown. The data show that, when the peak electric field in the collector region is greater than ~2.2 MV/cm (a biasing condition for $V_{CE} > 50$ V), $\alpha_F M$ increases and leads to higher phototransistor current gain. At $V_{CE} = 95$ V, the APT shows an enhancement of R_λ by a factor of > 68, compared to those at low V_{CE}.
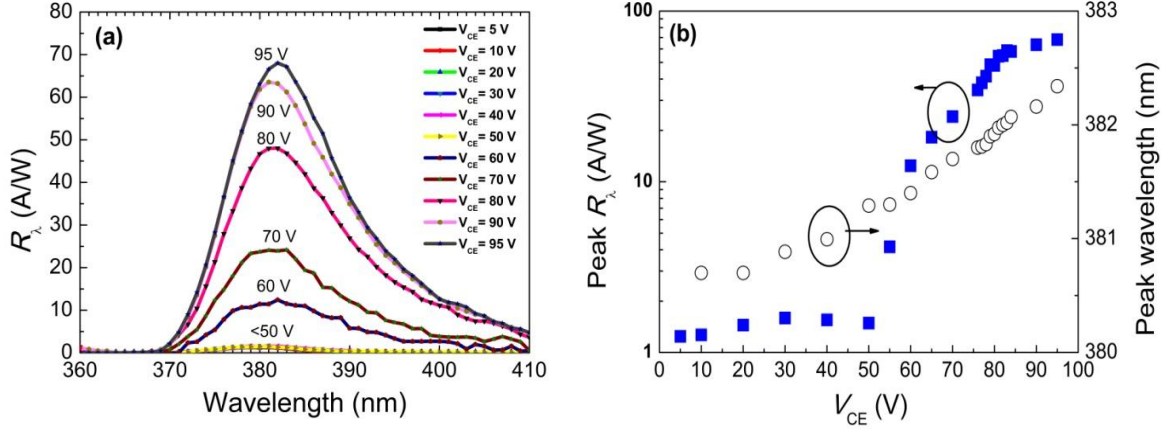
Figure 31. (a) A room-temperature V_{CE}-dependent spectral response of the phototransistor. The carrier multiplication in the collector leads to high R_λ under the APT operation mode (wafer#: 1-1793-6M-B10-RB3; $A_E= 20\times20$ μm^2). (b) A plot showing the peak R_λ values and the corresponding wavelengths of the peak R_λ as a function of V_{CE}.

Shown in Figure 32 is a plot of the measured d.c. collector current versus V_{CE} under the dark condition and the UV illumination at $\lambda= 380$ nm. For $P_{opt} = 51$ μW/cm^2, significant photocurrent multiplication was observed for $V_{CE} > 50$ V and R_λ of > 300 A/W is achieved at $V_{CE} = 140$ V. As P_{opt} is increased to 1291 μW /cm^2, the collector current avalanching occurs at $V_{CE} \sim130$ V. The reduced avalanche voltage of an APT under a higher photon flux is consistent with those observed in smaller-bandgap infrared III-V APTs [172]. To provide a first-order approximation of the device performance, β can be estimated by taking into account of the reflectivity at the air-GaN interface ($R\sim$ 30.5 %) and the absorption coefficient of the In$_{0.03}$Ga$_{0.97}$N base layer ($\alpha= 2.71\times10^4$ cm^{-1}). The photocurrent gain of the HPT can calculated as $\beta = hcI_C /[\eta_i q\lambda(1- R)(1-e^{-\alpha L_B})P_{opt}]-1$, where h is Planck's constant, c is the speed of the light, η_i is the internal quantum efficiency and L_B is the base width. For a conservative estimation, $\eta= 100\%$ was assumed for the photon absorption, which offers an underestimated photocurrent gain assessment. At $P_{opt} = 51$ μW/cm^2, β is ~15 and the

corresponding $\alpha_F M$ is 0.94 at low V_{CE}. At $V_{CE} = 140$ V, β reaches ~6000, and $\alpha_F M$ is greater than 0.9998. The corresponding external responsivity R_λ is greater than 300. Assuming that α_F stays approximately constant, which is evident from the fact that the GaN/InGaN HBT has a relatively high Early voltage and that M is unity at low V_{CE}, the required M to enable the GaN/InGaN APT operation is estimated to be ~1.06, which can be achieved at a voltage lower than the dielectric breakdown of the base-collector junction of the transistor. It should be noted that the intrinsic performance of the APT was underestimated as the residual below-the-bandgap abosorption of the FS-GaN substrate (with a measured transmittance of ~57% at $\lambda = 380$ nm), incomplete photon absorption in the thin base layer and the reflection loss were included as the cumulative effects in the evaluation of R_λ in this report.
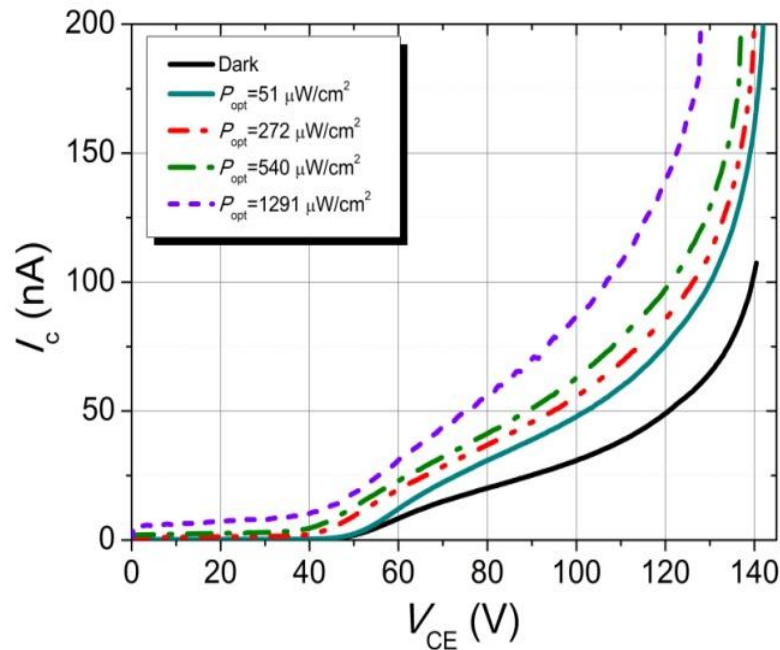
Figure 32. The V_{CE}-dependent current responses of the phototransistor under the dark and the UV illumination conditions. Significant photocurrent amplification was observed for V_{CE} stressed at the near-avalanche-breakdown biases. Higher photo flux results in lower avalanche voltage in the APT operation (wafer#: 1-1793-6M-B10-RB3; $A_E = 20 \times 20$ μm^2).

2.11.3 Conclusions

We report the observation of carrier multiplication of III-N HPTs using a typical GaN/InGaN HBT structure and demonstrated the first III-N APT operation in an open-base configuration under UV illumination from the backside of the wafer. A spectral response measurement shows that the photons absorbed in the InGaN base layer are responsible for the photocurrent generation, followed by subsequent current amplification. At low voltage (V_{CE} < 20 V), the device performs as an HPT with a photoresponsivity (R_λ) of >1 A/W for photons with $\lambda \approx$ 380 nm, the bandgap wavelength of the $In_{0.03}Ga_{0.97}N$ base layer. At high V_{CE} (> 50V), slight increase of the carrier multiplication in the reverse-biased base-to-collector junction (BCJ) leads to significantly enhanced photocurrent gain and the open-base transistor operates in the APT mode as the product of the common-base current gain (α_F) and the collector multiplication factor (M) approaches 1. R_λ of >68 A/W for an input photon density of 50 $\mu W/cm^2$ at $\lambda =$ 382 nm was achieved at $V_{CE} =$ 95 V, and it was further enhanced to > 300 A/W at $V_{CE} =$ 140 V.

2.12 Development and characterization of GaN/InGaN HPTs

2.12.1 Epitaxy layer structure and fabrication of GaN/InGaN HPTs

Figure 33 (a) illustrates a schematic cross section of a GaN/InGaN HPT. The device fabrication started with the mesa etching to expose the sub-collector layer using an ICP dry etching tool. After the mesa etching, the sample was treated in a diluted KOH-based solution under ultraviolet light illumination to remove the dry-etching-induced surface damage [173]. Ti/Al/Ti/Au metal stack was deposited in an e-gun evaporator to form the emitter and the collector contact. The contact resistance was 8.3×10^{-6} Ω-cm^2 and

9.1×10^{-6} Ω-cm^2 for the emitter and collector, respectively. The devices were coated by a SOG and a thick Ti/Au interconnect metal was deposited after via holes were opened in a RIE tool.

(a)

Device mesa etching
↓
Surface treatment
↓
Collector Ohmic contact
↓
Emitter Ohmic contact
↓
SOG passivation and via-hole etching
↓
Metal 1

(b)
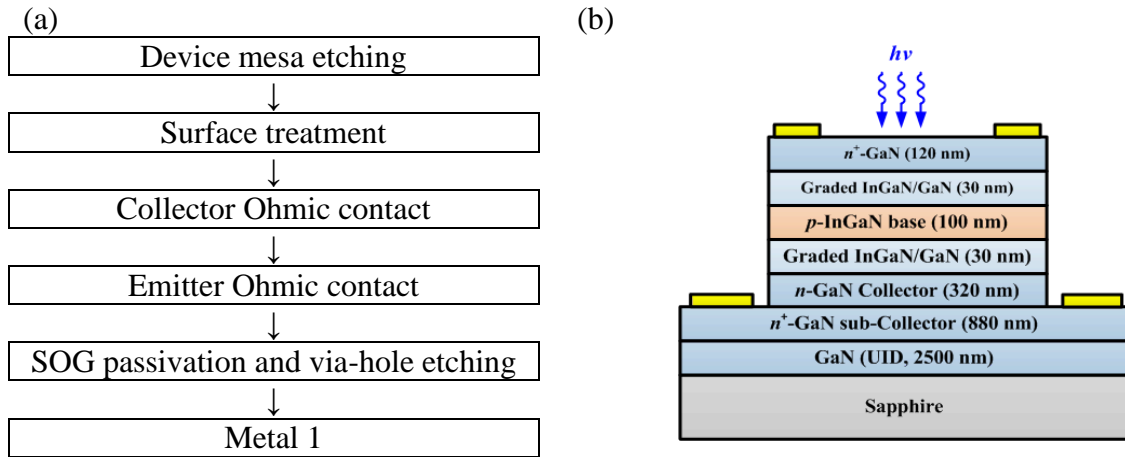
Figure 33. (a) The fabrication process flow and (b) the schematics of a GaN/InGaN HPT (wafer#: 2-3248-3) before passivation.

2.12.2 Characteristics of GaN/InGaN HPTs under dark condition

The devices were tested using a Keithley 4200 semiconductor characterization system. Figure 34 shows the *I-V* characteristics of a HPT device under the dark condition. The SEM image of the fabricated HPT before the SOG passivation is shown in the inset of Figure 34. The device has a circular mesa of 55 μm in diameter and the illumination area (*A*) is 1530 μm^2. The leakage current density is $< 10^{-7}$ A/cm^2 up to V_{CE}= 10 V. As V_{CE}> 10 V, the leakage current increases with V_{CE} due to the amplification by transistor gain. The BV_{CEO} is 41.7 V, corresponding to the breakdown electric field of 1.6 MV/cm in the BCJ.
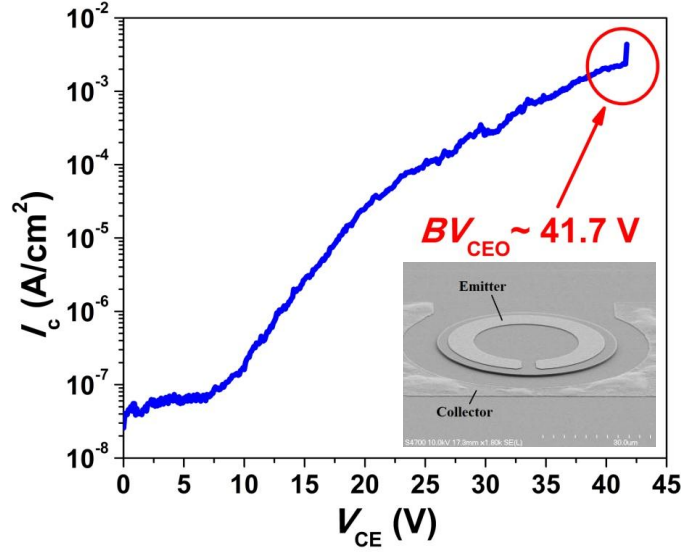
Figure 34. *I-V* **characteristics of a fabricated HPT device (wafer#: 2-3248-3B-B2D-D8) under the dark condition. The total illuminated area (*A*) is 1530 μm². The inset shows the SEM image of a fabricated HPT device before passivation.**

2.12.3 Characteristics of GaN/InGaN HPTs under UV illumination

Figure 35 (a) shows the photocurrent spectroscopy of the HPT illuminated from the backside and front-side of the wafer, respectively, at V_{CE} = 10 V. R_λ is determined as:

$$R_\lambda = I_{C(opt)} / P_{opt} A \tag{3.25}$$

where $I_{C(opt)}$ is the optical component of the collector current and P_{opt} is the total optical power density incident on the active transistor area. The surface reflection at air/GaN interface is ignored. For the backside illumination, the HPT possesses a bandpass spectral response with a peak R_λ of ~1 A/W at λ = 373 nm for P_{opt}= 7.84 μW/cm². This peak photon absorption energy is close to the bandgap energy of the $In_{0.03}Ga_{0.97}N$ in the base layer at room temperature. No significant photocurrent contribution from shorter wavelengths was observed as higher-energy photons with λ< 365 nm are absorbed by the underlying *n*-GaN layers before it reaches the HPT's active region. The photo-generated electron-hole pairs subsequently are recombined in the *n*-GaN layers and did not

contribute to the photocurrent. This explanation is supported by the transmission spectrum of n-GaN layer, as shown in the inset of Figure 35   (a), where the cut-off wavelength at $\lambda = 365$ nm is observed. On the other hand, for the same device illuminated from the front-side of the wafer under the same UV illumination condition, R_λ is greatly improved to 5 A/W at $V_{CE} = 10$ V and the DUV cut-off wavelength is well beyond $\lambda = 280$ nm. As the UV light is illuminated from the top of the mesa, photons with wavelength shorter than band-edge absorption of GaN are mostly absorbed through band-to-band transitions in the n-type emitter layer. Since the absorption coefficient of n-type GaN is $\sim 10^5$ cm^{-1} in the DUV spectral region [174], ~ 70 % of photons at $\lambda = 280$ nm could be absorbed in the emitter layer. Although the photon-generated carriers in the emitter layer contribute little to the overall photocurrent due to the relatively short diffusion length in GaN, the residual DUV photons could be absorbed in the base layer with effective photocurrent amplification. These photon-generated carriers also ensure the self-biasing of the transistor operation in the forward active mode. In the front-side illumination form, the UV-to-visible-band rejection ratio ($R_\lambda|_{\lambda=360nm}/R_\lambda|_{\lambda=450nm}$) is greater than 8×10^3.

Figure 35 (b) shows the measured photocurrent at the collector electrode ($I_{C(opt)}$) as a function of V_{CE} for the front-side illuminated device with various P_{opt} at $\lambda = 373$ nm and 280 nm, respectively. At low voltage operation ($V_{CE} < 10$ V), $I_{C(opt)}$ remains approximately constant for fixed P_{opt} and wavelength. Figure 35 (c) shows R_λ as a function of P_{opt} at $V_{CE} = 10$ V. For $\lambda = 373$ nm, R_λ is 4.2 A/W at $P_{opt} = 0.54$ μW/cm^2 and it increases with P_{opt} and reaches to > 8 A/W at 13.7 μW/cm^2. For photons with $\lambda = 280$ nm, R_λ is 3.1 A/W at $P_{opt} = 0.26$ μW/cm^2 and increases to 3.4 A/W at 1.31 μW/cm^2. This nonlinear R_λ dependency on the incident optical power is a favorable process for the

optoelectronic mixers, as discussed in [175]. R_λ stays nearly constant as the device is biased for V_{CE} between 1 and 10 V. Compared to typical III-N *p-i-n* and MSM PDs, the measured R_λ show a significant improvement by a factor of at least 5 in the near-UV and the deep-UV spectral regions [176, 177]. The HPT could be an alternative form of III-N PDs to achieve high-responsivity for low-light detection in the entire UV spectral region.

(a)

(b)

(c)
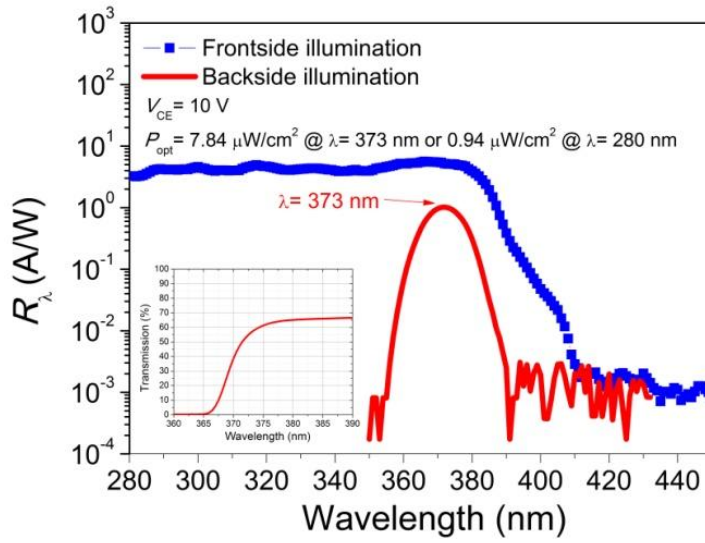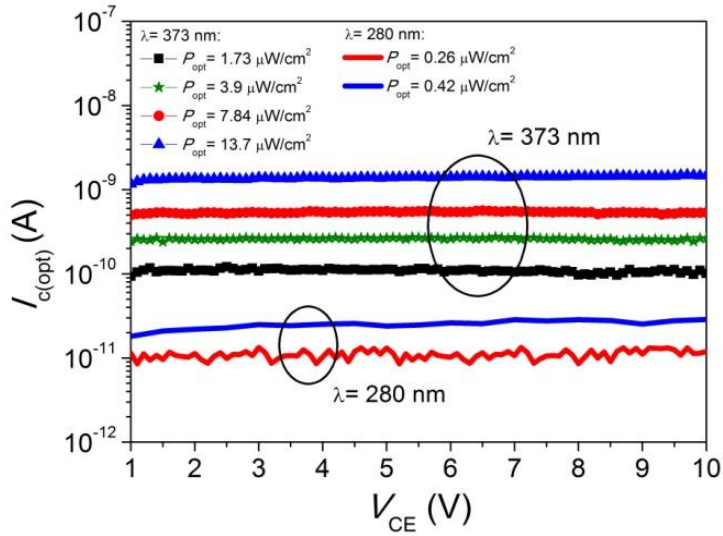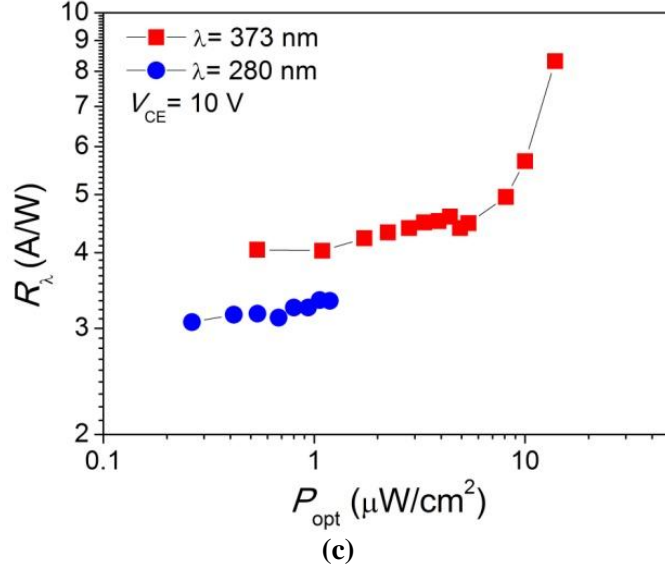
Figure 35. (a) The photoresponse spectroscopy of the HPT (wafer#: 2-3248-3B-B2D-D8) illuminated from either the substrate-side (red line) or frontside (blue line) of the wafer. The inset shows the transmission spectrum of *n*-GaN layer. (b) Low-voltage characteristics of the HPT under the front-side UV illumination at λ= 280 nm and 373 nm. (c) P_{opt}-dependent R_λ at V_{CE}= 10 V for the frontside-illuminated HPT at λ= 280 nm (blue circles) and 373 nm (red squares).

Figure 36 shows the voltage-dependence of the photocurrent response of the HPT at different P_{opt} inputs at λ= 373 nm. The photocurrent multiplication at the collector was observed for V_{CE} greater than 35 V. At P_{opt}= 1.73 μW/cm^2, R_λ stays ~ 5 A/W up to V_{CE}= 35 V; increases rapidly for V_{CE} > 35 V and reaches > 100 A/W at V_{CE} = 40 V. For P_{opt} = 13.7 μW/cm^2, R_λ is < 10 A/W up to V_{CE} = 35 V and reaches to 30 A/W at V_{CE} = 40 V. The enhancement of R_λ is due to the carrier multiplication in the reverse-biased BCJ as the device is biased near the breakdown voltage. Note also that the apparent breakdown moves to lower voltages as the incident optical power level increases. Considering the current continuity, $I_{C(opt)}$ can be expressed as [171]:

$$I_{C(opt)} = \frac{(h_{FE}+1)M}{1-(M-1)h_{FE}} I_{ph} = h'_{FE}I_{ph} \qquad (3.26)$$

83

, where h_{FE} is the photocurrent gain and I_{ph} is the photocurrent. M is the multiplication factor. Thus, the effective gain, h'_{FE}, is a function of the bias voltage through M and the incident optical power level through h_{FE}. h_{FE} is proportional to R_λ and is an increasing function of P_{opt}. For a higher h_{FE} value under higher P_{opt} illumination, a smaller M would be required to initiate the current multiplication process, leading to enhanced carrier multiplication at lower V_{CE} in the phototransistor, similar to that observed in narrow-bandgap infrared III-V APTs [172, 178]. At a specific V_{CE} near the breakdown voltage, furthermore, an increase in the collector current due to the carrier multiplication leads to an increase in h_{FE} which, if sufficient, can result in $(M-1)h_{FE} > 1$. Due to the singularity of $(M-1)h_{FE} = 1$, R_λ decreases for higher P_{opt} illumination. The behavior of the power-dependent breakdown voltage of our device is similar to that reported for the HPTs and can be attributed to the fact that the photocurrent gain increases with the photocurrent.
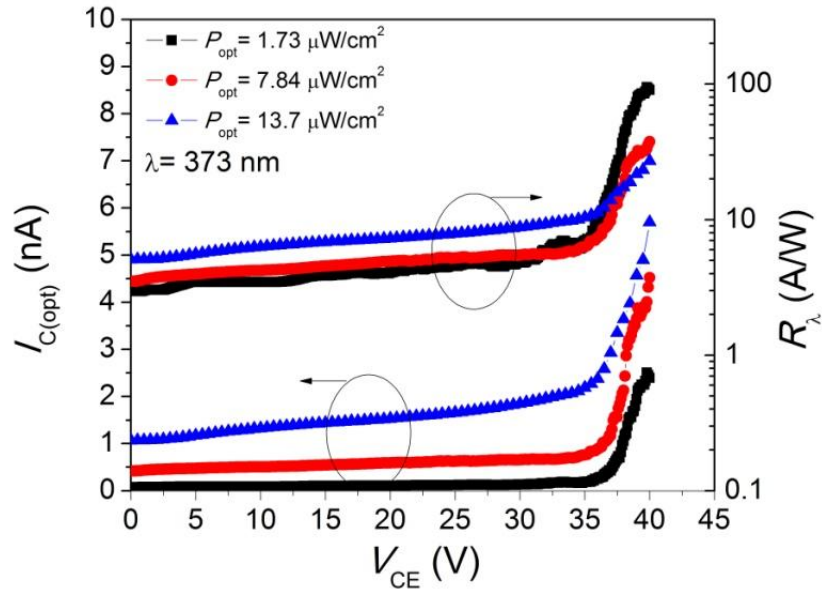
Figure 36. The V_{CE}-dependent photocurrent response and R_λ for a HPT (wafer#: 2-3248-3B-B2D-D8) under the front-side UV illumination. Significant photocurrent amplification was observed for V_{CE} stressed at the near-avalanche-breakdown biases. Higher photo flux results in lower avalanche voltage in the APT operation.

2.12.4 Conclusions

We report a high-responsivity GaN/InGaN HPT that can operate in both open-base phototransistor mode and the avalanche phototransistor mode for NUV-to-DUV photodetection applications. The substrate-side illuminated HPT shows a peak R_λ of 1 A/W at λ= 373 nm, the bandgap wavelength of the $In_{0.03}Ga_{0.97}N$ base layer, and the relatively narrow spectral response due to the absorption of high-energy UV photon from the underlying GaN materials. Under the front-side illumination, the HPT shows a wide-band photoresponse spectrum with the short-wavelength cut-off wavelength well beyond λ= 280 nm. The HPT exhibits a high UV-to-visible-band rejection ratio ($R_\lambda|_{360nm}/R_\lambda|_{450nm}$) greater than 8×10^3. At low voltage bias (V_{CE}< 10 V), R_λ is 8.2 A/W for P_{opt}= 13.7 μW/cm^2 at λ= 373 nm and R_λ is 3.4 A/W for P_{opt}= 1.31 μW/cm^2 at λ= 280 nm. As the HPT is biased at the near-avalanche-breakdown voltage (V_{CE}> 35 V), the responsivity performance was enhanced due to the carrier multiplication, resulting in R_λ >100 A/W at V_{CE}= 40 V for P_{opt}= 1.73 μW/cm^2 at λ= 373 nm. The results demonstrate the feasibility of using III-nitride HPTs as a new form of ultra-low light detection in the entire UV spectral regions.

2.13 Summary

We first conduct an analysis of *npn* GaN/InGaN HBTs to understand possible radiative recombination paths and their impacts on the device performance [179]. Through the EL study for devices operating at the diode modes and the forward-active modes, we are able to resolve the origins of three distinct radiative recombination paths and their possible origin of radiative recombination in physical devices. The I_B-dependent EL intensities for these three recombination paths are discussed. The results also show

the radiative emission under the forward-active transistor mode operation is more effective than that using a diode-based emitter due to the enhanced excess electron concentration in the base region as increasing the collector current increases.

By illuminating UV photons from the backside of an open-bas HBT device, we further observed the photocurrent amplification and multiplication from an open-base GaN/InGaN HBT and demonstrated the first III-N APT operation [180]. A responsivity of ~1 A/W was achieved for V_{CE}< 15 V and it was further increased to R_λ > 300 A/W as the device was operated near the avalanche breakdown voltage. The results suggest that the light absorbed in the base of HBT device can induce the photocurrent amplification and further multiplication.

After the light-emitting and photoresponse properties of GaN/InGaN HBTs were characterized, GaN/InGaB HPTs with single mesa structure were fabricated. We demonstrated a high-responsivity GaN/InGaN HPT that can operate in both open-base phototransistor mode and the avalanche phototransistor mode for NUV-to-DUV photodetection applications [181]. The substrate-side illuminated HPT shows a peak R_λ of 1 A/W at λ= 373 nm, the bandgap wavelength of the In$_{0.03}$Ga$_{0.97}$N base layer, and the relatively narrow spectral response due to the absorption of high-energy UV photon from the underlying GaN materials. Under the front-side illumination, the HPT shows a wide-band photoresponse spectrum with the short-wavelength cut-off wavelength well beyond λ= 280 nm. The HPT exhibits a high UV-to-visible-band rejection ratio ($R_\lambda|_{360nm}/R_\lambda|_{450nm}$) greater than 8×10^3. At low voltage bias (V_{CE}< 10 V), R_λ is 8.2 A/W for P_{opt}= 13.7 µW/cm^2 at λ= 373 nm and R_λ is 3.4 A/W for P_{opt}= 1.31 µW/cm^2 at λ= 280 nm. At high V_{CE} (> 35 V), the responsivity performance was enhanced as the device was biased in the

APT mode, resulting in $R_\lambda >100$ A/W at $V_{CE}= 40$ V for $P_{opt}= 1.73$ µW/cm^2 at $\lambda= 373$ nm. The results demonstrate the feasibility of using III-nitride HPTs as a new form of ultra-low light detection in the entire UV spectral regions.

CHAPTER 4

DEVELOPMENT OF ULTRAVIOLET LIGHT EMITTERS

3.1 Introduction

III-N-based optoelectronic devices have been actively studied and developed for over two decades. The wide range of the bandgap energy in III-N materials (from 0.7 eV to 6.2 eV) covers the full spectrum of photon emission from the near-infrared to DUV wavelengths. Today, III-N-based solid state lighting is the viable technology for future energy-efficient light sources. High-quality nitride-based LEDs and LDs have also been commercialized for water sanitation and bio-chemical agent detection applications. These UV and DUV emitters typically use AlGaN alloy system to achieve wavelengths below 300 nm [182-186]. In general, two kinds of LD structures were reported:

3.1.1 Edge emitting lasers

The major type of nitride-based laser diodes now is edge emitting laser (EEL). This kind of structure is currently the most mature and producible one among all nitride laser devices. It is featured by a stripe-type long cavity and a pair of cleaved facet as the mirrors. Typically, the cavity length of the structure is about several hundred micrometers. The light in the cavity is resonant in the horizontal direction and emits from the cleaved mirrors. The standard epi-layer structure of EELs usually is grown on sapphire and composes of p-n junction, multiple quantum wells (active region), and some cladding layer for photons and electrons. Over this decade, several improvements and researches on the growth and optimization of its structure were reported [187-190]. One is to

improve the great amounts of defects and threading dislocations existing in the grown nitride materials on sapphire substrate due to the large lattice-mismatch between the nitride material and sapphire. The epitaxally lateral overgrowth (ELOG) is a very efficient method to reduce threading dislocation and defect density [187, 188]. It is a method using the patterned SiO_x to make GaN laterally coalesce and bend threading dislocations to reduce the dislocation density. Generally, ELOG could decrease dislocation density down to the order of 10^8 cm^{-2}. Other one is to raise the low confinement factor of the optical field in the structure. Because the index difference between $Al_xGa_{1-x}N$ and GaN is small, the guiding of optical field in active region is usually weak. Nakamura *et. al* provided a solution that using modulation doped strain superlattice layer to improve the optical confinement [187, 188]. The other is to reduce spontaneous polarization and piezoelectric field in multiple quantum wells. Recently, M. Schmidt *et. al* [189] and D. Feezell *et. al* [190] demonstrated non-polar laser diode on m-plane GaN substrate. The laser diode emits violet light ~ 410 nm and has the threshold current density of 3.7-8.2 kA/cm^2. The spontaneous and piezoelectric polarization effect was eliminated and the performance of laser diode could be further improved using this lattice matched substrate. The fabrication of flat and high-reflectivity mirrors is also a key point for achieving an excellent lasing performance. In order to obtain a flat facet, the etching and cutting techniques were rapidly developed.

Although various AlGaN-based MQWs lasers operating in the UV and DUV spectral range were reported via optical pumping, the development of electrically-injected DUV LDs for λ< 280 nm has been challenging because of the difficulty in achieving high free-carrier concentrations in both *p*-type and *n*-type AlGaN layers with

high aluminum mole fraction. Also, the lattice mismatch in epitaxial layers when these structures are grown on foreign substrates results in high defect density. To date, electrically carrier-injection LDs have not been reported for the lasing wavelength shorter than 336 nm [191].

3.1.2 Vertical-cavity surface emitting lasers

Although the optimization of the edge emitting laser keeps going, some properties of this kind of laser are unfavorable. One of those properties is its elliptic beam shape. On one hand, the coupling efficiency would be low as the elliptic beam is coupled into optical fiber (typically in the form of circular core). On the other hand, for the application of storage, the elliptic beam not only makes each writing pixel larger but also raises expenses for correcting light shape. Usually, this kind of laser shows slightly large divergence angle to be over ten degree. This also is disadvantageous to the projection. Furthermore, the side emitting laser devices also makes the testing of devices a tough task. The wafer should be cut into several stripes (several laser devices on one strip) before the testing. For a commercial product, the complicated testing would result in a poor producing efficiency and be disadvantageous. Therefore, in order to have a superior laser device, K. Iga demonstrated a new kind of laser diodes, vertical cavity surface emitting laser, in 1977 [192]. VCSEL is a vertical-emitting-type laser. It is formed by sandwiching a few-lambda cavity in a pair of reflectors, usually in the form of DBR, with a very high reflectivity (> 99.9 %). In contrast to EELs, photons in the cavity of VCSEL are vertically in resonance and emit outside perpendicularly to the surface of the structure. This laser diode can have many advantageous properties than conventional edge emitting laser, such as circular beam shape, lower divergence angle, two-dimensional laser array

90

possible, efficient testing, low threshold, and so on. Owing to these superior performances, VCSELs had become very attractive and started to be applied to the commercial products at long wavelength range. In fact, short-wavelength VCSELs are also very promising for the applications of storage, display, and projection. In particular, the use of two-dimensional arrays of blue VCSELs could further reduce the read-out time in high density optical storage and increase the scan speed in high-resolution laser printing technology [193]. In recent years, several efforts have been devoted to the realization of optically-pumped GaN-based VCSELs operating in the violet-green spectral range [194-203]. Currently, three kinds of structures were reported:

Fully epitaxial grown VCSEL structure

In 2005, J. F. Carlin *et. al.* [202] and E. Feltin *et. al.* [203] demonstrated the wholly epitaxial and high quality nitride-based resonant-cavity (as shown in Figure 37 (a)) using metalorganic vapor phase epitaxy (MOVPE or MOCVD). They used the lattice-matched AlInN/GaN as the bottom and top reflectors to avoid cracks happened due to the accumulation of the strain after stacking large pairs of layers. The reflectivity of AlInN/GaN could be achieved as high as 99.4 %. They showed the 3/2-lambda cavity emitted a very narrow emission with a linewidth of 0.52 nm, corresponding to a quality factor of ~800.

VCSEL structure with two dielectric mirrors

Compared to epitaxial grown reflectors, the fabrication of dielectric mirrors is relatively simple. Furthermore, the large index difference of dielectric mirrors makes them could easily have wide stop band (> 50 nm) and high reflectivity (> 99 %) by

coating just few stacks of 1/4-lambda-thick layers. Therefore, using dielectric mirrors to accomplish nitride-based VCSELs had begun attractive (as shown in Figure 37 (b)). Song *et al.* [195], Tawara *et al.* [196] and J. T. Chu *et. al.* [198] successively reported the structure after 2000. They employed some process techniques such as wafer bonding, laser lift-off, high-quality polishing, and cavity control to make dielectric mirrors be coated onto both sides of nitride-based cavity. They showed a resonant cavity could have a very high quality factor to be greater than 400 and achieve lasing action using optical pumping. In recent years, the CW lasing action of electrically injected GaN-based VCSELs employing two dielectric DBRs were reported in the blue-violet spectral range [204-211].

<u>VCSEL structure with hybrid mirrors</u>

The so-called hybrid mirrors (as shown in Figure 37 (c)) are a combination of two different kinds of reflectors, for example, a dielectric mirror and an epitaxial reflector. Typically, the fabrication of this structure is to grow bottom reflector and cavity using MOCVD and then coat dielectric mirror to complete VCSEL structure. The hybrid-cavity nitride-based VCSEL formed by the dielectric mirror and the epitaxially grown high-reflectivity GaN/Al_xGa_{1-x}N DBR was reported earlier. In 1999, Someya *et al.* [194] used 43 pairs of $Al_{0.34}Ga_{0.66}$N/GaN as the bottom DBR and reported the lasing action at ~ 400 nm. Then, Zhou *et. al.* [197] also employed a bottom DBR of 60 pairs $Al_{0.25}Ga_{0.75}$N/GaN and observed the lasing action at 383.2 nm. Both these AlGaN/GaN DBR structures required large numbers of pairs due to the relatively low refractive index contrast between Al_xGa_{1-x}N and GaN. Therefore, recently some groups began to study the AlN/GaN for application in nitride VCSEL. The DBR structure using AlN/GaN has

higher refractive index contrast ($\Delta n/n=0.16$) [212] that can achieve high reflectivity with relatively less numbers of pairs. It has wide stop band that can easily align with the active layer emission peak to achieve lasing action. However, the AlN/GaN combination also has relatively large lattice mismatch ($\sim2.4\%$) and the difference in thermal expansion coefficients between GaN (5.59×10^{-6}/K) and AlN (4.2×10^{-6}/K) that tends to cause cracks in the epitaxial film during the growth of the AlN/GaN DBR structure and could result in the reduction of reflectivity and increase in scattering loss. With the mature of epitaxy techniques, the high-reflectivity AlN/GaN DBR structure with relatively smooth surface morphology has become possible with just twenty or thirty pairs [213]. In comparison of these three VCSELs, it doesn't require complicated process such as laser lift-off technique to complete a hybrid VCSEL device. This means the fabrication of such structure is stable and reliable comparing to other structures. Thus, the hybrid structure is more advantageous in the aspects of fabrication and commercialization. In recent years, Lu *et. al* announced the first electrically injected GaN-based blue VCSELs operating at 77 K with relatively thick ITO layer of 240 nm [214]. The laser structure employs AlN/GaN and Ta_2O_5/SiO_2 hybrid mirrors and the laser emitted a blue wavelength at $\lambda=$ 462 nm with a threshold current at 1.4 mA. By further reducing the high-absorption ITO layer to 30-nm-thickness, room temperature continuous wave (CW) lasing was obtained [215]. This improvement indicated that reducing internal cavity losses is crucial to achieve room temperature lasing. Recently, based on free-standing GaN substrate, In 2012, Cosendey *et. al* reported GaN-based VCSELs lasing employing InAlN/GaN and TiO_2/SiO_2 hybrid mirrors under pulsed electrical injection [216]. In these approaches, large self-heating and/or poor heat dissipation system prevented the devices from CW

93

lasing. Therefore, optical resonators with low internal cavity loss and excellent thermal management system are both significant to decrease the threshold that paving the way for VCSELs to achieve room temperature CW lasing.
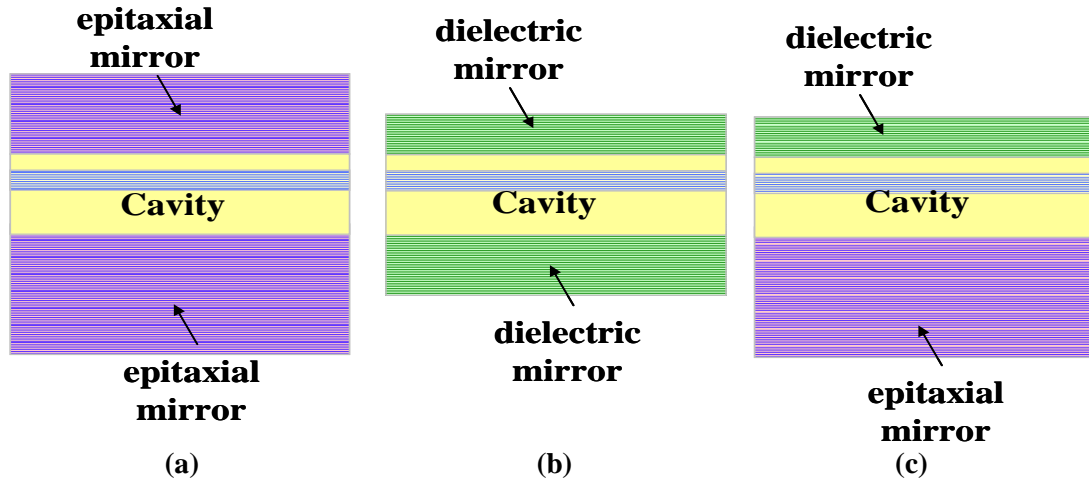
Figure 37. Schematic diagrams of three nitride-based VCSEL structures: (a) Fully epitaxial grown VCSEL structure (b) VCSEL structure with two dielectric mirrors (c) VCSEL structure with hybrid mirrors.

Although current-injection III-N-based VCSELs were reported with either a hybrid mirror structure or double-sided dielectric DBR structure, laser operation in sub-400 nm regime has rarely been reported. Even under the optical pumping excitation scheme, there are only few more VCSELs with operating peak wavelengths in sub-400 nm region [217, 218]. Besides the general challenges in the development of UV LDs, another limiting factor for realizing ultraviolet III-N VCSELs is having limited choices for optically transparent materials with large refractive index contrast for DBR formation. To date, electrically-pumped UV VCSELs have not been demonstrated for the lasing wavelength shorter than 400 nm.

In this chaper, both edge-emitting lasers and VCSEL device fundamentals will be addressed in Section 4.2. In Section 4.3, we will desbribe the processing development

including the Vanadium-based ohmic contact on n-type AlGaN, lapping/polishing of AlN substrates, HfO_2/SiO_2 dielectric mirrors, and indium tin oxide transparent contact. These developed processing schemes lead to successful demonstration of UV light emitters, including DUV LEDs, optically-pumped DUV lasers, and UV RCLEDs, which will be addressed in details in Section 4.4.

3.2 Device fundamentals

The first semiconductor lasers were fabricated in 1962 using homojunction [219, 220, 221]. In late 1970s, the concept of QW structures for semiconductor lasers was proposed and realized experimentally to improve the laser performance signifincanly [222]. Considering a double heterojunction laser diode with the injection current density of J, the electron concentration (n) in the active region can be given by: $n = J\tau_e / qd_a$, where τ_e is the carrier lifetime and d_a is the thickness of active region. Then the quasi-Fermi level in the active region for electrons (E_{Fn}) is determined by [223]:

$$n = N_C F_{1/2}(\frac{E_{Fn} - E_C}{k_B T}), \text{ where } N_C = 2(\frac{m_e^* k_B T}{2\pi\hbar^2})^{3/2} \tag{4.1}$$

Similarly, the quasi-Fermi level in the active region for holes (E_{Fv}) is given by:

$$p = N_V F_{1/2}(\frac{E_V - E_{Fv}}{k_B T}), \text{ where } N_V = 2(\frac{k_B T}{2\pi\hbar^2})^{3/2}(m_{hh}^{3/2} + m_{lh}^{3/2}) \tag{4.2}$$

The occupation probabilities can be described using Fermi statistics under non-equilibrium conditions for the conduction and valance bands:

$$f_1 = (e^{(E_1 - E_{Fv})/kT} + 1)^{-1}, \text{ for valance band} \tag{4.3}$$

$$f_2 = (e^{(E_2 - E_{Fc})/kT} + 1)^{-1}, \text{ for conduction band} \tag{4.4}$$

As long as the electron and hole concentrations or the quasi-Fermi levels are known, the gain can be directly calculated. The gain occurs when $f_2 > f_1$, that is, the population inversion is achieved. Typically, the peak gain coefficient versus the carrier density can be described as linear relation given by: $g(n) = a(n - n_{tr})$, where a is the differential gain and ntr is the transparency concentration when the gain is zero. For quantum-well lasers, an empirical formula using a logarithmic dependence for the gain versus carrier density is usally used [223].

In order to reach lasing threshold, the gain in the active section must be increased to the point when all the propagation and mirror losses are compensated. Most laser cavities can be divided into two general sections: an active section of length (d_a) and a passive section of length (d_p). For a laser, at the threshold, the gain is equal whole loss in the cavity, which includes cavity absorption and mirror loss. For convenience the mirror loss term can be expressed as: $\alpha_m \equiv (1/2L)\ln(1/R_1R_2)$. Noting that the cavity life time (photon decay rate) is given by the optical loss in the cavity, $1/\tau_p = 1/\tau_i + 1/\tau_m = v_g(\alpha_i + \alpha_m)$. Thus, the threshold gain in the steady state can be expressed with following equation:

$$\Gamma g_{th} = \alpha_i + \alpha_m = \frac{1}{v_g \tau_p} = \alpha_i + \frac{1}{2L} \ln\left(\frac{1}{R_1 R_2}\right) \tag{4.5}$$

, where Γ is the optical confinement factor. α_i is the average internal loss which is defined by $(\alpha_{ia}d_a + \alpha_{ip}d_p)/L$ (i.e., $\alpha_{ia}d_a$ and $\alpha_{ip}d_p$ are loss of active region and passive section, respectively), and R_1 and R_2 is the reflectivity of top and bottom mirror of the laser cavity, respectively.

When the laser reaches the threshold condition, the carrier concentration (n) will be pinned at the threshold value since the gain is pinned at the threshold gain:

$g_{th} = \dfrac{1}{\Gamma}(\alpha_i + \alpha_m)$. Therefore, $n_{th} = n_{tr} + (\alpha_i + \alpha_m)/\Gamma a$.

The characteristic of output power versus driving current (*L-I* characteristic) in a laser diode can be further derived as the following equation:

$$P_O = \eta_i \left(\frac{\alpha_m}{\alpha_i + \alpha_m} \right) \frac{h\nu}{q} (I - I_{th}) \tag{4.6}$$

, where η_i is the internal quantum efficiency. By defining $\eta_d = \eta_i \left(\dfrac{\alpha_m}{\alpha_i + \alpha_m} \right)$, the Eq.

(4.4) can be simplified as:

$$P_O = \eta_d \frac{h\nu}{q} (I - I_{th}) \qquad (I > I_{th}) \tag{4.7}$$

Thus, the η_d can be expressed as

$$\eta_d = \left[\frac{q}{h\nu} \right] \frac{dP_O}{dI} \qquad (I > I_{th}) \tag{4.8}$$

In fact, η_d is the *differential quantum efficiency*, defined as number of photons out per electron. Besides, dP_o/dI is defined as the *slope efficiency*, S_d, equal to the ratio of output power and injection current. Figure 38 shows the illustration of output power vs. current for a diode laser. Below threshold only spontaneous emission is important; above threshold the stimulated emission power increase linearly with the injection current, while the spontaneous emission is clamped at its threshold value.

$$g_{th} = \alpha_i + \frac{1}{2L}\ln\left(\frac{1}{R_1 R_2}\right)$$

$$\eta_d = \frac{\Delta P_o / h\nu}{\Delta I / q}$$

$$S_d = \frac{\Delta P_o}{\Delta I}$$
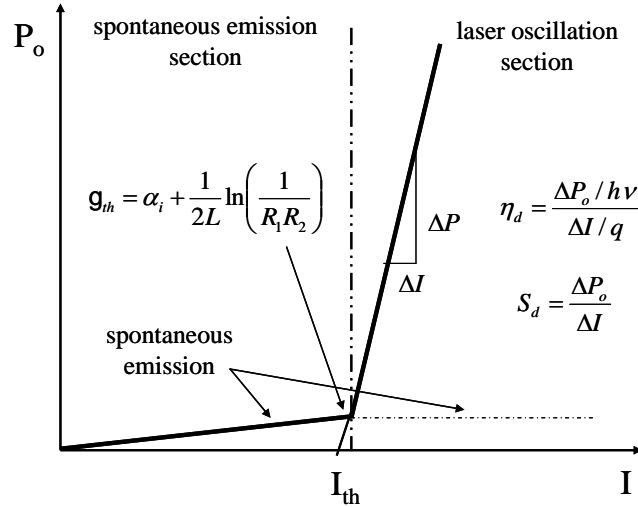
Figure 38. An illustration of output power vs. current for a diode laser.

3.3 Development of fabrication processes for UV light emitters

<u>**Edge-emitting lasers (EELs)**</u>

For the edge-emitting semiconductor LDs, there are two basic schemes for the lateral optical confinement and carrier confinement: the gain-guided structure and the ridge structure [223]. The gain-guided structure is easy in fabrication because of no mesa etching. The lateral carrier confinement is provided by the narrow metal strips. But the confinement is weak due to the carrier spreading. The optical confinement induced by the carrier injection is even weaker. Therefore, the device performance is limited with the gain-guided structure, which is rarely reported recently except for several groups [224-226]. On the other hand, the ridge structure provides better lateral optical confinement and carrier confinement, but the cost is the fabrication complexity. Narrow metal strips and via holes are difficult to be placed or opened on top of the narrow ridges (usually 1.4 μm ~ 10 μm wide). Furthermore, dry etchings for the via-hole opening bring plasma damages to the *p*-type III-N materials and the ohmic contact metal stack, resulting in contact resistance degradation.

Shown in Figure 39 (a) is the process flow of edge-emitting LDs operating in the DUV spectral range. The device fabrication starts with low-damage ridge waveguide and mesa etching using an ICP etching tool. A photo-enhanced surface treatment is conducted to remove post-dry-etching-induced surface damage. Low-resistivity n-type and p-type ohmic contact are deposited on n-type AlGaN (Al> 50 %) and p-type GaN contact layer, respectively. After the ohmic contact annealing, an additional metal layers (Ti/Au) will be deposited to help the current spreading for the metal contact regions. The devices are then passivated by SiO_2, followed by the via-hole opening. A Metal-1 interconnect layer will be deposited to conclude the front-side fabrication processing. The back-side processing starts with the substrate lapping and polishing, LD bar cleaving, and facet coating. Figure 39 (b) shows the schematics of the DUV edge-emitting LDs before passivation.
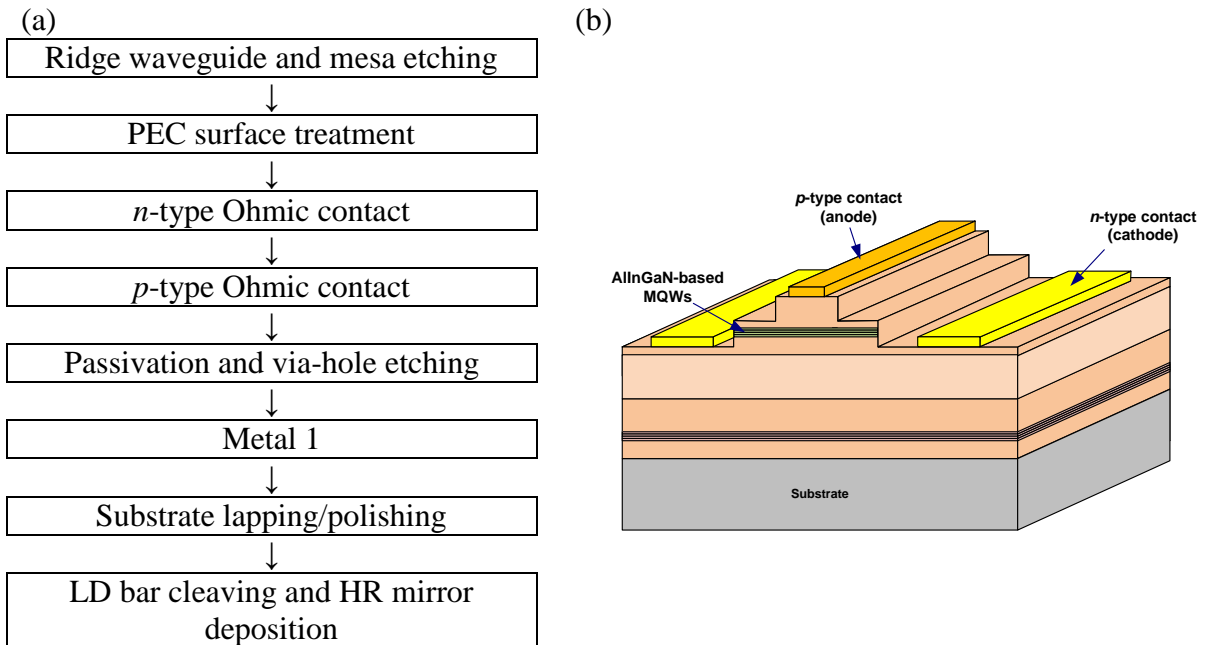
Figure 39. (a) The fabrication process flow and (b) the schematics of the DUV edge-emitting LDs before passivation.

<u>**Vertical-cavity surface emitting lasers (VCSELs)**</u>

On the other hand, shown in Figure 40 (a) is the processing flow of UV VCSELs employing hybrid mirror structures. The VCSEL fabrication begins with the low-damage mesa etching using ICP tool to expose the *n*-AlGaN layer. The current aperture is then defined using either dielectric layers or ion implantation approach. The current aperture areas range from 2 to 22 μm. A 45 nm-thick ITO was deposited using an e-beam evaporator for the *p*-type ohmic contact and was annealed at 500 ^{o}C for ten minutes under oxygen ambient. The UV DBR was then evaporated as the top mirror with high reflectivity > 99 % at the wavelength of interest. Finally, the Metal 1 using Ti/Au metal stacks was deposited to complete the VCSEL fabrication. Figure 40 (b) shows the schematics of UV VCSELs with semiconductor bottom DBRs and dielectric top DBRs.

(a)   (b)
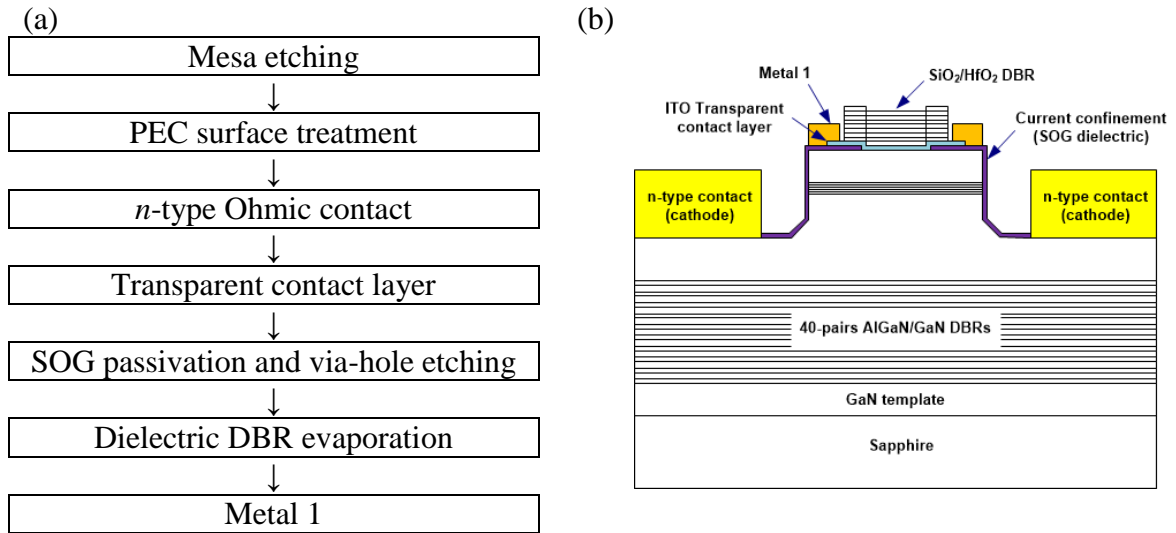
Figure 40. (a) The fabrication process flow and (b) the schematics of the UV VCSELs employing hybrid mirror structures.

At Georgia Tech, we focus on the following critical paths for the demonstration of optically-pumped and electrically-pumped DUV LDs: (1) low-resistivity *n*-type V-based ohmic contact on Al-rich *n*-AlGaN. (2) Lapping/polishing of AlN substrate and LD bar

cleaving. (3) Facet coating using high-reflectivity HfO_2/SiO_2 dielectric mirrors. The LD fabrication technology developed at Georgia Tech provides a solid base for further development of the near-UV HM-VCSELs. Basic processing steps such as n-type ohmic contact schemes, ICP, and wet-chemical-based mesa etching processes, and HfO_2/SiO_2 dielectric mirrors were integrated for the VCSEL fabrication. In addition, we also developed the transparent p-type contact and GaN substrate thinning/polishing for robust VCSEL fabrication scheme. These technology paths are discussed below.

3.3.1 Vanadium-based ohmic contact on n-AlGaN layers

Since the first demonstration of high efficiency blue LEDs, the development of UV and DUV LEDs had led to rapid commercialization of these devices in various applications. With the growing interest in nitride semiconductor emitters and detectors operating at DUV wavelengths, suitable ohmic contact for Al-rich n-AlGaN materials would be highly desired. In general, AlGaN has a work function of less than 4.0 eV. There would be a need to find appropriate methods to form an ohmic contact with intermediate transition layers. The issue of forming low-resistivity ohmic contact Al-rich AlGaN layers was also challenging with the increase of the dopant's activation energy as the aluminium composition increases.

The commonly reported ohmic contact systems for n-AlGaN are Titanium (Ti)-based metallization schemes since TiN has a work function of 3.74 eV and it could be formed at the interface after the annealing process. Miller et $al.$ reported the ohmic contact on n-$Al_xGa_{1-x}N$ ($x = 0.58$) can be achieved after the sample was annealed at 900-1000 ^{o}C under the nitrogen ambient, yielding a specific contact resistance (ρ_c) of 4.0×10^{-4}-1.7×10^{-3} Ω-cm^2 [227]. However, the high-temperature annealing process is

101

typically undesired as the ohmic contact morphology would become rough after high-temperature annealing process. There are also concerns of the device process integration compatibility as well as potential device reliability in lieu of the high-temperature process. Vanadium (V)-based ohmic contact could be a suitable choice for Al-rich n-AlGaN because thermally stable nitride complex can be created at the metal-III-N interface using low temperature annealing processes [228-231].

At Georgia Tech, we performed a study of the V-based ohmic contact properties on AlGaN films for various Al compositions. We studied the evolution of the contact resistance as a function of the annealing temperature and the material bonding characteristics at the V-AlGaN interface using a XPS measurement. When compared to the Ti-based contact, V-based ohmic contact consistently shows lower ρ_c and smoother surface morphology at lower annealing temperature for n-type $Al_xGa_{1-x}N$ films (x up to 0.55.) A study of the N:1s core-level peak at V-$Al_{0.55}Ga_{0.45}N$ interface shows that the formation of nitrogen-vanadium (N-V) bond helps shift the peak binding energy by 0.7 eV at the V-AlGaN interface when compared to annealed Ti-AlGaN interface. The increase in the binding energy facilitates the current conduction by providing more effective electron states for carrier transport at the metal-semiconductor interface. The results indicated that the use of V-based ohmic contact is a suitable choice of achieving low contact resistance for n-AlGaN layers.

The n-type $Al_xGa_{1-x}N$ films ($x = 0.06, 0.49, 0.55, 0.6$, and 0.73) were grown on c-plane sapphire substrates by a Thomas Swan MOCVD system. In this study, the $Al_{0.06}Ga_{0.94}N$ film was grown on a 2.5 µm-thick GaN buffer layer and its thickness is 250 nm. Other Al-rich $Al_xGa_{1-x}N$ films ($x = 0.49, 0.55, 0.6$, and 0.73) were 200 nm thick and

they were grown on a 1 μm-thick AlN buffer layer. V/Al/Ti/Au and Ti/Al/Ti/Au stacks were deposited on each of the AlGaN samples for contact study.

Shown in Figure 41 (a) is the comparison of transmission line method (TLM) results for V-based and Ti-based ohmic contact on $Al_{0.55}Ga_{0.45}N$ films. The V-based ohmic contact was annealed at 775 ^{o}C for 1 minute in N_2 and Ti-based ohmic contact was annealed at 825 ^{o}C for 1 minute in N_2. By linear extrapolation, V-based ohmic contact shows ρ_c and sheet resistance (R_{sh}) of 2×10^{-5} Ω-cm^2 and 700 $\Omega/\square$, respectively. The Ti-based ohmic contact shows one order of magnitude higher ρ_c (3×10^{-4} Ω-cm^2) with the same R_{sh}. Figure 41 (b) shows ρ_c as a function of the annealing temperature on $Al_{0.55}Ga_{0.45}N$ film. V/Al/Ti/Au metal stacks have lower ρ_c at a lower annealing temperature when compared to the Ti/Al/Ti/Au-based contact.
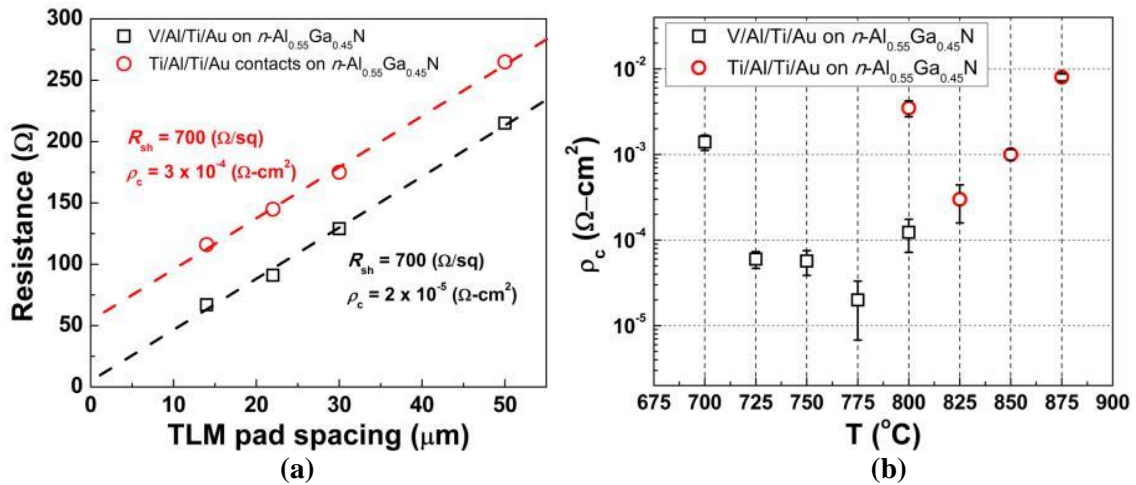
Figure 41. (a) TLM results of V/Al/Ti/A and Ti/Al/Ti/A ohmic contact on $Al_{0.55}Ga_{0.45}N$ film. The V-based ohmic contact was annealed at 775 ^{o}C for 1 minute in N_2. The Ti-based ohmic contact was annealed at 825 ^{o}C for 1 minute in N_2. (b) ρ_c as a function of annealing temperature for V/Al/Ti/Au and Ti/Al/Ti/Au ohmic contact on $Al_{0.55}Ga_{0.45}N$ film.

Shown in Figure 42 (a) and (b) are microscope and AFM images of the annealed V/Al/Ti/Au and Ti/Al/Ti/Au metal stacks on $Al_{0.55}Ga_{0.45}N$ film, respectively. The metallization using V/Al/Ti/Au ohmic contact is relatively shiny and smooth while

several bumps are visible on the surface of Ti/Al/Ti/Au contact. The root-mean-square (RMS) roughness of the annealed V/Al/Ti/Au and Ti/Al/Ti/Au metal stacks are 38.3 nm and 91.7 nm across a $20\times20\ \mu m^2$ area, respectively. The smoother surface of the V-based metal stacks could be attributed to the lower annealing temperature for achieving an optimum ρ_c. Figure 43 shows ρ_c as a function of the annealing temperature on $Al_{0.06}Ga_{0.88}N$ film. V/Al/Ti/Au ohmic contact provides a lower ρ_c at each annealing temperature compared to Ti/Al/Ti/Au ohmic contact. The optimum value of $\rho_c= 6.6\times10^{-6}\ \Omega$-$cm^2$ is found at 725 ^{o}C.

(a)

(b)
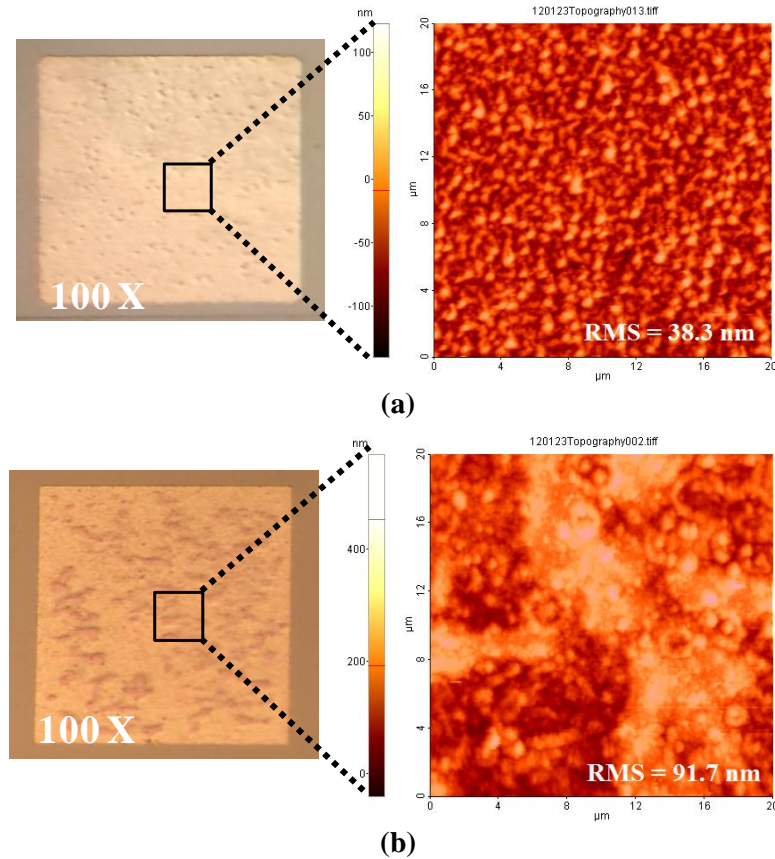
Figure 42. The microscopic and AFM images for the annealed (a) V/Al/Ti/Au and (b) Ti/Al/Ti/Au metal stacks.
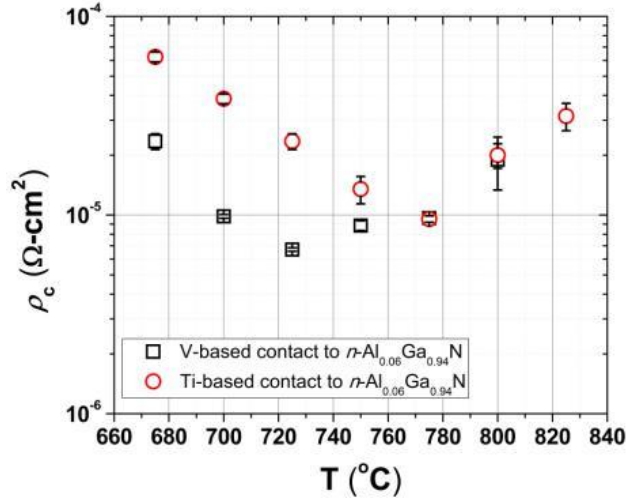
Figure 43. ρ_c **of V/Al/Ti/Au and Ti/Al/Ti/Au ohmic contact as a function of annealing temperature on Al$_{0.06}$Ga$_{0.94}$N film.**

The optimum annealing temperature for V-based ohmic contact was investigated on AlGaN films with different Al compositions. As shown in Figure 44, ρ_c is 6.6×10^{-6} Ω-cm^2 for Al$_{0.06}$Ga$_{0.94}$N film. As Al composition increases from 6 % to 73 %, ρ_c increases from 6.6×10^{-6} Ω-cm^2 to 4.4×10^{-3} Ω-cm^2 and the bulk resistivity (ρ_s) increases from 5×10^{-3} Ω-cm to 5.6 Ω-cm. The increase in ρ_c and ρ_s can be attributed to the low free carrier concentration of n-Al$_x$Ga$_{1-x}$N films as Al composition increases. It is also noted that Ti-based metal stacks cannot form ohmic contact as the Al composition is greater than 60 %.
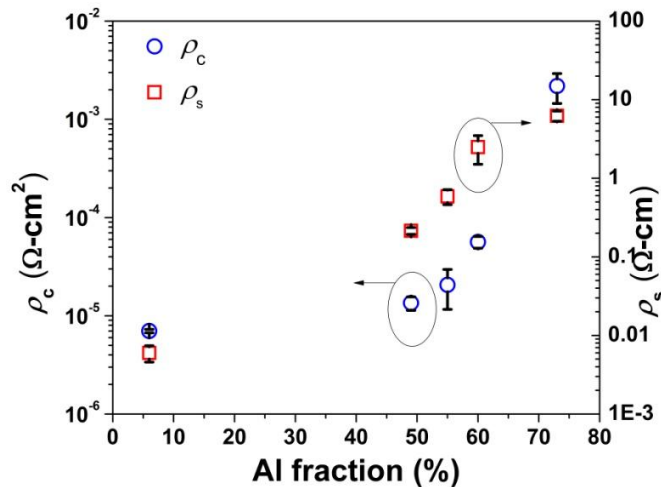
Figure 44. ρ_c **and** ρ_s **of V/Al/Ti/Au ohmic contact on** n-**Al$_x$Ga$_{1-x}$N films with various Al compositions (x= 0.06, 0.49, 0.55, 0.6, and 0.73).**

105

The binding energy at the metal/$Al_{0.55}Ga_{0.45}N$ interface was characterized by a XPS system to understand the formation of interfacial energy states created by either Ti-based or V-based ohmic contact. Figure 45 shows the N:1s core level spectra at the annealed V-$Al_{0.55}Ga_{0.45}N$ and Ti-$Al_{0.55}Ga_{0.45}N$ interfaces. Weaker intensity was observed on the sample with Ti-based contact, which implies severe nitrogen desorption due to the higher temperature annealing process. In addition, the N:1s core-level peak at the V-$Al_{0.55}Ga_{0.45}N$ interface shifts toward higher binding energy by 0.7 eV. Shown in Figure 45 is a fitting of the N:1s core level spectra at the Ti-$Al_{0.55}Ga_{0.45}N$ and V-$Al_{0.55}Ga_{0.45}N$ interfaces. Four common component peaks, i.e., N-Al (397.8 eV), N-Ga (397.4 eV), N-C (395.7 eV) and Ga LMM Auger electrons (393 eV), were found at both metal/AlGaN interfaces [232-234]. The shift of the N:1s core level spectrum at the V-$Al_{0.55}Ga_{0.45}N$ interface consists of to the N-V bond at a higher binding energy of 397.3 eV [235]. This binding energy is higher than that of the N-Ti bond at 396.8 eV [236]. Since the interface states help the surface pinning of the Fermi level, the increase in the binding energy facilitates the current conduction by providing N-V energy states for carrier transport at the metal-semiconductor interface. The results indicated that the use of V-based ohmic contact is a suitable choice of achieving low contact resistance for n-AlGaN layers.
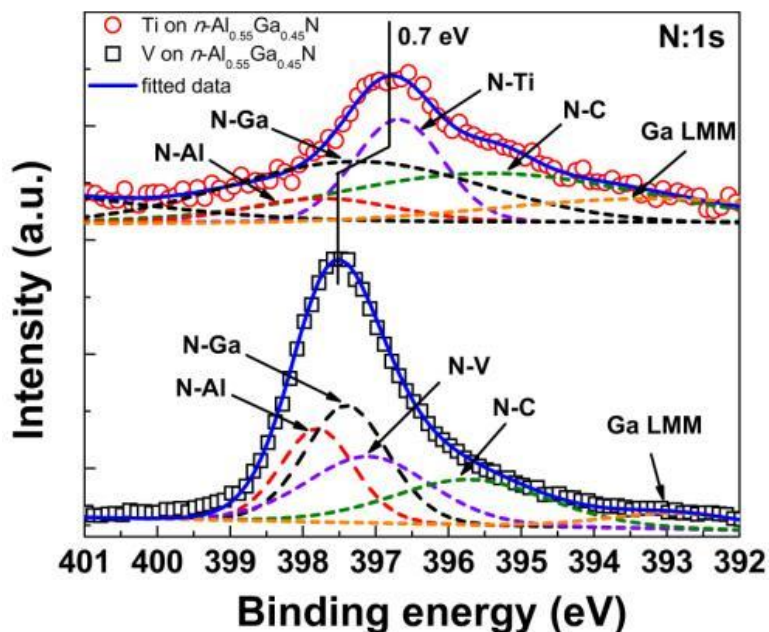
Figure 45. XPS spectra of N:1s core level at the annealed V-Al$_{0.55}$Ga$_{0.45}$N and Ti-Al$_{0.55}$Ga$_{0.45}$N interfaces. The N:1s core level was fitted using Shirley background and mixed Lorentzian-Gaussian line shapes.

In conclusion, we report a study of the V-based ohmic contact on AlGaN films using TLM and XPS analysis. When compared to the Ti-based ohmic contact, V-based ohmic contact consistently shows lower ρ_c and smoother surface morphology at lower annealing temperature for n-type Al$_x$Ga$_{1-x}$N films (x up to 0.55). A study of the N:1s core-level peak at V-Al$_{0.55}$Ga$_{0.45}$N interface shows that the formation of N-V bond helps shift the peak binding energy by 0.7 eV at the V-AlGaN interface when compared to the annealed Ti-AlGaN interface. The increase in the binding energy facilitates the current conduction by providing more effective energy states for carrier transport at the metal-semiconductor interface. As a result, using V-based contact helps achieve low annealing temperature requirement ($<$ 800 ^{o}C) that leads to better surface morphology than conventional Ti-based ohmic contact.

3.3.2 Lapping/polishing/cleaving of AlN substrates

The study goal is to develop and confirm the feasibility of the lapping process and mechanical strengths for any processing related issues for a thin AlN substrate with the thickness < 50 μm. The wafer lapping was performed in a Logitech LP50 system. As shown in Figure 46, a stable lapping rate of 15 μm/hr was obtained using the SiC powder (Grit: 600). The thickness uniformity of the lapped wafer is 45 +/- 1 μm across a 5 mm by 5 mm AlN substrate. After the wafer lapping, SF-1 polishing fluid (a polishing fluid manufactured by Logitech Inc.) was used to polish the surface in a Logitech PM5 system. Figure 47 (a) and (b) show the microscope pictures before and after the polishing, respectively. Smooth mirror-like surface is routinely achieved after the polishing step. The roughness is also improved from 99.7 nm to 2.6 nm before and after the polishing process, respectively.
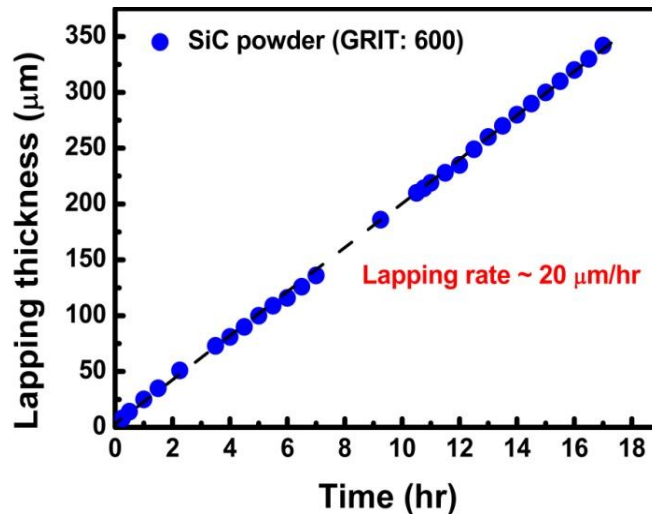
Figure 46. The lapping rate of bare AlN substrate (wafer: HT 433) using SiC powder (GRIT: 600)

Lapping only   **Lapping+ Polishing**

RMS = 99.7 nm   RMS = 2.6 nm

50 µm   50 µm

(a)   **(b)**
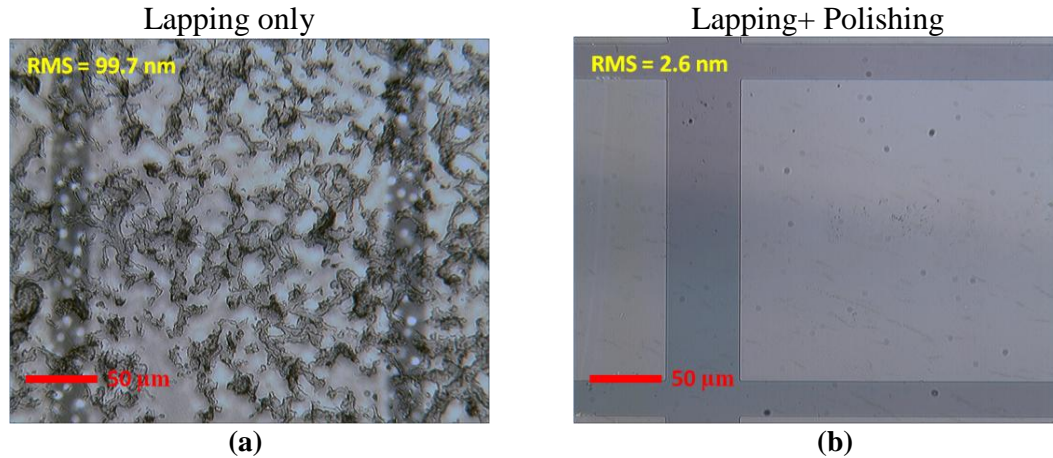
Figure 47. Microscope pictures of the backside AlN susbtrates (a) before and (b) after the polishing processing step. The polishing of the lapped surface provides smooth backside surface.

We further improved the AlN substrate thinning processing that we incidentally discovered in this program by using a presumably final-stage SF-1 polisher as a solution to fast and controllable chemical-mechanical lapping process. As shown in Figure 48 (a), an effective lapping rate of ~110 µm/hr was achieved using the SF-1 polishing fluid in a Logitech PM5 system. The thickness uniformity of the wafer is within +/- 1 µm across an AlN substrate with an area of 5×5 mm^2. The lapped surface is smooth without any observable scratches. An atomic force microscopy (AFM) measurement also indicates that the RMS roughness is ~2.6 nm on the backside of the wafer after the lapping process, as shown in Figure 48 (b)). This processing module allows us to reduce the lapping time from > 24 hours using the conventional powder-based lapping/polishing process to < 4 hours using the polishing fluid. We also achieved tremendous improvement in wafer uniformity and lapped surface morphology with this newly found processing step.
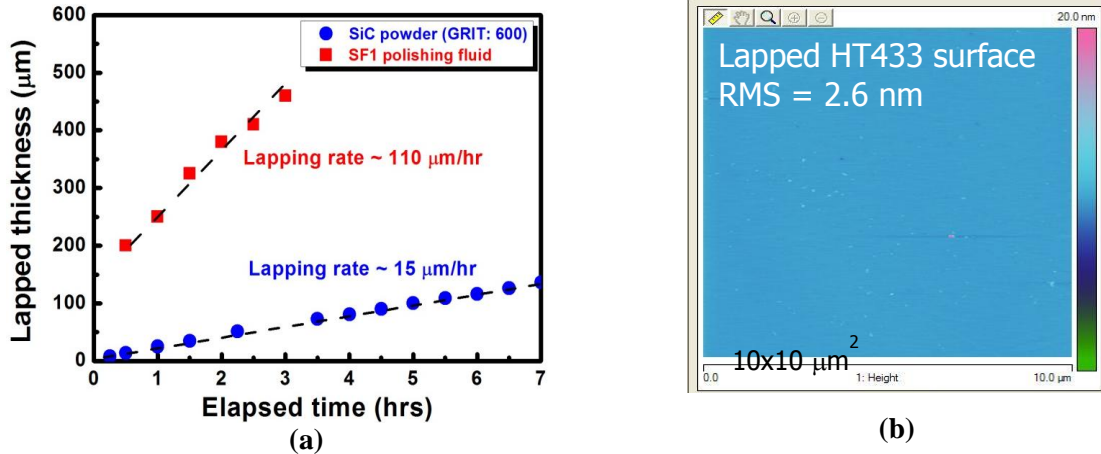
Figure 48. (a) The lapping rate of AlN substrate (HT 433) using SiC powder or SF-1 polishing fluid. (b) The AFM image of lapped AlN surface.

After the substrate thinning, the samples were cleaved into multiples bars with the lengths ranging from 1-1.25 mm as shown in Figure 49 (a). High-quality mirror-like facets can be formed by properly cleaving the wafer along the *m*-plane to form high-Q cavities. A SEM image on the cleaved facet of 1-2643-1 wafer is shown in Figure 49 (b).
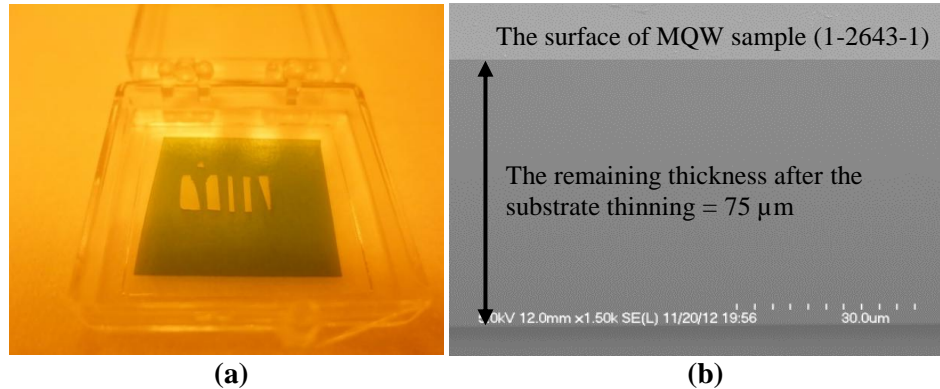
Figure 49. (a) Cleaved laser bars from HT 433 AlN substrate. (b) The SEM image of cleaved laser bar (wafer#: 1-2643-1).

3.3.3 Development of HfO$_2$/SiO$_2$ dielectric mirrors

A robust precision film deposition process control to reproduce high-quality HfO$_2$/SiO$_2$ dielectric mirrors and coatings with low degree of thickness variation was developed for VCSEL fabrication. The dielectric DBR mirrors were deposited using an electron-beam evaporator (CHA Marc 40) at GT. We first developed processing

110

parameters for each SiO_2 and HfO_2 single layer and have exercised several runs with 8-pair quarter-wave-plate HfO_2/SiO_2 dielectric mirrors for 250 nm LD facet coating. The 10-pairs DBR uses HfO_2/SiO_2 (30/39 nm) per pair with an intended center wavelength of the stop-band designed at 250 nm. Figure 23 (a) show the measured reflectivity of 8-pairs HfO_2/SiO_2 DBRs under the normal incidence. The center wavelength is at 250 nm and the reflectivity at 250 nm is ~ 97 %. We have exercised several runs with 8-pairs HfO_2/SiO_2 DBRs and the variation of center wavelength is < 2 nm across a 2×2 cm^2 square area.

By scaling each SiO_2 and HfO_2 layer thickness, we further developed the HfO_2/SiO_2 DBRs for VCSEL fabrication. Shown in Figure 23 (b) is the measured reflectivity of 10-pairs HfO_2/SiO_2 DBRs under the normal incidence. The center wavelength is at 368 nm and the reflectivity at 370 nm is > 99.9 %. In spite of an asymmetric stop-band response due to the thickness uniformity in these DBR pairs, the achieved wide stop band (> 60 nm) ensures to cover the full range of the VCSEL emission at 370 nm. It is also noted that the adhesion of these dielectric films on III-N materials is satisfactory and no peeling was observed for DBR stacks up to 10-pairs.

(a) (b)
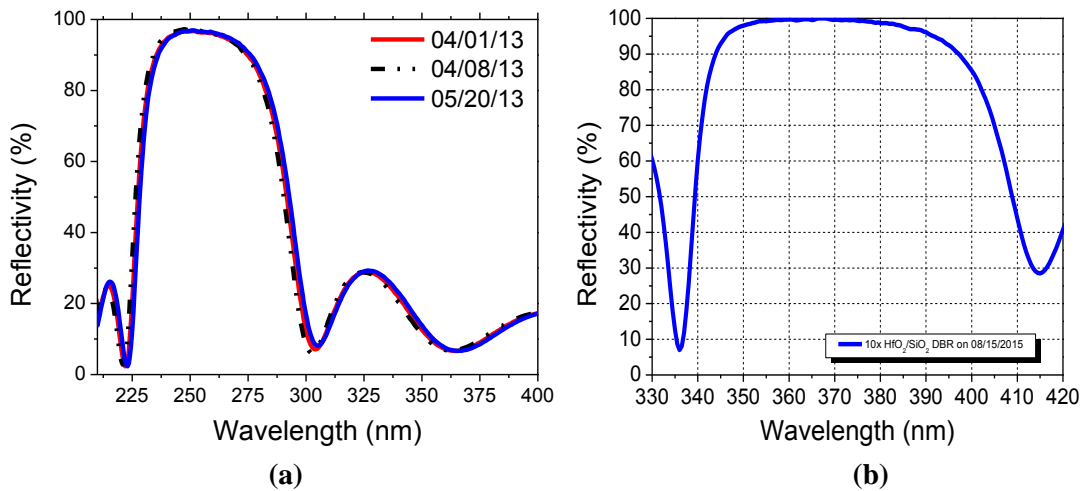
Figure 50. The measured reflectance for 8-pairs and 10-pairs dielectric DBRs using SiO_2/HfO_2 quarter-wave plates with an intended center wavelength of (a) 250 nm and (b) 370 nm.

Cross-section samples of the 10-pair HfO_2/SiO_2 DBRs were prepared for transmission electron microscopy (TEM) measurement using mechanical polishing and argon-ion milling. Figure 51 is a large-magnification cross-section image of the 10-pair HfO_2/SiO_2 DBRs. Abrupt and perfectly flat interfaces between HfO_2 and SiO_2 are clearly shown with distinctive contrasts. The brighter layers correspond to HfO_2 layers while the darker layers correspond to SiO_2 layers. The observed flat interfaces are important to improve the optical reflectivity by reducing interface roughness scattering. From these images, accurate values of the thicknesses of the HfO_2 and SiO_2 layers can be determined to be 48 nm and 66 nm, respectively. The TEM thickness measurements agree very well with the nominal deposition thickness values. The observed thicknesses deviation was determined to be less than 3% for both HfO_2 and SiO_2 layers.
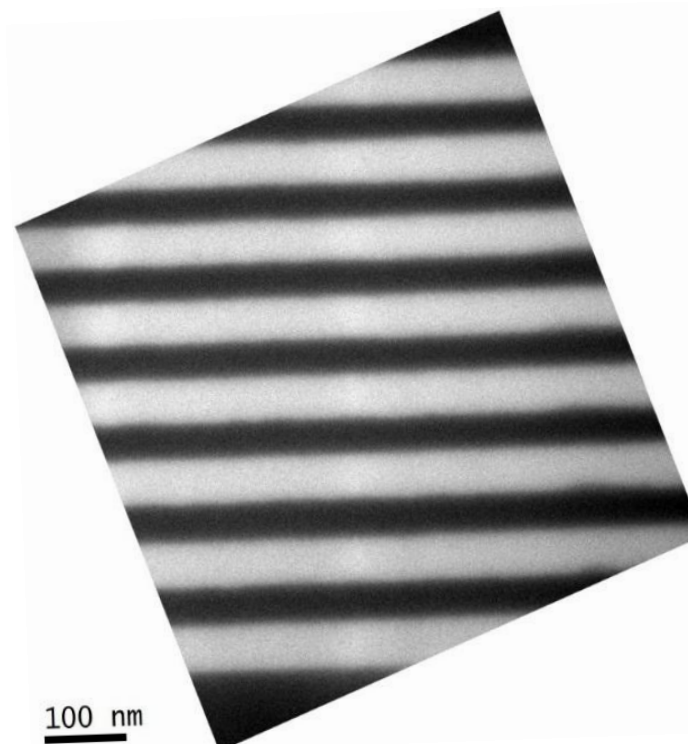
Figure 51. Large-magnification cross-section image performed by Dr. Ponce's group at Arizona State University for the 10-pair HfO_2/SiO_2 DBR structure. The brighter layers correspond to HfO_2 (48 nm) while the darker layers correspond to SiO_2 (66 nm). The observed thicknesses deviation was determined to be < 3% for both HfO_2 and SiO_2 layers.

3.3.4 Indium tin oxide (ITO) transparent contact

Low-loss transparent contact using ITO were developed for the near-UV VCSEL. Among the optically transparent contact available to date, ITO would probably be the only suitable, though not ideal, choices of the material for NUV VCSELs as it has a bandgap energy of ~3.64 eV. The optical properties have been extensively studied in the visible band but few reports were available for a study on the near-UV region. One would trade the transparency for the resistivity of the ITO film and these parameters are dependent on the deposition method and the post-annealing temperature. Shown in Figure 52 (a) are the optical properties at λ= 369.5 nm versus the post-deposition annealing temperature for an e-gun evaporated ITO film. The film has a thickness of 45 nm and was deposited using an e-beam evaporator system at GT. The post-deposition annealing step was carried out under oxygen ambient for a fixed annealing time of 10 minutes in a rapid thermal annealing system. The measured transmittance (T), reflectivity (R), and absorption loss (A) of the ITO film annealed at different temperatures. Clearly, the ITO film annealed at 500 ℃ shows lowest optical loss (< 5 %) at λ= 370 nm. The corresponding absorption coefficient (α) is 5800 (cm^{-1}). The T/R/A spectra of an ITO film annealed at annealed at 500 ℃ for 10 mins are shown in Figure 52 (b). On the other hand, the ITO film also needs to achieve suitable contact resistance in addition to satisfactory optical transparency. Shown in Figure 52 (c) are TLM results on p-Al$_{0.06}$Ga$_{0.94}$N film before and after annealing at 500 ℃ for 10 minute in O$_2$. ITO ohmic contact is achieved on p-Al$_{0.06}$Ga$_{0.94}$N and ρ_c is 7.4×10^{-2} Ω-cm^2. Clearly, further reduction of optical loss and ρ_c would be desired for ITO in the near-UV VCSEL.
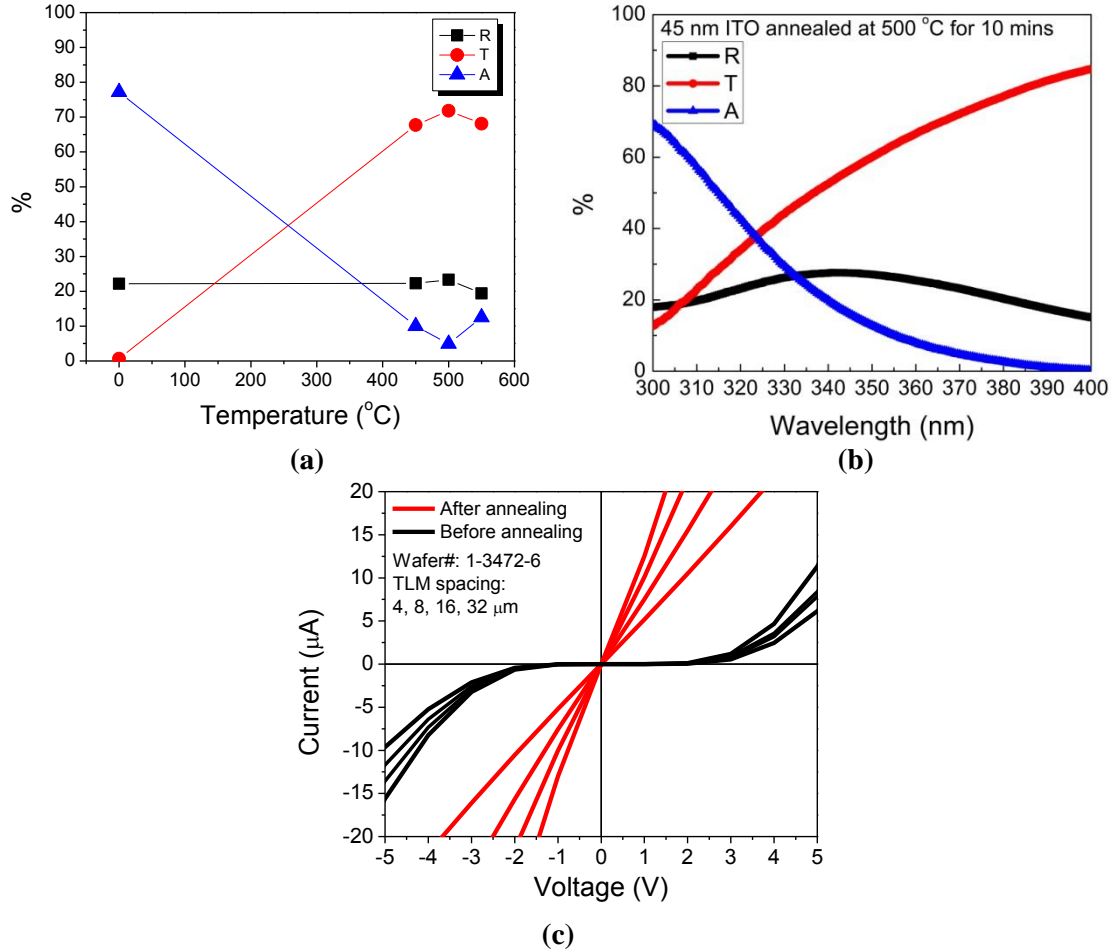
Figure 52. (a) The transmittance (T), reflectivity (R), and absorption loss (A) at λ= 370 nm of a 45 nm-thick ITO film annealed at different temperatures for 10 minutes under an oxygen ambient. (b) The *T/R/A* spectra of an ITO film annealed at annealed at 500 °C for 10 mins. (c) TLM results of ITO film on *p*-type AlGaN (wafer#: 1-3472-6) before and after RTA annealing.

3.4   Results and Discussions

3.4.1   DUV light-emitting diodes

The LED structures were grown on *c*-plane sapphire substrates by a Thomas Swan metal-organic chemical vapor deposition system. The layer structures consist of an AlN buffer, 50-pairs of un-doped AlN/$Al_{0.75}Ga_{0.25}N$ superlattice, 50-pairs of un-doped $Al_{0.75}Ga_{0.25}N$/$Al_{0.55}Ga_{0.45}N$ superlattice, 0.8 µm-thick layer of *n*-$Al_{0.55}Ga_{0.45}N$, 70 nm-thick layer of *n*-$Al_{0.7}Ga_{0.3}N$, three periods of $Al_{0.3}Ga_{0.7}N$/AlN (2/4 nm) multiple quantum

114

wells (MQWs), 20-pairs of p-$Al_{0.26}Ga_{0.74}N$/AlN superlattice, 20 nm-thick p-$Al_{0.26}Ga_{0.74}N$, and 20 nm-thick p^+-GaN as cap layer. After epitaxial growth, the baseline fabrication processing steps are established as shown in Figure 53. An ICP etching system is employed for the LED mesa etching (Figure 53 (a)) using a Cl_2/BCl_3-based gas mixture. Ti/Al/Ti/Au metal stack is deposited and annealed to form the ohmic contact on the n-type $Al_{0.5}Ga_{0.5}N$ waveguide layer (Figure 53 (b)). The specific contact resistance is $< 2 \times 10^{-5}$ Ω-cm^2, and the sheet resistance is 600 $\Omega/\square$. The p-type GaN contact layer uses a Ni/Ag/Pt metal stack (Figure 53 (c)) and the ohmic contact is also achieved. The specific contact resistance is $< 4.5 \times 10^{-3}$ Ω-cm^2, and the sheet resistance is 650 k$\Omega/\square$. The relatively high p-type sheet resistance is because the p-type region is very thin (40 nm) in the current design.

(a) (b) (c)
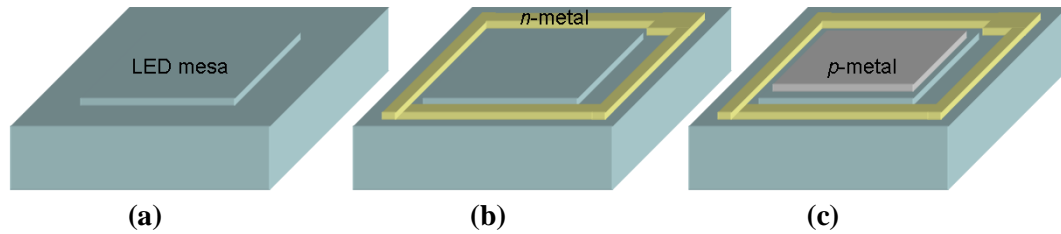
Figure 53. A schematic fabrication processing flow for DUV LED fabrication developed at the Georgia Tech.

Shown in Figure 54 (a) is the typical *I-V* curve of an AlGaN/AlN-based DUV LED device. The microscope picture of a fabricated LED device is shown in the inset of Figure 54 (a). The total illumination area is 0.122 mm^2. In the forward-biased region, the turn-on voltage is ~4 V and the series resistance is 95 Ω at 10 V. Figure 54 (b) shows the LED emission spectra with the CW-mode forward current of 100 mA. Light is collected from the backside of the sapphire substrate using an SPEX 500M spectrometer. Deep-UV emission is observed with a main peak at 283 nm. The full width at half maximum

(FWHM) of the DUV emission is around 13 nm. Another peak at 340 nm is observed, which could come from the re-absorption of the DUV emission followed by the subsequent deep-level luminescence in the underlying layers. By inserting a bandpass filter with the cutoff wavelength at $\lambda= 300$ nm, the optical power is collected from the backside of the sapphire substrate. As shown in the Figure 54 (a), the optical power for DUV emission is about 14 µW with the d.c current drive of 100 mA.
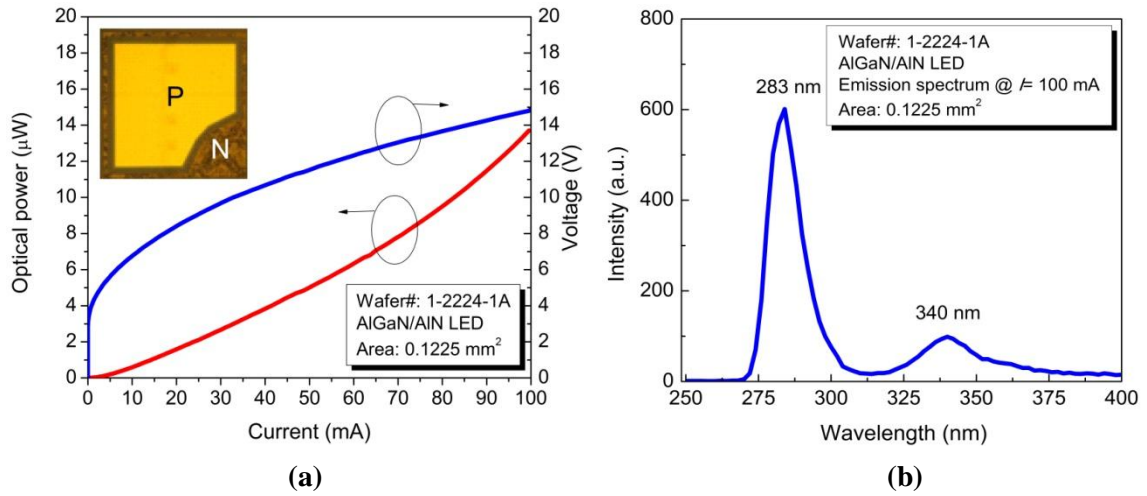
Figure 54. (a) The *L-I-V* curves of a DUV LED with the illumination area of 0.1225 mm^2. The inset shows the microscope pictures of the DUV LED under test (wafer#: 1-2224-1A). (b) The emission spectrum of the same DUV LED device under d.c current operation.

Since the sheet resistance of *n*-type AlGaN is high $(\rho_s >1.5$ kΩ/□), the radiative recombination mostly occurs around the mesa sidewall due to the current crowding, which inevitably reduce the light extraction efficiency. To mitigate the current crowding effect, a DUV micro-array LED with long perimeter is necessary to homogeneously distribute the current density through semiconductor materials, especially at the vicinity of the contacts and over the *p-n* junctions. Figure 55 (a) and (b) show the schematics and microscope pictures of a DUV micro-array LED with 400 pixels, respectively. Each pixel is 35×35 µm^2 and the total illumination area is 0.49 mm^2. A tapered current bus is

designed to ensure the maximum current drive is greater than 2 A. The *d.c I-V* and *L-I* curves of a fabricated microarray LED is shown in Figure 56 (a) and (b), respectively. The turn-on voltage is ~4 V and the series resistance is reduced to 16 Ω at 10 V. The maximum optical power for DUV emission ($\lambda < 300$ nm) is greater than 200 µW at the d.c current drive of 1 A.

(a)

(b)
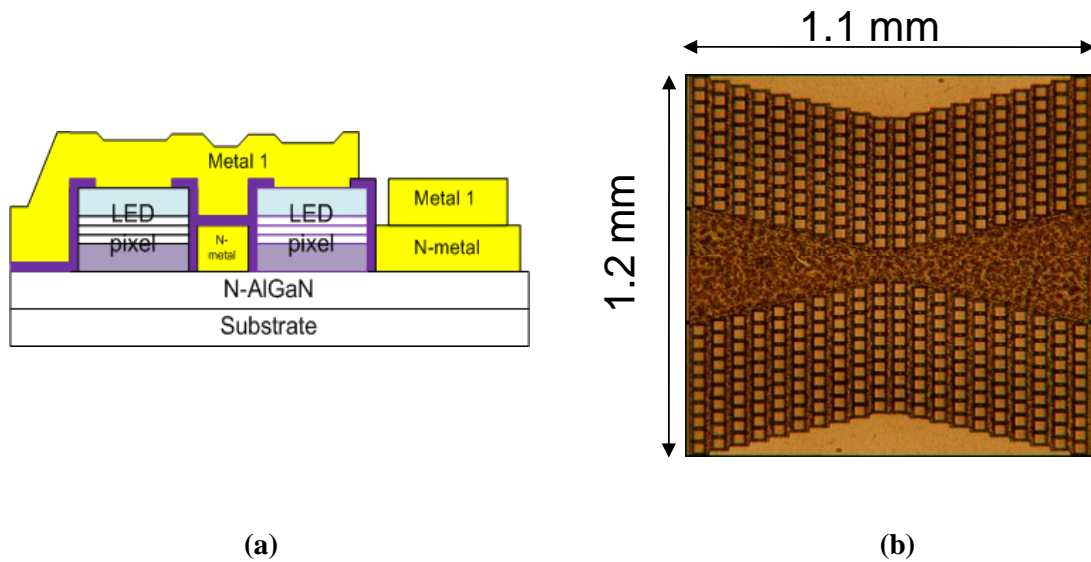
Figure 55. (a) A schematic cross-sectional view of the DUV microarray LED (wafer#: 1-2224-1D-2D1A). (b) The microscope picture of a fabricated DUV microarray LED with 400 pixels.

(a)

(b)
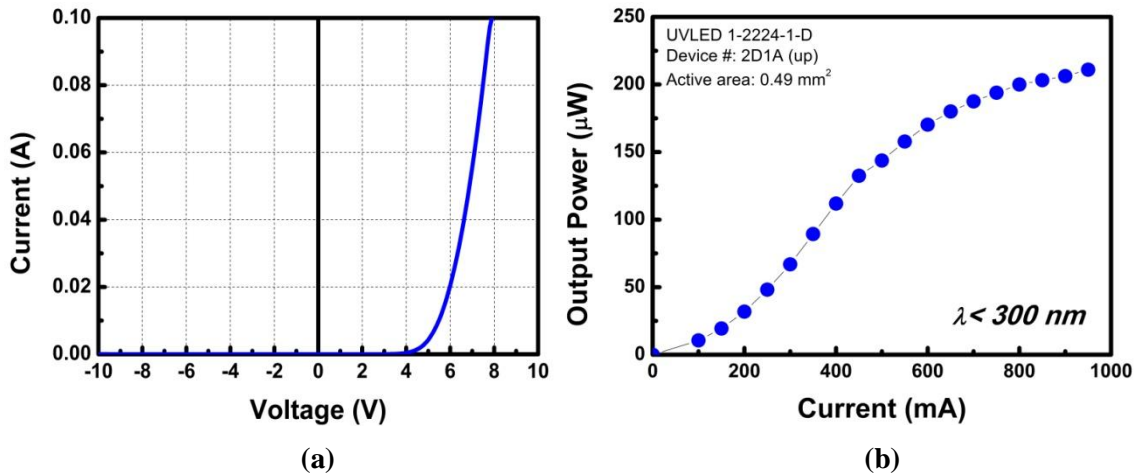
Figure 56. The d.c (a) *I-V* and (b) *L-I* curves of a fabricated DUV microarray LED with 400 pixels (wafer#: 1-2224-1D-2D1A).

3.4.2 Optically-pumped DUV laser employing HfO$_2$/SiO$_2$ dielectric mirrors

The AlGaN-based MQW structure was grown on an aluminum-polar (0001) native AlN substrate. Growth on a native substrate enables homoepitaxy of a buffer layer, which significantly reduces the density of dislocations in the epitaxial layers and improves subsequent active-region quality [237]. Prior to the growth, the AlN substrates were etched in a 3:1 H$_2$SO$_4$: H$_2$PO$_4$ acid solution at 90°C for removing surface hydroxide [238]. The wafer was then annealed in high-purity ammonia ambient at 1100 °C for the optimal condition for epitaxy. The epitaxial growth was performed in a Thomas-Swan (now Aixtron) 6×2″ close-coupled showerhead MOCVD reactor system. Due to the low ad-atom mobility of Al atoms on the growing surface and parasitic gas-phase reaction between aluminum precursor and ammonia, high temperature, low pressure, and low V/III ratio are required for two-dimensional growth and smooth surface formation. In this work, the relatively high growth temperature of 1130°C at 75 Torr was used while the V/III ratios for AlN buffer layer and active region growth are set to less than 100 and approximately 400, respectively.

A cross-section of the layer structure is shown in Figure 57 (a). The active region consists of eight periods of quantum wells, with 3-nm Al$_{0.60}$Ga$_{0.40}$N wells and 6-nm Al$_{0.75}$Ga$_{0.25}$N barriers, between a 200-nm AlN buffer layer and an 8-nm AlN cap layer for surface passivation. In order to maximize the overlap between the optical field and the active region, any underlying AlGaN layers or superlattice structure for the purpose of strain reduction were omitted from the design. Figure 57 (b) shows the refractive index profile and the simulated optical field distribution within the laser structure. The refractive indices for ternary AlGaN alloys are calculated from the refractive indices of

118

AlN and GaN using Vegard's law [239]. The optical confinement factor (Γ) is determined to be ~ 21.9 % under the fundamental waveguide mode.

<center>(a)   (b)</center>
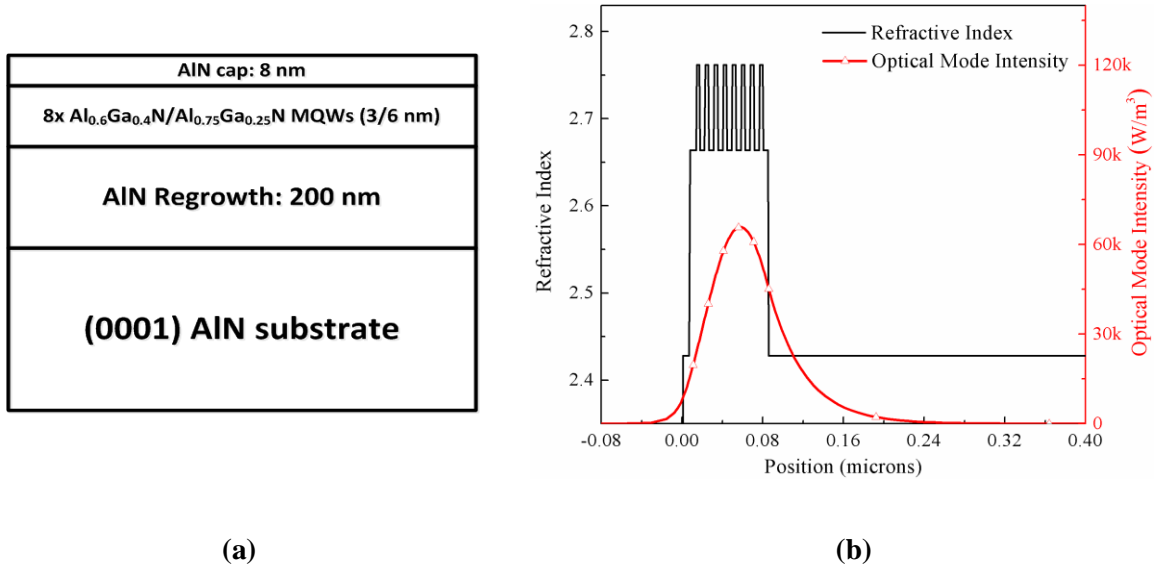
Figure 57. (a) A schematic cross-sectional view of the AlGaN-based laser epitaxial structure. (b) The refractive index profile and simulated optical field distribution performed by Dr. Yoder's group at GT.

     Following the epitaxial growth, the wafer was thinned to 80 µm by a chemical-mechanical polishing process and Fabry-Perot Etalons were formed by cleaving along the *m*-plane of the sample into a 1.4-mm-long resonant cavity. Five and six pairs of HfO_2/SiO_2 DBR mirrors were sequentially deposited to form the front- and rear-side facet mirrors, respectively. The dielectric mirrors are tuned to a target of a center wavelength of 250 nm. Shown in Figure 58 are the reflectivity spectra of the front-side and the backside facet mirrors deposited on the companion glass substrates using an ultraviolet-visible spectrometer (Shimadzu UV2401PC). Although the center wavelengths are slightly shifted due to processing variation, high-reflectivity mirrors with R = 92% and 97 % at λ = 249 nm were achieved on the front- and rear-side facets, respectively.

<center>119</center>
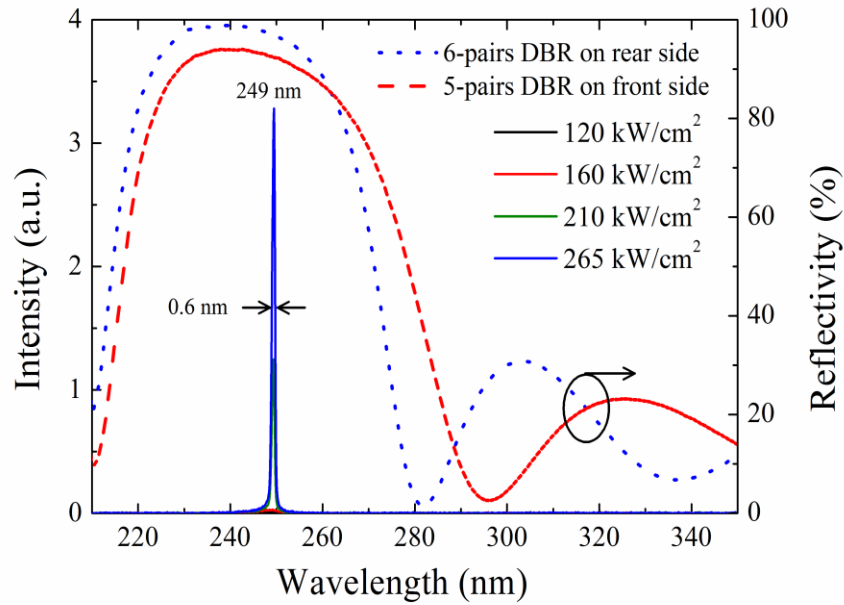
Figure 58. The power-dependent emission spectra of AlGaN-based MQW laser (wafer#: 1-2693-2) at RT with dielectric mirrors coated on both facets and the reflectivity spectra of 6-pairs and 5-pairs HfO₂/SiO₂ dielectric DBR mirrors.

The excitation source is ArF Excimer laser (λ= 193 nm) with a pulse width of 20 ns at a repetition rate of 10 Hz and the output power ranges from 10 mJ to 200 mJ. Shown in Figure 59 (a) and (b) are the beam controlling path setup and side view of the measurement system, respectively. The laser beam was shaped into a 0.1 cm × 1.27 cm² rectangle by passing through an optical aperture. A 45-degree DUV-grade mirror directs the beam to a calibrated power meter for pump power density measurement. The sapphire substrates were served as digital attenuators that can be inserted before optical aperture to further reduce the pump power density below threshold when necessary. A Glan-Laser α-BBO polarizer was used for selecting the polarization of the photon emission from the DUV laser bars. An optical fiber was placed in the proximity of the *m*-plane facets or the polarizer for light emission detection. An Ocean Optics Maya-2000 Pro spectrometer

120

with a spectral resolution of 0.2 nm was used for the photon emission spectroscopy measurement.
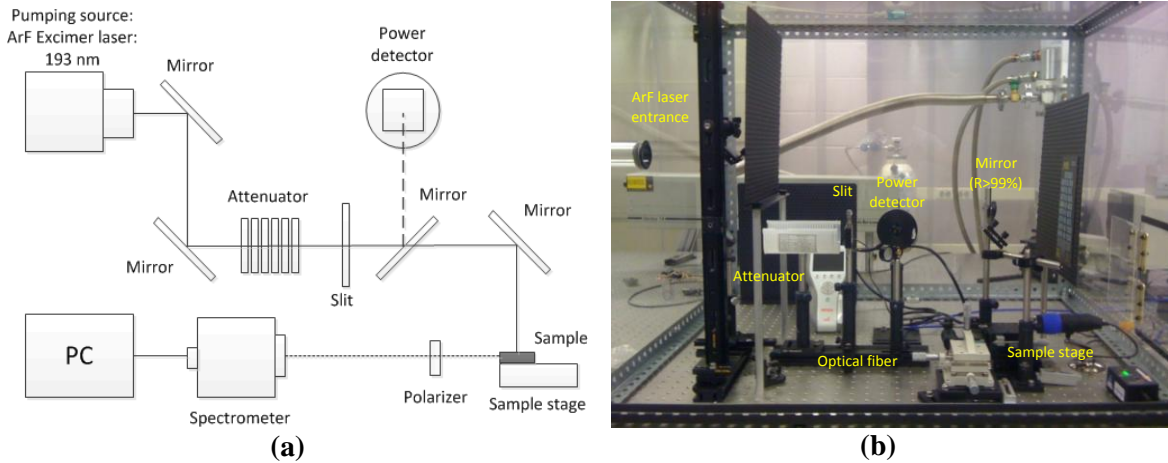
Figure 59. **(a) Schematic diagram of optical measurement system; (b) a side view of the measurement system.**

As shown in Figure 58, the laser bar with double-sided dielectric mirror coatings has an emission peak at λ = 249 nm with a spectral line-width of 0.6 nm at maximum pumping power density of 265 kW/cm^2. The stimulated emission spectrum exhibits a preferential TE polarization, as shown in Figure 60 (a), with a degree of polarization (P), defined as $P = (I_{TE} - I_{TM})/(I_{TE} + I_{TM})$, approaching 100%. The TE-dominant emission is attributed to the in-plane compressive strain in the quantum-confined structure [240]. The optical output intensity measured before and after the facet coatings versus the excitation power density (L-L curve) is plotted in Figure 60 (b). The threshold pumping power density (P_{th}) was reduced by ~ 14%, from 250 to 215 kW/cm^2 after the first dielectric reflector (R = 97%) was applied on the rear-side of the facet. Another 16% reduction in P_{th} (from 215 to 180 kW/cm^2) was also observed after the front-side high-reflectivity mirror (R = 92%) was coated on the laser bar. We also observed a significant drop in the

slope efficiency after both facet coatings were deposited, which suggests a reduction in the cavity round-trip loss was achieved by the application of the DBRs on the cleaved facets.

(a)   (b)
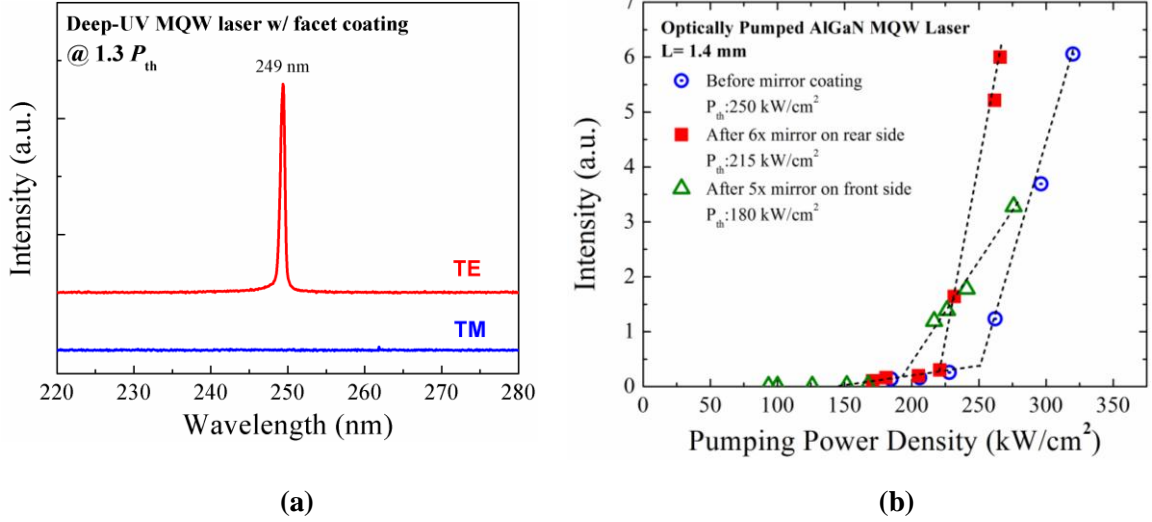
Figure 60. (a) The TE and TM-mode emission spectra of the same laser bar (wafer#: 1-2693-2) operating above the pump threshold at RT. An offset was applied on the TE emission spectrum for visual clarity. (b) Light-output intensity as a function of the optical pump power density for the AlGaN-based MQW laser without the facet mirror coating (hollow circle in blue), after the rear-side mirror coating (solid square in red) and after the double-sided facet coating (hollow triangle in green).

The internal loss and the threshold gain of the AlGaN-based MQW laser can be estimated using the differences of the facet reflectivity before and after mirror coatings. Assuming the modal reflectance is close to the externally measured value from the companion glass substrates, the internal loss (α_i) can be determined through the following equation [241]:

$$\alpha_i = \frac{1}{L} \times \frac{\eta'_d - \eta_d}{\left(\dfrac{\eta_d}{\ln\dfrac{1}{\sqrt{R_1 R_2}}} - \dfrac{\eta'_d}{\ln\dfrac{1}{\sqrt{R'_1 R'_2}}}\right)} \quad (4.9)$$

, where L (= 1.4 mm) is the cavity length; R_1 and R_2 (both 18%) are the reflectivity of the as-cleaved facets; and R_1' (92%) and R'_2 (97%) are the reflectivity of the front-side and

the backside facets with the facet coatings, respectively. The differential quantum efficiency (η_d) of the cleaved laser bar can be obtained by:

$$\eta_d \propto \frac{1}{F}\frac{dP_{out}}{dP_{in}} \propto \frac{1}{F}\frac{dI_{out}}{dP_{in}} \qquad (4.10)$$

,where P_{in} and P_{out} represent the input and output power, respectively. The light output intensity is denoted as I_{out}; therefore $\dfrac{dI_{out}}{dP_{in}}$ can be calculated from the *L-L* curves shown in Figure 60 (b). The differential quantum efficiency after the facet coating is denoted as η'_d. The fraction of the output power (*F*) measured from the front-side of the facet with respect to the total optical output power can be calculated by:

$$F = \frac{1-R_1}{(1-R_1 + \sqrt{R_1/R_2}\,(1-R_2))} \qquad (4.11)$$

In this case, *F* is 0.5 and 0.73 for the laser bar before and after facet coatings, respectively, and the α_i can be estimated to be 2 cm^{-1}. The threshold modal gain (g_{th}) can also be obtained by:

$$\Gamma g_{th} = \alpha_i + \frac{1}{L}\ln(\frac{1}{\sqrt{R_1 R_2}}) \qquad (4.12)$$

With the high-reflectivity facet mirrors coated on both sides of the laser bar, the g_{th} is reduced from 63 cm^{-1} to 10.9 cm^{-1}. This reduction in the threshold modal gain shows the HfO$_2$/SiO$_2$ dielectric mirror can effectively enhance the performance of deep-UV lasers. It is also noted that g_{th} is approximately an order of magnitude lower than that of AlGaN-based MQWs grown on 6H-SiC substrate at $\lambda\sim$ 250 nm [242].

In conclusion, we demonstrate an optically-pumped, AlGaN-based, MQW laser with HfO$_2$/SiO$_2$ dielectric mirrors at room temperature. Employing high-reflectivity

mirrors on the cleaved facets effectively reduces the threshold power density of a deep-UV laser from 250 to 180 kW/cm^2. The lasing wavelength of 249 nm and a preferential TE-type emission are observed with a degree of polarization ~100%. The internal loss and threshold gain of this deep-UV laser are estimated to be 2 cm^{-1} and 10.9 cm^{-1}, respectively.

3.4.3 Electrically-pumped AlGaN-based UV emitters

In order to achieve a laser diode, a more complex epitaxial structure is required to transport carriers to the active region efficiently while maximizing the optical confinement. An AlGaN-based UV MQW DH emitter structure was grown on an aluminum-polar (0001) native AlN "bulk" substrate. Figure 61 illustrates a schematic diagram of a graded-index separate confinement heterostructure (GRINSCH) MQWs ridge waveguide ultraviolet emitter. The active region consists of a four-period MQW structure, with 2 nm Al$_{0.32}$Ga$_{0.68}$N wells and 5 nm Al$_{0.47}$Ga$_{0.53}$N barriers, which emits photons with a peak wavelength of ~350 nm. Grading layers between the quantum barriers and the waveguide layers are employed to enhance carrier confinement as well as optical confinement.

Stripe-geometry ridge structures with various mesa widths (2-12 µm) were formed by ICP-RIE process. To avoid etching damage, a more chemically driven etching process was performed; therefore, the ridge sidewalls were formed with an angle of ~80° respect to the mesa. Once the ridge structure was formed for lateral confinement of optical mode, the mesa etch was then performed to access the n-contact layer. To ensure smooth sidewalls for reducing leakage currents, PEC etching of the mesa sidewalls was performed with a 150 W Xe arc lamp. Metal alloy stacks of V/Al/Ti/Au with thickness of

300A/500A/300A/500A, for n-type metal contact was deposited by an e-beam evaporator and annealed in nitrogen ambient at 450°C for ten minutes and $850\ ^{\circ}$C for 30 seconds. Next, a *p*-type metal alloy, Ni/Ag/Ni/Au with thickness of 50 Å/500 Å /100 Å /200 Å, was deposited and annealed in compressed air at 450°C for two minutes. Surface passivation using SOG was performed to enhance both electrical and optical confinement. The back-side processing starts with the substrate lapping and polishing, and facet cleaving. Figure 62 (a) and (b) show the photographs of fully processed UV laser diodes fabricated on a 1.5-cm-diameter wafer of bulk AlN before and after facet cleaving, respectively. The wafer contains several hundred gain-guided laser diodes for testing.

(a) **(b)**
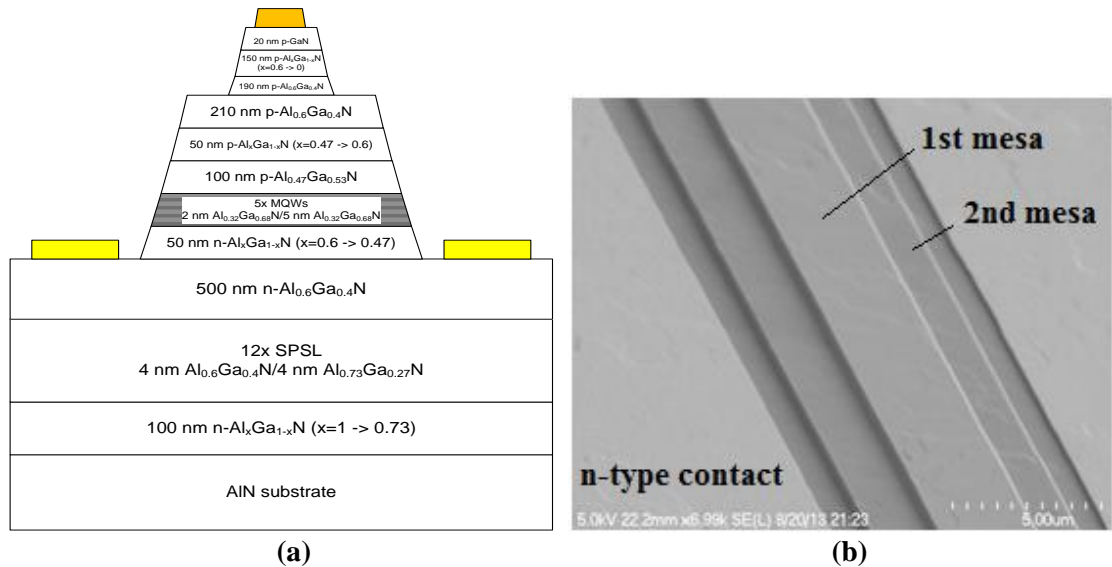
Figure 61. (a) A schematic diagram of an UV light emitter employing inverse taper design (wafer#: 1-3018-4). (b) SEM image of the ridge waveguide after *n*-type metal evaporation.

125
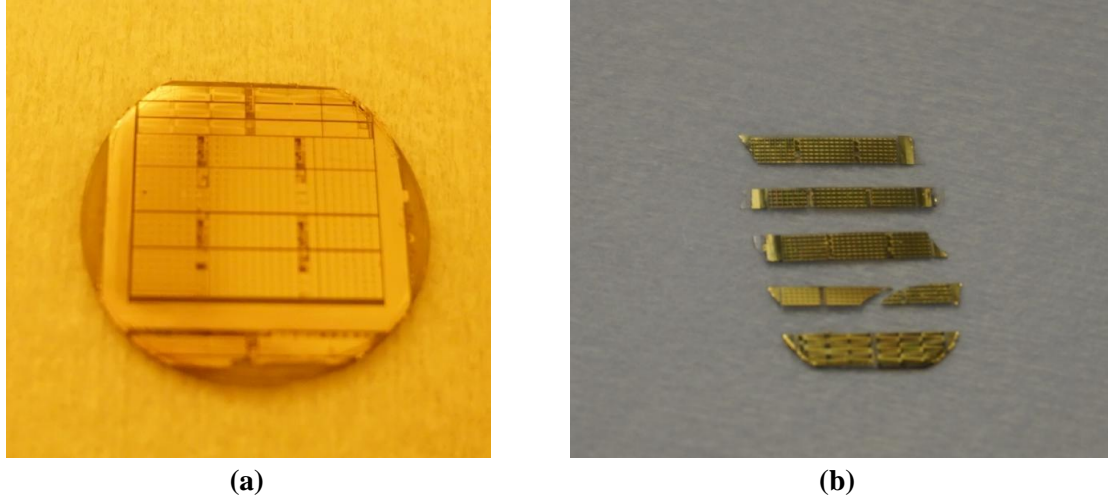
Figure 62 (a) and (b) show the photographs of fully processed UV light emitters (wafer#: 1-3018-4-SectionD-R3C5) fabricated on a 1.5-cm-diameter wafer of bulk AlN before and after facet cleaving, respectively. The wafer contains several hundred gain-guided laser diodes for testing.

Once the device was fabricated, a series of electrical and optical characterizations was performed. Figure 63 illustrates the TLM for both *p*-contact and *n*-contact. Schottky barriers were observed with potential barrier heights of (0.5 V) and (1 V) for the p-contact and n-contact, respectively. This non-ohmic behavior for the metal contact was only observed on the sample grown on AlN substrate and contributes an additional parasitic resistance and results in a relatively large turn on voltage (V_{on}). Although ohmic contact weren't successfully formed, the sheet resistance (R_{sh}) can still be estimated by measuring the total resistance at the bias above the Schottky barrier height. Utilizing the total resistance measured at 5 V, R_{sh} for the p-contact and n-contact layers were estimated to be 167 kΩ/□ and 233 Ω/□, respectively.
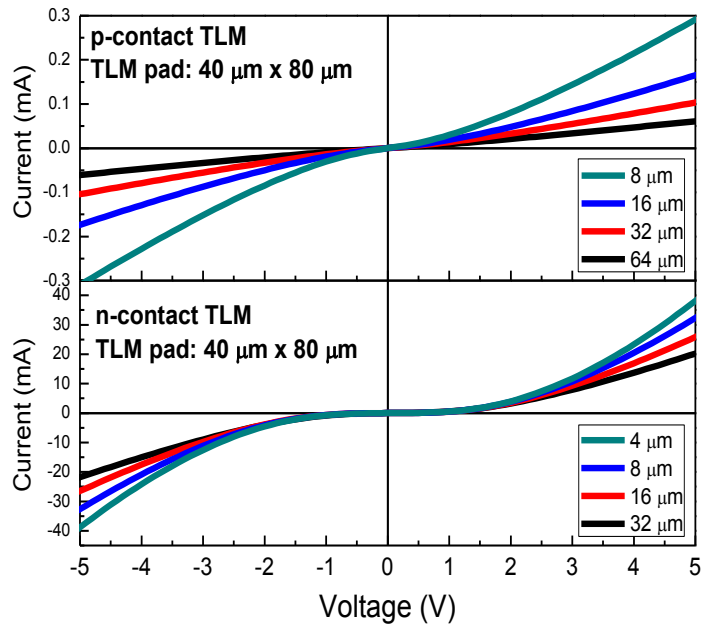
Figure 63. TLM results for *p*-contact (top) and *n*-contact (bottom).

Figure 64 (a) illustrates the *I-V* curves of the device under a d.c. condition. Based on the measurement results, the leakage current was determined to be less than 0.1 pA ($J<$ 2 nA/cm^2), suggesting a high-quality epitaxial material is achieved on AlN substrate. The ideality factor was extracted as 7.4 arising from the non-ohmic contact properties. Even though the non-ohmic metal contact contributed an additional voltage to the device turn-on voltage, the diode has a turn-on voltage at ~9 V , which is significantly lower than the value of ~15 V reported previously for similar structures [243]. At the maximum measured forward voltage of 15 V, the device sustained a current level of at least 500 mA, which is equivalent to a current density of ~10 kA/cm^2, and the series resistance at this current density was measured to be ~15 Ω. To further push the device performance to its limits, pulsed *I-V* measurements with a pulse width of 50 μs and a pulse period of 100 ms were made and the measured *I-V* curve is shown in Figure 64 (b). The maximum

measured forward voltage is 20 V with the measured current of 1.07 A, which is equivalent to a current density of ~18 kA/cm^2, and the measured series resistance at 20 V is determined to be ~11 Ω. From these current-voltage measurements, the electrical performance shows our inverse-tapered p-waveguide design MQW DH emitters meets our expectations in maintaining a high current density while providing a reduced forward turn on voltage.
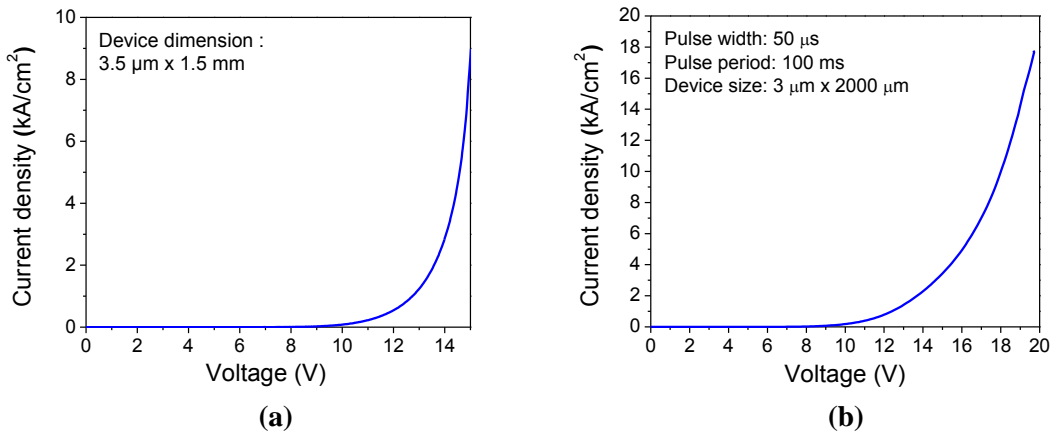
Figure 64. (a) CW and (b) pulsed *I-V* characteristic of an UV light emitter with the inverse-tapered Al$_x$Ga$_{1-x}$N *p*-waveguide (wafer#: 1-3018-4-SectionD-R3C5). The pulse width is 50 µs and pulse period is 100 ms.

The LD was driven under the pulsed current mode with a pulse duration of 300 ns and a repetition frequency of 1 kHz. Figure 65 shows the room-temperature spontaneous emission spectrum of a stripe laser heterostructure operating under the pulse conditions. The devices nevertheless show very wide emission spectra that are centered at 350 nm with a FWHM of > 60 nm; this indicates an inhomogeneous quantum well composition and very significant well width fluctuations. This result suggests the growth conditions are not transferable for different substrate platforms and we have to seek optimum growth conditions for the epitaxial growth on AlN substrate.
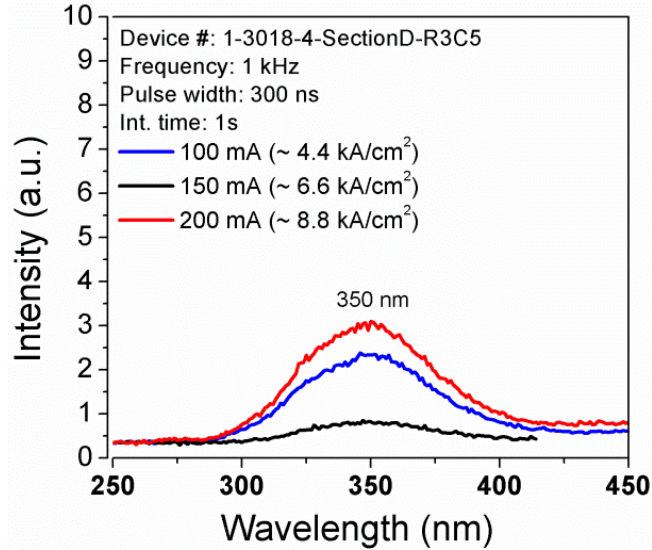
Figure 65. The room-temperature spontaneous emission spectrum of a stripe UV light emitter operating under the pulse conditions (wafer#: 1-3018-4-SectionD-R3C5).

In conclusion, we fabricated a high-aluminum-containing ([Al]~ 0.6) AlGaN MQW DH emitter employing an inverse-tapered-composition AlGaN:Mg p-type waveguide grown on a c-plane Al-polar AlN bulk substrate. Using numerical simulations, we have determined that the inverse-tapered p-type waveguide design is necessary for high [Al] containing p-n junction devices as any valence band discontinuity at the junction will limit the vertical hole transport and induce a larger voltage-drop across the structure. The fabricated ultraviolet MQW DH emitter can sustain a d.c. current of at least 500 mA and a pulsed current of at least 1.07 A, which corresponds to a current density of 10 kA/cm^2 and 18 kA/cm^2 at maximum measured voltage of 15 V and 20V with the measured series resistance of 15 Ω and 11 Ω, respectively.

3.4.4 NUV resonant-cavity light-emitting diodes employing hybrid mirrors

To demonstrate UV VCSELs, a 2-λ thick ultraviolet LED structure was grown on top of the 40-pairs Al$_{0.12}$Ga$_{0.88}$N/GaN DBRs. The LED structure started with a 118 nm silicon-doped Al$_{0.06}$Ga$_{0.94}$N layer followed by a MQW structure consisting of five-pairs

of InGaN/AlGaN. The growth was completed by the growth of 98 nm of Mg-doped $Al_{0.06}Ga_{0.94}N$ layer and a 20 nm layer of p^{++}-$Al_{0.06}Ga_{0.94}N$. The optical reflectivity spectrum for the bottom DBRs was taken by a Shimadzu UV2401PC ultraviolet-visible spectrometer. The spectrometer was equipped with halogen and deuterium lamps for visible and ultraviolet wavelength measurements, respectively. In this study, the halogen lamp was used for obtaining reflectivity above 283 nm while the deuterium lamp was used for the reflectivity between 200 to 283 nm and the measurement step was 0.5 nm. The peak reflectivity of the bottom DBRs was measured to be 91.6% at 368 nm with a stop-band of 11 nm [244].

The fabrication process started with mesa etching with ICP-RIE to expose *n*-AlGaN for forming the cathode contact region. We have investigated different ICP tools to explore the low-damage mesa etching recipe for the VCSEL fabrication. Two ICP tools were chosen: Plasma-Therm ICP in The Institute for Electronics and Nanotechnology (IEN) at GT and STS Multiplex ICP system for III-nitrides in GT-CCS. We used the same RCLED samples (Wafer ID: 1-3590-5) using Plasma-Therm ICP (Sample A) and STS-ICP (Sample B) for comparison. The device under evaluation has a nominal mesa size of 10 μm in diameter and no dielectric passivation was deposited to study the sidewall leakage behaviors.

As shown in the Figure 66 (a), Sample A (the PN junction that went through the Plasma-Therm ICP dry etching) shows unstable reverse biasing I-V characteristics: the leakage current tends to increases for a given reverse bias and the breakdown voltage reduces for multiple scans. On the other hand, as shown in Figure 66 (b), Sample B (the PN junction that went through the STS-ICP) shows no signs of device degradation over

multiple reverse bias scans, as opposed to the degrading characteristics as shown in the Sample A. The consistent reversed biased diode characteristics are beneficial and indicative of the effectiveness in the sidewall leakage suppression for UV VCSEL fabrication.
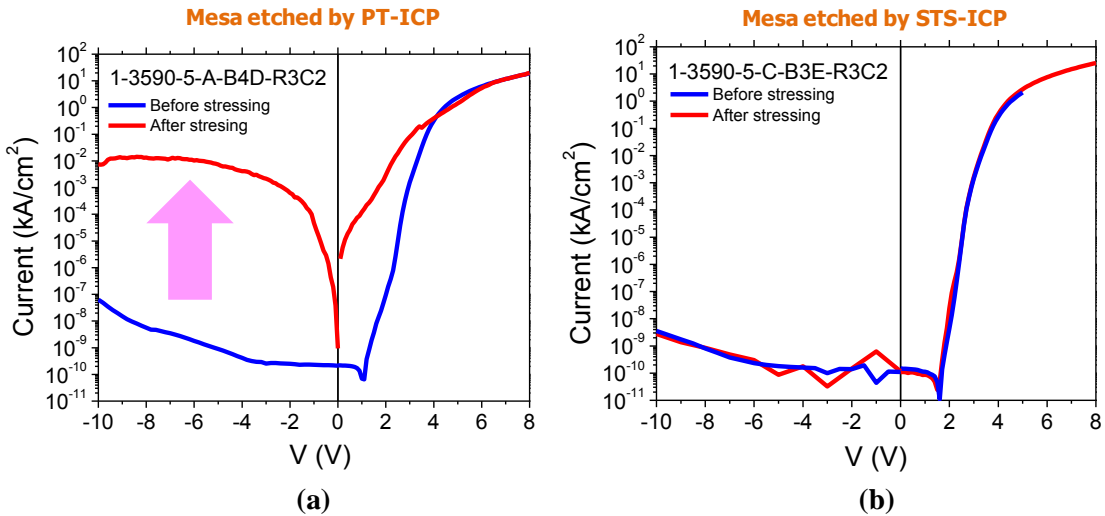
Figure 66. (a) The comparison of I-V characteristics of UV RCLEDs (wafer ID: 1-3590-5) (a) sample A: mesa etching by PT-ICP, (b) Sample B: mesa etching by STS-ICP.

After mesa etching using optimized ICP recipe, an identical ultraviolet PEC sidewall etching process was performed to ensure smooth sidewall formation. Next, vanadium-based (V/Al/Ti/Au) n-type ohmic contact was formed by E-beam evaporation. Instead of conventional nickel-based p-type ohmic metal, an ITO optically transparent contact was used in this case to enhance lateral current spreading. The ITO was deposited via E-beam evaporation and the deposited 45 nm thick film has optical absorption coefficient of 5.8×10^3 cm^{-1} near the RCLED peak emission of 370 nm. The devices were then passivated with SOG followed by the via hole opening and Metal-1 evaporation. Finally, a ten-pair HfO$_2$/SiO$_2$ dielectric DBRs formation concluded the device processing. The optical reflectivity was measured as 99.9 % at λ= 370 nm with a wide stop-band of

60 nm. The schematic cross-sectional view and SEM images of fabricated RCLED are shown in Figure 67 (a) and (b), respectively.

<div align="center">(a)   (b)</div>
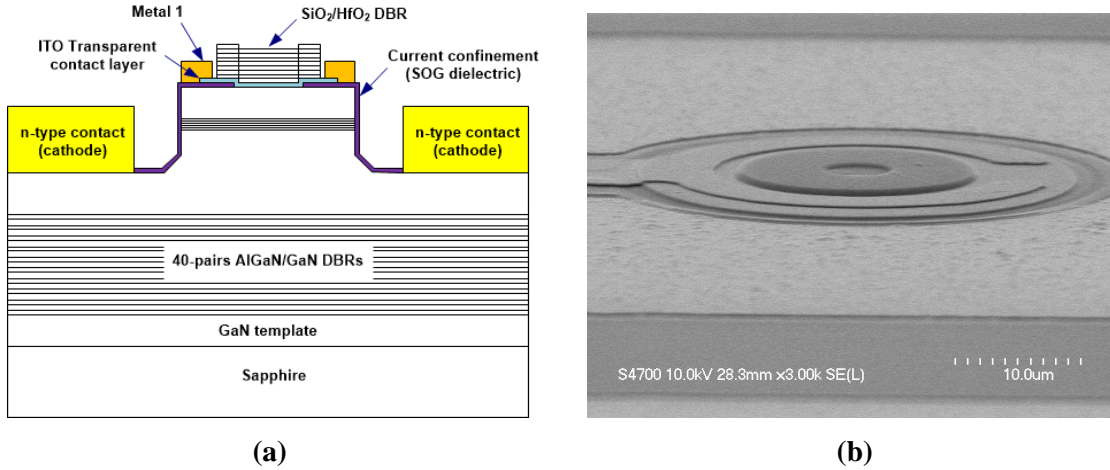
Figure 67. (a) A schematic cross-sectional view of the ultraviolet RCLED employing 40-pairs $Al_{0.12}Ga_{0.88}N$/GaN DBRs and 10-pairs HfO_2/SiO_2 DBRs. (b) The SEM images of fabricated UV RCLEDs.

Figure 68 (a) and (b) illustrate the TLM results for V-based *n*-contact and ITO *p*-contact, respectively. Ohmic contact was achieved on both *n*-type and *p*-type $Al_{0.06}Ga_{0.94}N$. By linear fitting, R_{sh} of the n-$Al_{0.06}Ga_{0.94}N$ is 120 $\Omega/\square$ and ρ_c is about 8.6×10^{-6} $\Omega\cdot cm^2$ after annealing V/Al/Ti/Au at 725 ^oC for 30 seconds under Nitrogen ambient. On the other hand, R_{sh} of the p^+-$Al_{0.06}Ga_{0.94}N$ is 100 $k\Omega/\square$ and ρ_c is about 5.2×10^{-2} $\Omega\cdot cm^2$ after annealing ITO at 500 ^oC for 10 mins under Oxygen ambient.
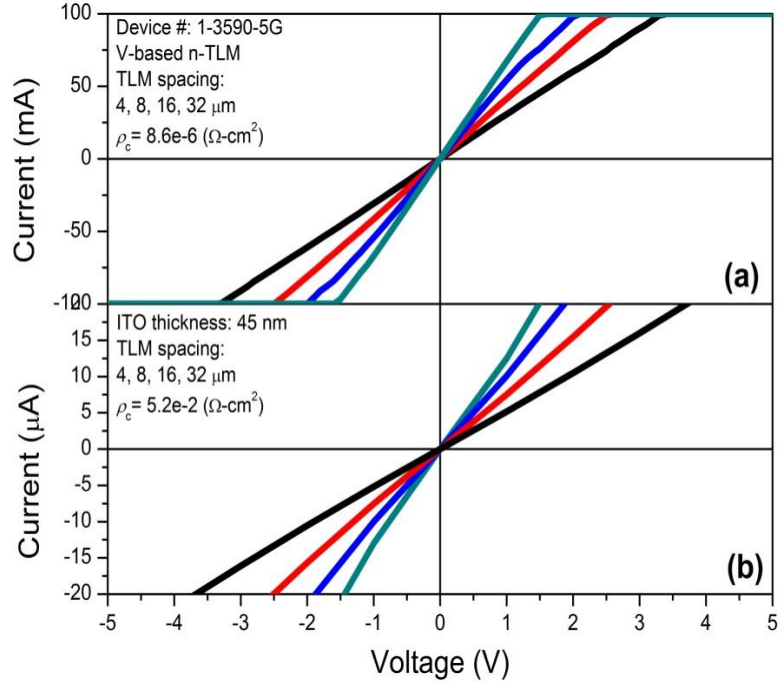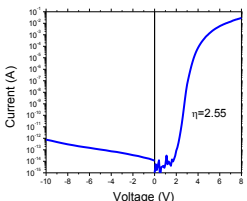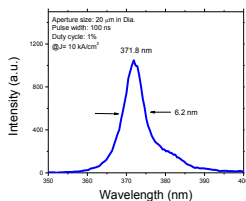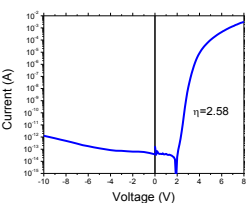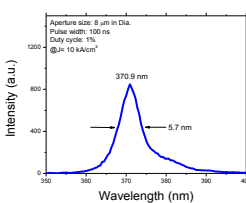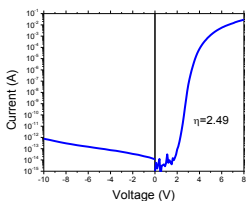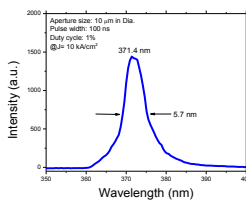
Figure 68. TLM results for (a) *n*-contact (top) and (b) *p*-contact (bottom).

I-V characteristics were performed using a Keithley 4200-SCS semiconductor parameter analyzer. The emission spectrum was collected by a 100 µm-diameter UV-grade fiber and fed into the spectrometer with a spectral resolution of 0.1 nm under the pulse operation. The pulse width is 1 µs and the duty cycle is fixed at 1 %. Table 8 summarizes the typical *I-V* and EL characteristics of fabricated RCLEDs with different aperture sizes. The turn-on voltage of the RCLED was about 4.2 V and the ideality factor is about 2.5. The full width at half maximum (FWHM) of the emission linewidth is between 5-7 nm as the driving current at 10 kA/cm^2. It is also noted that the FWHM of the devices is about 11 nm before the dielectric DBR deposition. The FWHM narrowing suggests a resonant cavity was formed after the dielectric DBR deposition. As the reflectivity of the top dielectric DBR is >99.9 % across a 1×1 cm^2 sample, the FWHM of RCLEDs is strongly affected by the reflectivity of bottom semiconductor DBRs. By

screening the fabricated RCLEDs, Figure 69 shows the best device performance on the same sample. As shown in Figure 69 (a), the serial resistance of the device is 95 Ω at 7 V and the maximum current density is >15 kA/cm^2. Figure 69 (b) and (c) show the emission spectra operating at different pulsed current densities from 2 kA/cm^2 to 15 kA/cm^2. As the injection current density increases, a single emission peak at ~371 nm becomes dominant with rapidly increasing intensity and narrowing linewidth. The variation of the emission linewidth and peak wavelength with increasing current is shown in Figure 69 (d). The FWHM of the emission linewidth decreased from 6 nm to 5.1 nm as the driving current was increased to 15 kA/cm^2. The corresponding cavity Q (= $\lambda/\Delta\lambda$) is estimated to be ~73. The emission peak wavelength was also invariant with increasing injection current density. These initial results provide a good basis for the further development of the GaN-based VCSELs.

Table 8. Typical *I-V* and EL characteristics of RCLEDs with different aperture sizes

Wafer ID	Aperture size (µm) in diameter	I-V curve	EL spectrum
1-3590-5F-B5C2	20	η=2.55	Aperture size: 20 µm in Dia. Pulse width: 100 ns Duty cycle: 1% @J= 10 kA/cm^2; 371.8 nm; 6.2 nm
1-3590-5F-B5A5	8	η=2.58	Aperture size: 8 µm in Dia. Pulse width: 100 ns Duty cycle: 1% @J= 10 kA/cm^2; 370.9 nm; 5.7 nm
1-3590-5F-B11A3	10	η=2.49	Aperture size: 10 µm in Dia. Pulse width: 100 ns Duty cycle: 1% @J= 10 kA/cm^2; 371.4 nm; 5.7 nm
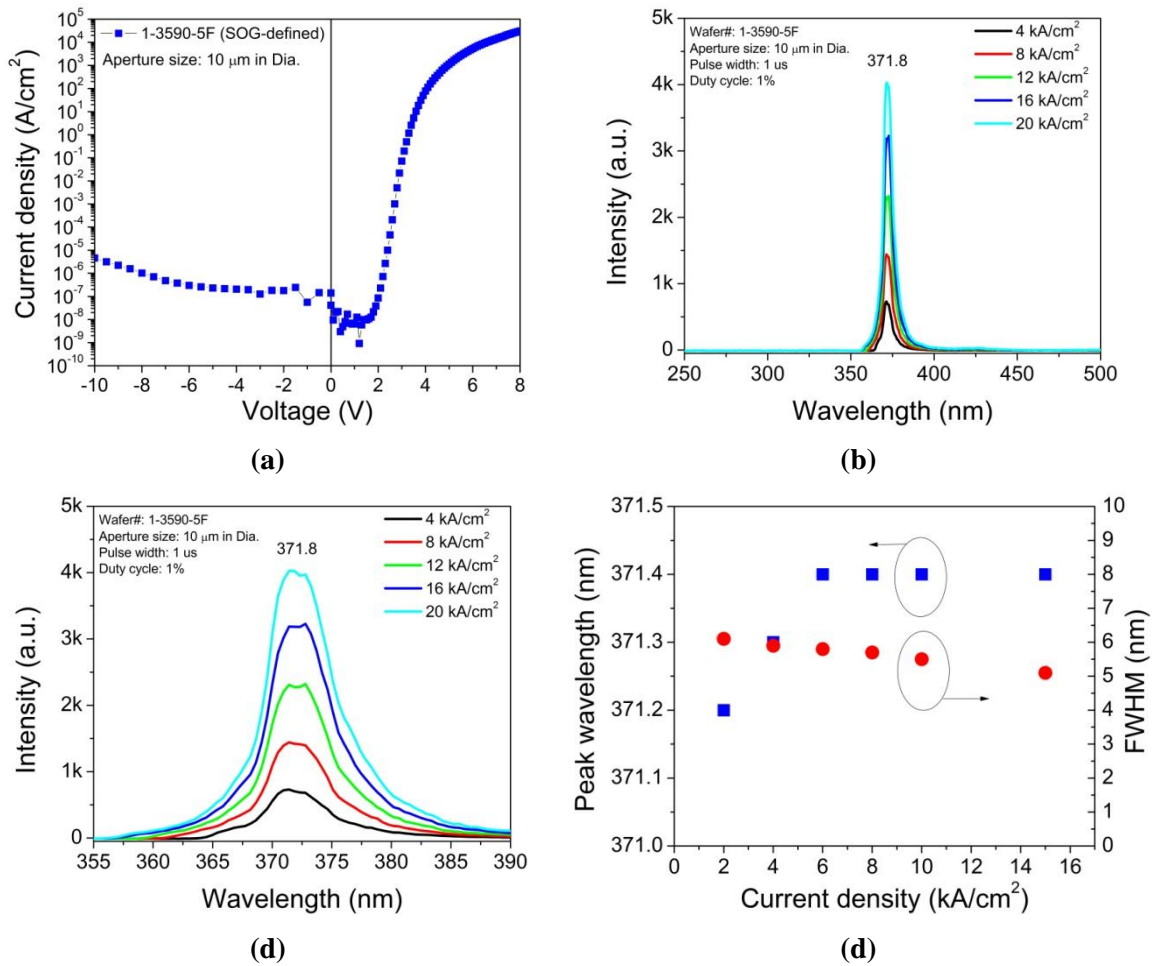
Figure 69. (a) *I-V* **characteristics of fabricated RCLED (wafer#: 1-3590-5F-B9C3). (b) and (c) Emission spectra as a function of pulsed current density. (d) Peak wavelength and FWHM as a function of pulsed current density of fabricated RCLEDs.**

3.4.5 Efficient current confinement technique using nitrogen ion implantation

Despite of demonstration of room temperature current injected GaN-based VCSELs [204-210,214-216], an efficient electrical confinement scheme was still of lack in these VCSEL structures, resulting in higher optical loss and difficulty in controlling the quality of output beams. The conventional method for fabricating the current blocking layer requires deposition of dielectric layers for insulation, which yields a non-planar surface and cannot effectively control the current flow inside the *p*-type region. The

135

selective oxidation has been realized on AlInN materials. However, a dramatic increase of the differential resistance is observed on oxidized LEDs [245,246]. In this work, we report the UV LEDs using Nitrogen ion implantation for current confinement. Employing Nitrogen ion implantation into p-$Al_{0.06}Ga_{0.94}N$ layer allows confining the injected current in a defined aperture without degrading the junction properties.

We performed a set of two-level designed experiments to study the current confinement using nitrogen implantation. Ion implantation energy and the dose along with the post-implantation annealing conditions were studied. The nitrogen implantation process was performed by a vendor. The chosen energy levels of nitrogen implantation were 20 KeV and 40 KeV. The ion doses of nitrogen species were 5E12 cm^{-2} and 5E13 cm^{-2}, respectively. The simulated distribution of implanted ions was performed in the TRIM software. As shown in Figure 70 (a) and (b), the peak depth is about 325 Å and 619 Å for the ion energy of 20 KeV and 40 KeV, respectively.

The UV LED samples used in this study have similar p-type, MQWs, and n-type regions to the 369-nm RCLED structure. The LED layer structure composed of 4 μm-thick GaN buffer layer, 30 nm-thick n-$Al_{0.06}Ga_{0.94}N$ waveguide, 3-pairs of $In_{0.03}Ga_{0.97}N$/$Al_{0.1}Ga_{0.9}N$ (3 nm/5 nm) MQWs, along with 98nm-thick p-$Al_{0.06}Ga_{0.94}N$ waveguide and 20 nm-thick p^+-$Al_{0.06}Ga_{0.94}N$ contact layer. The LEDs were fabricated to study the aperture forming and current confinement characteristics. Figure 71 shows the I-V curve of fabricated LED devices with a fixed current aperture of 10 μm in diameter, defined by either the SOG dielectric or nitrogen ion implantation. The inset of Figure 2 shows the schematics of nitrogen-implanted LEDs. It is shown that both on-state and off-state characteristics of the fabricated LEDs are similar between the devices using

previous SOG-based current aperture and the new devices using nitrogen-implanted current aperture. The turn-on voltages of these LEDs were about 4 V and the ideality factor is ~2.6. Maximum current density of > 20 kA/cm^2 and low leakage current density of < 1 μA/cm^2 were achieved on nitrogen-implanted LEDs. Figure 72 shows the microscope images of fabricated LEDs using different current confinement approaches. For fair comparison, the emission images of these devices were taken under the same current density of 100 A/cm^2. Clearly, nitrogen-implanted LEDs reveal the light emission is effectively confined in the defined aperture area. In contrast, the current spreading issues were observed, evidenced by the blurred emission edge, for the fabricated devices using the SOG as the current confinement. Furthermore, LEDs using ion-implanted current aperture with implantation energy of 40 KeV shows more distinct emission images compared to the ones implanted with 20 KeV. Figure 73 (a) and (b) show the series resistance as a function of current aperture (A) for nitrogen-implanted LEDs with implantation energy of 20 KeV or 40 KeV, respectively. It is evident that the resistance of nitrogen-implanted LEDs with an implantation energy of 40 KeV shows linear dependence with 1/A. On the other hand, the resistance of LEDs with implantation energy of 20 KeV shows non-linear dependence with the current aperture, especially for small aperture size. These results are in good agreement with the TRIM simulation, as most of the p-AlGaN layer is effectively highly resistive outside of the aperture region and less current spreading can be achieved. The current flow for LEDs with deep and shallow nitrogen implantation profiles are illustrated in the inset of Figure 73 (a) and (b), respectively. These results suggest the nitrogen-implantation with the ion energy of 40 KeV can effectively confine the current without degrading the junction properties. In

Figure 74, a constant current stressing test is performed by monitoring the change of the voltage on the nitrogen-implanted LED with implantation energy of 40 KeV. The voltage remains stable ($\Delta V < 0.1$ V) over a ten-hour constant current stressing at $J = 20$ kA/cm^2, indicating no significant device degradation during the current stressing.

In conclusion, we have demonstrated an efficient current confinement scheme in nitride-based LEDs by using a nitrogen ion implantation technique. Employing nitrogen ion implantation into p-Al$_{0.06}$Ga$_{0.94}$N layer effectively confines the injected current in a defined aperture without inducing excessive recombination centers. The nitrogen-implanted LEDs show a maximum current density of >20 kA/cm^2 with a stable electrical characteristics over a ten-hour constant current stressing. These results suggest the current confinement using nitrogen ion implantation provide a suitable electrical injection design for VCSEL fabrication.

(a)   (b)
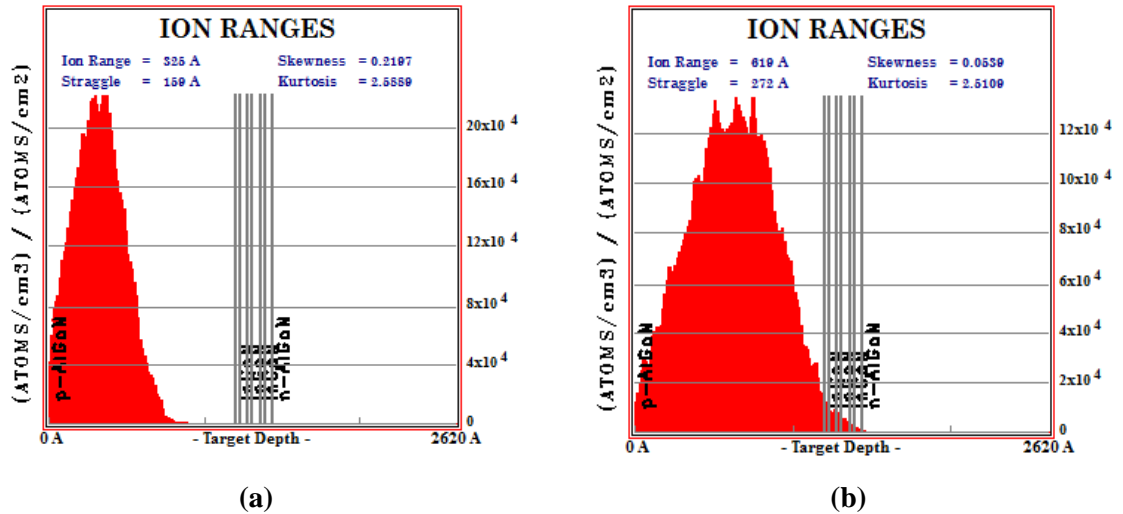
Figure 70. The TRIM simulation of nitrogen ion implantation with the ion energy of (a) 20 KeV and (b) 40 KeV. The layer structure in the simulation is the same as the UVLED layer structure used in the ion implantation study.
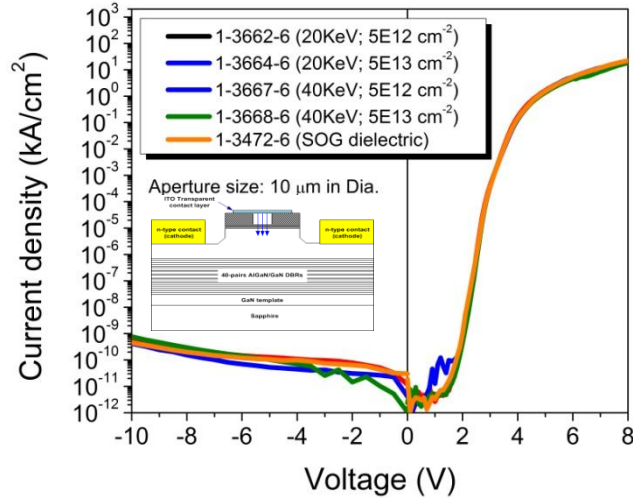
Figure 71. The *I-V* characteristics of nitrogen-implanted LED with different implantation conditions and the LED using SOG dielectric for aperture definition.

(a) (b) (c) (d) (e)
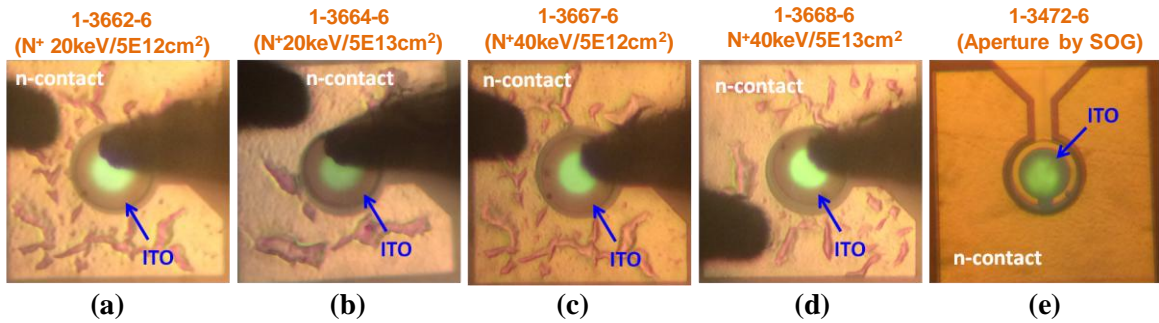
Figure 72. The emission images of fabricated LEDs at 100 A/cm^2 using different current confinement approaches: nitrogen ion implantation with ion energy and ion dose of (a) 20 KeV and 5E12 cm^{-2} (b) 20 KeV and 5E13 cm^{-2} (c) 40 KeV and 5E12 cm^{-2} (d) 40 KeV and 5E13 cm^{-2} (e) current confinement defined by SOG dielectric.

(a) (b)
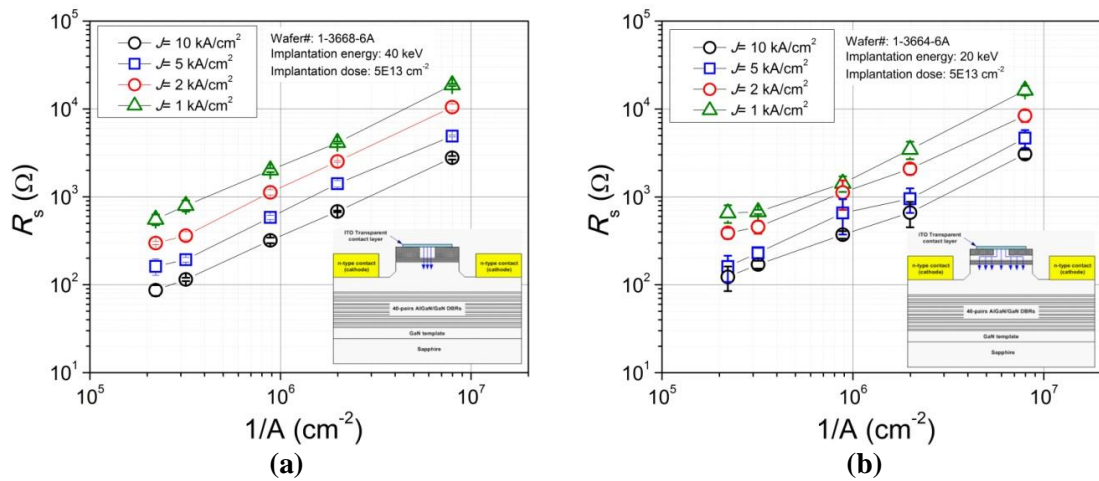
Figure 73. (a) The series resistance as a function of aperture size (A) for LEDs with the nitrogen ion implantation enegy of (a) 40 KeV and (b) 20 KeV.

139
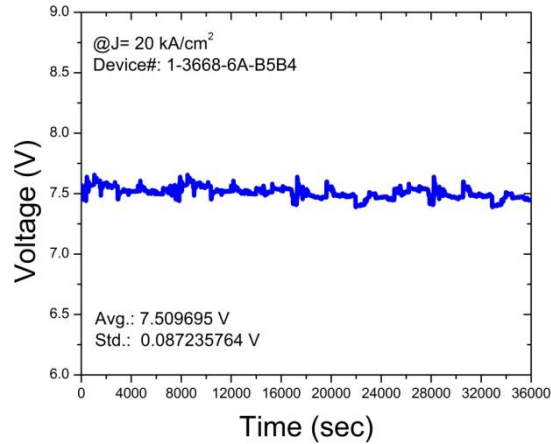
Figure 74. The time evolution of the measured voltage on a nitrogen-implanted LED biased at 20 kA/cm^2. The nitrogen-implanted LED has implantation energy of 40 KeV and ion dose of 5E13 cm^{-2} (wafer#: 1-3668-6A-B5B4).

3.4.6 Nitrogen-implanted resonant-cavity light-emitting diodes

The fabircation of implanted-RCLEDs started with the definition of current aperture. 2000 Å -thick Nickel mask was used to protect the emission aperture before the nitrogen ion implantation. The nitrogen implantation energy was chosen as 35 KeV and the ion doses of nitrogen species was 5E13 cm^{-2}. The simulated distribution of implanted ions (Figure 75) ensure the nitrogen ions didn't penetrate into the active region and the peak depth is about 482 Å for the ion energy of 35 KeV. After mesa etching using optimized ICP recipe, an identical ultraviolet PEC sidewall etching process was performed to ensure smooth sidewall formation. Next, vanadium-based (V/Al/Ti/Au) *n*-type ohmic contact was formed by E-beam evaporation. Instead of conventional nickel-based *p*-type ohmic metal, a 45nm-thick ITO transparent contact was used in this case to enhance lateral current spreading. A ten-pair HfO_2/SiO_2 dielectric DBRs were then evaporated on the ITO contact. Surface passivation with SOG and Metal-1 evaporation concluded the device processing. The schematic cross-sectional view and SEM images of fabricated RCLEDs are shown in Figure 76 (a) and (b), respectively.

140

Figure 75. The TRIM simulation of nitrogen ion implantation with the ion energy of 35 KeV. The layer structure in the simulation is the same as the RCLED layer structure.

| (a) | (b) |

Figure 76. (a) A schematic cross-sectional view of the nitrogen-implanted RCLED employing 40-pairs Al$_{0.12}$Ga$_{0.88}$N/GaN DBRs and 10-pairs HfO$_2$/SiO$_2$ DBRs. (b) The SEM images of implanted-RCLEDs.

After screening the fabricated devices, Figure 69 shows the best device performance on the nitrogen implanted-RCLEDs. As shown in Figure 77 (a), the serial resistance of the device is 80 Ω at 7 V and the maximum current density is >20 kA/cm^2. It is also noted the leakage current density at -10 V is about three times lower than that of RCLEDs using SOG for current confinement. Figure 77 (b) shows the emission spectra operating at different pulsed current densities from 5 kA/cm^2 to 20 kA/cm^2. The emission peak is located at 369.8 nm and the FWHM is about 9.6 nm at 5 kA/cm^2. However, the FWHM doesn't decrease as the driving current was increased to 20 kA/cm^2. This wide

141

FWHM value could be attributed to the lower optical reflectivity of the semiconductor bottom DBRs. The corresponding cavity Q (= $\lambda/\Delta\lambda$) is estimated to be ~38.
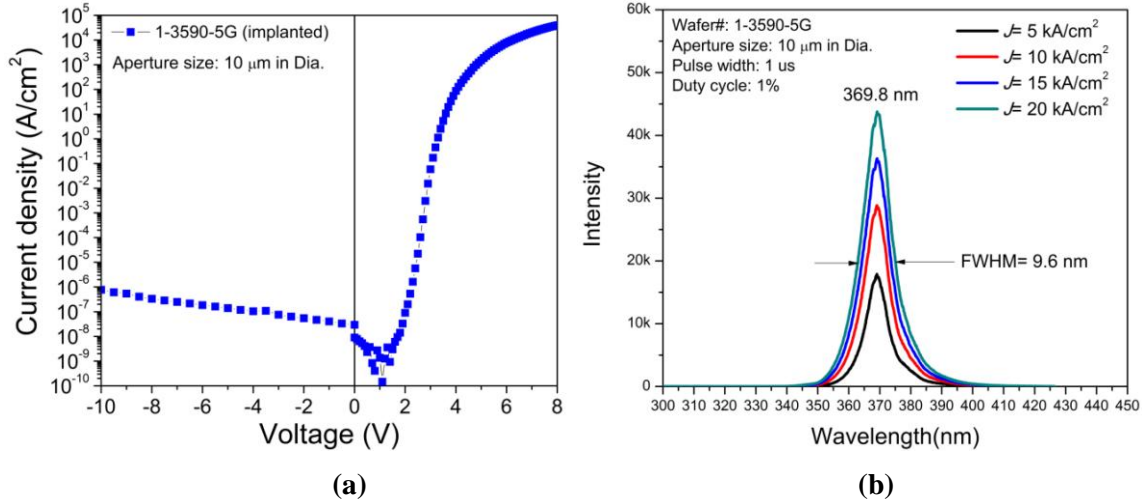
Figure 77. (a) *I-V* **characteristics of a nitrogen implanted-RCLED (wafer#: 1-3590-5G-B10B3). (b) Emission spectra as a function of pulsed current density.**

In conclusion, high reflectivity ($R>$ 99 %) and wide stop-band (> 60 nm) distributed Bragg reflectors (DBRs) were achieved at GT by using a small number of HfO_2/SiO_2 pairs to provide substantial optical feedback. Also, the lapping/polishing/cleaving processes of AlN and GaN substrates were developed and exercised multiple times to ensure high-quality mirror-like facets can be formed to create effective cavities. To realize electrically-drive UV light emitters, we first developed V-based ohmic contact on Al-rich *n*-AlGaN films using the transfer length measurement (TLM) and x-ray photoemission spectroscopy. The V-based ohmic contact shows lower contact resistance, smoother surface morphology, and lower annealing temperature when compared to the Ti-based ohmic contact. With the formation of the nitrogen-vanadium bond after the thermal annealing, the N:1*s* core-level peak at the V-$Al_{0.55}Ga_{0.45}N$ interface was shifted by 0.7 eV toward the higher binding energy. The interface states help the surface pinning of the Fermi level that

further facilitates the current conduction for the *n*-type AlGaN ohmic contact. The data demonstrated that the use of V as the first layer of the *n*-type ohmic contact for Al-rich *n*-AlGaN could be a better choice of ohmic contact metal than the conventional Ti/Al-based ohmic contact.

With the developed process recipes, we have demonstrated a sub-250 nm optically pumped deep-ultraviolet laser using an $Al_xGa_{1-x}N$-based multi-quantum-well structure grown on a bulk Al-polar *c*-plane AlN substrate. TE-polarization-dominant lasing action was observed at room temperature with a threshold pumping power density of 250 kW/cm^2. After employing high-reflectivity SiO_2/HfO_2 dielectric mirrors on both facets, the threshold pumping power density was further reduced to 180 kW/cm^2. The internal loss and threshold modal gain can be calculated to be 2 cm^{-1} and 10.9 cm^{-1}, respectively.

The achievements in the optical pumping experiments demonstrated the basic optical properties of these wide-bandgap ternary multiple-quantum-well (MQW) heterostructures. However, the demonstration of electrically-pumped UV laser diodes is still challenging and requires further processing recipe improvement. At Georgia Tech, we have established baseline processing flow and repeatable processing modules for AlGaN-based device frontside processing, including a photo-enhanced surface treatment to remove post-dry-etching-induced surface damage, Vanadium (V)-based *n*-type ohmic contact for Al-rich *n*-AlGaN, indium tin-oxide (ITO) transparent contact, and a high reflectance (HR) facet coating using HfO_2/SiO_2 alternative pairs. We also studied and developed repeatable back-side processing modules including wafer lapping and polishing steps for devices grown on AlN and GaN substrates, *m*-

plane facet cleaving, and device packaging. These processing modules in these development efforts will be directly transferred to the UV laser device development for processing integration. These pre-existing processing modules also helped formulate focused research subtasks for the device development. With these developed processing, we have fabricated a high-aluminum-containing ([Al]~ 0.6) AlGaN MQW light emitter employing an inverse-tapered-composition AlGaN:Mg p-type waveguide. The fabricated UV emitter can sustain a d.c. current of at least 10 kA/cm^2 and a pulsed current of at least 18 kA/cm^2 with the measured series resistance of 15 Ω and 11 Ω, respectively. We also established the processing modules for an UV vertical-cavity surface emitting lasers (VCSELs). Currently, resonant-cavity light-emitting diodes (RCLEDs) employing 40-pair GaN/AlGaN DBRs (R= 91%) and 10-pair HfO$_2$/SiO$_2$ high-reflectivity dielectric DBRs (R >99 %) were successfully fabricated. The device shows a dominant emission peak at 370 nm with a linewidth of 5.2 nm at a driving current density of 10 kA/cm^2. In addition, we further developed an efficient current confinement design using nitrogen ion implantation. Employing nitrogen ion implantation into p-Al$_{0.06}$Ga$_{0.94}$N layer effectively confines the injected current in a defined aperture without inducing excessive recombination centers. The N$^+$-implanted LEDs show the maximum current density of 20 kA/cm^2 and stable electrical characteristics over ten-hour constant current stressing. These results suggest the current confinement using nitrogen ion implantation provide a suitable electrical injection design for VCSEL fabrication. The possibility of an UV VCSEL could be realized by future optimization of higher DBR reflectivities, lower resistive heating and better lateral mode confinement.

CHAPTER 5

SUMMARY AND FUTURE WORK

During the course of this research work, III-N bipolar devices have been intensively studied and developed to achieve better device performance and reliability. High-voltage III-N bipolar devices for high-power switching applications and high-frequency III-N MMICs for microwave signal amplification have been announced and commercially available. With the progress and development of III-N bipolar devices, the market of III-N electronics is expected to grow rapidly in the next decade. However, Compared to silicon and III-V technologies, III-N technology is still relatively immature due to many technical challenges in material growth and device fabrication processes. Therefore, the purpose of this research work is aimed to develop and characterize the device performance for GaN homojunction *p-i-n* rectifiers, GaN/InGaN *npn* HBTs and phototransistors, and UV light emitters. The knowledge gained from the research work not only indicates the great potential of III-N bipolar devices but also provides more insight for further improvement on III-N bipolar devices fabrication processes.

In this study, high-performance GaN homojunction *p-i-n* rectifiers were developed and studied at Georgia Tech. The *p*-GaN ledge design and SOG passivation were developed and incorporated in the device fabrication to improve device performance. We first present a comparative study of GaN homojunction *p-i-n* rectifiers grown on either FS-GaN or sapphire substrate. The *p-i-n* rectifier grown on sapphire shows a V_B of 600 V and $R_{ON}A$ of 0.66 mΩ-cm^2. On the other hand, a *p-i-n* rectifier grown on a FS-GaN substrate shows substantial improvement with $V_B > 800$ V and $R_{ON}A$ = 0.28 mΩ-cm^2. The corresponding Baliga's Figure of Merit (BFOM) of >2.5 GW/cm^2 is

achieved. The device performance follows the same trend for GaN switches and demonstrated the lowest on-resistance for 800-V diode switches reported to date.

Furthermore, we study the temperature-dependent *I-V* and *C-V* characteristics of a GaN *p-i-n* rectifier grown on a FS-GaN substrate. The *C-V* data shows the free-carrier concentration of the drift layer is 1.3×10^{16} cm^{-3} at *T*= 298 K and increases to 2.0×10^{16} cm^{-3} at 448 K. *I-V* results show a low $R_{ON}A$ of 0.28 mΩ-cm^2 at 298 K and increases slightly (by <10 %) at 448 K. By performing OCVD measurement under high-level injection, τ_a can be extracted to be 9.6 ns at 298 K and increases to 22 ns at 448 K. The reverse *I-V* measurements reveal that the leakage current up to –200 V can be mainly attributed to a field-assisted ionization process from deep-level traps. These results can be well explained by the Poole-Frenkel effect and the corresponding Poole-Frenkel coefficient of 3.1×10^{-4} eV·V$^{-1/2}$·cm$^{-1/2}$ is obtained.

Although the fabricated GaN *p-i-n* rectifiers show the lower on-resistance for 800-V diode switches reported to date, the device performance can be further improved. The on-resistance can be further reduced by thinning FS-GaN substrate using the developed GaN lapping/polishing processing at GT. Besides, the remaining *p*-GaN ledge thickness and optimized field plate design have to be carefully studied to reduce the leakage current and increase the breakdown voltage. On the other hand, although SOG dielectric has been demonstrated as stable passivation layer, other dielectrics, such as SiN$_x$ and Al$_2$O$_3$, have been shown as an effective passivation layer in III-N devices. More studies on the choice of passivation layer and other dielectrics should be conducted to explore a better passivation solution for GaN *p-i-n* rectifiers.

III-N HBTs are promising devices for the next-generation RF and power electronics because of their advantages of high breakdown voltages, high power handling capability, high-temperature and harsh-environment operation stability. The radiative recombination processes in direct bandgap semiconductors provide an approach to understand the carrier transport and photon-electron interactions in transistors. We conduct an EL study on *npn* GaN/InGaN HBTs by operating HBTs under different biasing conditions. Three radiative recombination paths are resolved in HBTs, corresponding to the band-to-band transition (3.3 eV), conduction-band-to-acceptor-level transition (3.15 eV) and YL with the emission peak at 2.2 eV. The band-to-band and the conduction-band-to-acceptor-level transitions mostly arise from the intrinsic base region, while a defect-related YL band could likely originate from the quasi-neutral base region of a GaN/InGaN HBT. The I_B-dependent EL intensities for these three recombination paths are discussed. The results also show the radiative emission under the forward-active transistor mode operation is more effective than that using a diode-based emitter due to the enhanced excess electron concentration in the base region as increasing the collector current increases. The study of the EL emission spectrum provides a method to help resolve the carrier recombination paths in III-N HBTs for further transistor performance improvement in conventional HBT power amplification.

By illuminating UV photons from the backside of a GaN/InGaN *npn* HBT under an open-base configuration, R_λ of >1 A/W was measured for the device operating at V_{CE} <15 V in the phototransistor mode. As V_{CE} increases, the carrier multiplication in the reversed biased collector leads to a photocurrent avalanche and a high-R_λ of > 300 A/W is achieved at V_{CE}= 140 V. This is the first demonstration of

III-N APT and an open-base HBT under the UV illumination serves as proof-of-concept that the light absorbed in the InGaN base induces the photocurrent amplification.

On the other hand, the use of III-N materials allows for high-performance UV PDs due to the inherently high UV-to-visible-band rejection ratio, ultra-low dark current, and high-temperature operation. By taking advantage of the inherent current gain and the active mode operation, we demonstrated a high-responsivity GaN/InGaN HPT that can operate in both open-base phototransistor mode and the avalanche phototransistor mode for NUV-to-DUV photodetection applications. The substrate-side illuminated HPT shows a peak R_λ of 1 A/W at $\lambda=$ 373 nm, the bandgap wavelength of the $In_{0.03}Ga_{0.97}N$ base layer, and the relatively narrow spectral response due to the absorption of high-energy UV photon from the underlying GaN materials. Under the front-side illumination, the HPT shows a wide-band photoresponse spectrum with the short-wavelength cut-off wavelength well beyond $\lambda=$ 280 nm. The HPT exhibits a high UV-to-visible-band rejection ratio ($R_\lambda|_{360nm}/ R_\lambda|_{450nm}$) greater than 8×10^3. At low voltage bias ($V_{CE}<$ 10 V), R_λ is 8.2 A/W for $P_{opt}=$ 13.7 µW/cm^2 at $\lambda=$ 373 nm and R_λ is 3.4 A/W for $P_{opt}=$ 1.31 µW/cm^2 at $\lambda=$ 280 nm. At high V_{CE} (> 35 V), the responsivity performance was enhanced as the device was biased in the APT mode, resulting in R_λ >100 A/W at $V_{CE}=$ 40 V for $P_{opt}=$ 1.73 µW/cm^2 at $\lambda=$ 373 nm. The results demonstrate the feasibility of using III-N HPTs as a new form of ultra-low light detection in the entire UV spectral regions.

The future work for the GaN/InGaN HPT research is to study the optical modulation and noise performance. Although III-N HPTs have demonstrated their

feasibility for ultra-low light detection, it is thought that the HPT may come at a cost of noisy operation due to concurrent amplification of the leakage current and the photocurrent under high electric fields. The major issue may be from the layer structure design. Due to the background doping, the collector region is slightly n-doped, resulting in a non-uniform (triangle shape) electrical field distribution. Therefore, the avalanche breakdown more easily happens near the p-InGaN region, and the impact ionization may not be strong enough to support high optical avalanche gain elsewhere in the whole depletion region. Further study will be on the novel device layer structure design for improved electrical-field uniformity in the collector region.

III-N-based optoelectronic devices have been actively studied and developed due to a wide range in bandgap energy, which covers the full spectrum of optical emission from the near-infrared to DUV. However, the development of DUV light emitters has been challenging because of the difficulty in achieving high free-carrier concentrations in both p-type and n-type AlGaN layers with high aluminum mole fraction and high defect density arising from the lattice mismatch in epitaxial layers when these structures are grown on foreign substrates. At Georgia Tech, high reflectivity (R> 99 %) and wide stop-band (> 60 nm) DBRs were achieved by using a small number of HfO_2/SiO_2 pairs to provide substantial optical feedback. Also, the lapping/polishing/cleaving processes of AlN and GaN substrates were developed and exercised multiple times to ensure high-quality mirror-like facets can be formed to create high-Q cavities. With the developed process recipes, we have demonstrated a sub-250 nm optically pumped deep-ultraviolet laser using an $Al_xGa_{1-x}N$-based MQW

structure grown on a bulk Al-polar *c*-plane AlN substrate. TE-polarization-dominant lasing action was observed at room temperature with a threshold pumping power density of 250 kW/cm^2. After employing high-reflectivity SiO$_2$/HfO$_2$ dielectric mirrors on both facets, the threshold pumping power density was further reduced to 180 kW/cm^2. The internal loss and threshold modal gain can be calculated to be 2 cm^{-1} and 10.9 cm^{-1}, respectively.

The achievements in the optical pumping experiments demonstrated the basic optical properties of these wide-bandgap ternary MQW heterostructures. However, the demonstration of electrically-pumped UV laser diodes is still challenging and requires further processing recipe improvement. At Georgia Tech, we have established baseline processing flow and repeatable processing modules for AlGaN-based device frontside processing, including a photo-enhanced surface treatment to remove post-dry-etching-induced surface damage, V-based *n*-type ohmic contact for Al-rich *n*-AlGaN, ITO transparent contact, and a HR facet coating using HfO$_2$/SiO$_2$ alternative pairs. We also studied and developed repeatable back-side processing modules including wafer lapping and polishing steps for devices grown on AlN and GaN substrates, *m*-plane facet cleaving, and device packaging. These processing modules in these development efforts will be directly transferred to the UV laser device development for processing integration. These pre-existing processing modules also helped formulate focused research subtasks for the device development. With these developed processing, we have fabricated a high-aluminum-containing ([Al]~ 0.6) AlGaN MQW light emitter employing an inverse-tapered-composition AlGaN:Mg *p*-type waveguide. The

fabricated UV emitter can sustain a d.c. current of > 10 kA/cm^2 and a pulsed current of at least 18 kA/cm^2 with the measured series resistance of 15 Ω and 11 Ω, respectively.

We have also focused on the development of individual processing modules that are critical for the UV VCSEL demonstration. Several device implementation approaches were investigated and down-selected during this period. Based on the study of the most feasible device implementation approaches, we also design a new set of photomasks that can be used for the fabrication of high-quality 369-nm VCSELs. The processing modules for UV VCSELs including V-based ohmic contact, optimized dry etching recipe, high-reflectivity HfO$_2$/SiO$_2$ DBRs and ITO transparent contact layer have been established and individually exercised multiple times. By integrating all developed process recipes, RCLEDs employing 40-pair GaN/AlGaN DBRs and 10-pair HfO$_2$/SiO$_2$ dielectric DBR were successfully fabricated. The device shows a dominant emission peak at 370 nm with a linewidth of 5.2 nm at a driving current density of 10 kA/cm^2. In addition, we further developed an efficient current confinement design using nitrogen ion implantation. Employing N$^+$ ion implantation into p-Al$_{0.06}$Ga$_{0.94}$N layer effectively confines the injected current in a defined aperture without inducing excessive recombination centers. The nitrogen-implanted LEDs show the maximum current density of 20 kA/cm^2 and stable electrical characteristics over ten-hour constant current stressing. These results suggest the current confinement using nitrogen ion implantation provide a suitable electrical injection design for VCSEL fabrication.

Therefore, the next goal of the research will be focused on the realization of current-injected UV VCSELs. The nitrogen ion implantation will be incorporated in

the device fabrication for efficient current confinement. Future research will be mainly on the epitaxial material growth optimization on either *c*-plane FS-GaN or AlN substrates. Since it is a challenge to grow high-reflectivity semiconductor DBRs for UV VCSELs, the risk-mitigation approach to the hybrid mirror approach is to create the double-side dielectric DBR structure. The original plan was to create a deeply recessed via hole on the back side of the low-defect free-standing GaN substrate and to use an etch-stop AlN layer to provide a precision cavity control of the VCSEL for the subsequent backside dielectric DBR deposition. The device measurement will be also improved using an ultra-short pulsed current source for electrically-pumped VCSEL demonstration.

REFERENCES

[1]   http://www.ioffe.rssi.ru/SVA/NSM/Semicond/GaN/index.html.

[2]   http://www.ioffe.rssi.ru/SVA/NSM/Semicond/AlN/index.html.

[3]   http://www.ioffe.rssi.ru/SVA/NSM/Semicond/InN/index.html.

[4]   S. M. Sze and K. K. NG, Physics of Semiconductor Devices, 3rd ed. (Wiley-Interscience, Hoboken, N.J., 2007).

[5]   C.-M. Zetterling, Ed.,"Process technology for silicon carbide devices," in EMIS processing series, *IEE*, 2002.

[6]   H. Amano, N. Sawaki, I. Akasaki and Y. Toyoda, "Metalorganic vapor phase epitaxial growth of a high quality GaN film using an AlN buffer layer," *Appl. Phys. Lett.*, vol. 48, p. 353, 1986.

[7]   V. Kumar, A. Kuliev, T. Tanaka, Y. Otoki, and I. Adesida, "High transconductance enhancement-mode AlGaN/GaN HEMTs on SiC substrate," *Electron. Lett.*, vol. 39, pp 1758-60, Nov. 2003.

[8]   W. Lanford, T. Tanaka, Y. Otoki, and I. Adesida, "Recessed-gate enhancement-mode GaN HEMT with high threshold voltage," *Electron. Lett.*, vol. 41, no. 7, pp. 449-50, March 2005.

[9]   S. Maroldt, C. Haupt, W. Pletschen, S. Mu¨ller, R. Quay,O. Ambacher,C. Schippel, and F. Schwierz, "Gate-Recessed AlGaN/GaN Based Enhancement-Mode High Electron Mobility Transistors for High Frequency Operation," *Jpn. J. Appl. Phys.*, vol. 48, no. 4, pp. 04C083, April 2009.

[10]   W. Lim, J.-H. Jeong, H.-B Lee, J.-H. Lee, S.-B. Hur, J.-K. Ryu, K.-S. Kim, T.-H. Kim, S. Y. Song, W.-G. Hur, S. T. Kim, and S. J. Pearton, "Normally-off operation of recessed-gate AlGaN/GaN HFETs for high power applications," *Electrochem. Solid-State Lett.*, vol. 14, no. 5 pp. H205-H207, 2011.

[11]   Z. Mouffak, A. Bensaoula, and L. Trombetta, "The effects of nitrogen plasma on reactive-ion etching induced damage in GaN," *J. Appl. Phys.,* vol. 95, no. 2, pp. 727, Jan 2004.

[12]   M. Kato, K. Mikamo, M. Ichimura, M. Kanechika, O. Ishiguro, and T. Kachi, "Characterization of plasma etching damage on p-type GaN using Schottky diodes," *J. Appl. Phys.,* vol. 103, pp. 093701, 2008.

[13]   M. Tajima, J. Kotani, and T. Hashizume, "Effects of Surface Oxidation of AlGaN on d.c. Characteristics of AlGaN/GaN High-Electron-Mobility Transistors," *Jpn. J. Appl. Phys.,* vol. 48, pp. 020203, 2009.

[14]   S. T. Bradley, S. H. Goss, L. J. Brillson, J. Hwang, and W. J. Schaff, "Deep level defects and doping in high Al mole fraction AlGaN," *J. Vac. Sci. Technol. B,* vol. 21, pp. 2558, 2003.

[15]   B. Yang and P. Fay, "Etch rate and surface morphology control in photoelectrochemical etching of GaN," *J. Vac. Sci. Technol. B*, vol. 22, no. 4, pp. 1750-1754, July 2004.

[16]   C. Youtsey, T. Romano, and I. Adesida, "Gallium nitride whiskers formed by selective photoenhanced wet etching of dislocations," *Appl. Phys. Lett.*, vol. 73, no. 6, pp. 797-9, Aug. 1998.

[17] J. A. Bardwell, J. B. Webb, H. Tang, J. Fraser, and S. Moisa, "Ultraviolet photoenhanced wet etching of GaN in $K_2S_2O_8$ solution," *J. Appl. Phys.*, vol. 89, no. 7, pp. 4142-9, April 2001.

[18] Z. Fan, S. N. Mohammad, W. Kim, O. Aktas, A. E. Botchkarev, and H. Morkoc, "Very low resistance multilayer Ohmic contact to n-GaN," *Appl. Phys. Lett.*, vol. 68, pp. 1672, 1996.

[19] A. Motayed, R. Bathe, M. C. Wood, O. S. Diouf, R. D. Vispute, and S. N. Mohammad, "Electrical, thermal, and microstructural characteristics of Ti/Al/Ti/Au multilayer ohmic contact to n-type GaN,*" J. Appl. Phys.*, vol. 93, pp. 1087, 2003.

[20] H. K. Cho, T. Hossain, J. W. Bae, and I. Adesida, "Characterization of Pd/Ni/Au ohmic contact on p-GaN," *Solid-State Electron.*, vol. 49, pp. 774-778, 2005.

[21] J. K. Kim, J.-L. Lee, J. W. Lee, H. E. Shin, Y. J. Park, and T. Kim," Low resistance Pd/Au ohmic contact to p-type GaN using surface treatment," *Appl. Phys. Lett.,* vol. 73, No 20, Nov 1998.

[22] Isik C. Kizilyalli, Andrew P. Edwards, Hui Nie, Don Disney, and Dave Bour, "High voltage vertical GaN p-n diodes with avalanche capability," *IEEE Trans. Electron Devices.*, vol. 60, no. 10, pp. 3067–3070, Oct. 2013.

[23] Y. Hatakeyama, K. Nomoto, N. Kaneda, T. Kawano, T. Mishima, and T. Nakamura, "Over 3.0 GW/cm^2 figure-of-merit GaN p-n junction diodes on free-standing GaN substrates," *IEEE Electron Device Lett.*, vol. 32, no. 12, pp. 1674–1676, Dec. 2011.

[24] Y. Hatakeyama, K. Nomoto, A. Terano, N. Kaneda, T. Tadayoshi, T. Mishima, and T. Nakamura, "High-Breakdown-Voltage and Low Specific on Resistance GaN p–n junction diodes on free-Standing GaN substrates fabricated through low-damage field-plate process," *Jpn. J. Appl. Phys.*, vol. 52, pp. 028007, Jan. 2013.

[25] T. G. Zhu, D. J. H. Lambert, B. S. Shelton, M. M. Wong, U. Chowdhury, H. K. Kwon, and R. D. Dupuis, "High-voltage GaN pin vertical rectifiers with 2 μm thick i-layer," *Electron. Lett.*, vol. 36, no. 23, pp. 1971–1972,Nov. 2000.

[26] J. B. Limb, D. Yoo, J. H. Ryou, S. C. Shen, and R. D. Dupuis, "Low on-resistance GaN pin rectifiers grown on 6H-SiC substrates," *Electron. Lett.*, vol. 43, no. 6, pp. 67–68, Mar. 2007.

[27] X. A. Cao, H. Lu, S. F. LeBoeuf, C. Cowen, S. D. Arthur, and W. Wang, "High voltage vertical GaN p-n diodes with avalanche capability," *Appl. Phys. Lett.*, vol. 87, 053503, July 2005.

[28] Kazuki Nomoto, Bo Song, Zongyang Hu, Mingda Zhu, Meng Qi, Naoki Kaneda, Tomoyoshi Mishima, Tohru Nakamura, Debdeep Jena, and Huili Grace Xing, "1.7-kV and 0.55-mΩ·cm2 GaN p-n Diodes on Bulk GaN Substrates With Avalanche Capability," *IEEE Electron Device Lett.*, vol. 37, no. 2, pp. 161–164, Feb. 2016.

[29] Jeramy R. Dickerson, Andrew A. Allerman, Benjamin N. Bryant, Arthur J. Fischer, Michael P. King, Michael W. Moseley, Andrew M. Armstrong, Robert J. Kaplar, Isik C. Kizilyalli, Ozgur Aktas, and Jonathan J. Wierer, Jr., "Vertical GaN

Power Diodes With a Bilayer Edge Termination," *IEEE Trans. Electron Devices*, vol. 63, no. 1, pp. 419–425, Jan. 2016.

[30]   Y. Saitoh, K. Sumiyoshi, M. Okada, T. Horii, T. Miyazaki, H. Shiomi, M. Ueno, K. Katayama, M. Kiyama, and T. Nakamura, "Extremely low on-resistance and high breakdown voltage observed in vertical GaN Schottky barrier diodes with high-mobility drift layers on low dislocation-density GaN substrates," *Appl. Phys. Exp.*, vol. 3, no. 8, pp.081001-3, Jul. 2010.

[31]   G. Y. Lee, H. H. Liu, and J. I. Chyi, "High-performance GaN pin rectifiers grown on free-standing GaN substrates," *IEEE Electron Device Lett.*, vol. 32, no. 11, pp. 1519–1521, Nov. 2011.

[32]   J. H. Lee, J. K. Yoo, H. S. Kang, and J. H. Lee, "840 V/6 A-AlGaN/GaN Schottky barrier diode with bonding pad over active structure prepared on sapphire substrate," *IEEE Electron Device Lett.*, vol. 33, no. 8, pp. 1171–1173, Aug. 2012.

[33]   W. Chen, K. Y. Wong, W. Huang, and K. J. Chen, "High-performance AlGaN/GaN lateral field-effect rectifiers compatible with high electron mobility transistors," *Appl. Phys. Lett.*, vol. 92, pp. 253501, June 2008.

[34]   H. Ishida, D. Shibata, H. Matsuo, M. Yanagihara, Y. Uemoto, T. Ueda, T. Tanaka, and D. Ueda, "GaN-based natural super junction diodes with multi-channel structures," in *IEDM Tech. Dig.*, pp. 1–4, 2008.

[35]   M. K. Kelly, R. R. Vaudo, V. M. Phanse, L. Gorgens, O. A. Ambacher, and M. Stutzmann, "Large Free-Standing GaN Substrates by Hydride Vapor Phase Epitaxy and Laser-Induced Liftoff," *J. Appl. Phys.*, vol. 38, pp. L217-219, Feb. 2009.

[36]   J. B. Limb, D. Yoo, J. H. Ryou, W. Lee, S. C. Shen, and R. D. Dupuis, "High-performace GaN pin rectifiers grown on free-standing GaN substrates," *Electron. Lett.*, vol. 42, no. 22, pp. 1313–1314, Oct. 2006.

[37]   L. McCarthy, P. Kozodoy, M. Rodwell, S. Denbaars, and U. Mishra, "A first look at AlGaN/GaN HBTs," *Compd. Semicond.*, vol. 4, no. 8, pp. 16–18, Nov. 1998.

[38]   J. Han, A. Baca, R. Shul, C. Willison, L. Zhang, F. Ren, A. Zhang, G. Dang, S. Donovan, X. Cao, H. Cho, K. Jung, C. Abernathy, S. J. Pearton, and R. G. Wilson, "Growth and fabrication of GaN/AlGaN heterojunction bipolar transistor," *Appl. Phys. Lett.,* vol. 74, no. 18, pp. 2702-2704, May 1999.

[39]   J. J. Huang, M. Hattendorf, M. Feng, D. Lambert, B. Shelton, M. Wong, U. Chowdhury, T. Zhu, H. Kwon, and R. D. Dupuis, "Graded-emitter AlGaN/GaN heterojunction bipolar transistors," *IEEE Electron. Lett.,* vol. 36, no. 14, pp. 1239-1240, Apr. 2000.

[40]   X. Cao, G. Dang, A. Zhang, F. Ren, J. M. Van Hove, J. J. Klaassen, C. J. Polley, A. M. Wowchak, P. P. Chow, D. J. King, C. R. Abernathy, and S. J. Pearton, "High current, common-base GaN/AlGaN heterojunction bipolar transistors," *Electrochem. Solid-State Lett.,* vol. 3, no. 3, pp. 144-146, Jan. 2000.

[41]   H. G. Xing and U. K. Mishra,"Temperature dependent I-V characteristics of AlGaN/GaN HBTs and GaN BJTs," *Int. J. High Speed Electron. Syst.,* vol. 14, no. 3, pp. 819-824, Sep. 2004.

[42] H. G. Xing and U. K. Mishra, "Temperature dependent I-V characteristics of AlGaN/GaN HBTs and GaN BJTs," *Int. J. High Speed Electron. Syst.*, Vols. 14, no. 3, pp. 819-824, Sep. 2004.

[43] D. Keogh, P. Asbeck, T. Chung, J. Limb, D. Yoo, J.-H. Ryou, W. Lee, S. C. Shen and R. D. Dupuis, "High current gain GaN/InGaN HBTs with 300C operating temperature," *Electron. Lett.*, vol. 42, p. 661, 2006.

[44] A. Nishikawa, K. Kumakura and T. Makimoto, "Temperature dependence of current-voltage characteristics of npn-type GaN/InGaN double heterojunction bipolar transistors," *Appl. Phys. Lett.*, vol. 91, p. 133514, 2007.

[45] K. Kumakura, T. Makimoto and N. Kobayashi, "Low-resistance nonalloyed ohmic contact to p-type GaN using strained InGaN contact layer," *Appl. Phys. Lett.*, vol. 79, no. 16, pp. 2588-2590, Oct. 2001.

[46] T. Makimoto, K. Kumakura and N. Kobayashi, "High current gains obtained by GaN/InGaN double heterojunction bipolar transistors with *p*-InGaN base," *Appl. Phys. Lett.*, vol. 79, no. 3, pp. 380-381, 2001.

[47] K. P. Lee, A. P. Zhang, G. Dang, F. Ren, J. Han, S. N. G. Chu, W. S. Hobson, J. Lopata, C. R. Abernathy, S. J. Rearson, and J. W. Lee, "Self-aligned process for emitter- and base-regrowth GaN HBTs and BJTs," *Solid-State Electron.,* vol. 45, no. 2, pp. 243-247, 2001.

[48] T. Makimoto, K. Kumakura, and N. Kobayashi, "Extrinsic base regrowth of p-InGaN for Npn-type GaN/InGaN heterojunction bipolar transistors," *Jpn. J. Appl. Phys., Part 1,* vol. 43, no. 4B, pp. 1922-1924, Apr. 2004.

[49] T. Makimoto, K. Kumakura, and N. Kobayashi, "High current gain (2000) of GaN/InGaN double heterojunction bipolar transistors using base regrowth of *p*-InGaN," *Appl. Phys. Lett.,* vol. 83, pp. 1035-1037, Aug. 2003.

[50] L. S. McCarthy, P. Kozodoy, M. J. W. Rodwell, S. P. DenBaars, and U. K. Mishra, "AlGaN/GaN heterojunction bipolar transistor," *IEEE Electron Device Lett.,* vol. 20, no. 6, pp. 277-279, 1999.

[51] Y.-C. Lee, Y. Zhang, Z. Lochner, H.-J. Kim, J. H. Ryou, R. D. Dupuis, and S.-C. Shen, "Ultra-high-power characteristics of GaN/InGaN HBTs," in *2011 9th Int. Conf. Nitride Semicond., Glasgow*, UK, 2011

[52] S.-C. Shen, R. D. Dupuis, Y.-C. Lee, H.-J. Kim, Y. Zhang, Z. Lochner, P. D. Yoder, and J.-H. Ryou, "GaN/InGaN Heterojunction Bipolar Transistors with f_T > 5 GHz," *IEEE Electron Dev. Lett.*, vol. 32, no. 8, pp. 1065-1067, Aug. 2011.

[53] R. D. Dupuis, J. Kim, Y. C. Lee, Z. Lochner, T. Kao, M. H. Ji, T. T. Kao, J. H. Ryou, T. Detchphrom, and S. C. Shen, "III-N High-power bipolar transistors," *ECS Transactions*, vol. 58 (4), pp. 261, 2013.

[54] L. S. McCarthy, I. Smorchkova, P. Fini, M.J.W. Rodwell,J. Speck, S.P. DenBaars and U.K. Mishra, "Small signal RF performance of AIGaN/GaN heterojunction bipolar transistors," *Electron. Lett.,* vol. 38, no. 3, Jan. 2002.

[55] M. Feng, N. Holonyak, Jr., and W. Hafez, "Light-emitting transistor: Light emission from InGaP/GaAs heterojunction bipolar transistors," *Appl. Phys. Lett.*, vol. 84, pp. 151, 2004.

[56]   G. Walter, N. Holonyak, Jr., M. Feng, and R. Chan, "Laser operation of a heterojunction bipolar light-emitting transistor," *Appl. Phys. Lett.*, vol. 85, pp. 4768, 2004.

[57]   H. Then, M. Feng, N. Holonyak, Jr., C. Wu, "Experimental determination of the effective minority carrier lifetime in the operation of a quantum-well n-p-n heterojunction bipolar light-emitting transistor of varying base quantum-well design and doping," *Appl. Phys. Lett.*, vol. 91, pp. 033505, 2007.

[58]   B. F. Chu-Kung, M. Feng, G. Walter, N. Holonyak, T. Chung, "Graded-base InGaN∕GaN heterojunction bipolar light-emitting transistors," *Appl. Phys. Lett.*, vol. 89, pp. 082108, 2006.

[59]   B. F. Chu Kung, C. H. Wu, G. Walter, M. Feng, N. Holonyak, T. Chung, J. H. Ryou, and R. D. Dupuis, "Modulation of high current gain (β>49) light emitting InGaN∕GaN heterojunction bipolar transistors," *Appl. Phys. Lett.*, vol. 91, pp. 232114, 2007.

[60]   T. T. Kao, Y. C. Lee, H. J. Kim, J. H. Ryou, J. Kim, T. Detchprohm, R. D. Dupuis, and S. C. Shen, "Radiative Recombination in *npn* GaN/InGaN Heterojunction Bipolar Transistors," *Appl. Phys. Lett.*, vol. 107, pp. 242104, 2015.

[61]   S. C. Shen, T. T. Kao, H. J. Kim, Y. C. Lee, J. Kim, M. H. Ji, J. H. Ryou, T. Detchprohm, and R. D. Dupuis, "GaN/InGaN Avalanche Phototransistor," *Appl. Phys. Exp.*, vol. 8, no. 3, pp. 032101, 2015.

[62]   http://www.hamamatsu.com/jp/en/index.html

[63]   B. Yang, K. Heng, T. Li, C. Collins, S. Wang, R. D. Dupuis, J. C. Campbell, M. Schurman and I. Ferguson, "Low Dark Current GaN Avalanche Photodiodes," *IEEE J. Quantum Electron.*, vol. 36, pp. 1229, 2000.

[64]   Y. Zhang, S. -C. Shen, H. -J Kim, S. Choi, J. -H. Ryou, R. D. Dupuis, and B. Narayan, "Low-noise GaN ultraviolet p-i-n photodiodes on GaN substrates" *Appl. Phys. Lett.*, vol. 94, pp. 221109, 2009.

[65]   C. J. Collins, T. Li, D. J. H. Lambert, M. M. Wong, R. D. Dupuis, and J. C. Campbell, "Selective regrowth of $Al_{0.30}Ga_{0.70}N$ p–i–n photodiodes," *Appl. Phys. Lett.*, vol. 77, pp. 2810, 2000.

[66]   F. Xie, H. Lu, D. J. Chen, X. Q. Xiu, H. Zhao, R. Zhang, and Y. D. Zheng, "Metal–Semiconductor–Metal Ultraviolet Avalanche Photodiodes Fabricated on Bulk GaN Substrate," *IEEE Electron Device Lett.*, vol. 32, no. 9, pp. 1260–1262, Sep. 2011.

[67]   K. Lee, P. Chang, S. Chang and S. Wu, "InGaN Metal-Semiconductor-Metal Photodetectors with Aluminum Nitride Cap Layers," *IEEE J. Quantum Electron.*, vol. 47, pp. 1107, 2011.

[68]   S. -C. Shen, Y. Zhang, D. Yoo, J. -B. Limb, J. -H. Ryou, P. D. Yoder, and R. D. Dupuis, "Performance of Deep Ultraviolet GaN Avalanche Photodiodes Grown by MOCVD," *IEEE Photon. Technol. Lett.*, vol. 19, pp. 21, 2007.

[69]   S. Verghese, K. A. McIntosh, R. J. Molnar, L. J. Mahoney, R. L. Aggarwal, M. W. Geis, K. M. Molvar, E. K. Duerr, and I. Melngailis, "GaN avalanche photodiodes operating in linear-gain mode and Geiger mode," *IEEE Trans. Electron Devices*, vol. 48, pp. 502, 2001.

[70] R. A. Milano, T. H. Windhorn, E. R. Anderson, G. E. Stillman, R. D. Dupuis and P. D. Dapkus, "Al$_{0.5}$Ga$_{0.5}$As‐GaAs heterojunction phototransistors grown by metalorganic chemical vapor deposition," *Appl. Phys. Lett.*, vol. 34, pp. 562, 1979.

[71] J. C. Campbell, A. G. Dental, G. -J. Qua, and J. F. Ferguson, "Avalanche InP/InGaAs heterojunction phototransistor," *IEEE J. Quantum Electron.*, vol. 19, pp. 1134, 1983.

[72] F.-Y. Huang, and H. Morkoc, "GaAs/InGaAs/AlGaAs optoelectronic switch in avalanche heterojunction phototransistor vertically integrated with a resonant cavity," *Appl. Phys. Lett.*, vol. 64, vol. 405, 1994.

[73] J. C. Campbell, C. A. Burrus, A. G. Dentai, and K. Ogawa, "Small-area high-speed InP/InGaAs phototransistor," *Appl. Phys. Lett*., vol. 39, pp. 820, 1981.

[74] W. Yang, T. Nohava, S. Krishnankutty, R. Torreano, S. McPherson, and H. Marsh, "High gain GaN/AlGaN heterojunction phototransistor,"*Appl. Phys. Lett.,* vol. 73, pp. 978, 1998.

[75] R. Mouillet, A. Hirano, M. Iwaya, T. Detchprohm, H. Amano, and I. Akasaki, "Photoresponse and Defect Levels of AlGaN/GaN Heterobipolar Phototransistor Grown on Low-Temperature AlN Interlayer," *Jpn. J. Appl. Phys*, vol. 40, pp. L498, 2001.

[76] M. L. Lee, J. K. Sheu, and Y. -R. Shu, "Ultraviolet bandpass Al$_{0.17}$Ga$_{0.83}$N/GaN heterojunction phototransitors with high optical gain and high rejection ratio,"*Appl. Phys. Lett*., vol. 92, pp. 053506, 2008.

[77] T. T. Kao, J. Kim, Y. C. Lee, M. H. Ji, A. Haq, T. Detchprohm, R. D. Dupuis, and S. C. Shen, "Performance Evaluation of GaN/InGaN Heterojunction Phototransistors," *Conference on Lasers and Electro-Optics (CLEO 2015)*, SW4N, San Jose, MD, USA, 2015.

[78] T. T. Kao, J. Kim, T. Detchprohm, R. D. Dupuis, and S. C. Shen, "High-responsivity GaN/InGaN Heterojunction Phototransistors," *IEEE Photon. Technol. Lett*., vol. 8, no. 3, pp. 032101, 2016.

[79] J. R. Grandusky, S. R. Gibb, M. C. Mendrick, C. Moe, M. Wraback, and L. J. Schowalter, "High Output Power from 260 nm Pseudomorphic Ultraviolet Light-Emitting Diodes with Improved Thermal Performance," *Appl. Phys. Express*, vol. 4, pp. 082101, 2011.

[80] M. S. Shur, and R. Gaska, "Deep-Ultraviolet Light-Emitting Diodes," *IEEE Trans. Electron Devices*, vol. 57, pp. 12, 2010.

[81] H. Hirayama, Y. Tsukada, T. Maeda, and N. Kamata, "Marked Enhancement in the Efficiency of Deep-Ultraviolet AlGaN Light-Emitting Diodes by Using a Multiquantum-Barrier Electron Blocking Layer," *Appl. Phys. Exp.*, vol. 3, pp. 031002, 2010.

[82] V. Adivarahan, A. Heidari, B. Zhang, Q. Fareed, S. Hwang, M. Islam, and A. Khan, "280 nm Deep Ultraviolet Light Emitting Diode Lamp with an AlGaN Multiple Quantum Well Active Region,"*Appl. Phys. Express*, vol. 2, pp. 102101, 2009.

[83] A. Yasan, R. McClintock, K. Myes, D. Shiell, L. Gautero, S. Darvish, P. Kung, and M. Razeghi, "4.5 mW operation of AlGaN-based 267 nm deep-ultraviolet light-emitting diodes," *Appl. Phys. Lett.*, vol. 83, pp. 4701, 2003.

[84] H. Yoshida, Y. Yamashita, M. Kuwabara, H. Kan, "Demonstration of an ultraviolet 336 nm AlGaN multiple-quantum-well laser diode," *Appl. Phys. Lett.*, 93, 241106 (2008).

[85] J. Xie, S. Mita, Z. Bryan, W. Guo, L. Hussey, B. Moody, R. Schlesser, R. Kirste, M. Gerhold, R. Collazo, and Z. Sitar, "Lasing and longitudinal cavity modes in photo-pumped deep ultraviolet AlGaN heterostructures," *Appl. Phys. Lett.*, vol. 102, pp. 171102, 2013.

[86] V. N. Jmerik, A. M. Mizerov, A. A. Sitnikova, P. S. Kop'ev, S. V. Ivanov, E. V. Lutsenko, N. P. Tarasuk, N. V. Rzheutskii, and G. P. Yablonskii, "Low-threshold 303 nm lasing in AlGaN-based multiple-quantum well structures with an asymmetric waveguide grown by plasma-assisted molecular beam epitaxy on c-sapphire," *Appl. Phys. Lett.*, vol. 96, pp. 141112, 2010.

[87] T. Wunderer, C. L. Chua, Z. Yang, J. E. Northrup, N. M. Johnson, G. A. Garrett, H. Shen, and M. Wraback, "Pseudomorphically Grown Ultraviolet C Photopumped Lasers on Bulk AlN Substrates," *Appl. Phys. Express*, vol. 4, pp. 092101, 2011.

[88] J. Mickevičius, J. Jurkevičius, s, K. Kazlauskas, A. Žukauskas, G. Tamulaitis, M. S. Shur, M. Shatalov, J. Yang, and R. Gaska, "Stimulated emission in AlGaN/AlGaN quantum wells with different Al content," *Appl. Phys. Lett.*, vol. 100, pp. 081902, 2012.

[89] Z. Lochner, X. H. Li, T. T. Kao, Md. M. Satter, H. J. Kim, S. C. Shen, P. D. Yoder, J. H. Ryou, R. D. Dupuis, K. Sun, Y. W, T. Li, A. Fischer, F. A. Ponce, "Stimulated emission at 257 nm from an optically pumped AlGaN heterostructure on AlN substrate," *Phys. Status Solidi (A)*, pp. 1-3, 2013.

[90] T. Takano, Y. Narita, A. Horiuchi, H. Kawanishi, "Room-temperature deep-ultraviolet lasing at 241.5 nm of AlGaN multiple-quantum-well laser," *Appl. Phys. Lett.*, vol. 84, pp. 3567, 2004.

[91] Z. Lochner, T. T. Kao, Y. S. Liu, X. H. Li, Md. M. Satter, S. C. Shen, P. D. Yoder, J. H. Ryou, R. D. Dupuis, Y. W, H. Xie, A. Fischer, and F. A. Ponce, "Deep-ultraviolet lasing at 243 nm from photo-pumped AlGaN/AlN heterostructure on AlN substrate," *Appl. Phys. Lett.*, vol. 102, pp. 101110, 2013.

[92] T. T. Kao, Y. S. Liu, M. M. Satter, X. H. Li, Z. Lochner, P. D. Yoder, T. Detchprohm, R. D. Dupuis, S. C. Shen, J. H. Ryou, A. M. Fischer, Y. O. Wei, H. Xie, F. A. Ponce, "Sub-250 nm, low-threshold deep-ultraviolet AlGaN-based heterostructure laser employing HfO_2/SiO_2 dielectric mirrors," *Appl. Phys. Lett*., vol. 103, pp. 211103, 2013.

[93] T. Takano, Y. Narita, A. Horiuchi, and H. Kawanishi, "Room-temperature deep-ultraviolet lasing at 241.5 nm of AlGaN multiple-quantum-well laser," *Appl. Phys. Lett*., vol. 84, pp. 3567, 2004

[94] V. N. Jmerik, A. M. Mizerov, A. A. Sitnikova, P. S. Kop'ev,1 S. V. Ivanov, E. V. Lutsenko, N. P. Tarasuk, N. V. Rzheutskii, and G. P. Yablonskii, "Low-threshold

303 nm lasing in AlGaN-based multiple-quantum well structures with an asymmetric waveguide grown by plasma-assisted molecular beam epitaxy on c-sapphire,"*Appl. Phys. Lett*., vol. 96, pp. 141112, 2010.

[95] T. Wunderer, C. Chua, Z. Yang, J. Northrup, N. Johnson, G. Garrett, H. Shen, and M. Wraback, "Pseudomorphically Grown Ultraviolet C Photopumped Lasers on Bulk AlN Substrates,"*Appl. Phys. Exp*., vol. 4, pp. 092101, 2011.

[96] X. H. Li, T. T. Kao, M. M. Satter, Y. O. Wei, S. Wang, H. Xie, S. C. Shen, P. D. Yoder, A. M. Fischer, F. A. Ponce, T. Detchprohm, and R. D. Dupuis,, "Demonstration of transverse-magnetic deep-ultraviolet stimulated emission from AlGaN multiple-quantum-well lasers grown on a sapphire substrate," *Appl. Phys. Lett*., vol. 106, pp. 041115, 2015.

[97] Y. S. Liu, T. T. Kao, M. M. Satter, Z. Lochner, S. C. Shen, T. Detchprohm, P. D. Yoder, R. D. Dupuis, J. H. Ryou, A. M. Fischer, Y. O. Wei, H. Xie, F. A. Ponce, "Inverse-Tapered p-Waveguide for Vertical Hole Transport in High-[Al] AlGaN Emitters*," IEEE Photon. Technol. Lett*., vol. 27, no. 16, pp. 1768-1771, 2015.

[98] T.-C. Lu, C.-C. Kao, H.-C. Kuo, G.-S. Huang, and S.-C. Wang, "CW lasing of current injection blue GaN-based vertical cavity surface emitting laser," *Appl. Phys. Lett*. vol. 92, 141102, 2008.

[99] Y. Higuchi, K. Omae, H. Matsumura, and T. Mukai, "Room-Temperature CW Lasing of a GaN-Based Vertical-Cavity Surface-Emitting Laser by Current Injection," *Appl. Phys. Exp*., vol. 1, 121102, 2008.

[100] K. Omae, Y. Higuchi, K. Nakagawa, H. Matsumura, and T. Mukai, "Improvement in Lasing Characteristics of GaN-based Vertical-Cavity Surface-Emitting Lasers Fabricated Using a GaN Substrate," *Appl. Phys. Exp*., vol. 2, 052101, 2009.

[101] T.-C. Lu, S.-W. Chen, T.-T. Wu, P.-M. Tu, C.-K. Chen, C.-H. Chen, et al., "Continuous wave operation of current injected GaN vertical cavity surface emitting lasers at room temperature," *Appl. Phys. Lett*. vol. 97, 071114, 2010.

[102] D. Kasahara, D. Morita, T. Kosugi, K. Nakagawa, J. Kawamata, Y. Higuchi, et al., "Demonstration of Blue and Green GaN-Based Vertical-Cavity Surface-Emitting Lasers by Current Injection at Room Temperature," *Appl. Phys. Exp*., vol. 4, 072103, 2011.

[103] T. Onishi, O. Imafuji, K. Nagamatsu, M. Kawaguchi, K. Yamanaka, and S. Takigawa, "Continuous Wave Operation of GaN Vertical Cavity Surface Emitting Lasers at Room Temperature," *IEEE J. Quantum Electron*., vol. 48, pp. 1107-1112, 2012.

[104] G. Cosendey, A. Castiglia, G. Rossbach, J.-F. Carlin, and N. Grandjean, "Blue monolithic AlInN-based vertical cavity surface emitting laser diode on free-standing GaN substrate," *Appl. Phys. Lett*., vol. 101, pp. 151113, 2012.

[105] C. Holder, D. Feezell, J. S. Speck, S. P. DenBaars, and S. Nakamura, "Demonstration of nonpolar GaN-based vertical-cavity surface-emitting lasers," *Appl. Phys. Exp*., vol. 5, 092104, 2012.

[106] W.-J. Liu, X.-L. Hu, L.-Y. Ying, J.-Y. Zhang, and B.-P. Zhang, "Room temperature continuous wave lasing of electrically injected GaN-based vertical cavity surface emitting lasers," *Appl. Phys. Lett.*, vol. 104, 251116, 2014.

[107] S. Izumi, N. Fuutagawa, T. Hamaguchi, M. Murayama, M. Kuramoto, and H. Narui, "Room-temperature continuous-wave operation of GaN-based vertical-cavity surface-emitting lasers fabricated using epitaxial lateral overgrowth," *Appl. Phys. Exp.*, vol. 8, 062702, 2015.

[108] J. T. Leonard, E. C. Young, B. P. Yonkee, D. A. Cohen, T. Margalith, S. P. DenBaars, J. S. Speck, and S. Nakamura, " Demonstration of a III-nitride vertical-cavity surface-emitting laser with a III-nitride tunnel junction intracavity contact," *Appl. Phys. Lett.*, vol. 107, 091105, 2015.

[109] M. Bakowski, P. Ranstad, J.-K. Lim, W. Kaplan, S. A. Reshanov, A. Schoner, F. Giezendanner, and A. Ranstad, "Design and Characterization of Newly Developed 10 kV 2 A SiC p-i-n Diode for Soft-Switching Industrial Power Supply", *IEEE Trans. of Electron. Devices*, vol. 62, no. 2, pp 366-373, Feb. 2015.

[110] R. N. Hall, "Large Free-Standing GaN Substrates by Hydride Vapor Phase Epitaxy and Laser-Induced Liftoff," *Phys. Rev.* vol. 87, pp. 387, July 1952

[111] M. B. Prince, *Bell System Tech. J.*, vol. 35, pp. 661, 1956.

[112] J. Lutz, H. Schlangenotto, U. Scheuermann, R. D. Doncker, "Semiconductor power devices, physics, characteristics, reliability", Springer-Verlag Berlin Heidelberg, pp. 167, 2011.

[113] S. M. Sze, "*Physics of Semiconductor Devices*", 2nd ed. Hoboken, NJ: Wiley, pp. 124, 1981.

[114] M. E. Levinshtein, T.T. Mnatsakanov, P.A. lvanov, R. Singh, K.G. Irvine and J.W. Palmour, "Carrier lifetime measurements in 10 kV 4H-SiC diodes", *Electron Lett.*, vol. 39, No. 8, pp 689-690, 2003.

[115] M. Jameleddine, B. Hamouda, and W. Gerlach, "Determination of the carrier lifetime from the open-circuit voltage decay of p-i-n rectifiers at high-injection levels", *IEEE Trans. Electron Device*, vol. ED-29, No. 6, pp 953-955, 1982.

[116] H. Schlangenotto and W. Gerlach, "On the post-injection voltage decay of p-s-n rectifiers at high injection levels", *Solid-State Electronics*, vol. 15, pp 393-402, 1972.

[117] D. H. J. Totterdell, J. W. leake, and S. C. Jain, "High-injection open-circuit voltage decay in pn-junction diodes with lightly doped bases", *IEE Proceedings*, vol. 133, no. 5, pp 181-184, 1986.

[118] M. T. Fresina, Q. J. Hartmann, S. Thomas, D. A. Ahmari, D. Caruth, M. Feng and G.E. Stillman, "InGaP/GaAs HBT with novel layer structure for emitter ledge fabrication," in *IEDM Tech. Dig.* pp. 207-210, 1996.

[119] T. Kimoto, N. Miyamoto, and H. Matsunami, "Performance limiting surface defects in SiC epitaxial p-n junction diodes," *IEEE Trans. Electron Devices*, vol. 46, no. 3, pp. 471-477, March 1999.

[120] Z. Hu, K. Nomoto, B. Song, M. Zhu, M. Qi, M. Pan, X. Gao, V. Protasenko, D. Jena, and H. G. Xing, "Near unity ideality factor and Shockley-Read-Hall lifetime

in GaN-on-GaN p-n diodes with avalanche breakdown," *Appl. Phys. Lett.*, vol. 107, 243501, 2015.

[121] R. H. Caverly, and G. Hiller, "*The temperature dependence of P-I-N diode attenuators*," IEEE MTT-S Digest, pp. 553-556, June 1993.

[122] J. Frenkel, "On Pre-Breakdown Phenomena in Insulators and Electronic Semi-Conductors," *Phys. Rev.* vol. 54, pp. 647-648, Aug. 1938.

[123] P. Hacke, T. Detchprohm, K. Hiramatsu, N. Sawaki, K. Tadatomo, and K. Miyake, "Analysis of deep levels in n-type GaN by transient capacitance methods," *J. Appl. Phys.*, vol. 76, pp. 304, July 1994.

[124] P. Kamyczek, E. Placzek-Popko, VI. Kolkovsky, S. Grzanka, and R. Czernecki, "A deep acceptor defect responsible for the yellow luminescence in GaN and AlGaN," J. of *Appl. Phys.*, vol. 111, pp. 113105, 2012.

[125] B. J. Baliga, "Power semiconductor device figure of merit for high-frequency applications," *IEEE Electron Device Lett.*, vol. 10, no. 10, pp. 455–457, Oct. 1989.

[126] S. C. Shen, R. D. Dupuis, Y. C. Lee, H. J. Kim, Y. Zhang, Z. Lochner, P. D. Yoder, and J. H. Ryou, "GaN/InGaN Heterojunction Bipolar Transistors with $f_T >$ 5 GHz," *IEEE Electron Device Lett.*, vol. 32, pp. 1065, 2011.

[127] K. Kumakura and T. Makimoto, "High-temperature characteristics up to 590 °C of a *pnp* AlGaN/GaN heterojunction bipolar transistor," *Appl. Phys. Lett.*, vol. 94, pp. 103502, 2009.

[128] R. D. Dupuis, J. Kim, Y. C. Lee, Z. Lochner, T. Kao, M. H. Ji, T. T. Kao, J. H. Ryou, T. Detchphrom, and S. C. Shen, "III-N High-power bipolar transistors," *ECS Transactions*, vol. 58 (4), pp. 261, 2013.

[129] D. Keogh, P. Asbeck, T. Chung, J. Limb, D. Yoo, J.-H. Ryou, W. Lee, S.C. Shen, and R. D. Dupuis, "High current gain GaN/InGaN HBTs with 300 °C operating temperature," *Electron. Lett.*, vol. 42, pp. 661, 2006.

[130] M. Feng, N. Holonyak, Jr., and W. Hafez, "Light-emitting transistor: Light emission from InGaP/GaAs heterojunction bipolar transistors," *Appl. Phys. Lett.*, vol. 84, pp. 151, 2004.

[131] G. Walter, N. Holonyak, Jr., M. Feng, and R. Chan, "Laser operation of a heterojunction bipolar light-emitting transistor," *Appl. Phys. Lett.*, vol. 85, pp. 4768, 2004.

[132] H. Then, M. Feng, N. Holonyak, Jr., C. Wu, "Experimental determination of the effective minority carrier lifetime in the operation of a quantum-well n-p-n heterojunction bipolar light-emitting transistor of varying base quantum-well design and doping," *Appl. Phys. Lett.*, vol. 91, pp. 033505, 2007.

[133] B. F. Chu-Kung, M. Feng, G. Walter, N. Holonyak, Jr., T. Chung, J.-H. Ryou, J. Limb, D. Yoo, S.-C. Shen, R. D. Dupuis, D. Keogh, and P, M. Asbeck, "Graded-base InGaN∕GaNInGaN∕GaN heterojunction bipolar light-emitting transistors," *Appl. Phys. Lett.*, vol. 89, pp. 082108, 2006.

[134] B. F. Chu-Kung, C. H. Wu, G. Walter, M. Feng, N. Holonyak, T. Chung, J. H. Ryou, and R. D. Dupuis, "Modulation of high current gain (β>49) light-

emitting InGaN∕GaNInGaN∕GaN heterojunction bipolar transistors," *Appl. Phys. Lett.*, vol. 91, pp. 232114, 2007.

[135] http://sales.hamamatsu.com/en/products/electron-tube division/detectors/photomultiplier tubes.php

[136] Y. Zhang, S. -C. Shen, H. -J Kim, S. Choi, J. -H. Ryou, R. D. Dupuis, and B. Narayan, "Low-noise GaN ultraviolet p-i-n photodiodes on GaN substrates," *Appl. Phys. Lett.*, vol. 94, pp. 221109, June 2009.

[137] C. J. Collins, T. Li, D. J. H. Lambert, M. M. Wong, R. D. Dupuis, and J. C. Campbell, "Selective regrowth of $Al_{0.30}Ga_{0.70}N$ p–i–n photodiodes," *Appl. Phys. Lett.* vol. 77, no. 18, pp. 2810-2812, Sep. 2000.

[138] S. -C. Shen, Y. Zhang, D. Yoo, J. -B. Limb, J. -H. Ryou, P. D. Yoder, and R. D. Dupuis, "Performance of Deep Ultraviolet GaN Avalanche Photodiodes Grown by MOCVD," *IEEE Photon. Technol. Lett.*, vol. 19, no. 21, pp. 1744-1746, Nov. 2007.

[139] J. Kim, M.-H. Ji, T. Detchprohm, J. -H. Ryou, R. D. Dupuis, A.-K. Sood, and N.-K. Dhar, "AlxGa1−xN Ultraviolet Avalanche Photodiodes With Avalanche Gain Greater Than 10^5," *IEEE Photon. Technol. Lett.*, vol. 27, no. 6, pp. 642-645, March 2015.

[140] S. Verghese, K. A. McIntosh, R. J. Molnar, L. J. Mahoney, R. L. Aggarwal, M. W. Geis, K. M. Molvar, E. K. Duerr, and I. Melngailis, "GaN avalanche photodiodes operating in linear-gain mode and Geiger mode," *IEEE Trans. Electron Devices*, vol. 48, no. 3, pp. 502-511, March 2001.

[141] Q. Zhou, D. C. Mclntosh, Z. Lu, J. C. Campbell, A. V. Sampath, H. Shen, and M. Wraback, "GaN/SiC avalanche photodiodes," *Appl. Phys. Lett.*, vol. 99, pp. 131110, Sep. 2011.

[142] K. H. Lee, P. C. Chang, S. J. Chang, C. L. Yu, Y. C. Wang, and S. L. Wu, "GaN MSM photodetectors with an unactivated Mg-doped GaN cap layer and sputtered ITO electrodes," *Journal of the Electrochemical Society,* vol. 155, pp. 165-167, 2008.

[143] K. T. Lam, P. C. Chang, S. J. Chang, C. L. Yu, Y. C. Lin, Y. X. Sun, and C. H. Chen, "Nitride-based photodetectors with unactivated Mg-doped GaN cap layer," *Sensors & amp; Actuators: A. Physical,* vol. 143, pp. 191-5, 2008.

[144] M. L. Lee, C. Ping-Feng, and J. K. Sheu, "Photodetectors formed by an indium tin oxide/zinc oxide/p-type gallium nitride heterojunction with high ultraviolet-to-visible rejection ratio," *Appl. Phys. Lett.,* vol. 94, pp. 013512, 2009.

[145] R. A. Milano, T. H. Windhorn, E. R. Anderson, G. E. Stillman, R. D. Dupuis and P. D. Dapkus, "$Al_{0.5}Ga_{0.5}As$‐GaAs heterojunction phototransistors grown by metalorganic chemical vapor deposition," *Appl. Phys. Lett.*, vol. 34, pp. 562, 1979.

[146] J. C. Campbell, A. G. Dental, G. -J. Qua, and J. F. Ferguson, "Avalanche InP/InGaAs heterojunction phototransistor," *IEEE J. Quantum Electron.*, vol. 19, pp. 1134, 1983.

[147] F.-Y. Huang, and H. Morkoc, "GaAs/InGaAs/AlGaAs optoelectronic switch in avalanche heterojunction phototransistor vertically integrated with a resonant cavity," *Appl. Phys. Lett.*, vol. 64, vol. 405, 1994.

163

[148] J. C. Campbell, C. A. Burrus, A. G. Dentai, and K. Ogawa, "Small-area high-speed InP/InGaAs phototransistor," *Appl. Phys. Lett*., vol. 39, pp. 820, 1981.

[149] J. C. Campbell, and K. Ogawa, "Heterojunction phototransistors for long-wavelength optical receivers," J. of *Appl. Phys.*, vol. 53, pp. 1203, 1982.

[150] J. C. Campbell, G. J. Qua, and A. G. Dentai, "Optical comparator: A new application for avalanche phototransistors," *IEEE Trans. Electron Dev*., vol. 30, no. 4, pp. 408-411, Apr. 1983.

[151] W. Yang, T. Nohava, S. Krishnankutty, R. Torreano, S. McPherson, and H. Marsh, "High gain GaN/AlGaN heterojunction phototransistor," *Appl. Phys. Lett.*, vol. 73, no. 7, pp. 978-980, June 1998.

[152] R. Mouillet, A. Hirano, M. Iwaya, T. Detchprohm, H. Amano, and I. Akasaki, "Photoresponse and Defect Levels of AlGaN/GaN Heterobipolar Phototransistor Grown on Low-Temperature AlN Interlayer," *Jpn. J. Appl. Phys*., vol. 40, L498-501, March 2001.

[153] M. L. Lee, J. K. Sheu, and Y. R. Shu, "Ultraviolet bandpass $Al_{0.17}Ga_{0.83}N$/GaN heterojunction phototransitors with high optical gain and high rejection ratio," *Appl. Phys. Lett*., vol. 92, pp. 053506, Feb. 2008.

[154] S.-C. Shen, T.-T. Kao, H.-J. Kim, Y.-C. Lee, J. Kim, M.-H. Ji, J.-H. Ryou, T. Detchprohm, and R. D. Dupuis, "GaN/InGaN avalanche phototransistors," *Appl. Phys Exp.*, vol. 8, pp. 032101, Feb. 2015.

[155] W. Liu, Foundamentals of III-V Devices - HBTs, MESFETS and HFETs/HEMTs. (John Wiley & Sons, Inc, 1999).

[156] J. C. Campbell, G. -J. Qua, and A. G. Dental, "Optical Comparator: A New Application for Avalanche Phototransistors," *IEEE J. Quantum Electron.*, vol. ED-30, no. 4, pp. 408-411, Apr. 1983.

[157] S. L. Miller and J. J. Ebers, "Alloyed junction avalanche transistors," *Bell Sysr. Tech. J.*, vol. 34, pp. 883-902, Sept. 1955.

[158] J. W. Shi, Y. S. Wu, F. C. Hong, and W. Y. Chiu, "Separate absorption-charge multiplication heterojunction phototransistors with the bandwidth-enhancement effect and ultrahigh gain-bandwidth product under near svalanche operation," *IEEE Electron Device Lett*., vol. 29, no. 7, pp. 714–717, July 2008.

[159] Z. Lochner, H.-J. Kim, Y.-C. Lee, Y. Zhang, S. Choi, S.-C. Shen, P. D. Yoder, J.-H. Ryou, and R. D. Dupuis, "NpN-GaN/$In_xGa_{1−x}$N/GaN heterojunction bipolar transistor on free-standing GaN substrate," *Appl. Phys. Lett.*, vol. 99, 193501, 2011.

[160] S.-C. Shen, R. D. Dupuis, A. Lochner, Y. Lee, T. T. Kao, Y. Zhang, H.-J. Kim and J.-H Ryou, "Working toward high-power GaN/InGaN heterojunction bipolar transistors," *Semicond. Sci. and Technol*., vol. 28, pp. 074025, 2013.

[161] K. P. O'Donnell, I. Fernandez-Torrente, P. R. Edwards, and R. W. Martin, "The composition dependence of the In_xGa_{1-x}N bandgap," *J. Cryst. Growth*, vol. 269, pp. 100-105, 2004.

[162] K. Kumakura, T. Makimoto, and N. Kobayashi, "Mg-acceptor activation mechanism and transport characteristics in *p*-type InGaN grown by metalorganic vapor phase epitaxy," *J. Appl. Phys.*, vol. 93, pp. 3370, 2003.

[163] O. Gelhausen, H. N. Klein, M. R. Phillips, and E. M. Goldys, "Low-energy electron-beam irradiation and yellow luminescence in activated Mg-doped GaN," *Appl. Phys. Lett.*, vol. 83, pp. 3293, 2003.

[164] M. A. Reshchikova and H. Morkoç, "Luminescence properties of defects in GaN," *J, Appl. Phys.*, vol. 97, pp. 061301, 2005.

[165] B. Han, M. P. Ulmer, and B. W. Wessels, "Investigation of deep-level luminescence in $In_{0.07}Ga_{0.93}N$:Mg," *Physica B*, vol. 340-342, pp. 470, 2003.

[166] Q. Yan, A. Janotti, M. Scheffler, and C. G. Van de Walle, "Role of nitrogen vacancies in the luminescence of Mg-doped GaN," *Appl. Phys. Lett.*, vol. 100, pp. 142110, 2012.

[167] William Liu, Fundamentals of III-V Devices: HBTs, MESFETs, and HFETs/HEMTs (Wiley, New York, 1999, p. 151.

[168] S. C. Shen, Y. C. Lee, H. J. Kim, Y. Zhang, S. Choi, R. D. Dupuis, and J. H. Ryou, "Surface leakage in GaN/InGaN double heterojunction bipolar transistors," *IEEE Electron Device Lett.*, vol. 30, pp. 1119, 2009.

[169] S.-C. Shen, R. D. Dupuis, Z. Lochner, Y.-C. Lee, T.-T. Kao, Y. Zhang, H.-J. Kim and J.-H. Ryou, "Working toward high-power GaN/InGaN heterojunction bipolar transistors," *Semicond. Sci. Technol.*, vol. 28, pp. 074025, 2013

[170] L. Zhang, K. Cheng, S. Degroote, M. Leys, M. Germain, and G. Borghs, "Strain effects in GaN epilayers grown on different substrates by metal organic vapor phase epitaxy," *J. of Appl. Phys.*, vol. 108, pp. 073522, 2010.

[171] J. C. Campbell, G. -J. Qua, and A. G. Dental, "Optical Comparator: A New Application for Avalanche Phototransistors," *IEEE J. Quantum Electron.*, vol. ED-30, no. 4, pp. 408-411, April 1983.

[172] J. C. Campbell, A. G. Dental, G. -J. Qua, and J. F. Ferguson, "Avalanche InPAnGaAs Heterojunction Phototransistor," *IEEE J. Quantum Electron.*, vol. QE-19, no. 6, pp. 1134-1138, June 1983.

[173] Y. Zhang, J.-H. Ryou, R. D. Dupuis, and S.-C. Shen, "A surface treatment technique for III-V device fabrication," in Proc. *Int. Conf. Compd. Semicond. Manuf. Technol. Dig. Papers*, Chicago, IL, pp. 13.3, Apr. 2008.

[174] J. F. Muth, J. H. Lee, I. K. Shmagin, R. M. Kolbas, H. C. Casey Jr., B. P. Keller, U. K. Mishra, and S. P. DenBaars, "Absorption coefficient, energy gap, exciton binding energy, and recombination lifetime of GaN obtained from transmission measurements," *Appl. Phys. Lett.*, vol. 71, no. 18, pp. 2572-2574, Sep. 1997.

[175] C. P. Liu, A. J. Seeds, and D. Wake, "Two-terminal edge-coupled InP/InGaAs heterojunction phototransistor optoelectronic mixer," *IEEE Microw.Guided Wave Lett.*, vol. 7, no. 3, pp. 72–74, Mar. 1997.

[176] Y. Zhang, S. -C. Shen, H. -J Kim, S. Choi, J. -H. Ryou, R. D. Dupuis, and B. Narayan, "Low-noise GaN ultraviolet p-i-n photodiodes on GaN substrates," *Appl. Phys. Lett.*, vol. 94, pp. 221109, June 2009.

[177] F. Xie, H. Lu, D. J. Chen, X. Q. Xiu, H. Zhao, R. Zhang, and Y. D. Zheng, "Metal–Semiconductor–Metal Ultraviolet Avalanche Photodiodes Fabricated on Bulk GaN Substrate," *IEEE Electron Device Lett.*, vol. 32, no. 9, pp. 1260–1262, Sep. 2011.

[178] J. W. Shi, Y. S. Wu, F. C. Hong, and W. Y. Chiu, "Separate absorption-charge multiplication heterojunction phototransistors with the bandwidth-enhancement effect and ultrahigh gain-bandwidth product under near svalanche operation," *IEEE Electron Device Lett.*, vol. 29, no. 7, pp. 714–717, July 2008.

[179] T. T. Kao, Y. C. Lee, H. J. Kim, J. H. Ryou, J. Kim, T. Detchprohm, R. D. Dupuis, and S. C. Shen, "Radiative Recombination in npn GaN/InGaN Heterojunction Bipolar Transistors," *Appl. Phys. Lett.*, vol. 107, pp. 242104, 2015.

[180] S. C. Shen, T. T. Kao, H. J. Kim, Y. C. Lee, J. Kim, M. H. Ji, J. H. Ryou, T. Detchprohm, and R. D. Dupuis, "GaN/InGaN Avalanche Phototransistor," *Appl. Phys. Express*, vol. 8, no. 3, pp. 032101, 2015

[181] T. T. Kao, J. Kim, Y. C. Lee, M. H. Ji, A. Haq, T. Detchprohm, R. D. Dupuis, and S. C. Shen, "Performance Evaluation of GaN/InGaN Heterojunction Phototransistors," *Conference on Lasers and Electro-Optics (CLEO 2015)*, SW4N, San Jose, MD, USA, 2015.

[182] J. R. Grandusky, S. R. Gibb, M. C. Mendrick, C. Moe, M. Wraback, and L. J. Schowalter, "High Output Power from 260 nm Pseudomorphic Ultraviolet Light-Emitting Diodes with Improved Thermal Performance," *Appl. Phys. Express*, vol. 4, pp. 082101, 2011.

[183] M. S. Shur, and R. Gaska, "Deep-Ultraviolet Light-Emitting Diodes," *IEEE Trans. Electron Devices*, vol. 57, pp. 12, 2010.

[184] H. Hirayama, Y. Tsukada, T. Maeda, and N. Kamata, "Marked Enhancement in the Efficiency of Deep-Ultraviolet AlGaN Light-Emitting Diodes by Using a Multiquantum-Barrier Electron Blocking Layer," *Appl. Phys. Exp.*, vol. 3, pp. 031002, 2010.

[185] V. Adivarahan, A. Heidari, B. Zhang, Q. Fareed, S. Hwang, M. Islam, and A. Khan, "280 nm Deep Ultraviolet Light Emitting Diode Lamp with an AlGaN Multiple Quantum Well Active Region," *Appl. Phys. Exp.*, vol. 2, pp. 102101, 2009.

[186] A. Yasan, R. McClintock, K. Myes, D. Shiell, L. Gautero, S. Darvish, P. Kung, and M. Razeghi, "4.5 mW operation of AlGaN-based 267 nm deep-ultraviolet light-emitting diodes," *Appl. Phys. Lett.*, vol. 83, pp. 4701, 2003.

[187] S. Nakamura, M. Senoh, S. Nagahama, N. Iwasa, T. Yamada, T. Matsushita, H. Kiyoku, Y. Sugimoto, T. Kozaki, H. Umemoto, M. Sano, and K. Chocho, "GaN/InGaN/AlGaN-based laser diodes with modulation-doped strained-layer superlattices grown on an epitaxially laterally overgrown GaN substrate," *Appl. Phys. Lett.*, vol. 72, pp. 211, 1998.

[188] S. Nakamura, "InGaN multiquantum-well-structure laser diodes with GaN-AlGaN modulation-doped strained-layer superlattices," *IEEE J. Select. Topics Quantum Electron.*, vol. 4, pp. 483-489, 1998

[189] M. C. Schmidt, K. C. Kim, R, M. Farrell, D. F. Feezell, D. A. Cohen, M. Saito, K. Fujito, J. S. Speck, S. P. Denbaars, and S. Nakamura, "Demonstration of Nonpolar m-Plane GaN/InGaN Laser Diodes," *Jpn. J. Appl. Phys*, vol. 46, pp. L190, 2007.

[190] D. F. Feezell, M. C. Schmidt, Robert M. Farrell, K. C. Kim, M. Saito, K. Fujito, D. A. Cohen, J. S. Speck, S. P. Denbaars, and S. Nakamura, "AlGaN-Cladding-Free Nonpolar GaN/InGaN Laser Diodes," *Jpn. J. Appl. Phys*, vol. 46, pp. L284, 2007.

[191] H. Yoshida, Y. Yamashita, M. Kuwabara, H. Kan, "Demonstration of an ultraviolet 336 nm AlGaN multiple-quantum-well laser diode," *Appl. Phys. Lett*. vol. 93, pp. 241106, 2008.

[192] K. Iga, "Surface emitting semiconductor lasers," *IEEE J. Quantum Electron*., vol. 24, pp. 1845-1855, 1988.

[193] K. Iga: *Proc. 1st Int. Symp. on Blue Lasers and Light Emitting Diodes*, Chiba, Th-11, 1996.

[194] T. Someya, R. Werner, A. Forchel, M. Catalano, R. Cingolani, Y.Arakawa, "Room temperature lasing at blue wavelengths in gallium nitride microcavities," *Science*, vol. 285, pp. 1905-1906, 1999.

[195] Y.-K. Song, H. Zhou, M. Diagne, A. V. Nurmikko, R. P. Schneider, Jr., C. P. Kuo, M. R. Krames, R. S. Kern, C. Carter-Coman, and F. A. Kish, "A quasicontinuous wave, optically pumped violet vertical cavity surface emitting laser," *Appl. Phys. Lett*., vol. 76, pp. 1662, 2000.

[196] T. Tawara, H. Gotoh, T. Akasaka, N. Kobayashi, and T. Saitoh, "Low-threshold lasing of InGaN vertical-cavity surface-emitting lasers with dielectric distributed Bragg reflectors," *Appl. Phys. Lett*., vol. 83, pp. 830, 2003.

[197] H. Zhou, M. Diagne, E. Makarona, A. V. Nurmikko, J. Han, K. E. Waldrip and J. J. Figiel, "Near ultraviolet optically pumped vertical cavity laser," *Electron. Lett*., vol. 36, pp. 1777, 2000.

[198] J.-T. Chu, T.-C. Lu, H.-H. Yao, C.-C. Kao, W.-D. Liang, J.-Y. Tsai, H.-C. Kuo, and S.-C. Wang, "Room-temperature operation of optically pumped blue-violet GaN-based vertical-cavity surface-emitting lasers fabricated by laser lift-off," *Jpn. J. Appl. Phys*, vol. 45, pp. 2556, 2006.

[199] J.-T. Chu, T.-C. Lu, M. Yu, B.-J. Su, C.-C. Kao, H.-C. Kuo, and S.-C. Wang, "Emission characteristics of optically pumped GaN-based vertical-cavity surface-emitting lasers," *Appl. Phys. Lett*., vol. 89, pp. 121112, 2006.

[200] C.-C. Kao, Y. C. Peng, H. H. Yao, J. Y. Tsai, Y. H. Chang, J. T. Chu, H. W. Huang, T. T. Kao, T. C. Lu, H. C. Kuo, S. C. Wang, and C. F. Lin, "Fabrication and performance of blue GaN-based vertical-cavity surface emitting laser employing AlN∕GaN and Ta_2O_5∕SiO_2 distributed Bragg reflector," *Appl. Phys. Lett*., vol. 87, pp. 081105, 2005.

[201] C-C. Kao, T. C. Lu, H. W. Huang, J. T. Chu, Y. C. Peng, H. H. Yao, J. Y. Tsai, T. T. Kao, H. C. Kuo, S. C. Wang, and C. F. Lin, "The Lasing Characteristics of GaN-Based Vertical-Cavity Surface-Emitting Laser With AlN–GaN and Ta_2O_5–SiO_2 Distributed Bragg Reflectors," *IEEE Photon. Technol. Lett*., vol. 18, pp. 877, 2006.

[202] J. F. Carlin, J. Dorsaz, E. Feltin, R. Butté, N. Grandjean, M. Ilegems, and M. Laügt, "Crack-free fully epitaxial nitride microcavity using highly reflective AlInN∕GaN Bragg mirrors," *Appl. Phys. Lett*., vol. 86, pp. 031107, 2005.

[203] E. Feltin, R. Butté, J. F. Carlin, J. Dorsaz, N. Grandjean, and M. Ilegems, "Lattice-matched distributed Bragg reflectors for nitride-based vertical cavity surface emitting lasers," *Electron. Lett.*, vol. 41, pp. 94, 2005.

[204] Y. Higuchi, K. Omae, H. Matsumura, and T. Mukai, "Room-Temperature CW Lasing of a GaN-Based Vertical-Cavity Surface-Emitting Laser by Current Injection," *Appl. Phys. Exp.*, vol. 1, pp. 121102, 2008.

[205] K. Omae, Y. Higuchi, K. Nakagawa, H. Matsumura, and T. Mukai, "Improvement in Lasing Characteristics of GaN-based Vertical-Cavity Surface-Emitting Lasers Fabricated Using a GaN Substrate," *Appl. Phys. Exp.*, vol. 2, pp. 052101, 2009.

[206] D. Kasahara, D. Morita, T. Kosugi, K. Nakagawa, J. Kawamata, and Y. Higuchi, "Demonstration of Blue and Green GaN-Based Vertical-Cavity Surface-Emitting Lasers by Current Injection at Room Temperature," *Appl. Phys. Exp.*, vol. 4, pp. 072103, 2011.

[207] T. Onishi, O. Imafuji, K. Nagamatsu, M. Kawaguchi, K. Yamanaka, and S. Takigawa, "Continuous Wave Operation of GaN Vertical Cavity Surface Emitting Lasers at Room Temperature," *IEEE J. Quantum Electron.*, vol. 48, pp. 1107-1112, 2012.

[208] C. Holder, D. Feezell, J. S. Speck, S. P. DenBaars, and S. Nakamura, "Demonstration of nonpolar GaN-based vertical-cavity surface-emitting lasers," *Appl. Phys. Exp.*, vol. 5, 092104, 2012.

[209] W.-J. Liu, X.-L. Hu, L.-Y. Ying, J.-Y. Zhang, and B.-P. Zhang, "Room temperature continuous wave lasing of electrically injected GaN-based vertical cavity surface emitting lasers," *Appl. Phys. Lett.*, vol. 104, pp. 251116, 2014.

[210] S. Izumi, N. Fuutagawa, T. Hamaguchi, M. Murayama, M. Kuramoto, and H. Narui, "Room-temperature continuous-wave operation of GaN-based vertical-cavity surface-emitting lasers fabricated using epitaxial lateral overgrowth," *Appl. Phys. Exp.*, vol. 8, pp. 062702, 2015.

[211] J. T. Leonard, E. C. Young, B. P. Yonkee, D. A. Cohen, T. Margalith, S. P. DenBaars, J. S. Speck, and S. Nakamura, "Demonstration of a III-nitride vertical-cavity surface-emitting laser with a III-nitride tunnel junction intracavity contact," *Appl. Phys. Lett.*, vol. 107, pp. 091105, 2015.

[212] T. Ive, O. Brandt, H. Kostial, T. Hesjedal, M. Ramsteiner, and K. H. Ploog, "Crack-free and conductive Si-doped AlN∕GaN distributed Bragg reflectors grown on 6H-SiC (0001)," *Appl. Phys. Lett.*, vol. 85, pp. 1970, 2004.

[213] H. H. Yao, C.F. Lin, H.C. Kuo, S.C. Wang, ""MOCVD growth of AlN/GaN DBR structures under various ambient conditions," *J. Crystal Growth*, vol. 262, pp. 151, 2004.

[214] T.-C. Lu, C.-C. Kao, H.-C. Kuo, G.-S. Huang, and S.-C. Wang, "CW lasing of current injection blue GaN-based vertical cavity surface emitting laser," *Appl. Phys. Lett.* vol. 92, pp. 141102, 2008.

[215] T.-C. Lu, S.-W. Chen, T.-T. Wu, P.-M. Tu, C.-K. Chen, C.-H. Chen, et al., "Continuous wave operation of current injected GaN vertical cavity surface emitting lasers at room temperature," *Appl. Phys. Lett.*, vol. 97, pp. 071114, 2010.

[216] C. Holder, D. Feezell, J. S. Speck, S. P. DenBaars, and S. Nakamura, "Demonstration of nonpolar GaN-based vertical-cavity surface-emitting lasers," *Appl. Phys. Exp.*, vol. 5, pp. 092104, 2012.

[217] J. M. Redwing, D. A. S. Loeber, N. G. Anderson, M. A. Tischler and J. S. Flynn, "An optically pumped GaN–AlGaN vertical cavity surface emitting laser," *Appl. Phys. Lett.*, vol. 69, pp. 1, 1996.

[218] H. Zhou, M. Diagne, E. Makarona, A. V. Nurmikko, J. Han, K. E. Waldrip and J. J. Figiel, "Near ultraviolet optically pumped vertical cavity laser," *Electron. Lett.*, vol. 36, pp. 1777, 2000.

[219] R. N. Hall, G. E. Fenner, J. D. Kingsley, T. J. Soltys, and R. O. Carlson, "Coherent light emission from GaAs junctions," *Phys. Rev. Lett.*, vol. 9, pp. 366-368, 1962.

[220] M. I. Nathan, W. P. Dumke, G. Burns, F. H. Dill, Jr., and G. Lasher, "Stimulated emission of radiation from GaAs *p-n* junctions," *Appl. Phys. Lett.*, vol. 1, pp. 62-64, 1962.

[221] N. Holonyak Jr. and S. F. Bevacqua, "Coherent (visible) light emission from Ga(As$_{1-x}$P$_x$) junctions," *Appl. Phys. Lett.*, vol. 1, pp. 82-83, 1962.

[222] R. D. Dupuis, P. D. Dapkus, N. Holonyak Jr., E. A. Rezek, and R. Chin, "Room-temperature multiple-quantum-well Al$_x$Ga$_{1-x}$As-GaAs injection lasers grown by metalorganic chemical vapor deposition," *Appl. Phys. Lett.*, vol. 32, pp. 295-297, 1978.

[223] L. A. Coldren and S. W. Corzine, Diode lasers and photonic integrated circuits, 1st ed. (Wiley, New York, 1995).

[224] D. Queren, A. Avramescu, G. Brüderl, A. Breidenassel, M. Schillgalies, S. Lutgen, and U. Straub, "500 nm electrically driven InGaN based laser diodes," *Appl. Phys. Lett.* vol. 94, pp. 081119, 2009.

[225] A. Avramescu, T. Lermer, J. Müller, S. Tautz, D. Queren, S. Lutgen, and U. Straub, "InGaN laser diodes with 50 mW output power emitting at 515 nm," *Appl. Phys. Lett.*, vol. 95, pp. 071103, 2009.

[226] J. Müller, G. Brüderl, M. Schillgalies, S. Tautz, D. Dini, A. Breidenassel, B. Galler, and S. Lutgen, "Burn-in mechanism of 450 nm InGaN ridge laser test structures," *Appl. Phys. Lett.*, vol. 95, pp. 051104, 2009.

[227] M. A. Miller, B. H. Koo, K. H. A. Bogart, and S. E. Mohney, "Ti/Al/Ti/Au and V/Al/V/Au Contact to Plasma-Etched n-Al$_{0.58}$Ga$_{0.42}$N," *J. Electron. Mater.*, vol. 37, pp. 564, Sep. 2008.

[228] V. S. Fomenko, "Handbook of Thermionic Properties: Electronic Work Functions and Richardson Constants of Elements and Compounds," (Plenum, New York, 1966).

[229] K. O. Schweitz, P. K. Wang, S. E. Mohney and D. Gotthold, "V/Al/Pt/Au Ohmic contact to n-AlGaN/GaN heterostructures," *Appl. Phys. Lett.*, vol. 80, pp. 1954, Jan. 2002.

[230] M. A. Miller and S. E. Mohney, "V/Al/V/Ag Ohmic contact to n-AlGaN/GaN heterostructures with a thin GaN cap," *Appl. Phys. Lett.*, vol. 91, pp. 012103, July 2007.

[231] R. France, T. Xu, P. Chen, R. Chandrasekaran, and T. D. Moustakas, "Vanadium-based Ohmic contact to n-AlGaN in the entire alloy composition," *Appl. Phys. Lett.*, vol. 90, pp. 062115, 2007.

[232] P. Y. Jouan, M. C. Peignon, Ch. Cardinaud, G. Lempérière, "Characterization of TiN coatings and of the TiN/Si interface by X-ray photoelectron spectroscopy and Auger electron spectroscopy," *Appl. Surf. Sci.*, vol. 68, pp. 595-603, Aug. 1993.

[233] Y. Baba, T. A. Sasaki, and I. Takano, "Preparation of nitride films by Ar^+-ion bombardment of metals in nitrogen atmosphere," *J. Vac. Sci. Technol. A*, vol. 6, pp. 2945, April 1988.

[234] K. Li, A.T.S. Wee, J. Lin, Z. C. Feng and S. J. Chua, "X-ray Photoelectron Spectroscopy Evaluation on Surface Chemical States of GaN, InGaN and AlGaN Heteroepitaxial Thin Films Grown on Sapphire by MOCVD," *Mat. Res. Soc. Symp. Proc.*, vol. 618, pp. 303, 2000.

[235] P. K. Barhai, N. Kumari, I. Banerjee, S. K. Pabi, S. K. Mahapatra, "Study of the effect of plasma current density on the formation of titanium nitride and titanium oxynitride thin films prepared by reactive d.c. magnetron sputtering," *Vacuum*, vol. 84, pp. 896-901, 2010.

[236] I. Galesic, B.O. Kolbesen, "Formation of vanadium nitride by rapid thermal processing," *Thin Solid Films*, vol. 349, pp. 14-18, 1999.

[237] M. Kneissl, Z. Yang, M. Teepe, C. Knollenberg, O. Schmidt, P. Kiesel, N. M. Johnson, S. Schujiman, and L. J. Schowalter, "Ultraviolet semiconductor laser diodes on bulk AlN," *J. Appl. Phys.* vol. 101, pp. 123103 2007.

[238] A. Rice, R. Collazo, J. Tweedie, R. Dalmau, S. Mita, J. Xie, and Z. Sitar, "Surface preparation and homoepitaxial deposition of AlN on (0001)-oriented AlN substrates by metalorganic chemical vapor deposition," *J. Appl. Phys.* vol. 108, pp. 043510, 2010.

[239] M. E. Levinshtein, S. L. Rumyantsev, and M. S. Shur, "*Properties of Advanced Semiconductor Materials GaN, AlN, InN, BN, SiC, SiGe*," New York: Wiley, 2001.

[240] R. G. Banal, M. Funato, and Y. Kawakami, "Optical anisotropy in [0001]-oriented $Al_xGa_{1-x}N$/AlN quantum wells (x> 0.69)," *Phys. Rev. B*, vol. 79, pp. 121308, 2009.

[241] L. A. Coldren and S. W. Corzine, "*Diode lasers and photonic integrated circuits*," 1st ed. (Wiley, New York, 1995).

[242] E. F. Pecora, W. Zhang, A. Y. Nikiforov, J. Yin, R. Paiella, L. D. Negro, and T. D. Moustakas, "Sub-250 nm light emission and optical gain in AlGaN materials," *J. Appl. Phys.*, vol. 113, pp. 013106, 2013.

[243] B. Cheng, S. Choi, J. E. Northrup, Z. Yang, C. Knollenberg, M. Teepe, et al., "Enhanced vertical and lateral hole transport in high aluminum-containing AlGaN for deep ultraviolet light emitters," *Appl. Phys. Lett.*, vol. 102, p. 231106 2013.

[244] Y.-S. Liu, T.-T. Kao, K. Mehta, S.-C. Shen, T. Detchprohm, P. D. Yoder, H. Xie, F. Ponce, and R. D. Dupuis, "Development for Ultraviolet Vertical Cavity Surface

Emitting Lasers," *SPIE Photonics West OPTO*, San Francisco CA (February 13-18, 2016).

[245] J. Dorsaz, H.-J. Bühlmann, J.-F. Carlin, N. Grandjean, and M. Ilegems, "Selective oxidation of AlInN layers for current confinement in III–nitride devices," *Appl. Phys. Lett.*, vol. 87, pp. 072102, 2005.

[246] A. Castiglia, D. Simeonov, H. J. Buehlmann, J.-F. Carlin, E. Feltin, J. Dorsaz, R. Butté, and N. Grandjean, "Efficient current injection scheme for nitride vertical cavity surface emitting lasers," *Appl. Phys. Lett.*, vol. 90, pp. 033514, 2007.